UNIVERSITY OF LONDON

Imperial College of Science and Technology

Blackett Laboratory

Optics Section

# HOLOGRAPHIC MEASUREMENT OF GRADIENT REFRACTIVE INDEX PROFILES

Neil Richard Haigh

Thesis submitted for the degree of

Doctor of Philosophy of the University of London

and

The Diploma of Imperial College

October 1987

PHYSICS LIBRARY
BLACKETT LABORATORY
IMPERIAL COLLEGE
PRINCE CONSORT ROAD
LONDON SW7 2BZ

## ABSTRACT

A measurement of the refractive index profile in a graded index rod lens or an optical fibre is extremely important as it can be used to determine the transmission characteristics of the device and also verify the accuracy of the fabrication process. However, despite the existence of a large number of profiling methods there is a requirement for a technique which is relatively simple and could form the basis of a quality control test at the production stage.

This thesis investigates the application of holographic interferometry to the field of refractive index profiling and describes the construction of a real time holographic interferometer for studying graded index samples. Measurements are made upon two types of graded index rod: the graded index optical fibre preform (from which an optical fibre is drawn) and the graded index rod micro lens. Both these elements are characterised by having approximately parabolic refractive index profiles.

There is particular emphasis on a technique which will allow the direct comparison between a new unknown graded index sample and a sample with a previously established index profile. The theoretical accuracy of such a method is investigated along with the problems that are likely to be encountered. Index profiling via the established technique of shearing interferometry is also studied.

In the conclusion of the thesis, the results of the research project are reviewed and the use of holographic interferometry in index profile analysis is discussed.

**To my parents and Jancy.**

## ACKNOWLEDGEMENTS

I would like to thank my supervisor Robin Smith for his advice and encouragement during the period of this research project. I am also grateful to Morris Pimm of the students workshop for teaching me many invaluable workshop techniques.

I would also like to thank my friends and colleagues in the Applied Optics section at Imperial College for their support. In particular I pass on my thanks to Messrs A. Harley and P.M Channon for many enjoyable discussions on almost every topic under the Sun. The computing expertise of Don Burridge and Nick Wooder is also gratefully acknowledged. I am particularly indebted to Nick for taking the time and trouble to help me in the production of the theoretical interferograms plotted throughout this thesis.

Funding for this research project was provided by the Scientific and Engineering Research Council and by Pilkington Brothers PLC, Lathom, Lancashire. Pilkington Ltd also very kindly provided a generous maintenance grant.

I would also like to thank the many companies who supplied graded index samples for use during this research: Pilkington Ltd in Lancashire, The Nippon Sheet Glass Company of Japan, BICC Ltd Shepherds Bush in London, York Technology in Hampshire and Optical Fibres Ltd in Deeside.

CONTENTS

page

ABSTRACT 2

ACKNOWLEDGEMENTS 4

CONTENTS 5

LIST OF FIGURES 10

INTRODUCTION 15

1. CHARACTERISATION AND MANUFACTURE OF GRADED INDEX ELEMENTS

1.1 Introduction 17

1.2 Graded index rod micro-lens characteristics 19

1.2.1 The parabolic profile

1.2.2 Ray propagation in a GRIN micro-lens

1.2.3 The general profile equation

1.3 The graded index fibre 22

1.3.1 The alpha profile for an optical fibre

1.3.2 Ray propagation in optical fibres

1.3.3 The optical fibre preform

1.4 Fabrication of graded index optical fibres and rod lenses 26

1.4.1 Ion diffusion

1.4.2 Ion deposition

2. REFRACTIVE INDEX PROFILING TECHNIQUES AND ACCURACIES

2.1 Approaches to index profiling 28

2.1.1 Axial methods

2.1.2 Transverse methods

2.2 Measured parameters and accuracy requirements 30

2.2.1 Fibre/Preform Profiling

2.2.2 Micro lens profiling

2.3 Profile measurement characteristics 32

2.3.1 Absolute index values

2.3.2 Circular symmetry of the index profile.

2.3.3 Profile variation with rod length.

2.4 Transverse profiling principles 34

2.4.1 The transverse interference method

2.4.2 The transverse refraction angle method

2.4.3 The relationship between the transverse wavefront and the deflection function

2.4.4 Transverse shearing interferometry

3. THEORY OF HOLOGRAPIC INTERFEROMETRY

3.1 The Basic Holographic Process 45

3.2 The Fundamental Holography Equations 45

3.3 Holographic Interferometry 49

3.3.1 Double-exposure holographic interferometry

3.3.2 Single-exposure holographic interferometry

3.4 Single-exposure holographic interferometry applied to refractive index measurements 50

3.4.1 Introduction

3.4.2 Recording and reconstruction procedure

3.4.3 Introducing tilt fringes to the interferogram

4. HOLOGRAPHIC MEASUREMENT OF GRADIENT REFRACTIVE INDEX PROFILES: THE COMPARISON METHOD

4.1 The technique of holographic comparison 57

4.2 Computer simulation of the comparison method 59

4.3 The transverse wavefront 60

4.4 Parameters affecting the index distribution 64

4.4.1 The gradient constant

4.4.2 The absolute index values of the profile

4.4.3 Non-circularity of profile

4.4.4 Variation of profile with rod length

4.4.5 Conclusion

4.5 Change in rod diameter 73

4.6 Misalignment between rod positions 76

4.6.1 Transverse displacement (shear)

4.6.2 Longitudinal displacement (defocus)

4.6.3 Rotation of the rod about the optical axis (tilt)

4.7 Refractive index matching oil 84

4.7.1 Effect of an index mismatch

4.7.2 Temperature stability of the matching oil

4.7.3 Conclusion

4.8 The comparison method applied to preform rods 89

5. DESIGN AND CONSTRUCTION OF A LIVE FRINGE HOLOGRAPHIC INTERFEROMETER

5.1 The basic layout and components 92

5.1.1 The laser

5.1.2 Beamsplitter and beam ratios

5.1.3 Beam expansion

5.1.4 Beam collimation

5.2 Practical recording of the object wave 97

5.3 Hologram processing technique 98

5.3.1 Silver halide chemistry

5.3.2 The holographic plate and plateholder

5.3.3 Processing procedure

5.4 Choice of observation plane 104

5.5 Fringe analysis 105

5.5.1 The digitiser

5.5.2 Following a fringe shift

5.6 Choice of index matching oil 107

5.7 Graded index rod mounting techniques 108

6. PRACTICAL IMPLEMENTATION OF THE HOLOGRAPHIC COMPARISON METHOD

6.1 Temperature control of the index matching oil 111

6.2 Calibration of the refractive index of the matching oil 115

6.3 Accurate repositioning of the rod samples 118

6.3.1 Initial alignment and elimination of shear

6.3.2 Elimination of a longitudinal misalignment (defocus)

6.4 Conclusion 127

7. REFRACTIVE INDEX PROFILE RECONSTRUCTION IN THE HOLOGRAPHIC COMPARISON METHOD

7.1 Profile reconstruction and the Abel transform pair 128

7.2 Optical pathlength computation in the refractionless limit 132

7.3 Ray curvature and optical pathlength 136

7.3.1 Preliminaries

7.3.2 Ray optical pathlength through the field

7.3.3 The refraction angle

7.3.4 The apparent ray height y'

7.3.5 Optical pathlength from input to object plane

7.4 Ray curvature error analysis for index profiling via the comparison method 145

7.4.1 The fringe shift function

7.4.2 Reconstructing the index difference and the index profile

7.4.3 Misfocussing error

7.5 Practical Reconstruction of the Index Profile 153

7.5.1 The inverse Abel transform in the prescence of signal noise

7.5.2 Power series smoothing

7.5.3 Fringe fitting procedure

7.6 The effect of rod diameter variations upon index profile reconstruction 159

7.7 Summary 162

8. RESULTS: HOLOGRAPHIC SHEARING INTERFEROMETRY

8.1 Experimental procedure for the shearing method 164

8.2 BICC ion deposition preform 166

8.3 Pilkington ion stuffing preform 168

8.4 Nippon Sheet Glass Company - rod micro-lens 173

9. RESULTS: HOLOGRAPHIC COMPARISON INTERFEROMETRY

9.1 Introduction 177

9.2 BICC Ion deposition preform 177

9.3 Pilkington ion stuffing preform 181

9.4 Nippon Sheet Glass Company - rod micro-lens 185

9.4.1 Comparison of rods from the same production lot

9.4.2 Comparison of rods from different production lots

9.5 Summary 197

CONCLUSION 199

APPENDICES 205

# LIST OF FIGURES


| Figure | Title | Page |
|---|---|---|
| | Chapter One | |
| 1.1 | The refractive index profile of a graded index rod. | 18 |
| 1.2 | Ray propagation in a graded index rod. | 20 |
| 1.3 | The rod micro-lens. | 21 |
| 1.4 | The step index optical fibre. | 24 |
| | Chapter Two | |
| 2.1 | Basic index profiling principles. | 29 |
| 2.2 | The transverse interference method. | 35 |
| 2.3 | The transverse wavefront. | 36 |
| 2.4 | The transverse refraction angle method. | 38 |
| 2.5 | Ray direction on a wavefront. | 40 |
| 2.6 | The transverse shearing method. | 42 |
| | Chapter Three | |
| 3.1 | The basic holographic process. | 46 |
| 3.2 | Holographic phase interferometry. | 51 |
| 3.3 | Introducing tilt fringes to an interferogram. | 55 |
| | Chapter Four | |
| 4.1 | The holographic comparison method. | 58 |
| 4.2 | The refractionless limit approximation. | 61 |
| 4.3 | Theoretical interferogram: Change in the gradient constant. | 65 |
| 4.4 | Index difference due to a change in the gradient constant. | 66 |
| 4.5 | Theoretical interferogram: Change in the absolute refractive index values. | 68 |
| 4.6 | Constant index difference between the profiles. | 69 |
| 4.7 | Theoretical interferogram: Change in both the absolute refractive index values and the gradient constant. | 70 |
| 4.8 | Theoretical interferogram: 0.5% Change in the diameter of the rod. | 72 |

| Figure | Title | Page |
|---|---|---|
| 4.9 | Theoretical interferogram: Change in profile parameters corresponding to an ambiguous fringe pattern | 74 |
| 4.10 | Misalignment of the test rod. | 75 |
| 4.11 | Theoretical interferogram: Shearing misalignment of the test rod. | 77 |
| 4.12 | Defocus between similar wavefronts. | 78 |
| 4.13 | Theoretical interferogram: Defocus misalignment of the test rod. | 79 |
| 4.14 | Rotation of the rod about the optical axis. | 83 |
| 4.15 | Theoretical interferogram: Rotation of the rod about the optical axis. | 82 |
| 4.16 | Theoretical interferogram: Effect of an imperfect index match at the rod boundary and a diameter variation. | 85 |
| 4.17 | Theoretical interferogram: Effect of an imperfect index match at the rod boundary and a shearing misalignment. | 86 |
| 4.18 | Theoretical interferogram: Change in the matching oil temperature of 1°C. | 87 |
| | Chapter Five | |
| 5.1 | The holographic interferometer. | 93 |
| 5.2 | Through focus images of a transversly illuminated GRIN rod. | 96 |
| 5.3 | Effect of emulsion shrinkage upon a volume hologram. | 99 |
| 5.4 | The liquid gate holographic plateholder. | 101 |
| 5.5 | Digitised interferogram and fitted fringe centre. | 106 |
| 5.6 | Translation stages for manipulating rod lens position. | 109 |
| | Chapter Six | |
| 6.1 | Experimental interferogram: Change in matching oil temperature of 1°C. | 112 |
| 6.2 | The temperature controlled optical cell. | 114 |
| 6.3 | Experimental interferogram: Calibration of the index matching oil. | 116 |
| 6.4 | Experimental interferogram: Effect of an imperfect index match at the rod boundary and a shearing misalignment. | 117 |
| 6.5 | Experimental interferogram: Tilt misalignment of the test rod. | 119 |

| Figure | Title | Page |
|---|---|---|
| 6.6 | Experimental interferogram: Towards a re-alignment of the test rod. | 120 |
| 6.7 | Experimental interferogram: Defocus misalignment of the test rod. | 122 |
| 6.8 | Apparatus for the elimination of the defocus problem. | 123 |
| 6.9 | Experimental interferogram: Elimination of the defocus problem. | 125 |
| 6.10 | Experimental interferogram: Rod lens re-aligned in the optical cell | 126 |
| | Chapter Seven | |
| 7.1 | The forward and inverse Abel transform as applied to refractive index profiling | 129 |
| 7.2 | Computation of the inverse Abel transform | 131 |
| 7.3 | Computing a fringe shift for profiles having a random error | 133 |
| 7.4 | Ray path through a graded index field | 135 |
| 7.5 | Refractive index profiling and ray curvature | 137 |
| 7.6 | The deflection function for a graded index rod lens | 144 |
| 7.7 | Difference between the apparent ray height and the input ray height | 144 |
| 7.8 | Fringe shift computation error of the refractionless limit applied to the holographic comparison method | 147 |
| 7.9 | Error of reconstructing the refractive difference using the refractionless limit approximation. | 149 |
| 7.10 | Error in the refractive index values of the profile reconstructed using the refractionless limit. | 150 |
| 7.11 | Fringe shift as a function of the misfocus of the observation plane | 150 |
| 7.12 | Computation of the inverse Abel transform in the prescence of noise | 152 |
| 7.13 | Fitting an even order power series to the reconstructed index difference | 154 |
| 7.14 | Fitting a power series to the noisy fringe data | 155 |
| 7.15 | Profile reconstruction by fringe fitting with expected functions | 158 |
| 7.16 | Profile reconstruction error for a GRIN rod with a slight diameter variation | 161 |
| 7.17 | Theoretical interferogram: A 2 micron change in the diameter of a 2mm rod. | 160 |

| Figure | Title | Page |
|---|---|---|
| | Chapter Eight | |
| 8.1 | Dependence of the magnitude of the fringe shift upon the shearing distance | 166 |
| 8.2 | Shearing interferogram: Ion deposition preform | 167 |
| 8.3 | Shearing interferogram: Ion stuffing preform | 169 |
| 8.4 | Refractive index profile of an ion stuffing preform measured via holographic shearing interferometry | 170 |
| 8.5 | Deflection function of the ion stuffing preform measured via the transverse refraction angle method | 171 |
| 8.6 | Refractive index profile of the ion stuffing preform calculated from the transverse refraction angle method | 172 |
| 8.7 | Shearing interferogram: Graded index rod micro-lens | 174 |
| 8.8 | Refractive index profile of a graded index micro-lens measured via holographic shearing interferometry | 175 |
| | Chapter nine | |
| 9.1 | Experimental interferogram - Ion deposition preform: Preform rotated about its axis by 90°. | 178 |
| 9.2 | Experimental interferogram - Ion deposition preform: Axial variation of the index distribution. | 179 |
| 9.3 | Experimental interferogram - Ion stuffing preform: Preform rotated about its axis by 0.5°. | 182 |
| 9.4 | Experimental interferogram - Ion stuffing preform: Preform rotated about its axis by 90°. | 183 |
| 9.5 | Experimental interferogram - Ion stuffing preform: Axial variation of the index distribution. | 184 |
| 9.6 | Experimental interferogram - Selfoc micro lens: Comparison of rods produced within the same production lot. | 186 |

| Figure | Title | Page |
|---|---|---|
| 9.7 | Experimental interferogram - Selfoc micro lens: Comparison of rod samples A and B. | 188 |
| 9.8 | Results for the comparison of rod samples A and B. | 189 |
| 9.9 | Experimental interferogram - Selfoc micro lens: Comparison of rod samples A and C. | 191 |
| 9.10 | Results for the comparison of rod samples A and C. | 192 |
| 9.11 | Further analysis of the comparison of rod samples A and C. | 193 |
| 9.12 | Experimental interferogram - Selfoc micro lens: Comparison of rod samples B and C. | 195 |
| 9.13 | Results for the comparison of rod samples B and C. | 196 |

# INTRODUCTION

This thesis investigates the application of holographic interferometry to the measurement of the refractive index distributions in graded index (or GRIN) media. In particular, there is emphasis on the development of a technique for directly comparing the refractive index distributions within nominally identical graded index rods. Such a method could have great potential at the production stage of a GRIN element where a fast and accurate measurement of the index profile is frequently desired.

Before we can describe the proposed method in detail, it will be necessary to discuss some important preliminary topics, and so the first three chapters of this thesis briefly review several relevant fields.

In the first chapter, we describe the typical characteristics of two classes of graded index element : the graded index optical fibre preform (from which an optical fibre is drawn) and the rod micro lens. There is also a brief summary of their methods of fabrication.

The second chapter discusses the important features that are required in a refractive index profiling method. Several 'transverse' profiling techniques are also described.

The field of holographic interferometry is introduced in chapter three, where we describe how the technique of wavefront reconstruction can be used to monitor changes in the refractive index distribution of a transparent (phase) object.

In chapter four, we introduce the proposed application of holographic interferometry to refractive index profiling; the technique is referred to as the holographic comparison method. Appropriate expressions for the fringe shifts that we would expect to observe in a practical interferometer are derived, and the theoretically expected interferograms are plotted using a computer program. The potential accuracy of the method is assessed along with the problems that are likely to be encountered when developing the practical system.

Chapter five describes the design and construction of a live fringe holographic interferometer for studying the refractive index distributions in transparent (phase) media. The design of the interferometer is quite general and chapter six considers how the apparatus

must be particularly adapted for the practical development of the holographic comparison method. This includes the design of an optical cell for maintaing a small volume of refractive index matching oil at a specified temperature, and an interferometric method for accurately positioning graded index rods in an optical cell. Several experimental interferograms are plotted and these may be compared with the theoretical predictions of chapter four.

In chapter seven we digress from the holographic method, and consider how we 'reconstruct' a refractive index distribution from measured 'transverse' profiling data. Of importance is the verification of the refractionless limit approximation for analysing ray paths in graded index media.

Chapter eight presents the experimental results for index profiling via a 'live fringe' shearing interference method. The principles of the method are based upon an established refractive index profiling technique.

Chapter nine presents the experimental results for the interferometric comparison of the refractive index distributions in GRIN rod preforms and micro-lenses.

Finally, we conclude the thesis with a review of some of the important issues raised by the research project. In particlar we must discuss whether the comparison method would be a viable technique for measuring the refractive index distributions in graded index rod elements ; particularly at the production stage.

# CHAPTER ONE

# CHARACTERISATION AND MANUFACTURE OF GRADED INDEX ELEMENTS

## 1.1 Introduction

During the last two decades, there has been great interest in the fabrication of optical elements that have an inhomogeneous refractive index distribution. In particular, the graded index optical fibre has begun to be widely used in optical communication systems and the graded index rod micro-lens has found useful application in the field of integrated optics as well as conventional imaging systems.

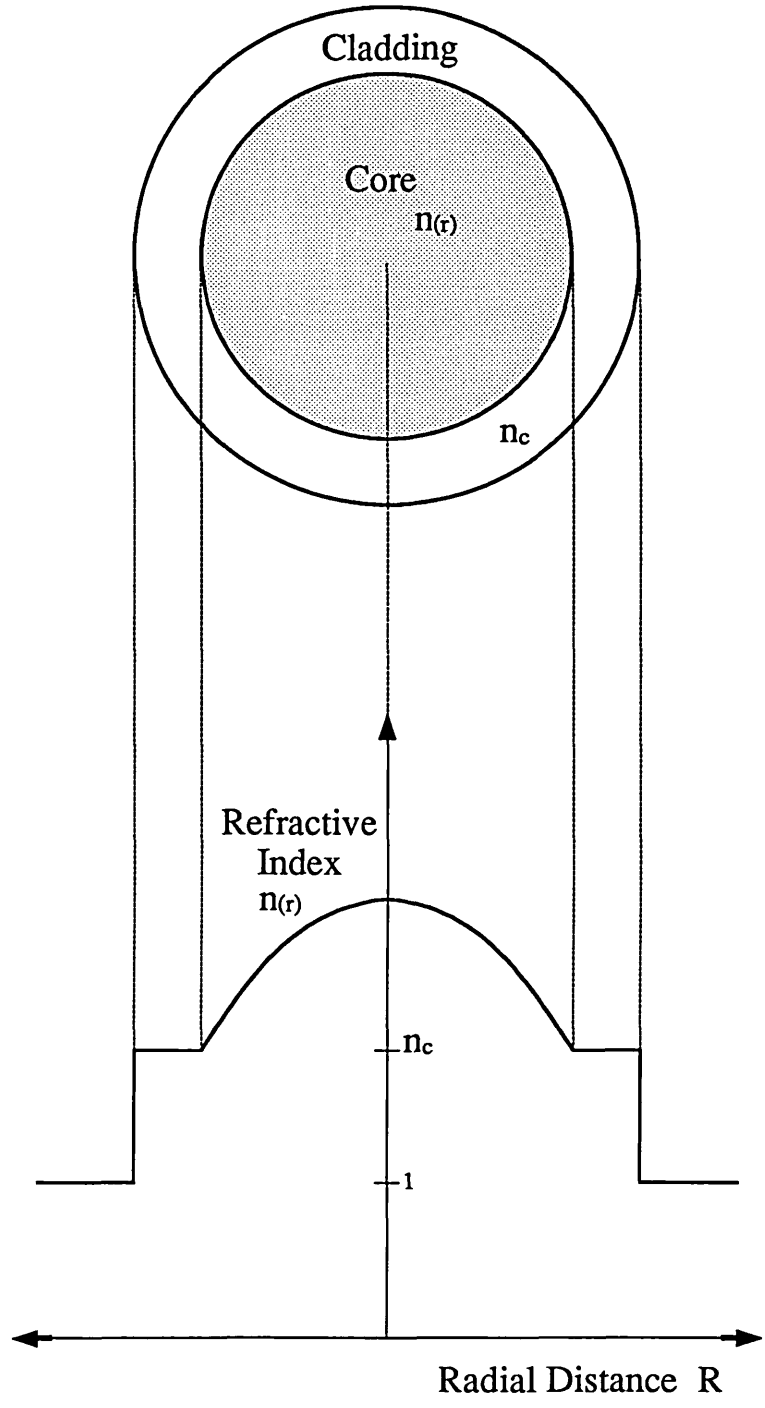
These elements are similar devices having cylindrical symmetry and a refractive index distribution that decreases in an approximately parabolic manner in the radial direction. A typical graded index rod profile is illustrated in figure 1.

The graded index (or GRIN) distribution determines all of the major transmission properties of the element, and so there is a great emphasis on the accurate fabrication and subsequent measurement of the index profile in the field of gradient index design.

This thesis investigates the application of holography to the measurement of the refractive index distribution in a graded index element, and in particular is concerned with establishing a technique that is both fast and accurate and could form the basis of a go/no-go test at the production stage.

Two types of GRIN element are studied: the graded index optical fibre preform (from which an optical fibre is drawn) and the graded index rod micro-lens. In this chapter the various parameters that are used to characterise these elements are introduced along with a brief discussion of common techniques of their manufacture.

Figure 1.1: The Refractive Index Profile of a Graded Index Rod



## 1.2 Gradient Index Rod Micro-lens Characteristics

### 1.2.1 The Parabolic Refractive Index Profile

A gradient index rod lens (figure 1.3a) is a cylindrical glass rod typically 1-2mm in diameter, 4-6mm in length and it has a refractive index distribution usually described[1] by

1.1) $$n^2(r) = n_0^2(1 - A(r/a)^2)$$

where $r$ = Radial distance from rod axis

$n_o$ = Axial refractive index

$A$ = gradient constant.

In general, rod lenses do not have a cladding and the edge (or peripheral) refractive index is given by $n_1 = n_o[1-A]^{1/2}$.

The difference between the axial and peripheral index values is only small ($\delta n \approx 0.04$) so that $A \approx 0.05$,thus the profile equation (1.1) is frequently simplified to

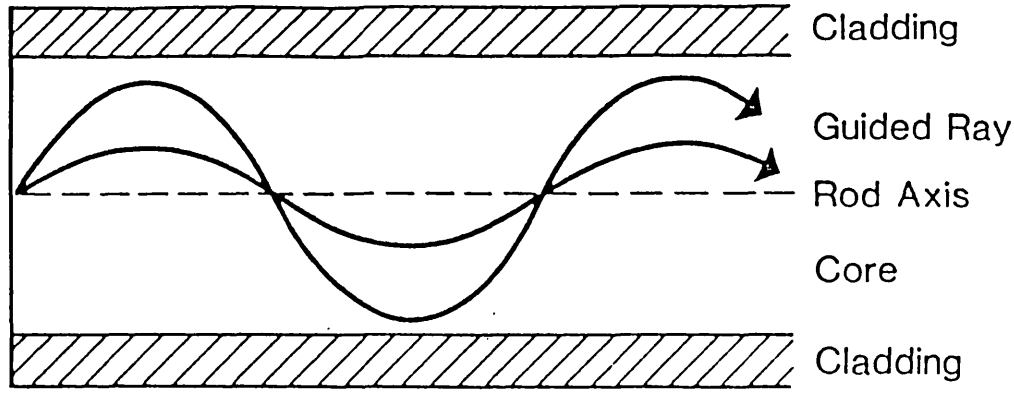
1.2) $$n(r) = n_0(1 - \tfrac{1}{2} A(r/a)^2)$$

### 1.2.2 Ray Propagation in a GRIN Micro-lens

In a graded index medium, light rays follow curved paths rather than the more familiar straight lines in conventional refractive media. We can show [Appendix A] that for a rod lens with an ideal index distribution (§1.2.3), all rays entering the lens follow sinusoidal paths and are periodically focussed along the length of the rod (see figure 1.2). Furthermore, the amplitude of the sinusoidal oscillation is dependent upon the angle at which the light enters the rod, and the focussing period is determined by the strength of the index gradient.

In practice, errors in the fabrication process will lead to aberrations in the transmission properties of the lens. For example, the focussing period may be dependant upon the ray input angle or the profile may have an ideal form over only a small radial range.

Figure 1.2 : Ray Propagation in a Graded Index Rod



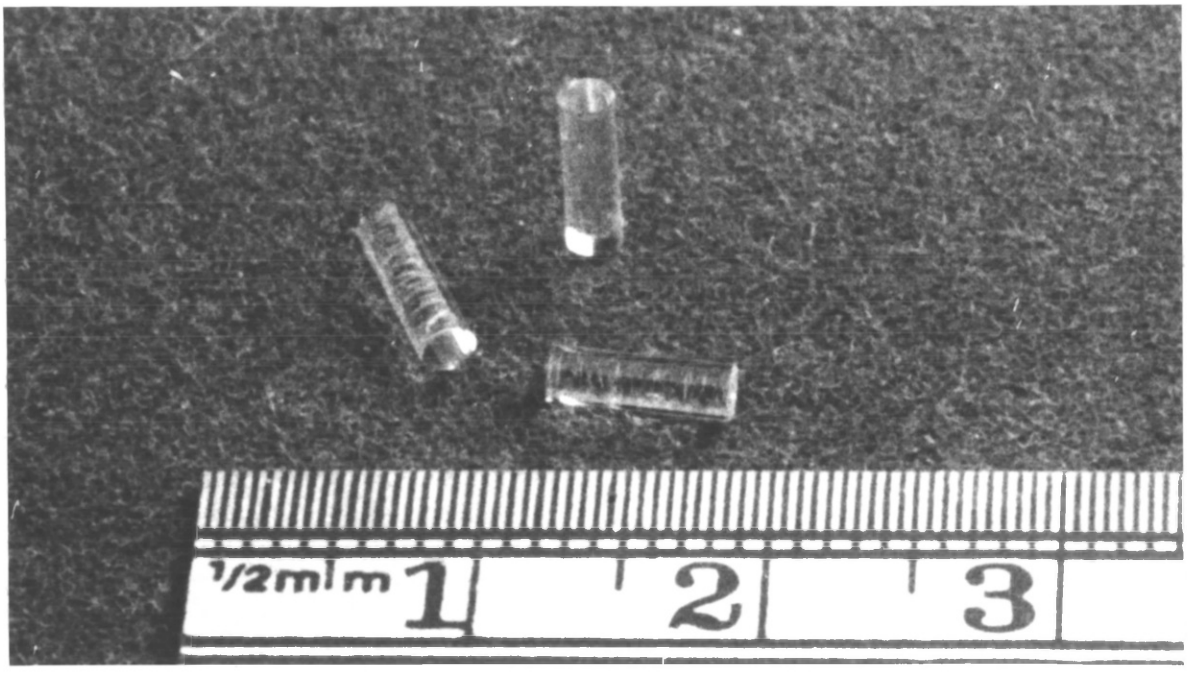

An illustration of imaging through a microlens is given in figure 1.3b. Note that unlike a conventional lens, the rod endfaces are flat and imaging is achieved entirely by the index gradient. Micro-lenses are useful because of their small size and because imaging can be achieved over a very small distance compared to conventional lens systems. For example, an array of rod lenses can be used as a compact and lightweight 1:1 imaging system and indeed such a system has been used to replace the conventional lens system in certain photocopiers[2].

Another useful property of a rod lens is that the imaging properties are dependant upon the length of the rod. For example, in their application to integrated optics, rod lenses are commonly designed to be quarter 'pitch' in length so that collimated light incident upon one face of the rod is brought to a point image on the rear face. In this manner, rod lenses are useful for efficiently coupling light into or out of optical fibres (figure 1.3c).

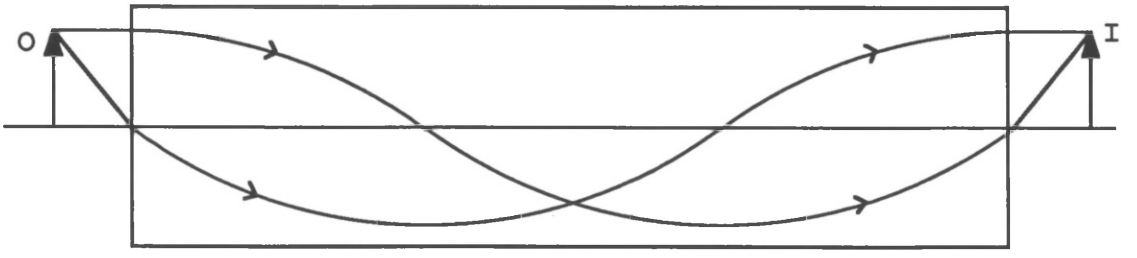
In this research, measurements were made upon 2mm diameter graded index rod lenses supplied by the Nippon Sheet Glass Company of Japan.

## Figure 1.3 : The Rod Micro-lens

a) Size

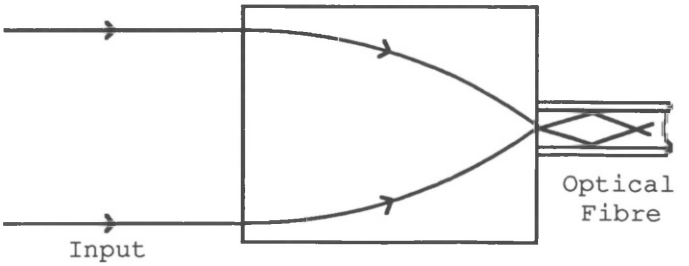



b) Imaging using A GRIN rod




Three Quarter Pitch Lens

c) Coupling Light into an Optical Fibre




Quarter Pitch Rod Lens

1.2.3 The General Profile Equation

Equation 1.2 is the most common expression for a parabolic index profile in a micro-lens. However, such a square law medium will not focus all rays identically (see Appendix A) and only those rays that propagate at small angles to the optic axis (paraxial rays) are focussed with equal period.

A more general profile description is a power series expression[2]

$$(1.3) \qquad n^2(r) = n_0^2(1 - h_2(gr^2) + h_4(gr^4) - h_6(gr^6) + \ldots\ldots\ldots\ldots$$

where g = Quadratic gradient constant (similar to $\sqrt{A}$). The higher orders in this series can be used to take profile fabrication errors into account[3]. There is in theory, no one set of optimum values for the coefficients $h_2, h_4, h_6$ ....to satisfy the exact focussing criterion. Their values will be determined by any focussing or imaging conditions stipulated for the lens.

For example the ideal distribution for focussing meridional rays (rays that pass through the rod axis) is given[2] as

$$(1.4) \qquad n^2(r) = n_0^2 \mathrm{sech}^2(gr)$$

Such a medium would not focus skew rays (ie. rays not passing through the rod axis). Ray trajectories in media governed by equations (1.1) and (1.4) are examined in detail in the appendix (A).

1.3 The Graded Index Optical Fibre

1.3.1 The Alpha Profile for an Optical Fibre

The graded index optical fibre has an index profile similar to that in a rod micro-lens with the exception that there is a constant index cladding surrounding the GRIN core (figure 1.1). The index profile is described by the Alpha profile

(1.5) Core: $n^2(r) = n_0^2(1 - 2\Delta(r/a)^\alpha)$

Cladding: $n_c = n_0(1 - 2\Delta)^{1/2}$

where $n_0$ = Axial refractive index

$n_c$ = Cladding refractive index

$\Delta$ = Delta Parameter

The delta parameter is closely related to the gradient constant A used in rod lens profile expressions ( $\Delta = {}^1/_2A$). The core diameter is around 60 microns and the overall diameter is usually around 125 microns. The exponent alpha has a value close to 2 and again the profile is often described as being parabolic.

The profile expression is often simplified to

(1.6) $n(r) = n_0(1 - \Delta(r/a)^2)$

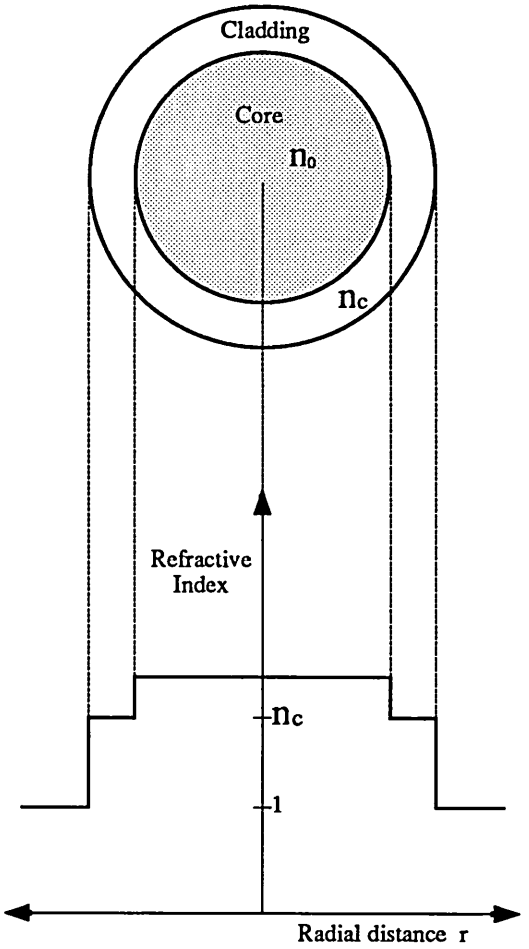
1.3.2 Ray paths in Optical fibres

The conventional step index fibre (figure 1.5a) has a constant index core, and light propagates down the fibre via the process of total internal reflection (fig. 1.5b). Only rays with certain discrete angles of propagation are guided and these rays are referred to as guided modes.

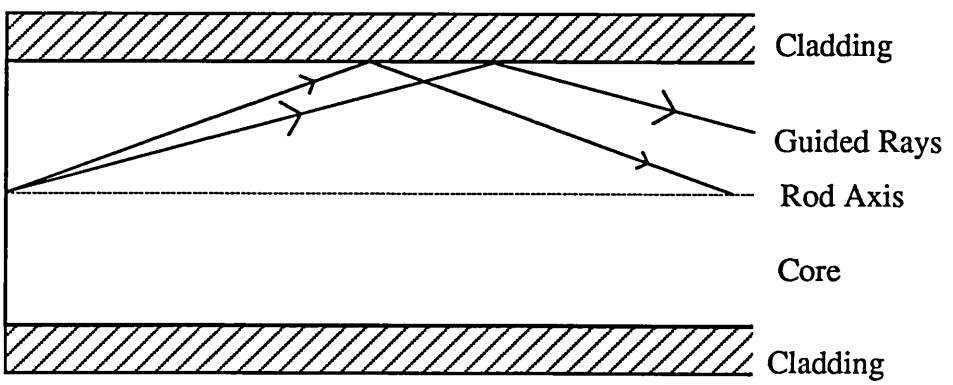
Signal transmission in a step index fibre is limited by an effect known as intermodal dispersion, in that the various guided modes take differing times to reach the end of the fibre. (The propagating light rays follow different geometric paths.) A consequence of this effect is that a pulse launched into the fibre tends to spread out and lengthen in proportion to the fibre length. Intermodal dispersion dramatically reduces the signal rate (bandwidth) of the fibre and it can only be overcome by making a fibre with a small core diameter ($\approx 5\mu m$) so that essentially only 1 mode (ray) propagates. The problem with these 'monomode' fibres is that fibre coupling and light launching is difficult at such a small dimension.

Figure 1.5: The Step Index Optical Fibre

a) The Refractive Index Profile




b) Ray Propagation in a Step Index Fibre



The graded index fibre was designed to overcome the above limitations of the step index fibre. As in the rod micro-lens, ray paths in a GRIN fibre are approximately sinusoidal (fig. 1.2) and the periodic focussing of the propagating rays ensures that the guided modes arrive at the fibre end at about the same time. Thus intermodal dispersion is reduced GRIN fibres can maintain high-bandwidth performance whilst having a conveniently large core diameter (approx. 60 microns). In theory, the maximum achievable bandwidth is in the giga-hertz region. However, there is no manufacturing process that can produce the corresponding index profile with sufficient accuracy. The currently achievable bandwidth is around 250 MHz.km and this is approximately 5 times that in the multimode fibre.

### 1.3.3 The Optical Fibre Preform

To fabricate an optical fibre it is usually necessary to produce a preform rod. A preform being essentially a giant glass rod having the same refractive index distribution as the target fibre, although on a much larger scale. Typical preform dimensions are, a diameter of between 5-50mm and a length of 1-2 metres. The optical fibre is pulled from the heated tip of the preform rod into a hair-like thread. The final fibre diameter ( ~ 130 microns) is only a fraction of the preform diameter and thus several kilometres of fibre may be drawn from just one preform rod.

When producing fibres in this way, it is vital that the index profile in the preform is identically preserved in the fibre and is therefore unaffected by the drawing process. Work by H.M.Presby[4] has shown that with a carefully controlled drawing procedure this will be the case.

Because the aim of this research was to investigate the potential use of holography in assessing the quality of GRIN rods at the production stage, the work in this thesis involves measurements made upon preform rods rather than fibres.

In chapter two, several profiling methods are described but it is worth noting at this stage that any preform profiling method must be inherently non-destructive.

## 1.4 Fabrication of Graded Index Optical Fibres and Rod Lenses

Having introduced and characterised graded index elements, we conclude this chapter with a brief description of GRIN production methods. There are many techniques available [for review see Ghatak[5]], however only two relevant methods are described.

To produce graded index materials, it is necessary to vary the chemical composition or internal structure of a glass. In particular the refractive index of a glass will depend upon the presence of certain cations and indeed in graded index design the presence and proportion of these ions is usually under strict control.

Fabrication techniques can be broadly divided into two major classes:

### 1.4.1 Ion Diffusion

In the ion diffusion technique a homogeneous glass rod (diameter between 1-10mm) is placed in a fused salt bath and dopant ions (Li+,K+,Na+,Tl+) diffuse into and out of the rod. The resulting distribution of ions in the rod determines the refractive index profile and this may depend upon several process parameters, such as the diameter of the rod, the bath temperature andthe diffusion period. By empirically varying these parameters and utilising computer simulations of the diffusion process, a prescribed refractive index profile may be produced.

Rod lenses are produced by a diffusion process called the Ion exchange method[5].

### 1.4.2 Ion Deposition

In the deposition methods[5], layers of doped glass are deposited sequentially onto the inside or outside of a rotating seed rod. Typical dopant ions are Ge+, Al+, Tl+, P+, B+ and the index variation is produced by gradually changing the concentration of the dopant ions as the glass layers build up. Thus the profile is dynamically constructed in a 'staircase' manner. The individual deposition layers can be observed by eye in the fibre preform, however they are too small to be seen in the drawn fibre.

The deposition technique is favoured in the production of optical fibre preforms.

## REFERENCES

1.1) K. Koizuma, K. Nishizawa and K.Sono, " Selfoc Lens Handbook," Nippon Sheet Glass Company Limited, 1981.

1.2) K. Iga and I. Kokubun, M. Oikawa, "Fundamentals of Micro-optics," Academic Press, 1984.

1.3) N. Yamamoto and K. Iga, "Evaluation of gradient index rod lenses by imaging," Applied Optics 19, 1101, 1980.

1.4) H.M.Presby, Bell Systems Technical Journal 54, 1681, (1975).

1.5) A. Ghatak and K. Thyagarjan, "Graded Index Optical Waveguides: A Review," Progess in Optics XVIII, North-Holland Publishing Company, Oxford, 1980.

# CHAPTER TWO

## REFRACTIVE INDEX PROFILING TECHNIQUES AND ACCURACIES

Having introduced graded index elements in chapter one, we now go on to discuss the various techniques for measuring their most important property: the graded index profile. Such a measurement is essential not only for the determination of the transmission characteristics of the device but also for quality control and assessment at the production stage. A large number of profiling techniques have been developed over the last decade or so and a comprehensive account is beyond the scope of this thesis. For a complete review of the field, the interested reader is referred to the works of Marcuse[1], Stewart[2] and Iga[3].

In the following sections, we will be restricted to methods that highlight important and relevant details for use later on in this work.

### 2.1 Approaches to index profiling

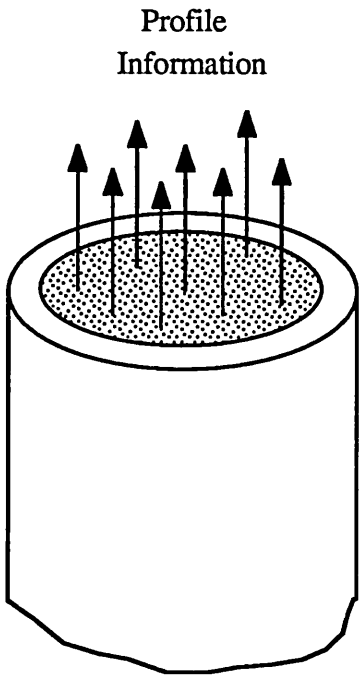
There are many profiling techniques available,to the user. Factors vital to any technique will include accuracy, adaptability, cost of equipment and measurement time. For convenience, the profiling methods are best split into two main categories: axial and transverse.

#### 2.1.1 Axial methods

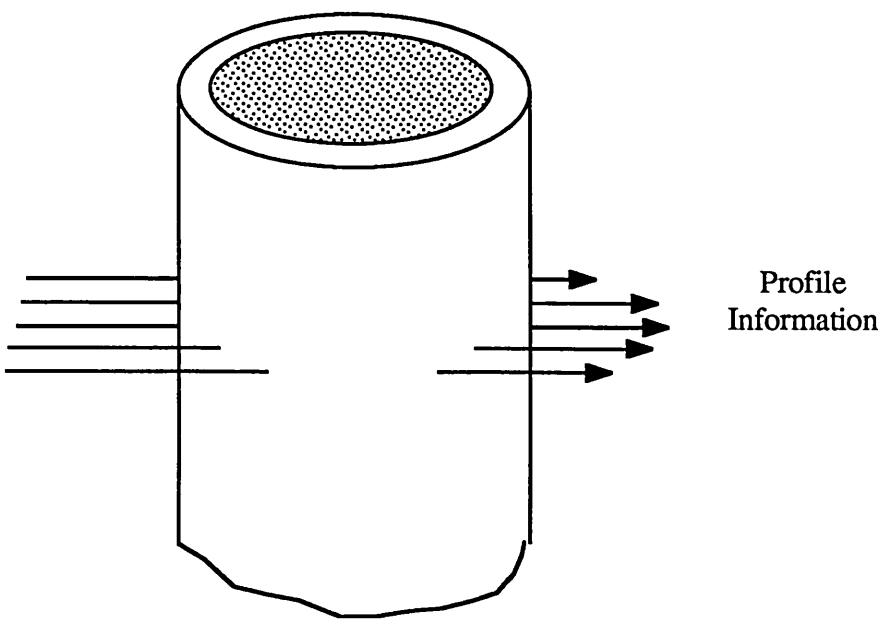
The axial methods (figure 2.1a) require access to at least one endface of the rod and in some techniques the sample must be cut to a chosen length. The main advantage of these methods is that the index profile is invariably yielded directly from the measured data, in most cases leading to accurate and unambiguous results. Another useful property of the axial methods is that the refractive index distribution may be measured across the whole core and so there is no need to assume any circular symmetry of the profile.

Figure 2.1: Basic Index Profiling Principles

a) Axial Methods




b) Transverse Methods



The disadvantage with the axial methods is that they are frequently destructive and cannot be used to evaluate the variation of the index profile with rod length. For these reasons axial methods are not too suitable for preform profiling.

### 2.1.2 Transverse methods

In the transverse methods (fig. 2.1b), the rod is usually probed with light incident transversely to the fibre axis. Frequently the rod is immersed in refractive index matching oil to eliminate the otherwise strong refraction at the air-cladding boundary. The incident light is then only affected by the index distribution in the graded index core. After passing through the sample, the form of the transmitted light is detected and the index profile calculated.

The main advantages of the transverse methods are that they are inherently non-destructive with minimal sample preparation time. They can also be readily adapted to determine the axial variation of the index profile. For these reasons, transverse methods are preferred for rod-lens and fibre preform profiling.

The main disadvantage lies in the fact that the measured data has to undergo a fairly complicated mathematical transform before the profile can be revealed. Further problems can also be created if the index distribution cannot be assumed to be circularly symmetric (see § 2.3.2).

## 2.2 Measured parameters and accuracy requirements

In fibre index profiling, some or all of the following parameters are usually determined: $n_0$ (the axial index), $n_1$ ( the edge or cladding index), $\Delta$ (the delta parameter) and $\alpha$ ( the profile exponent). (With similar parameters for a rod lens.)

We may define the accuracy of a refractive index profiling method as the precision with which the refractive index values are determined thus

$$(2.1) \qquad \varepsilon_n(r) = n_{calc}(r) - n_{true}(r).$$

In this equation, $n_{calc}(r)$ may be an experimentally calculated index value or it may be produced by a theoretical simulation. For an accurate profiling method, the precision should be $\varepsilon_n( ) \approx 1 \times 10^{-5}$ (Presby[4]). ie we are confident of knowing the refractive index values and profile parameters to around the fifth decimal place.We shall also use this expression to gauge the accuracy of the holographic profiling method described in this thesis.

2.2.1 Fibre/Preform profiling

Refractive index profiling is obviously important for quality assurance in optical fibre production. However, a preform profile can also be used to predict the bandwidth performance of a fibre before it is drawn (Marcuse[1]). It is this application to bandwidth prediction that has led to the very high accuracy requirements for index profiling techniques.

The achievable bandwidth is heavily dependent upon the profile shape and so a measure of the accuracy requirements can be obtained by considering the effect of profile distortions upon the bandwidth[5]. For example, Presby[4] states that $\alpha$ must be determined to within 0.05% of its optimum value and $\Delta$ must be measured with a precision of 1 part in $10^4$ if a meaningful assessment of the bandwidth is to be obtained.

2.2.2 Micro-lens profiling

A measurement of the index profile for a rod lens is used to predict the imaging and focusing properties of the lens. As in fibre profiling, determination of the profile shape is a vital factor. Usually, the profile equation (1.3) is fitted to the measured data and the exapansion coeficients h2,h4 and h6 are determined [Ohtsuka[6]]. Deviations of these coefficients from their ideal values can then be directly related to aberrations for the rod lens [Yamamoto[7]].

Most rod lens profiling techniques are based upon established preform profiling methods. However, it is worth mentioning that there are also methods [ Yamamoto[7] and

Cline[8]] that study the imaging capabilities of the lens directly. The quality of the index profile can then be inferred from this measurement.

Rod lens profiling techniques are required to have the same degree of accuracy as fibre profiling methods ($\varepsilon n \approx 1 \times 10^{-5}$). The specification sheets supplied by the Nippon Sheet Glass Company for their GRIN rod lenses reveal the profile information by quoting the axial refractive index ($n_0$) and the quadratic gradient constant $\sqrt{A}$ to three figures only. Most of the lens properties (eg. focal length and pitch) can be calculated with sufficient accuracy from this information.

It is important to note that these parameters cannot be used reliably to reproduce the complete index profile of the lens. This is because $\sqrt{A}$ is fitted to only the axial region of the profile (typically up to half the rod radius)[9], where the lens properties are of most importance.

## 2.3 Profile measurement characteristics

We now consider some further characteristics that may be required in an index profiling method.

### 2.3.1 Absolute index values

The variation of the refractive index of glass with wavelength (material dispersion) gives rise to wavelength dependant transmission properties of a GRIN element. The major effect is chromatic aberration, as the imaging quality is otherwise only dependent upon the strength of the index gradient and the profile shape. Chromatic aberration of the lens implies that the focal length, magnifying power and focussing period will all depend upon the wavelength at which the device is used. Thus ideally, the gradient constant and axial index for a lens must be determined for a range of wavelengths. However it is quite common for a profiling method to measure the index distribution using the most convenient light source available and interpolate the index values at another wavelength from the dispersion relationship for the glass. The dispersion relationship is usually assumed to be linear and thus any distortion of the index profile across the range of

wavelengths is ignored[2].

Visible light sources are typically used in index profiling despite the fact that most GRIN elements are designed to operate in the (longer) infra-red. As well as convenience, this also yields a suitable improvement in the resolution of the method. A Helium-Neon laser ($\lambda$ = 632 nm) was chosen for this project, largely because this is one of the most practical sources for holographic work.

### 2.3.2 Circular symmetry of the index profile.

Profiling techniques should be able to detect whether the refractive index distribution is circularly symmetric. There is usually no problem with axial methods as the whole core area may be investigated. The transverse methods must be modified to detect departure from circularity by measuring the index profile at different angular orientations of the rod under test. The 2-d profile can then be calculated by using computer aided tomographic techniques[10,11,12]. For example, around 3 angular projections are required to check a near-circular preform whereas a fairly complex asymmetric profile may require upwards of 30.

### 2.3.3 Profile variation with rod length.

Axial profiling methods can only measure the index profile at one position (usually an end) of a graded index rod. In fibre profiling, the bandwidth of the fibre is then calculated with the assumption that this profile is identically maintained along the length of the fibre. However, it is usually important that preform profiling methods can determine the axial variation of the profile. Such a measurement will reveal which sections of the rod should not be used for fibre production as well as indicate failings of the fabrication process.

With a transverse profiling method, finding the axial variation of the profile is relatively easy as the rod may simply be profiled at intervals along the length of the rod.

## 2.4 Transverse profiling principles

The holographic profiling methods described elsewhere in this thesis are based upon transverse profiling principles (§2.1.2) and so we now describe some of the most common transverse profiling methods. Most of the practical and theoretical details are omitted for brevity, however some of the more important aspects of the transverse profiling techniques are expanded upon in chapter 7.

### 2.4.1 Transverse interference method

The transverse interference (TI) method[1] requires the use of a Mach-Zehnder interferometer, usually in the form of an interference microscope. Such an instrument is schematically illustrated in figure 2.2. A plane wavefront is input to the interferometer and this is split by a beamsplitter into two waves W1 and W2 and these are directed around the two branches of the apparatus. One branch is referred to as the reference arm and the other is referred to as the test arm. It is very important that the optical components in these two arms are of a very high quality and are identically matched to ensure that there are no aberrations introduced into either of the split waves. The two waves are then recombined by the second beamsplitter and they interfere; the resultant interference pattern (interferogram) is then viewed on a screen. In this initial state, both waves W1 and W2 are plane and the interferogram will be uniformly light or dark depending upon the relative phase difference between the two beams. Usually, the beam in the reference arm is tilted so that the interferogram contains uniformly spaced reference (or tilt) fringes. The graded index rod is placed into the sample arm of the interferometer and the plane beam passes through the rod transversely to the fibre axis. The sample should be immersed in a matching oil whose refractive index value is close to the peripheral index of the rod; this will be the cladding in the case of an optical fibre. The primary effect of the graded index distribution upon the incident light is to to retard that portion of the wavefront that passes through the graded index core of the sample. The wavefront in this region is phase shifted with respect to the (still plane) wavefront passing through the uniform index matching oil.

## Figure 2.2: The Transverse Interference Method

The Mach-Zehnder Interferometer

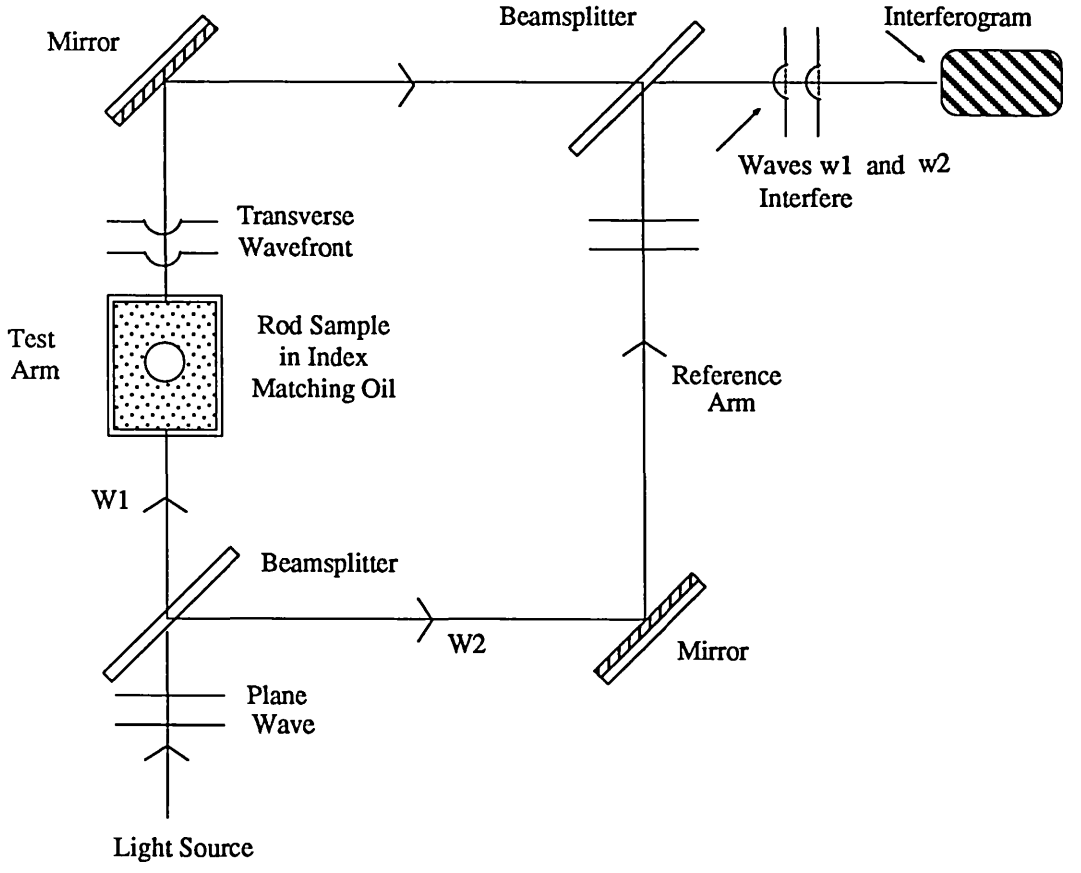
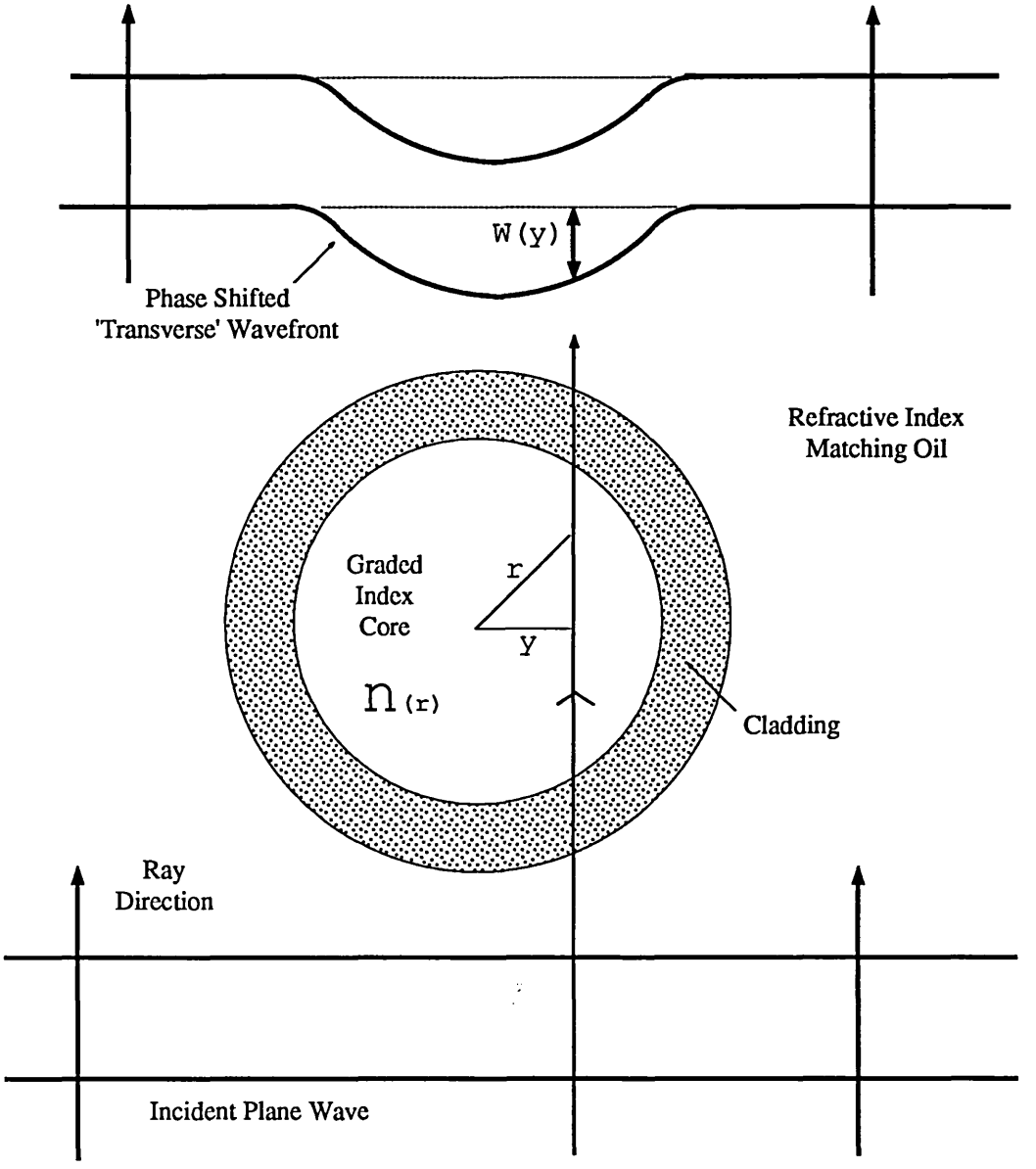


Figure 2.3: The Transverse Wavefront



This phase delay is illustrated in figure 2.3 and for the sake of simplicity, we shall continue to refer to this transmitted wave as the transverse wavefront.

Thus in the TI method, the transverse wavefront W(y) is recombined with the plane reference wave and the phase delay produced by the GRIN core is revealed as a fringe shift on the resulting interferogram. This fringe shift cannot be related directly to the index distribution in the core, and a mathematical inversion is required to calculate the profile (see chapter Seven). In practice, the fringe pattern is detected by a video camera, digitised,and the fringe shift data can be fed directly into a computer for computation of the index profile.

The TI method can only be applied to optical fibre index profiling, where the fringe shift on the interference pattern is around 1-2 fringes. In the case of rod lenses and preforms, the corresponding shift is of the order of a few hundred fringes (due to the relatively large dimensions of the rod) and consequently this cannot be resolved on the interference pattern.

A further drawback with the method lies in the calculation of the index profile from the measured data. There is a term proportional to dW(y)/dy in the reconstruction algorithm and thus there is a need to differentiate the data and great care must be taken to ensure that this calculation does not lead to erroneous results. This is important as a similar problem will arise in the holographic profiling method described in this thesis.

Despite these drawbacks, the method is excellent for revealing large refractive index fluctuations and is the most accurate technique for resolving the central index dip that appears in many GRIN fibres[1].

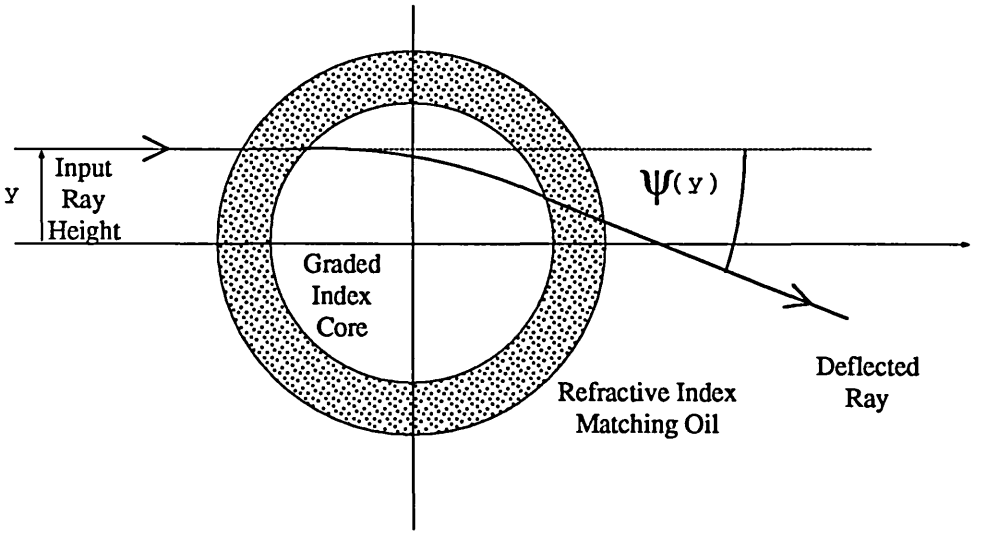
### 2.3.2 Transverse refraction angle Method

There are a large number of similar techniques that all fit under this heading. These methods, often termed deflection function methods, are all improvements on an idea first reported by Chu[13] in 1977.

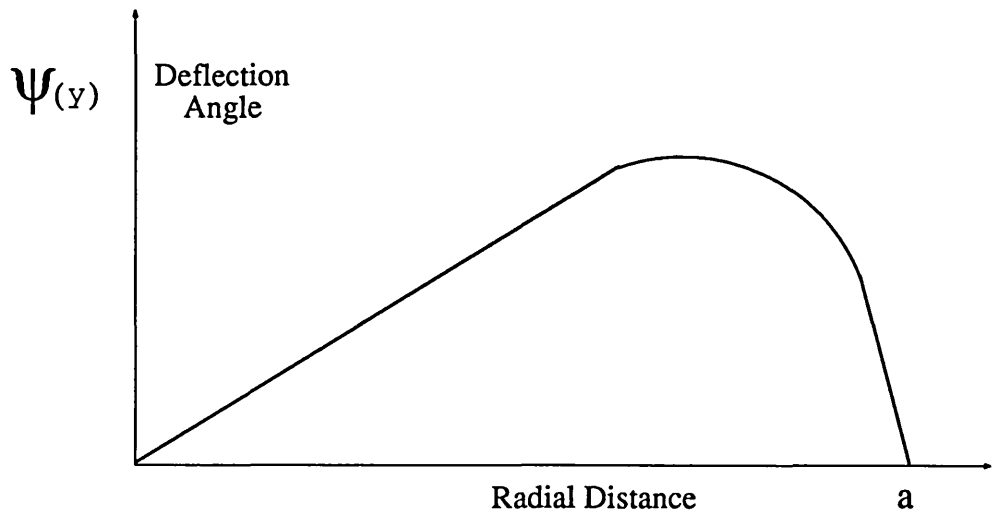
When a ray of light passes transversely through a GRIN rod, it is refracted by the

Figure 2.4: The Transverse Refraction Angle Method

a) Basic Principle




b) The Deflection Function



index gradient and it follows a curved path through the GRIN core. The nett effect of this is to deflect the ray away from it s original direction and this is schematically illustrated in figure 2.4. In the transverse refraction angle (TRA) techniques the exit angle of the ray is recorded as a function of the incident ray height, this function is referred to as the deflection function $\Psi(y)$ and the typical form is illustrated in figure 2.4b. The refractive index profile can be reconstructed from this function by using an inversion algorithm similar to that used in the TI method.

The original TRA methods [Chu[14], Watkins[15]] directed a thin pencil-like beam of laser light towards a preform and measured the ray exit angle by detecting the position of the transmitted spot of light at an observation plane at a large distance from the rod. This method was experimentally simple but lacked accuracy as there was a problem in locating the ray centre after deflection: the input beam tended to spread out due to diffraction and was also disturbed by the layer structure of the core. The method could not be applied to small diameter fibres and lenses[1].

The idea of using a pencil-like input beam was superceded by two superior techniques: dynamic spatial filtering [Marcuse[16]] and the focussing method [Sasaki[17]]. In these methods, the rod is probed by an expanded plane wave and the deflection function is calculated by following individual ray paths in the beam. These methods have extended the use of TRA methods to profiling fibres, preforms and lenses. Dynamic spatial filtering is now one of the most commonest techniques for preform profiling.

### 2.4.3 The relationship between the transverse wavefront and the deflection function

The need to differentiate measured data can be problematical and a large source of error in the TI method. However, this problem does not arise in the deflection function methods, and this is because of an important relationship between the transverse wavefront and the deflection function.

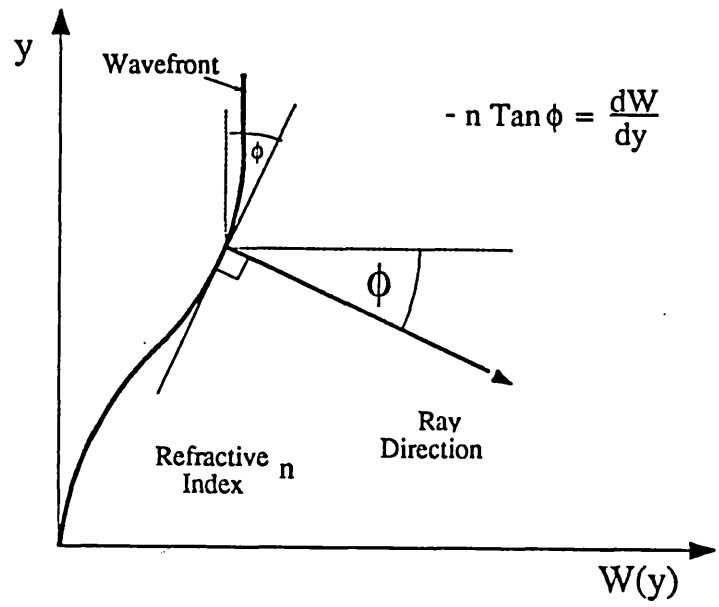
The theorem of Malus[20], states that for a propagating light wave, the ray direction at any point is normal to the slope of the wavefront at that point. Thus for any given wave

W, the ray direction at point y can be calculated from

(2.2) $n \tan \phi = - dw/dy$

The following figure schematically illustrates this relationship.

Figure 2.5: Ray Direction on a Wavefront




Note that in this figure, we have followed conventional geometrical optics so that the angle of a ray deflected towards the axis is negative. In refractive index profiling, this sign convention is ignored so that the ray deflection is always positive (assuming an increasing gradient.

The angle $\Phi_{(y)}$, is equivalent to the deflection function $\Psi_{(y)}$, measured in the refraction angle methods. Because $\Psi_{(y)}$ is determined directly, one also finds dW/dy from equation 2.2 without needing to differentiate data. Thus the deflection function is directly related to the differential or slope of the transverse wavefront.

2.4.4 Transverse shearing interferometry

Transverse shearing interferometry[18,6](TSI) is a popular technique for index profiling of rod micro-lenses. The method combines important aspects of both the transverse interference and the refraction angle methods described above; in particular it utilises the above relationship between the deflection function and the transverse wavefront. The method is also relevant because holographic shearing interferometry has been applied to index profiling [Chu[19]] and this technique can also be used using the apparatus described in this thesis (see chapter eight).

The conventional technique requires the use of an interference microscope as in the TI method, however it is used in a slightly different manner. The GRIN rod is illuminated transversely to it s axis as usual, but the difference in this case is that the resultant Transverse Wavefront is input to the Mach-Zehnder (see Fig. 2.6).

The wave is split into two equal parts, however before the waves are recombined and made to interfere, one of the waves is displaced by a small distance s, normal to the rod axis. Thus two identical but slightly displaced wavefronts are interfered and the resulting interference pattern is called a shearing interferogram. This pattern has a fringe shift of a form given by

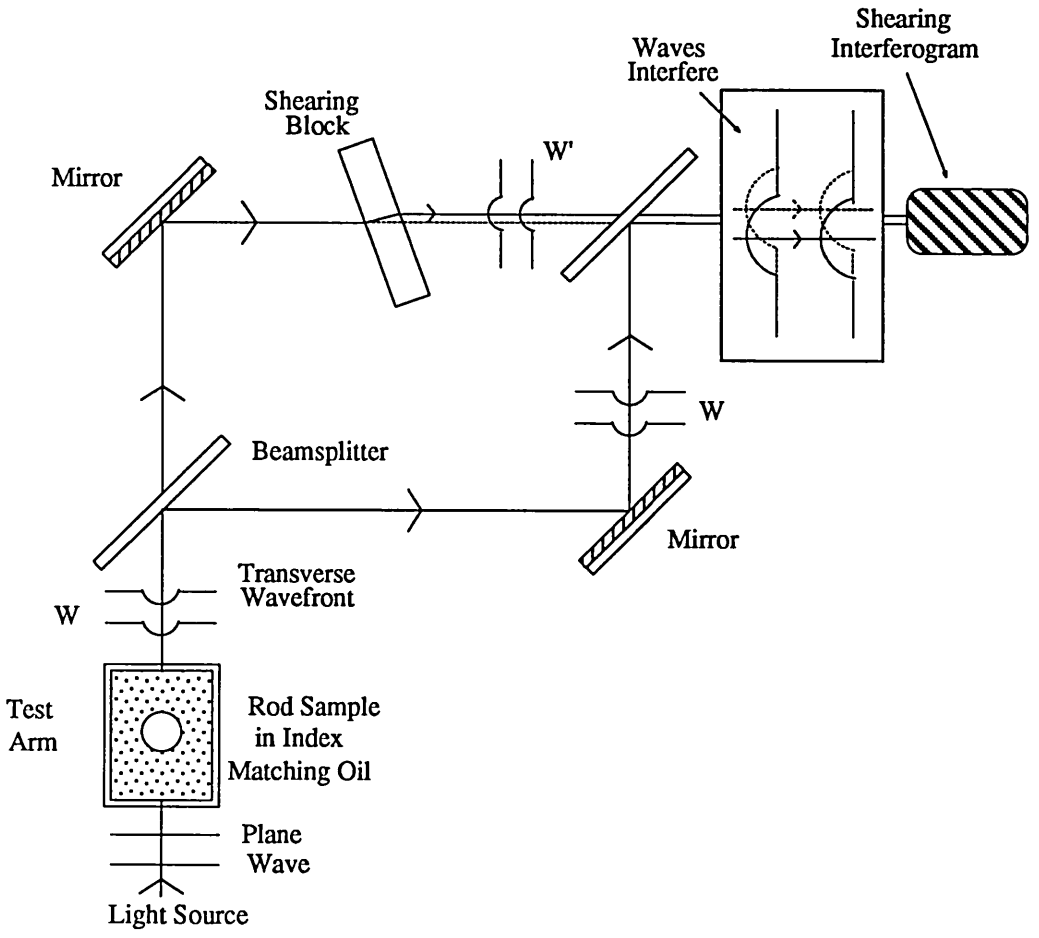
(2.3) $S(y) = W(y) - W'(y) = W(y) - W(y+s)$ (fig. 2.6b)

where s is the displacement distance and W(y) is the transverse wavefront. By using the first two terms in a Taylor series expansion, S(y) can be approximated to

(2.4) $S(y) = s\ dW(y)/dy$

Thus the fringe shift is directly related to dW/dy and hence the deflection function for the rod (fig. 2.6b). S(y) is in fact a map of the transverse refraction angles for all the rays in the transverse wavefront. The profile may be reconstructed by using the same

Figure 2.6: The Transverse Shearing Method



inversion procedure as for the TRA method but in this case there is the advantage that the deflection function has been determined by the inherently accurate technique of interferometry.

Unlike the Transverse Interference method, the Shearing method can cope with rods having a relatively large diameter because the magnitude of the fringe shift can be controlled by the shearing distance. The method is not readily applicable to optical fibres as the shearing fringe shift is too small to be accurately measured and in this case conventional transverse interferometry is prefered.

## References

2.1 D. Marcuse, "Principles of Optical Fibre Measurements", Academic Press, 1981.

2.2 W.J. Stewart, "Optical Fibre and Preform Profiling Technology," IEEE Journal of Quantum Electronics, 18, 1451 (1982).

2.3 K. Iga and I. Kokubun, M. Oikawa, "Fundamentals of Micro-optics," Academic Press, 1984.

2.4 H.M. Presby, "Profile Characterisation of Optical Fibres - A Comparative Study," Bell System Technical Journal 60, 1335, (1981).

2.5 D. Marcuse and H.M. Presby, "Effects of Profile Deformations on Fibre Bandwidth," Applied Optics, 18, 3758 (1979).

2.6 Y. Ohtsuka and Y. Shimzu, "Radial Distribution of the Refractive Index in Light Focussing Rods: Determination using Interphako Interference Microscopy," Applied Optics 16, 1050, (1977).

2.7 N. Yamamoto and K. Iga, "Evaluation of Gradient-Index Rod Lenses by Imaging," Applied Optics 19, 1101, (1980).

2.8 T.W. Cline and R.B. Jander, "Wavefront Aberration Measurements on GRIN Rod lenses," Applied Optics 21, 1035, (1982).

2.9 K. Koizuma, K. Nishizawa and K.Sono, " Selfoc Lens Handbook," Nippon Sheet

Glass Company Limited, 1981.

2.10 D.W. Sweeney and C.M. Vest, "Reconstruction of Three-dimensional Refractive Index Fields from Multidirectional Interferometric Data," Applied Optics 12, 2649, (1973).

2.11 T. Okoshi and M. Nishimura, "Measurement of Axially Non-symmetrical Refractive Index Distributions of Optical Fibre Preforms by a Triangular Mask Method," Applied Optics 20, 2407, (1981).

2.12 P.L. Francois, I. Sasaki and M.J. Adams, "Practical Three-dimensional Profiling of Optical Fibre Preforms," IEEE Journal of Quantum Electronics, 18, 524, (1982).

2.13 P.L. Chu, "Non-destructive measurement of the Index Profile of an Optical-Fibre Prefrom," Electronics Letters 13, 736, (1977).

2.14 P.L. Chu, "Measurement of the Refractive Index Profile of an Optical-Fibre Prefrom," Electronics Letters 15, 295, (1979).

2.15 L.S.Watkins, "Laser Beam Refraction Traversely through a Graded Index Preform to determine Refractive Index Ratio and Gradient Profile," Applied Optics 18, 2214, (1979).

2.16 D. Marcuse, "Refractive Index Determination by the Focussing Method," Applied Optics 18, 9, (1979).

2.17 I. Sasaki, D.N.Payne and M.J. Adams, "Measurement of Refractive Index Profiles in Optical Fibre Preforms by a Spatial Filtering Technique," Electronics Letters 16, 219, (1980).

2.18 Y.Kokubun and K.Iga, "Precise Measurement of the Refractive Index Profile of Optical Fibres by a Non-destructive Interference Method," Transactions of the IECE of Japan, 60, 702, (1977).

2.19 P.L.Chu, "Holographic Measurement of the Refractive-Index Profile of an Optical Fibre Preform," Electronics Letters 16, 876, (1980).

2.20 W.T. Welford, "Aberrations of Optical Systems," Adam Hilger Ltd, (1986).

# CHAPTER THREE

# THEORY OF HOLOGRAPHIC INTERFEROMETRY

In this chapter it will be necessary to briefly review the technique of holographic interferometry prior to describing its application to refractive index profiling. Only the most relevant aspects of holography are described here, a more detailed analysis may be found in Collier[1] and Hariharan[2].

## 3.1 The basic holographic process

Holography is a technique for recording and reconstructing the complete (amplitude and phase) information in a chosen object wave. The basic holographic process is schematically illustrated in figure 1.3.

The recording procedure requires the superposition of a coherent reference wave upon the object wave at a chosen location (the hologram plane). The two waves interfere and the hologram is a photographic record of the resulting interference pattern. In the reconstruction step, the processed hologram is re-illuminated by the reference beam and a replica of the original object wave is then diffracted out of the hologram.

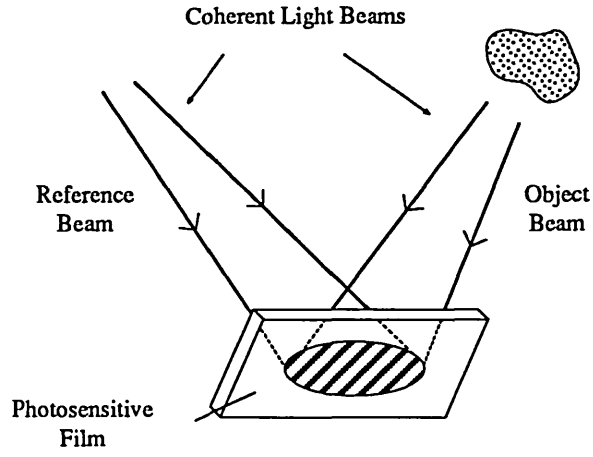
In a practical situation, the coherent reference and object beams are derived from a single (laser) source, and beamsplitters, mirrors and beam expansion optics must be used to provide the correct illumination conditions. The hologram recording material is usually high resolution photographic film, although other sources are available[3].

## 3.2 The fundamental holography equations

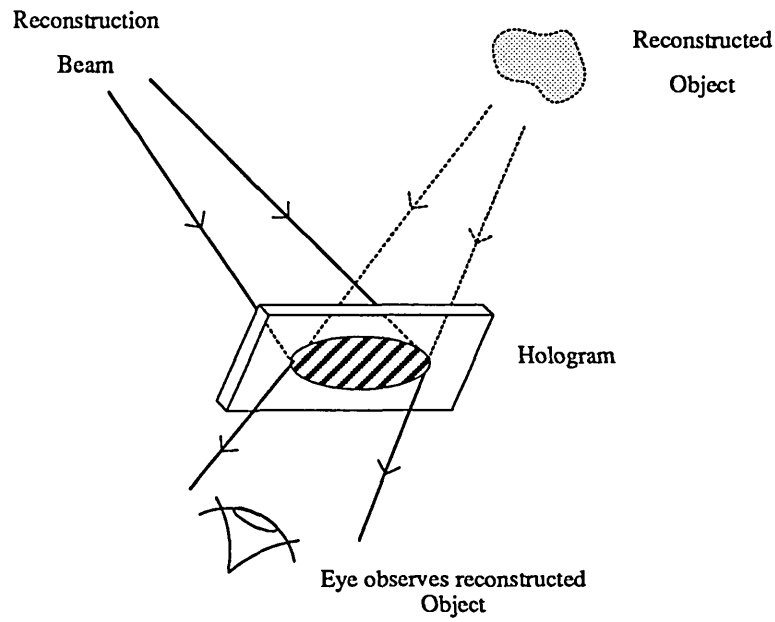
The holographic process described above can be analysed mathematically. Using complex representation, the complex amplitude of an optical wave at a point in space is expressed by

## Figure 3.1 : The Basic Holographic Process

a) Recording Stage




a) Reconstruction Stage



(3.1) $$U_q(r) = A_q(r) \exp\{-i\,\varphi(r)\}$$

In this equation $A_q$ is the maximum amplitude, $\phi$ is the phase and r is the position vector from the origin to the point in space. The wave varies in time as well as position, but the time variation has been suppressed as it is essentially a constant term in the following representation.

Consider the object and reference beams to be subscripted by o and r respectively. At the hologram plane, where the two beams are superposed the total complex amplitude is

(3.2) $$U_t = U_o + U_r$$

Photosensitive film can only respond to the time-averaged intensity of a wave[1] and this is proportional to the square modulus of the complex amplitude ie.

(3.3) $$I_q \propto U_q.U_q^* \propto A_q^2.$$

Note that the phase information is lost. Thus at the hologram plane, the total intensity is

(3.4) $$I_t = U_t.U_t^* = (U_o + U_r)(U_o + U_r)^*$$

$$= U_oU_o^* + U_rU_r^* + U_oU_r^* + U_rU_o^*$$

The photosensitive film records this intensity distribution and for convenience, a linear relationship between the amplitude transmittance T of the processed film and the exposure is assumed. Thus

(3.5) $$T = T_a - b\ I_t$$

where Ta is the transmittance of the unexposed plate , $I_t$ is the the intensity of the interference pattern and b is a proportionality constant related to the sensitivity of the emulsion .

After chemical processing, the film becomes a hologram of amplitude transmittance

$$(3.6)\quad T = T_a - b\,( I_0 + I_r + U_0 U_r^* + U_0^* U_r )$$

To reconstruct the object wave, the hologram must be illuminated with a reconstruction beam $U_c$ . This reconstruction beam should be similar in form to the original reference beam and in most cases the hologram is replaced into the original recording plane and re-illuminated by the reference beam so that $U_c = U_r$

The complex amplitude distribution of the light transmitted through the hologram is given by

$$(3.7)\quad U = U_c\, T$$
$$= U_c\, T_a - b\, I_0 U_c - b\, I_r\, U_c - b\, U_c\, U_r^* U_0 - b\, U_c U_r U_0^* .$$

Writing $E = T_a - b.I_0 - b.I_r$ , this becomes

$$(3.8)\quad U = E\, U_c - b\, U_c\, U_r^*\, U_0 - b\, U_c\, U_r\, U_0^*$$

Each of the three terms in the above equation corresponds to a wave propagating from the re-illuminated hologram. The first term represents the reconstruction beam which has been attenuated proportionally to the mean transmittance of the plate. The third term represents a wave referred to as the conjugate wave and its appearance will only be of consequence under certain reconstruction conditions (for example see Hariharan[2]).

The second term is of most importance in this work and this can be written as

$$(3.9)\quad U_w = b\, U_c U_r^* U_0 = b\, U_r\, U_r^*\, U_0 = C\, U_0 .$$

Where $C = b I_r$ assumes that the reconstruction beam is constant in intensity across the hologram (valid in most holographic set-ups). Thus $U_w$ corresponds to a wave proportional to the original object beam. It is this reconstructed wave that produces the familiar three-dimensional image observed in display holography.

## 3.3 Holographic interferometry

We now describe how the technique of wavefront reconstruction introduced above can be applied to interferometric testing. [For review see "Holographic Interferometry" by Vest[4]].

A conventional interferometric test is performed by analysing the interference pattern produced by two light waves. Usually, one wave is a 'reference' wave that has an established form, the other wave emerges from the object under test. In most cases there are practical restrictions upon the type of reference wave that can be used, thus limiting the range of objects that can be tested. Typically, the object must have a relatively simple shape (spherical or flat) and optically smooth surfaces.

In holographic interferometry, one of the waves used for the interferometric test is reconstructed from a hologram. This gives a significant advantage over the conventional methods in that almost any wave can be stored and reconstructed to act as the 'reference' wavefront for the test. There is no restriction to plane or spherical wavefronts.

Holographic interferometry can be readily used as an accurate method for monitoring changes in the physical state of an object over a period of time or after an applied stress. This technique, often referred to as 'differential' interferometry[5] has found many applications. For example it has been used for measuring the deformation, displacement or vibration of fairly complex and rough surfaces, and in the case of transparent (phase) objects, changes in the refractive index distribution can be monitored [4].

The basic principle of holographic differential interferometry is record the wave emerging from the test object in an initial state, and reconstruct and interfere this wave with the wave emerging from the object after the applied stress. The resulting interference

pattern (interferogram) reveals the nature of any changes in the state of the object.

There are two general approaches and these are the techniques of double and single exposure holographic interferometry.

### 3.3.1 Double-exposure holographic interferometry

In double-exposure interferometry, the two slightly differing object waves are recorded independently at the hologram plane. When the hologram is illuminated by the reconstruction beam, both the object waves are reconstructed and they interfere and produce a 'frozen' fringe pattern. Double exposure holography is useful for work involving transient events or in situations where adjustment of the object in 'real time' is not required.

### 3.3.2 Single-exposure holographic interferometry

In single-exposure interferometry, only one wavefront, corresponding to the object in its initial state is stored in the hologram. This wave is then reconstructed and interfered with the wave emerging from the re-illuminated object. The object can then be disturbed, giving rise to interference fringes which change in accordance to the applied stress. This technique is often referred to as real-time or 'live'fringe holographic interferometry and it is by far the most flexible of the two methods. However, it can require stability of the apparatus over quite a long period of time.

This single-exposure technique is adopted in this research.

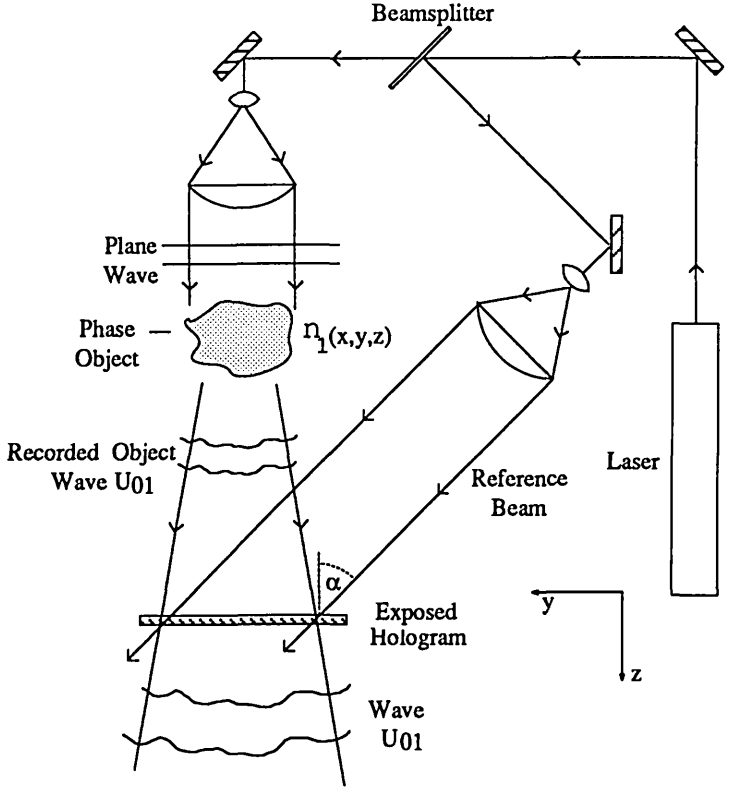
## 3.4 Single-exposure holographic interferometry applied to refractive index measurements

### 3.4.1 Introduction

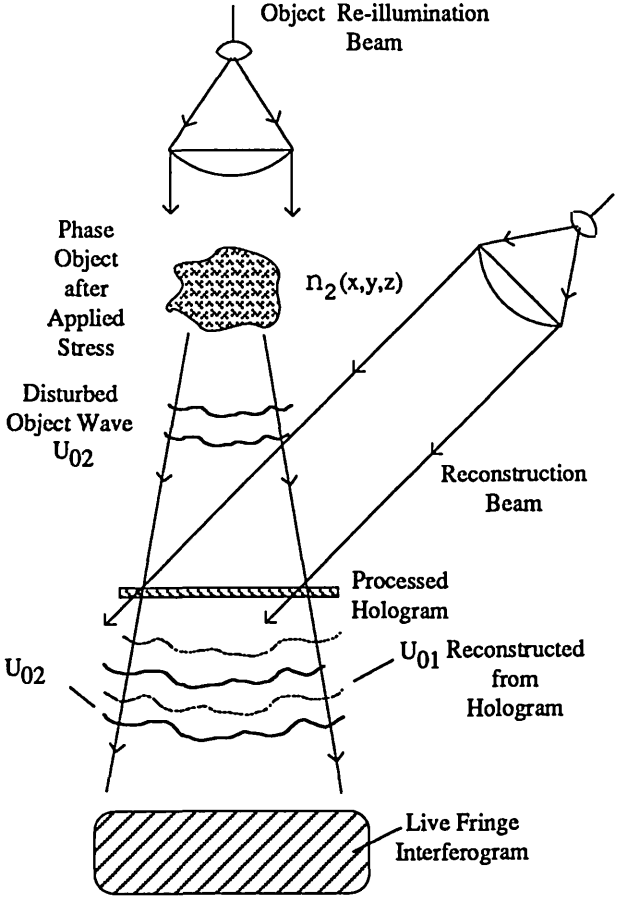
Figure 3.2 schematically illustrates a holographic interferometric system for measuring the change in the refractive index distribution in a phase object. In an initial state, the object has a known (possibly constant) refractive index distribution $n_1(x,y,z)$. After the applied stress this index changes to the unknown distribution $n_2(x,y,z)$. We are

Figure 3.2: Holographic Phase Interferometry

a) Recording Step




b) Reconstruction Step



interested in how this change in index can be detected using single-exposure holographic interferometry.

3.5.2 Recording and reconstruction procedure

Figure 3.2a illustrates the recording procedure. The object is illuminated with a plane object wave propagating in the z direction. This beam is phase shifted as it passes through the index distribution and the transmitted wave is

(3.10) $U_{O1}(x,y,z) = \exp(-i\,\varphi_1(x,y,z))$.

The wave has unit amplitude and the phase $\varphi_1(x,y,z)$ for any ray in the wave can be determined from optical pathlength considerations to be

(3.11) $\varphi_1(x,y,z) = k\int n_1(x,y,z).dS$

This wave is incident normally at the hologram (x-y) plane, and it interferes with the plane reference beam $U_r$, incident at angle $\alpha$ to the normal (fig. 3.2a). At the hologram plane (z=0), the reference wave is

(3.12) $U_r(y) = \exp(-ik.y.\sin\alpha)$

The hologram is exposed and processed and it has an amplitude transmittance (from eq. 3.6)

(3.13) $T(x,y) = 2 + U_O U_r^* + U_O^* U_r$

$= 2\,(1 + \cos(k\,y\sin\alpha - \varphi_1(x,y,z))$

The hologram thus consists of a set of cosinusoidal interference fringes running normal to the y-axis, modulated by the phase term $\varphi_1(x,y,z)$. The fringe spacing is $f_y = \lambda/\sin\alpha$, which is 790 lines per mm for a typical recording angle of 30° [4]. (Hence the need for high resolution holographic film.)

The processed hologram is replaced in it s original recording position and the object wave $U_{O1}$ is reconstructed by re-illuminating the hologram with the reference beam $U_r$.

If the object is disturbed so that it s refractive index distribution undergoes a change, the transmitted object wave has the form

3.14) $U_{O2}(x,y,z) = \exp(-i\,\varphi_2(x,y,z))$

where $\varphi_2(x,y,z) = k \int n_2(x,y,z).dS$ .

Thus there are two waves propagating beyond the hologram (fig. 3.2b), one is the reconstructed object wave $U_{O1}$, and the other is the wave emerging from the disturbed object $U_{O2}$. These two waves interfere and produce an interferogram of intensity

(3.15) $I(x,y) = |U_{O1} + U_{O2}|^2$

(3.16) $I(x,y) = 2(1 + \cos(k(\varphi_1(x,y,z) - \varphi_2(x,y,z))))$

The intensity of the interferogram depends upon the relative phase difference between the two object waves and hence indirectly upon the refractive index changes in the object. With no index change and hence no relative phase difference between the two beams, the interference pattern will be uniformly bright (or possibly dark). However, upon an index change,a dark fringe will appear whenever the phase difference between the two beams is modulo $(m+1)\pi$. Thus by measuring the shape of the fringe pattern the change in the index distribution can be monitored.

3.4.3 Introducing tilt fringes to the interferogram

The information contained in the interferogram described by eq.(3.16) is liable to misinterpretation because there is no way of discriminating between a positive and a negative phase difference between the beams. This ambiguity must be removed for a useful analysis, and in order to achieve this, uniformly spaced reference (or tilt) fringes must be added to the pattern. The phase difference information is then revealed as either a positive or negative shift in the position of the tilt fringes and the sign ambiguity is thus eliminated.

Tilt fringes can be introduced by tilting the reconstruction beam through a small angle and this is illustrated in figure 3.3. Figure 3.3a, illustrates the recording procedure with the plane reference beam incident upon the hologram (x-y) plane at the $\alpha$ angle to the normal.

After the recording step, the reference beam is tilted out of the y-z plane by the angle $\beta$ (figure 3.3b) to become the reconstruction beam $U_c$ defined by

(3.17) $U_c(x,y) = \exp( -i.k(y \sin\alpha \cos\beta - x.\sin\beta) ).$

For small $\beta$, this becomes

(3.18) $U_c(x,y) = \exp ( -ik(y.\sin\alpha - \beta.x))$

Following the analysis in section 3.3, the reconstructed wave is

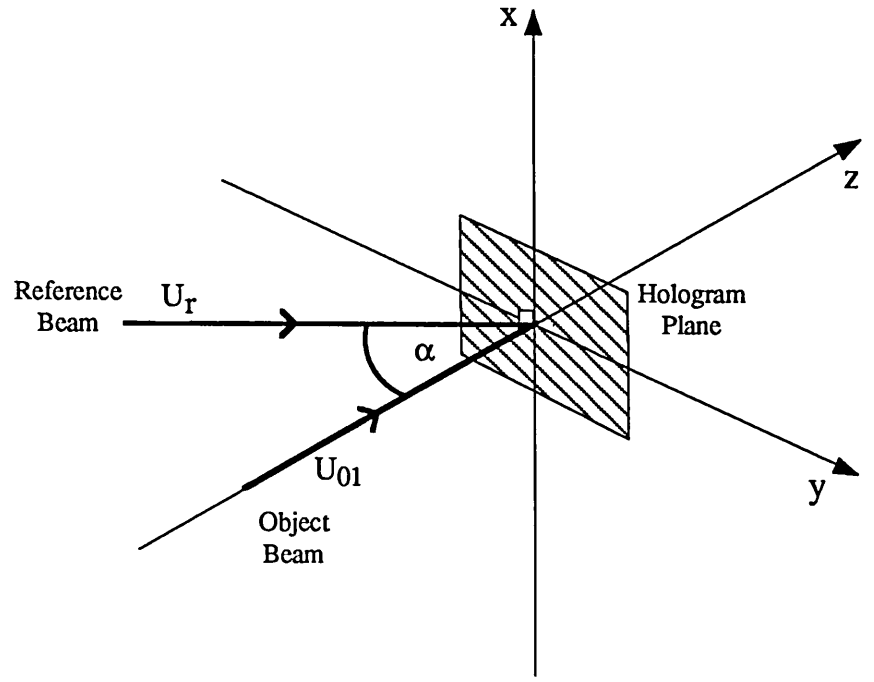
(3.19) $$U_w = U_c.U_r^*.U_{O1}$$
$$= \exp( -ik(y \sin\alpha - \beta.x)) .\exp(+ik\, y \sin\alpha).U_{O1}$$

(3.20) $$U_w = \exp (- i(\varphi_1(x,y,0) - k\, \beta\, x))$$

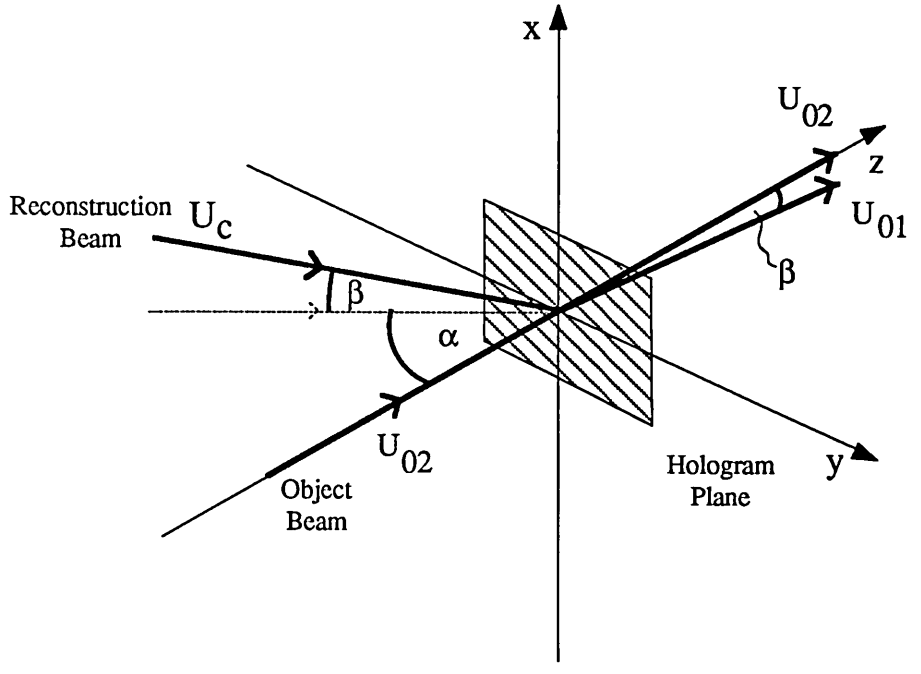
When this reconstructed wave is interfered with the disturbed object wave $U_{O2}$, an

Figure 3.3 : Introducing Tilt Fringes to an Interferogram

a) Recording




b) Reconstruction



interference pattern is produced with an intensity

$$(3.21) \quad I(x,y) = |(U_{O2} + U_w)|^2$$

and thus

$$(3.22) \quad I(x,y) = 2\{1 + \cos[(\varphi_1(x,y,0) - \varphi_2(x,y,0) - k\beta x)]$$

The tilt fringe interferogram expressed by eq. (3.22) consists of a set of horizontal fringes running parallel to the y-axis, modulated in the vertical x direction by the phase difference term $(\varphi_1(x,y,0) - \varphi_2(x,y,0))$. This pattern is far easier to analyse than that corresponding to eq. (3.16) as the phase differences are directly revealed as shift in the otherwise horizontal tilt fringes. The resulting interferograms (theoretical and experimental) produced in this thesis have the form of eq. (3.22).

In the following chapter, we shall go on to describe how we may use holographic interferometry to measure differences between the known refractive index distribution in a standard graded index rod to that in an recently manufactured sample that has an unknown index distribution. We shall use a system to that described above and plot out some theoretically expected interferograms using eq. (3.22).

## References

3.1 R.J. Collier, C.B. Burkhardt and L. H. Lin, "Optical Holography," Academic Press, (1971).

3.2 P. Hariharan, "Optical Holography," Cambridge University Press, (1984).

3.3 H.M. Smith, "Holographic recording materials," Springer-verlag, (1977).

3.4 C.M. Vest, "Holographic Interferometry," Wiley, (1979).

3.5 H.M. Smith "Principles of Holography,"Wiley, (1969).

# CHAPTER FOUR

# HOLOGRAPHIC MEASUREMENT OF GRADIENT REFRACTIVE INDEX PROFILES: THE COMPARISON METHOD

In this chapter, the proposed holographic technique for assessing gradient index profiles is introduced. The technique, referred to as the comparison method involves the principles of real time holographic interferometry and transverse refractive index profiling, described in previous chapters.

## 4.1 The technique of holographic comparison

The aim of the holographic comparison method is to perform index profile analysis by comparing the unknown refractive index distribution in a recently manufactured graded index rod with the distribution in a rod that has a previously established profile. The method is schematically illustrated in Figure 4.1.

### Recording

The GRIN rod with known profile (standard rod) is placed in index matching oil in an optical cell and illuminated by a plane wave incident transversly to it s axis. The emergent wavefront (referred to as the transverse wavefront) is then recorded holographically by interfering it with a plane reference beam (figure 4.1a).

### Reconstruction

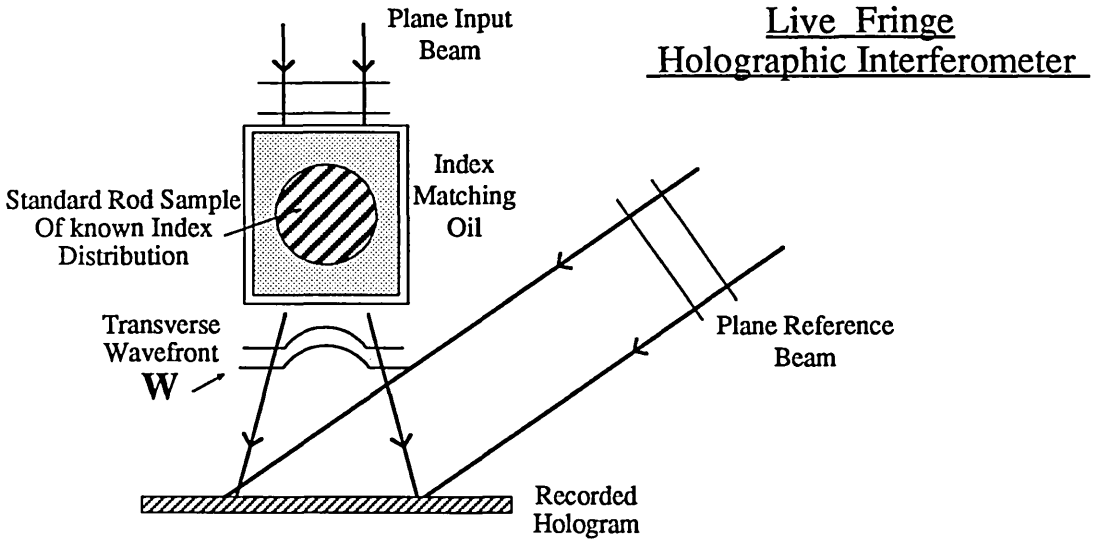
After chemical processing, the hologram is re-illuminated by the reference beam and the transverse wave is reconstructed. The standard GRIN rod is then removed from the optical cell and replaced with the rod sample to be tested (figure 4.1b).

### Analysis

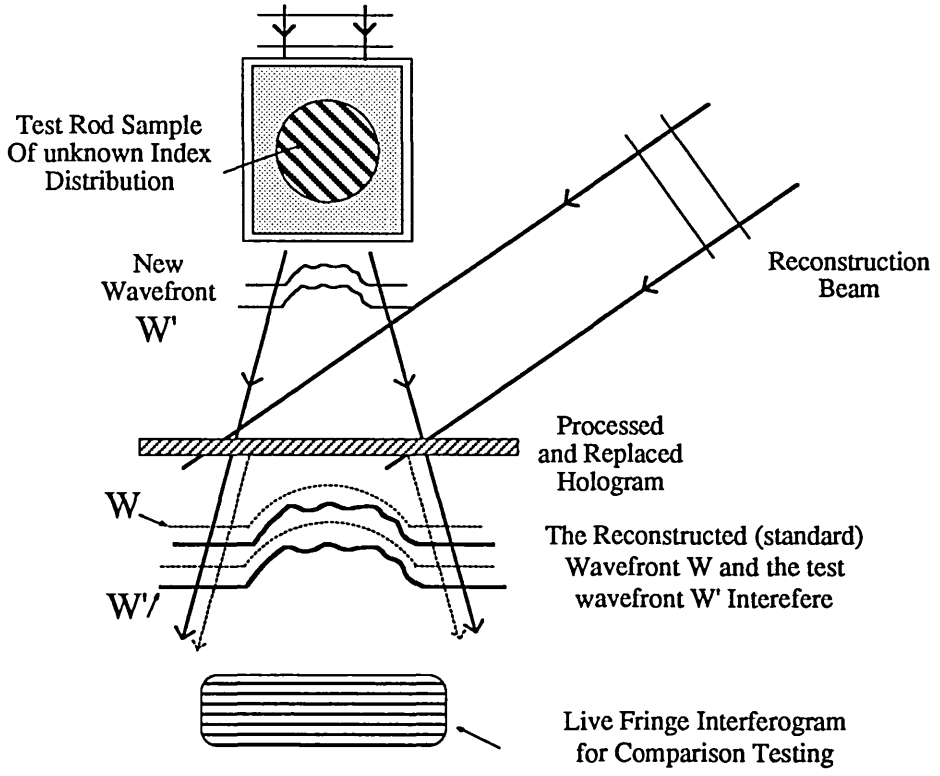
A live fringe interferogram is formed between the wavefront reconstructed from the hologram and the wavefront transmitted through the new rod. This interferogram reveals

Figure 4.1: The Holographic Comparison Method

a) Recording Step




a) Reconstruction Step



any differences between the two wavefronts and consequently, the index distributions in the two rods. Prior to comparing the two wavefronts, tilt fringes are added to the interferogram by tilting the reference beam (§3.4.3), and this reveals any fringe shifts in a convenient manner.

In the ideal case, GRIN rods having the same index profile would produce correspondingly identical transverse wavefronts and therefore no shift or deviation of the tilt fringes. However, rods with differing profiles produce a disturbed fringe pattern, and the magnitude and shape of the fringe shift can be used by the operator to determine the index difference.

The comparison technique is, at least in principle, a simple and direct method for analysing GRIN rods. Ideally, any number of rods could be quickly compared with the standard rod and the method could be potentially very useful for examining rods at the production stage. Because the method is based on transverse profiling principles, it should be readily adaptable to measuring profile variations along the axis and the circular symmetry of the profile. It is also an inherently non-destructive technique.

The index distribution of the standard rod can be determined by using any of the established profiling method (see chapter 2). However, it is also possible to measure the profile using the holographic interferometer and such a method is discussed in chapter 8.

## 4.2 Computer simulation of the comparison method

To assess the accuracy and practicability of the comparison method, the theoretically expected interference patterns are calculated and plotted using a computer program that simulates the working holographic interferometer. (The computer program (HOLOCOMP) is listed in appendix B.)

The fringe shift information is calculated and plotted using equation (3.22) derived in the preceding chapter. Thus the intensity distribution I(x,y) across the interferogram is

$$(4.1)\quad I(x,y) = 2\{1 + \cos(\Phi(x,y) - k\beta x)\}$$

where $k \beta x$ determines the tilt fringe spacing and $\Phi(x,y) = \varphi_1(x,y) - \varphi_2(x,y)$ is related to the phase differences between the two transverse waves W and W' and in turn to the difference between the refractive index distributions in the standard and test graded index rods.

In the following sections we shall consider ways in which the wavefront emerging from a GRIN rod under test may be affected by changes in the index distribution and by other spurious effects. The expected interferograms are plotted and these may be compared with results obtained later from the working interferometer.

## 4.3 The transverse wavefront and the refractionless limit

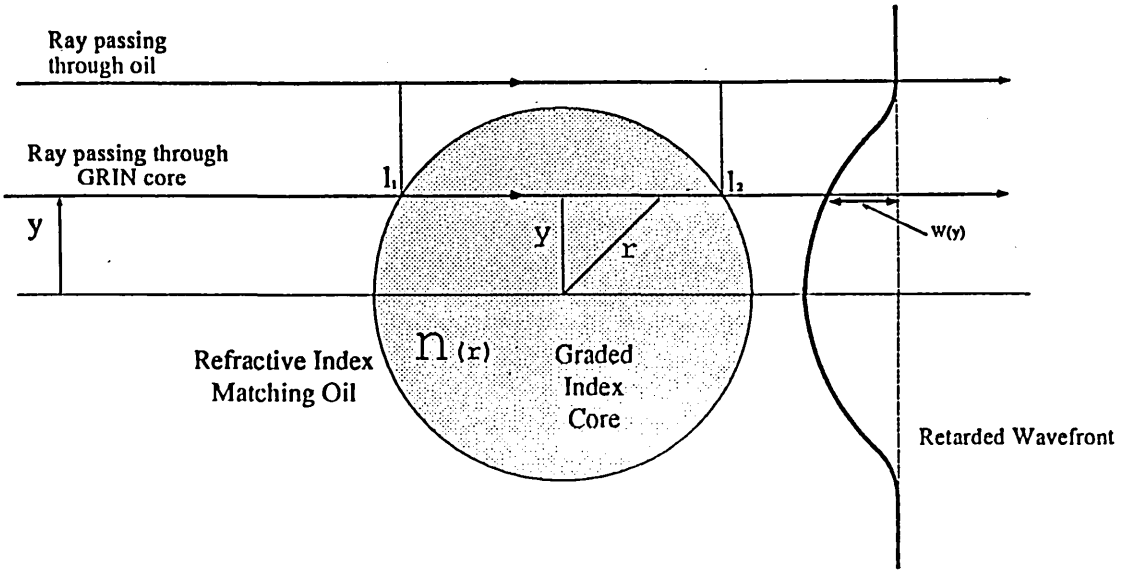
The phase terms $\varphi_i(x,y)$ in eq. (4.1), are essentially defined by

$$(4.2)\quad \varphi_i(x,y) = k\, w_i(x,y) \qquad (k = 2p / \lambda).$$

where $w_i(x,y)$ is the optical pathlength retardation across the transverse wavefront, which will depend upon the nature of the index distribution in the GRIN rod. This retardation can be evaluated by comparing the optical pathlength of a ray passing transversely through the GRIN sample with the optical pathlength of a ray that travels the same distance through the uniform index matching oil. The calculation of the optical pathlength retardation is greatly simplified if all ray refraction is ignored so that all ray paths are considered to be straight lines. This simplification is commonly referred to as the refractionless limit approximation, and it does not necessarily imply a significant loss of accuracy. This is quite surprising when we consider that graded index elements are fabricated for the specific purpose of bending rays of light. To quantify the error of the refractionless limit approximation and to justify it's validity requires the solution of some fairly lengthy integrals, and so we shall return to this topic in chapter 7, where ray paths in GRIN media are described in detail.

In figure 4.2 (below) we calculate the optical pathlength retardation for the ray incident at height y from the optic axis. Any deflection of the ray is ignored and the

Figure 4.2: The Refractionless Limit Approximation




pathlength calculation is based upon the straight through chord length $l_1l_2$. The optical pathlength of the ray is thus given by the integral

$$(4.3) \qquad W(y) = \int_{l_1}^{l_2} (n_{oil} - n_{(l)})\,dl$$

(This integral will turn out to be negative thus implying *retardation* of the wave). Making a change of variable, $l = (r^2 - y^2)^{1/2}$ and $dl = r\,(r^2 - y^2)^{-1/2}\,dr$. We finally arrive at the important expression that relates the optical pathlength of the ray to the index distribution

$$(4.4) \qquad W(y) = -2\int_{y}^{a} \frac{(n(r) - n_{oil})\,r\,dr}{\sqrt{r^2 - y^2}}$$

We calculate this integral assuming a parabolic index distribution given by the simplified profile equation (1.2)

$$(4.5) \qquad n(r) = n_0\,(1 - {}^1/_2 A\,({}^r/_a)^2)$$

with $n_0$ = axial index, A = gradient constant and $n_{oil} = n_0(1 - {}^1/_2 A)$. Therefore

$$(4.6) \qquad W(y) = n_0 A \left[ \frac{1}{a^2} \int_y^a \frac{r^3 dr}{\sqrt{r^2 - y^2}} - \int_y^a \frac{r\, dr}{\sqrt{r^2 - y^2}} \right]$$

Looking up these integrals (Marcuse[1] or Gradsteyhn[2] (§2.27))

$$(4.7) \qquad \int_y^a \frac{r\, dr}{\sqrt{r^2 - y^2}} = (a^2 - y^2)^{1/2} \qquad : \int_y^a \frac{r^3 dr}{\sqrt{r^2 - y^2}} = \tfrac{1}{3}(a^2 - y^2)^{3/2} + y^2(a^2 - y^2)^{1/2}$$

Yields the following expression for the optical pathlength change due to a parabolic graded index distribution.

$$(4.8) \qquad W(y) = -\left(\frac{2 n_0 A}{3 a^2}\right)(a^2 - y^2)^{3/2}$$

We can use equation 4.8 to calculate the form of the wavefronts for insertion into equations 4.2 and 4.1. We can simulate index distribution changes by varying the values of $n_0$ and A for each wavefront. However, it will be advantageous at this stage to rearrange both equations (4.8) and (4.5) into a more useful form by replacing the $n_o$ axial index term with an expression that only involves the edge (peripheral) index value $n_1$ and the gradient constant A. Thus the expression for the index profile becomes

$$(4.9) \qquad n(r) = \left(\frac{n_1}{(1 - \frac{1}{2}A)}\right)(1 - \tfrac{1}{2} A (r/a)^2)$$

The transverse wavefront becomes

$$(4.10) \qquad W(y) = \left(\frac{-2 n_1 A}{3 a^2 (1 - \frac{1}{2}A)}\right)(a^2 - y^2)^{3/2}$$

The difference between equations (4.5) and (4.9) is basically in the labelling of the profile. In equation (4.9) the refractive index values vary from a fixed peripheral value to a

maximium value $n_0$, determined by the value of the gradient constant A. If we alter the value of A in equation (4.9) then this will result in a new value for the axial index ($n_0$) but $n_1$ remains unaltered. This re-labelling simplifies the analysis in the following sections, where $n_0$, $n_1$ and A can vary. In particular it allows changes in the absolute values of the index profile to be easily taken into account (§4.4.2).

In chapter two (§2.4.4) we found that the angular deviation of a ray on a wavefront is given by

$$(4.11) \qquad -n \tan\phi = \frac{dW(y)}{dy}$$

thus we can also find the deflection function $\phi(y)$ for a parabolic profile rod by differentiating equation 4.10.

$$(4.12) \quad \tan\phi = \left( \frac{-2A}{a^2(1 - {}^1\!/_2 A)} \right) y(a^2 - y^2)^{1/2}$$

From this expression we find that the maximum deflection angle of a ray is $\phi_{max} \approx 0.07$ radians (see figure 7.6 for plot of the deflection function for a rod lens).

In the following sections, the initially known profile parameters will be taken to be those of a typical 2mm diameter GRIN lens. Thus a=1, A=0.0625, $\sqrt{A}$=0.25, $n_0 = 1.565$ and $n_1 = 1.516$. The practical tolerance on these parameters is determined by the GRIN fabrication process. Some typical tolerance values for rod micro-lens production are given in the Nippon Sheet Glass Handbook[3]. In the following sections, we will use these values to estimate the probable sizes of the fringe shifts observed in the interferometer. Because a complete documentation on the fabrication procedure could not be readily obtained, some of the following process considerations may not be totally valid for practical GRIN lens production.

The implications of the comparison technique for optical fibre preforms will be discussed at the end of the chapter.

## 4.4 Parameters affecting the index distribution

### 4.4.1 The gradient constant

We now consider the comparison of two rod lenses having 'ideal' parabolic profiles but differing gradient constants. We shall also assume that the peripheral index values of the two rods are identical. We calculate the shapes of the two differing transverse waves using eq. 4.10 and plot the theoretical interferogram using eq. (4.1). The fringe shift on the interferogram is directly related to the differences in optical pathlength between the two index distributions thus

$$(4.13) \quad S_1(y) = w(y) - w'(y)$$

where prime denotes the wavefront transmitted through a different rod sample.

Equation (4.13) has the approximate form

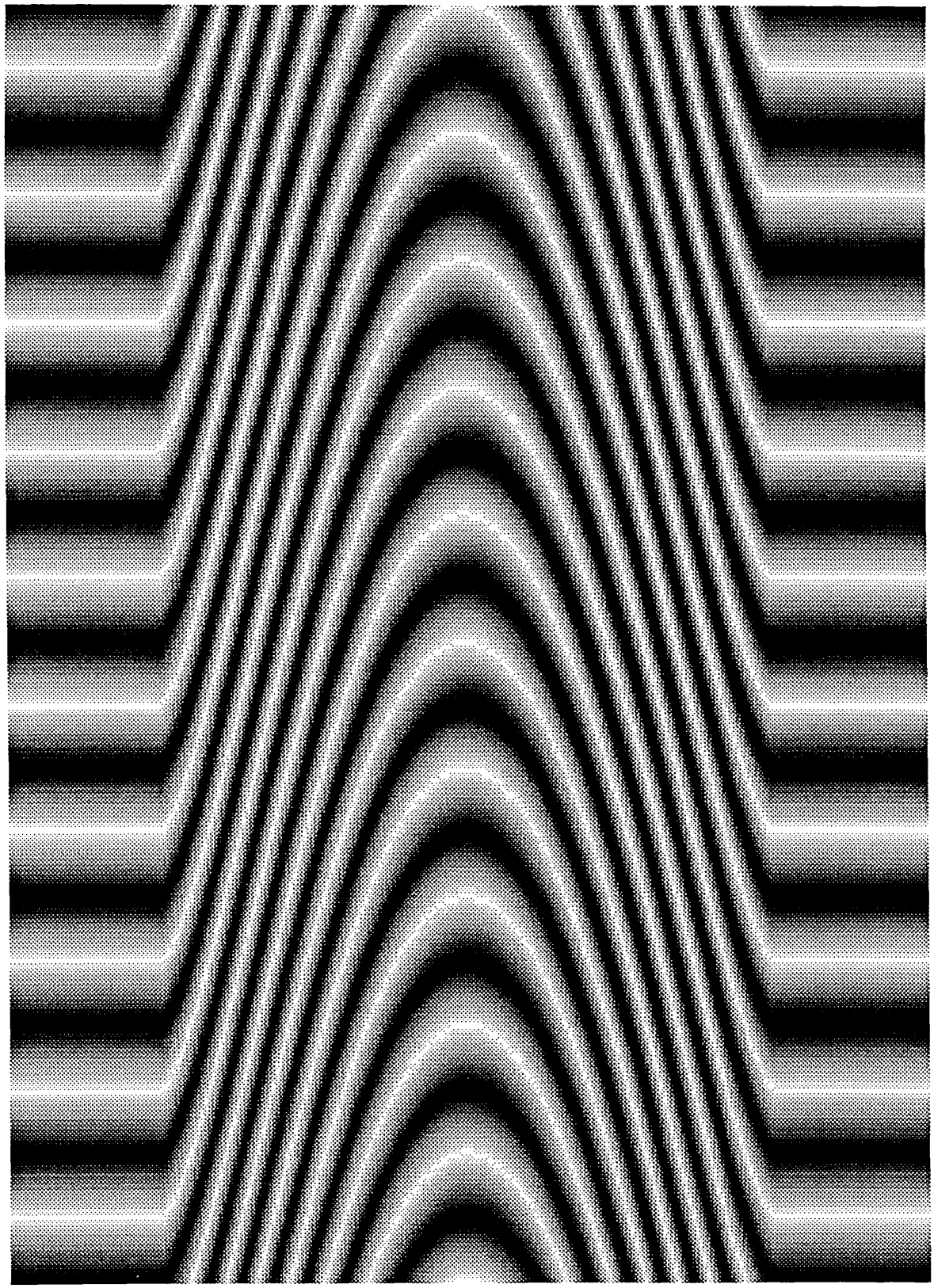
$$(4.14) \qquad S_1(y) = \left(\frac{2n_1}{3a^2}\right)\left(\frac{dA}{1-A}\right)(a^2 - y^2)^{3/2}$$

where $dA = A - A'$ is the difference in the gradient constants.

The value of the quadratic gradient constant ($\sqrt{A}$) is dependent upon the ion exchange process (§1.4.1) and this may vary between lenses produced both within the same production lot and also between different batch productions. In the former case, about 30,000 lenses are produced in one ion exchange treatment; the fluctuation of $\sqrt{A}$ is[4] $\pm$ 1%. The deviation of $\sqrt{A}$ between 14 different production lots is also reported by the Nippon Sheet Glass company[4] to be approximately $\pm$3%. The difference in refractive index between the profiles of two GRIN rods with a 3% difference in $\sqrt{A}$ is plotted in figure 4.4 below.The corresponding theoretical interferogram is plotted in Figure 4.3.

From figure 4.3 it can be seen that the maximum fringe shift (which occurs on axis) is around 6.5 fringes. This is a fairly high value for an interferometric test and it indicates that an accurate measurement of the gradient constant is feasible. For example, a 3% change in $\sqrt{A}$ ($\sqrt{A} \approx 0.25$) implies that $dA \approx 0.004$. If a shift of one tenth of a fringe can

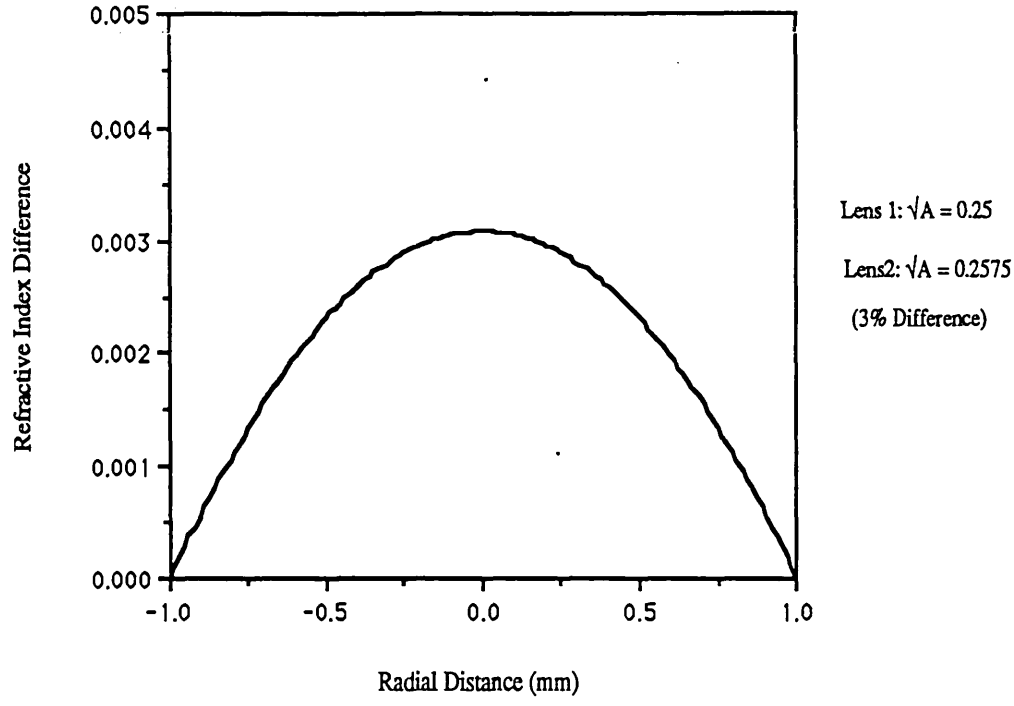
Figure 4.3: Theoretical interferogram :
Change in the gradient constant



Rod 1 : $\sqrt{A}$ = 0.2500
Dn = 0.0000
Rod 2 : $\sqrt{A}$ = 0.2575
Dn = 0.0000

Matching oil index = 1.516
Diameter variation = 0

Figure 4.4 Index difference due to a change in the gradient constant




be resolved on the interferogram, then this would indicate a theoretical accuracy in the determination of A of at least 1 part in $10^4$.

Thus if we could consider that the gradient constant is the only parameter effected by the fabrication process, then the comparison method would seem to be an excellent technique for comparing rod lenses. Ideally, the error in A could be assessed approximately by observing the magnitude of the fringe shift on the interferogram.

4.4.2 The Absolute index values of the profile

We must consider the effect of a change in the absolute index values of the profile. In this case, the profile shape is maintained with a shape identical to the standard rod but the index values are raised or lowered by a constant amount. Although such a change is not particularly important in determining the transmission quality of the rod, it will produce a fringe shift on the interferogram and hence it must be taken into account.

Consider the test rod to have an offset of it s index profile of magnitude Dn with

respect to the standard rod. The index profile of the new rod may be written (eq. 4.9) as

$$(4.15) \qquad n(r) = \left(\frac{n_1}{(1 - \frac{1}{2}A)}\right)\left(1 - \frac{1}{2}A\left(\frac{r}{a}\right)^2\right) + Dn$$

The effect of this extra term on the transverse wavefront W(r) can be calculated by incorporating Dn into equation (4.4) and this yields the following integral expression

$$(4.16) \qquad W(y) = -2\int_{y}^{a} \frac{Dn \; r\,dr}{\sqrt{r^2 - y^2}}$$

The solution of this integral is

$$(4.17) \qquad S_2(y) = -2\,Dn\,(a^2 - y^2)^{1/2}$$

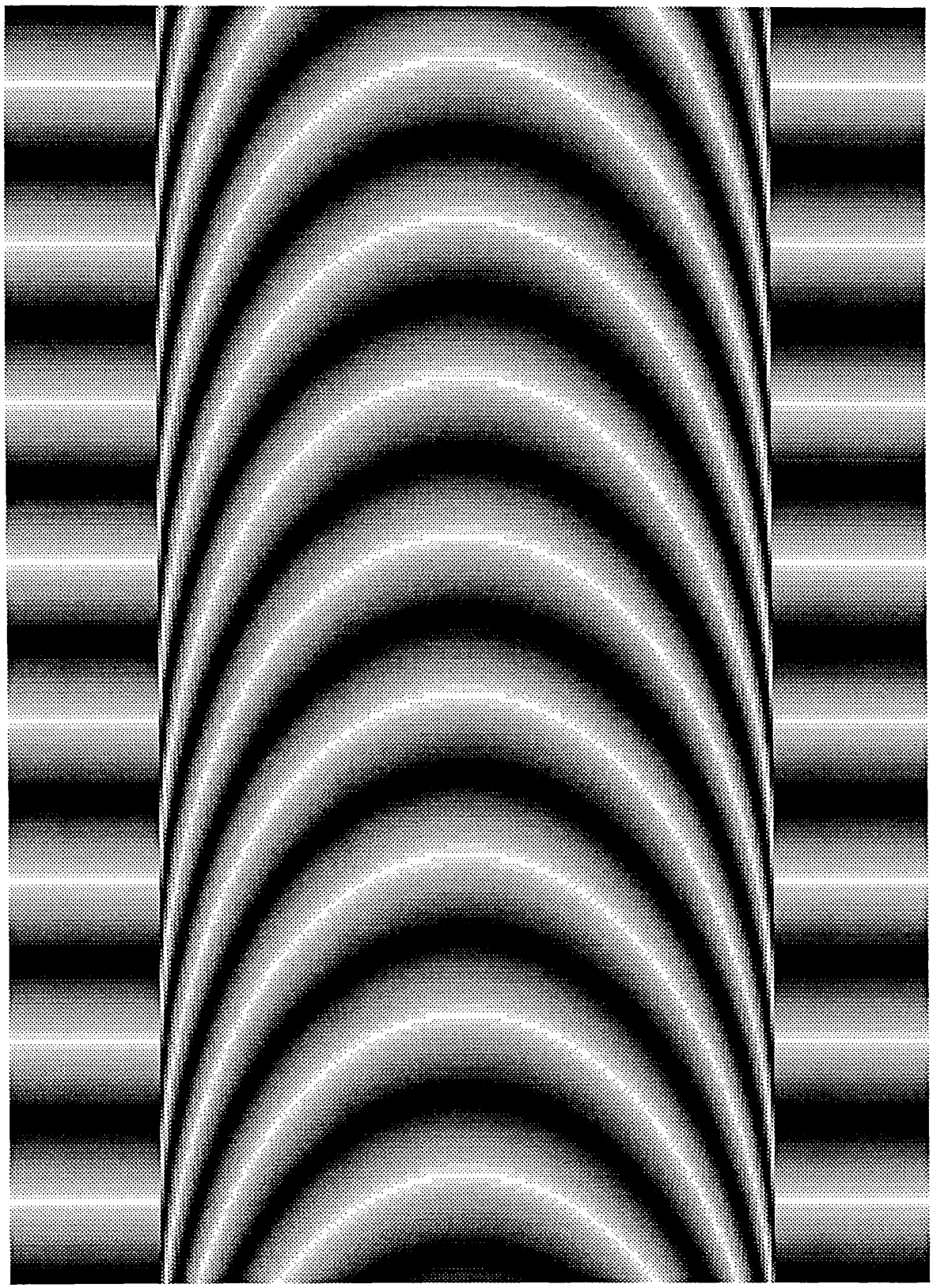
Thus for a rod with the same profile shape as the standard rod, but with a constant offset we must include an optical pathlength retardation term of the form of equation 4.17 and this will produce a fringe shift in the interferogram. For example, the theoretical interferogram for a change in the absolute index values of the profile of Dn = 0.001 is plotted in figure 4.5. The (constant) index difference is plotted in figure 4.6 (below).

The fringe shift in figure 4.5 has a notably different shape to that of fig. 4.3. and it is comparatively large in value. The effect of a constant offset in the index values cannot therefore be neglected.

The absolute values of the refractive index are essentially determined by the refractive index value of the (homogeneous) mother glass from which the lenses are made. Around 240,000 lenses are produced in one production lot, and hence the fluctuation of the absolute index values within a production lot is considered to be negligible[3].

The quoted tolerance on the batch to batch variation in index is given as Dn = ± 0.01. If we compared two rods with a constant index difference of this amount then from eq. (4.15) the corresponding maximum fringe shift would be about 30 fringes. This is really

Figure 4.5: Theoretical interferogram :
Change in the absolute index values

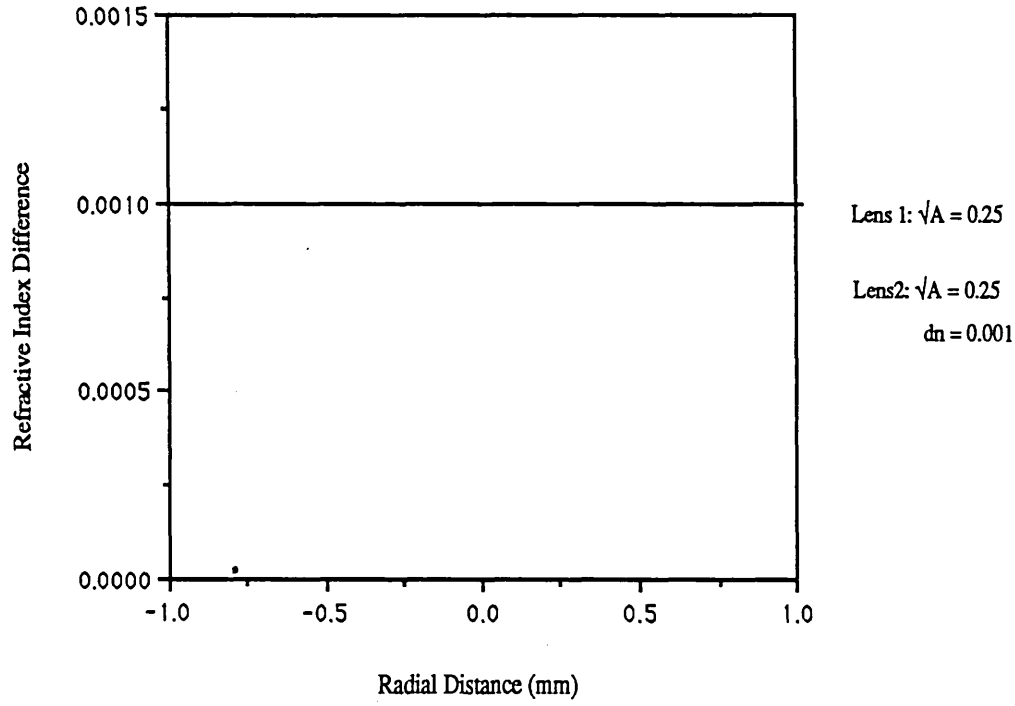


Rod 1 : $\sqrt{A}$ = 0.2500
Dn = 0.0000
Rod 2 : $\sqrt{A}$ = 0.2500
Dn = 0.0010

Matching oil index = 1.516
Diameter variation = 0

too high a value to try and resolve on an interferometer and therefore caution must be exercised when attempting to compare rods with a substantial change in the absolute index values.

Figure 4.6: A constant index difference between the profiles

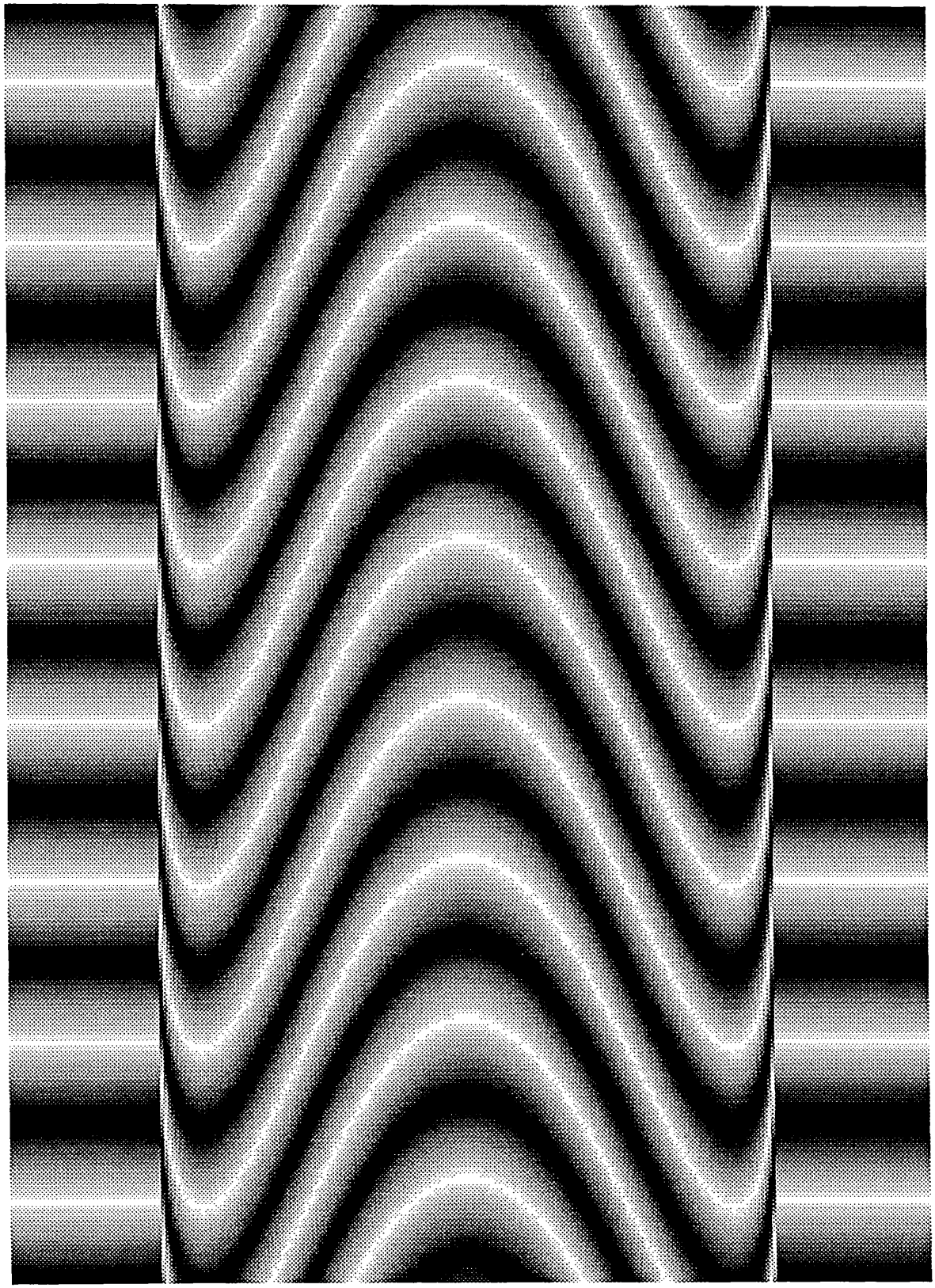



4.4.3 Non-Circularity of Profile

Testing the circular symmetry of the profile is in principle fairly simple in transverse profiling methods; the rod is merely rotated and the index profile is measured at several angular orientations (§2.3.2). In the comparison method, this implies that the interferogram is monitored as the rod sample is rotated. Perfect symmetry of the profile would leave the fringe pattern undeviated.

The circularity of the index distribution in a rod can also be established without the need of the standard rod of known index profile. For example, the transverse wavefront can be recorded and compared with the wavefront produced when the same rod is rotated about its axis. This technique is applied to preform rods in chapter 9.

Figure 4.7: Theoretical interferogram :
Change in both the absolute index values
and the gradient constant



Rod 1 : $\sqrt{A}$ = 0.2500
Dn = 0.0010
Rod 2 : $\sqrt{A}$ = 0.2550
Dn = 0.0000

Matching oil index = 1.516
Diameter variation = 0

4.4.4 Variation of profile with rod length

Testing for a variation of the index profile along the length of the rod can in principle be acheived quite simply by monitoring the interferogram whilst raising or lowering the rod in the test cell.

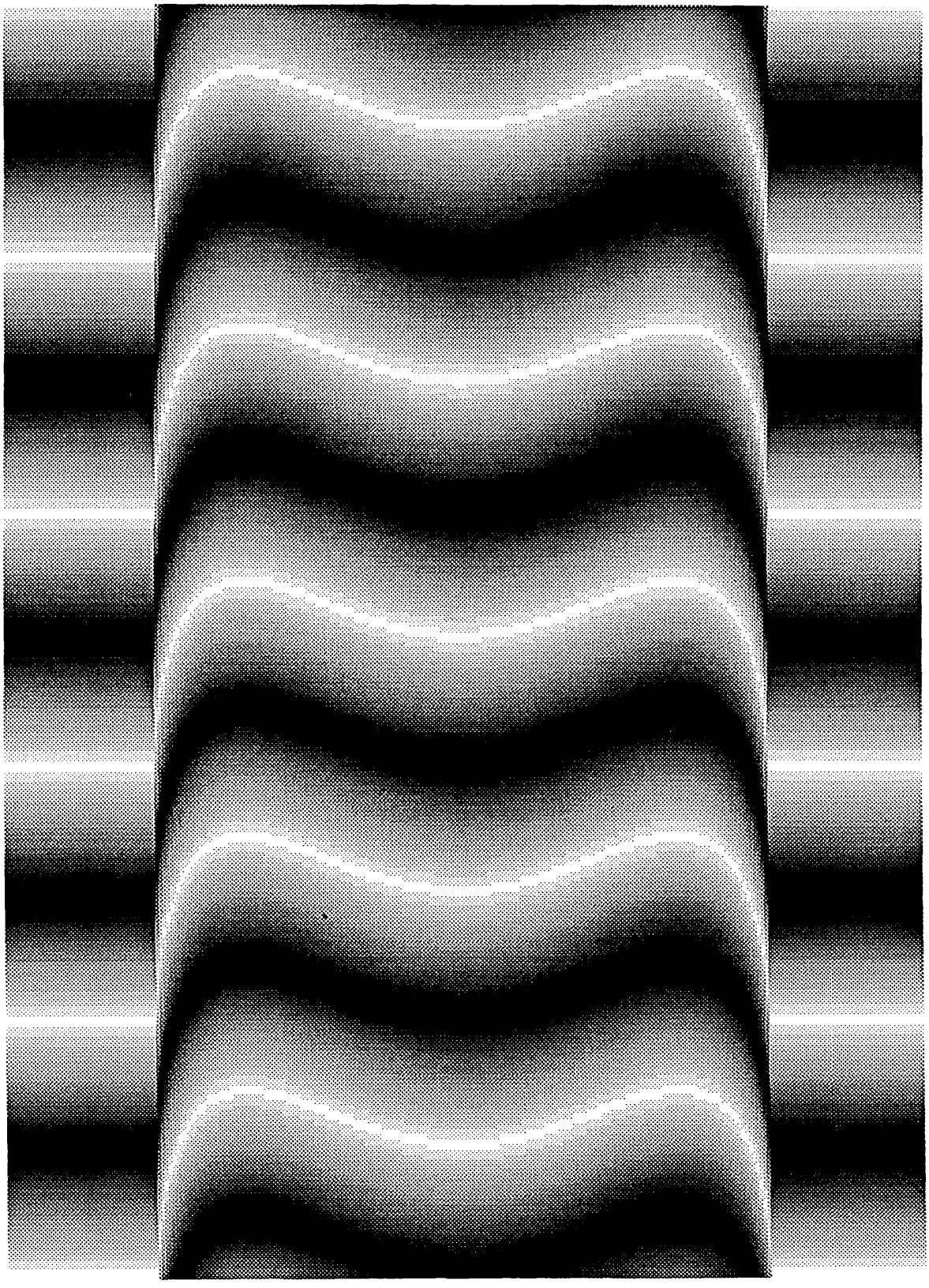
4.4.5 Conclusion

The comparison method has been shown to be in theory, very sensitive to changes in both the profile shape and the absolute index values. The theoretical fringe patterns (fig. 4.3 and 4.5) due to these effects are different in form and in general, the expected pattern due to both effects occuring simultaneously will be given by a simple combination of the two (see figure 4.7 )using equations 4.10 and 4.12. Because the fringe shift is likely to contain information concerning both of these kinds of profile change, we cannot necessarily rely upon an observation of the interferogram to instantly assess the nature of the index change.

The method for calculating the difference between the index distributions from the observed fringe pattern is very similar to the algorithm used for index profile reconstruction in the transverse profiling techniques described in chapter two. Essentially, we are required to find the inverse of the integral equation (4.4) and this is known as the inverse Abel transform and much more will be said about it's computation in chapter seven.

In this section we have only considered parabolic index profiles undergoing straightforward changes in the index distribution. To describe the fringe shifts that would be produced by interferometrically comparing other types of index profile, we would need to solve the integral equation 4.4 either numerically or analytically (if a solution exists) (see §7.1).

Figure 4.8: Theoretical interferogram :
10 micron change in the diameter of the rod



Rod 1 : $\sqrt{A}$ = 0.2500
Dn = 0.0000
Rod 2 : $\sqrt{A}$ = 0.2500
Dn = 0.0000

Matching oil index = 1.516
Reference rod diameter = 2.0 mm
Diameter variation = 10 microns

4.5 Change in rod diameter

As well as detecting profile changes, the comparison method is sensitive to changes in the dimensions of a rod. For example, the standard rod and the test rod may have identical refractive index distributions but differing diameters. We can also not discount a possible ellipticity of the rod. These effects may hinder the desired profile measurement and so the magnitude of the corresponding fringe shifts must be calculated.

The variation of the diameter of a rod lens is almost always less than 0.5%[3]. For a 2mm diameter lens this implies a maximum tolerance on the diameter of ± 10 microns. Measurements made upon a set of rod lenses using a micrometer revealed an approximate ± 3 micron discrepancy. The effect of a diameter variation can be calculated by changing the value of a in equation 4.10. The theoretically observed fringe shift due to 10 micron (0.5%) variation in the diameters of two otherwise identical rods is plotted in figure 4.8. This fringe shift corresponds to the maximum expected deviation of the rod diameter and it will certainly complicate the analysis of a comparison test.

Furthermore, a more fundamental problem is posed when we consider how we might discriminate between the effects of a diameter variation and those due to a change in the refractive index distribution by merely observing the form of the interferogram. For example, figure 4.9 below illustrates the theoretical fringe pattern that would be produced by the comparison of two rod lenses with the following profile parameters:

Lens 1: $\sqrt{A_1} = 0.25$, $Dn_1 = 0.001$.

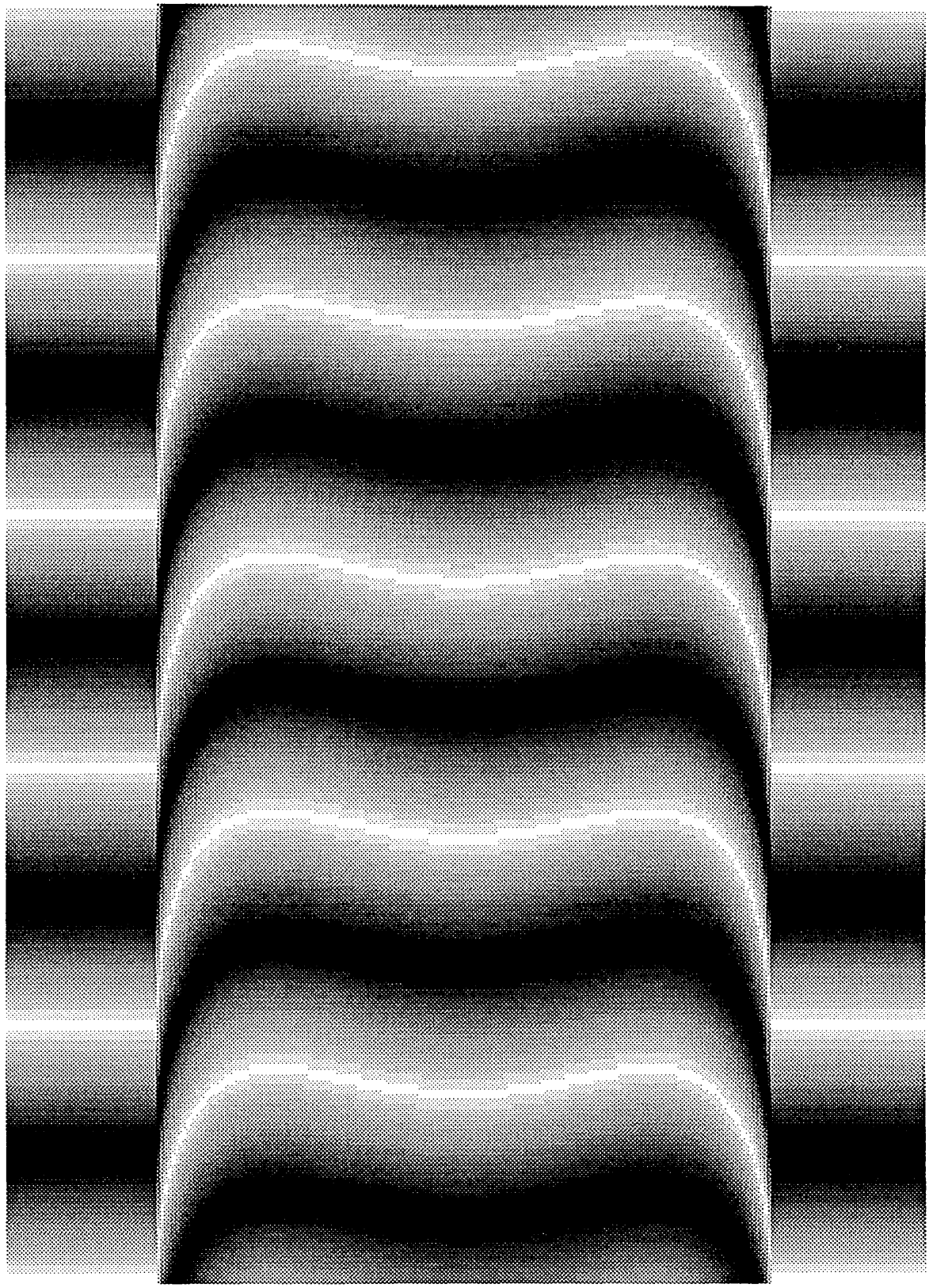
Lens 2: $\sqrt{A_2} = 0.249$, $Dn_2 = 0.0005$.

(Dn measured to a fixed oil refractive index, see §4.7.1.)

The fringe shift looks very similar to that produced by a change in diameter and so it will be important to check the diameters of the rods under test before we analyse the comparison interferogram.

The problem posed by a comparison testing rods with differing diameters is decribed in further detail in chapter seven and also in the conclusion of this thesis.

Figure 4.9: Theoretical interferogram :
Change in the profile parameters corresponding
to an ambiguous fringe pattern

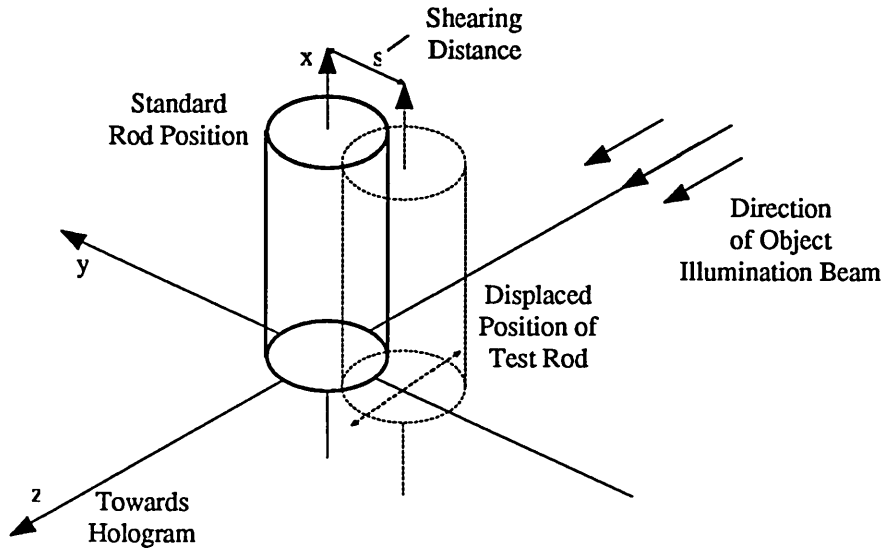


Rod 1 : $\sqrt{A}$ = 0.2500
Dn = 0.0010
Rod 2 : $\sqrt{A}$ = 0.2490
Dn = 0.0005

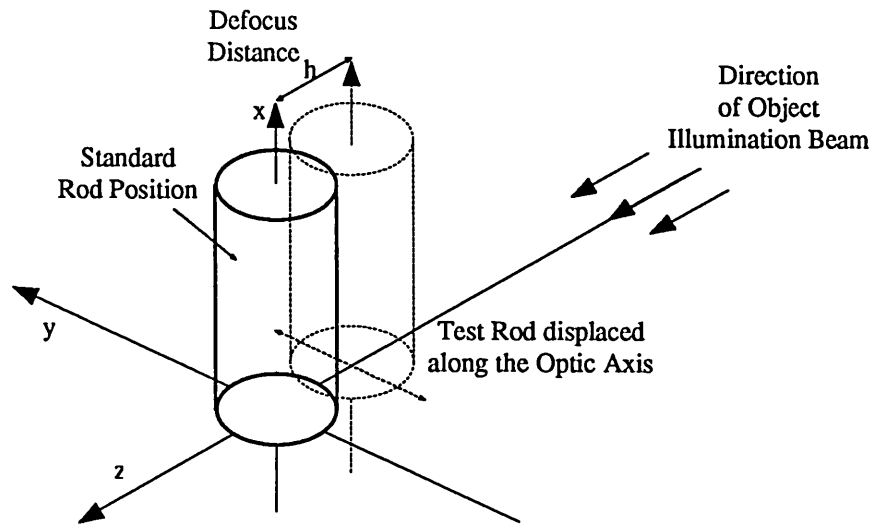
Matching oil index = 1.516
Reference rod diameter = 1.0 mm
Diameter variation = 0

Figure 4.10: Misalignment of the Test Rod

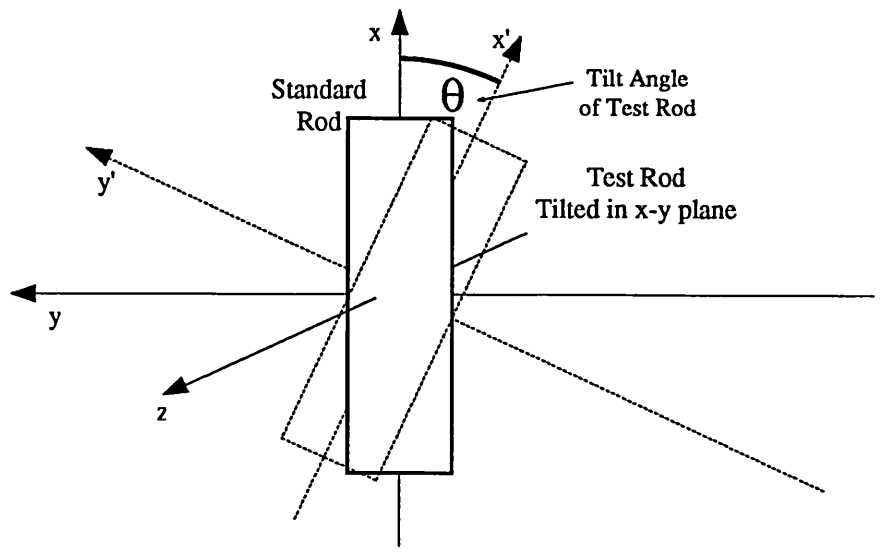
a) Shearing Displacement




b) Defocus Displacement




c) Tilt about the Optical Axis



4.6 Misalignment between rod positions

One practical problem in comparison testing is ensuring that the test rod is replaced and re-aligned identically with the original standard rod. In the practical interferometer the test rod will almost certainly be misaligned and we must consider the magnitude and form of the fringe shifts that such an error will contribute to the interferogram.

A rod misalignment can occur in a combination of ways (schematically illustrated in figure 4.10) and these are now discussed in turn.

4.6.1 Transverse displacement (shear)

A transverse misalignment (fig. 4.10a) arises when the rod is displaced at right angles to the optical axis and the two interfering wavefronts are said to be sheared with respect to each other.

The fringe pattern has a form that is directly related to that produced in the Transverse Shearing interferometric method described in chapter two (§2.4.4)ie.

$$(4.18') \qquad S_3(y) = W(y) - W'(y + S).$$

We may use the above expression to compute the fringe shift in equation 4.1, however we can derive an approximate expression for the form of $S_3(y)$ if we consider the comparison of two identical but displaced GRIN rods. Thus from chapter 2 we have

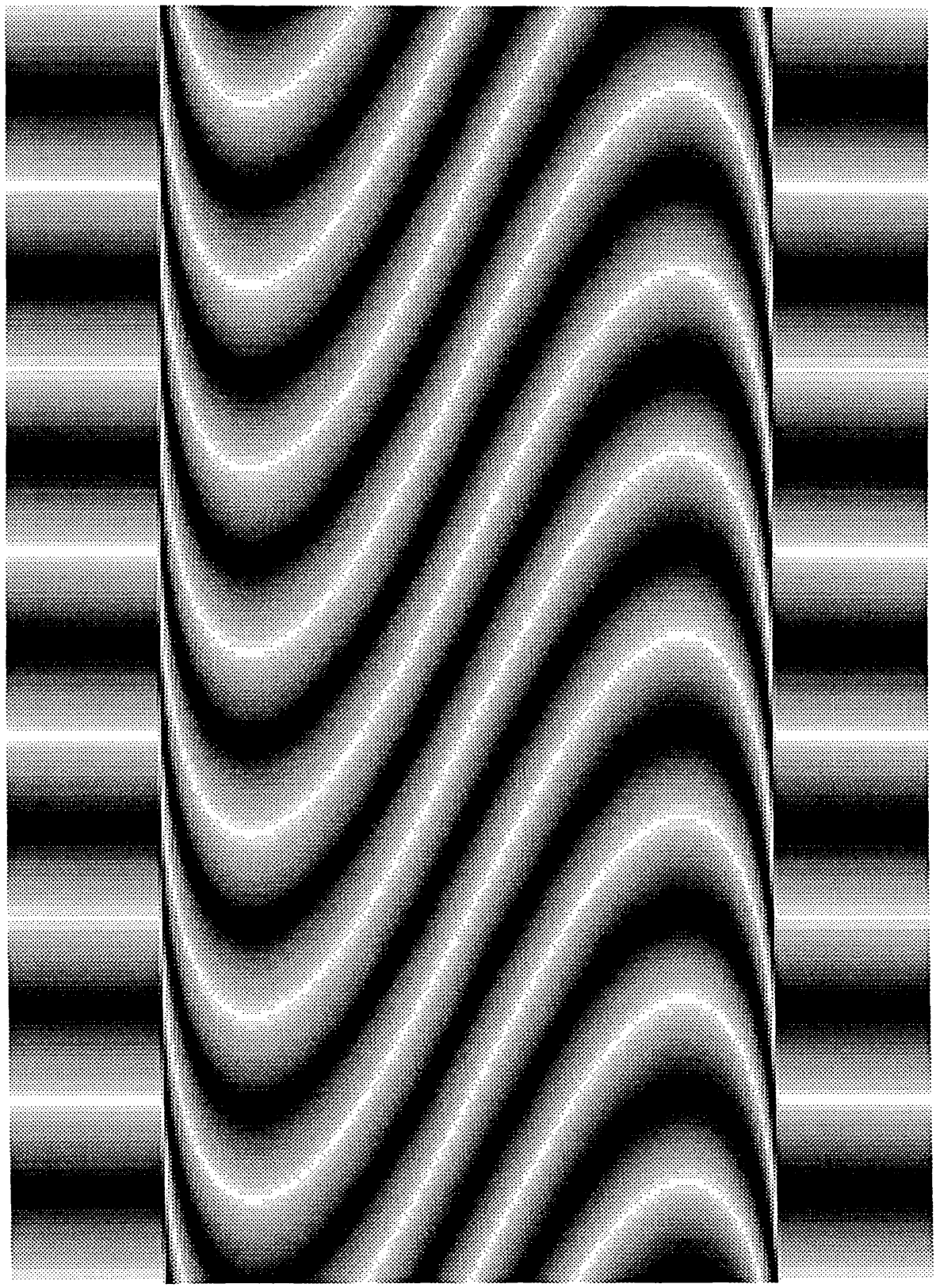
$$(4.18) \qquad S_3(y) = S \frac{dW(y)}{dy}$$

where dw/dy is the derivative of the wavefront W(y) and S is the shearing distance..

It will be useful to calculate the form of S(y) for the transverse wavefront, thus differentiating eq. (4.10)

$$(4.19) \qquad S_3(y) = \left( \frac{2n_1 A}{a^2 (1 - \frac{1}{2}A)} \right) (y\ S)\ (a^2 - y^2)^{1/2}$$

Figure 4.11: Theoretical interferogram :
Shearing misalignment of the rod



Rod 1 : √A = 0.2500
Dn = 0.0000
Rod 2 : √A = 0.2500
Dn = 0.0000

Matching oil index = 1.516
Reference rod diameter = 2.0 mm
Diameter variation = 0
Shear displacement = 10 microns

The interferogram resulting from a shearing displacement of S = 10 microns is plotted in figure 4.11. The fringe shift has the form given by equation 4.19 and the important point to note from the figure is the asymmetry of the pattern. This asymmetry implies that the effect of a transverse misalignment can be removed by translating the rod across the optical axis until the interferogram has symmetry (s=0).

Shearing interferometry is discussed in more detail in chapter 8 where the technique is used for index profile measurement.

4.6.2 Longitudinal displacement (defocus)

A longitudinal misalignment corresponds to the test rod being displaced along the optical axis either side of the correct position (fig. 4.10b). The effect on the interferogram is similar to the shearing effect discussed above and is analogous to defocus in a conventional interferometer. Essentially, the interferogram corresponds to the interference of two waves which are similar but have suffered a relative displacement along the optical axis. When studying this effect, the propagation of a wave along the direction of the optical axis (and consequent change in the wave shape) must be taken into account.

Figure 4.12 below, schematically illustrates the defocus effect.

Figure 4.12: Defocus between Two Similar Wavefronts

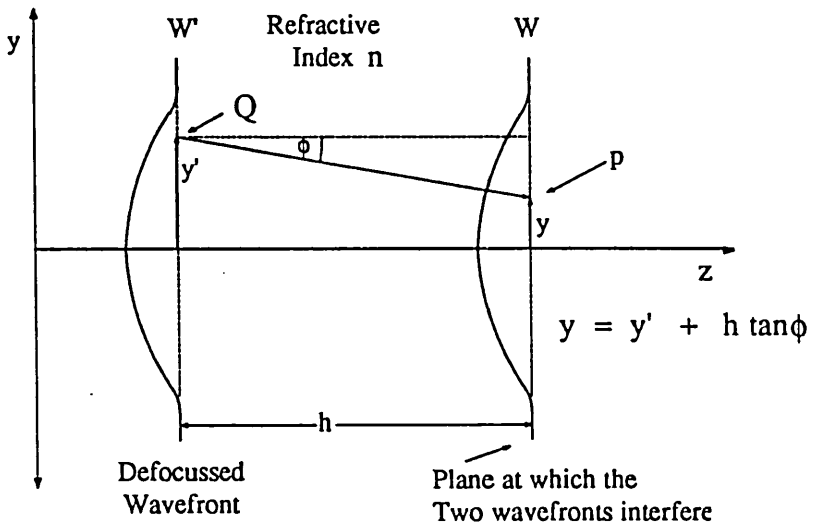
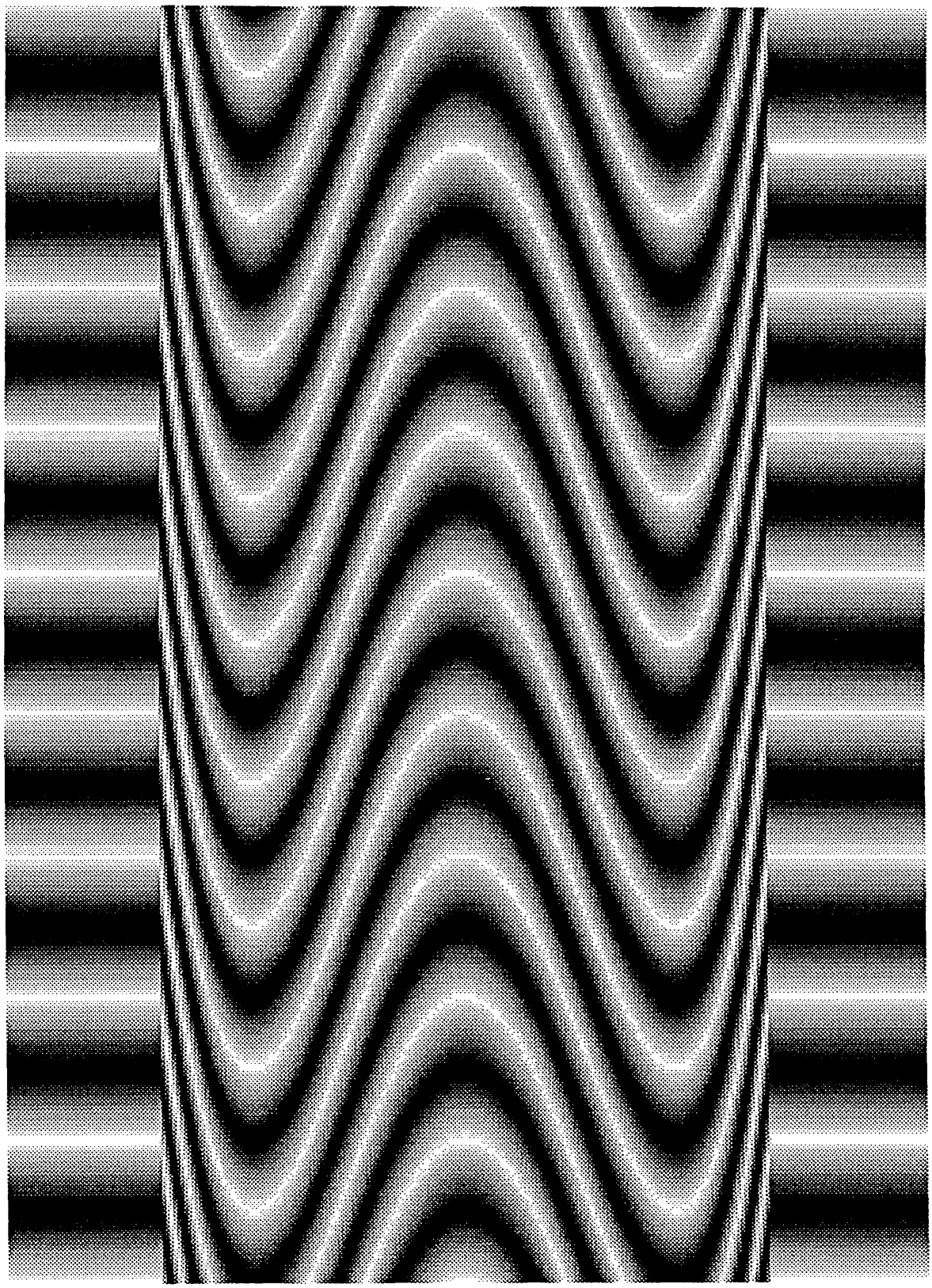


Figure 4.13: Theoretical interferogram :
Defocus misalignment of the rod



Rod 1 : √A = 0.2500
Dn = 0.0000
Rod 2 : √A = 0.2500
Dn = 0.0000

Matching oil index = 1.516
Reference rod diameter = 2.0 mm
Defocus displacement = - 500 microns

We consider the case of two wavefronts displaced along the optical axis by an amount h. At the point P in the interference plane, the undisplaced wavefront has an optical pathlength delay of W(y), at this position the wave interferes with the point Q on the defocussed wavefront that has propagated to P. The pathlength delay for the defocussed wavefront at Q is W(y') and from the figure we see that

(4.20) $y' = y - h \tan \phi_{(y')}$

Thus at point P the total optical pathlength difference between the two waves is

(4.21) $S_4(y) = W(y) - W'(y') - n\,h\,(\sec \phi_{(y')} - 1)$

where the last term includes the optical pathlength difference produced by the ray propagating through the oil (index n) at angle $\phi$. We may use this expression to plot out the form of the defocus interferogram, see figure 4.13 where h = -500 microns.

We can however derive an approximate expression for the form of the fringe shift, if we assume that the two GRIN rods are identical so that W(y) = W'(y), thus we have

(4.22) $S_4(y) = W(y' + h \tan \phi_{(y')}) - W(y') - n\,h\,(\sec \phi_{(y')} - 1)$

Inserting equation (4.11) into equation (4.22) and making use of a Taylor series approximation we have

(4.23) $$S_4(y) = \left(\frac{h}{n}\right)\left(\frac{dW(y')}{dy}\right)^2 - n\,h\,(\sec\phi_{(y')} - 1)$$

We can simplify this further by noting that $\cos \phi = (1 - \sin^2 \phi)^{1/2}$ and for small refraction angles we have $\sin \phi \approx \tan \phi$. (From equation 4.13 the error is less than 0.2% for $\phi_{max} \approx 0.07$ radians). Thus inserting the expression for $\tan \phi$ (eq.4.11) we have

(4.24) $$\sec \phi_{(y')} = \left(1 - \left(\frac{1}{n^2}\right)\left(\frac{dW(y')}{dy}\right)^2\right)^{-1/2}$$

Using a binomial expression to first order we have $(1+x)^{\alpha} \approx 1 + \alpha x$. Thus rewriting equation 4.24, we can simplfy the right hand side of equation 4.23 so that we finally have an approximate expression for the defocus pathlength difference of

$$(4.25) \qquad S_4(y) = \left(\frac{h}{2n}\right)\left(\frac{dW(y')}{dy}\right)^2$$

Calculating this for the transverse wave yields

$$(4.26) \qquad S_4(y) = \left(\frac{2n_1A^2}{a^4(1 - \frac{1}{2}A)}\right)(y'^2h)\,(a^2 - y^2)$$

and this is the contour of the fringe shift plotted in figure (4.13).

This fringe pattern of fig. 4.13 is similar to the shearing interferogram with the exception that there is a symmetry to the defocus pattern and the sign of the fringe shift depends upon h. The pattern will remain symmetrical regardless of the values of h and thus unlike the shear misalignment (which is markedly asymmetrical). defocus cannot be removed from the system merely by adjusting the rod position and observing the interferogram. In chapter six we shall consider a practical solution that enables a defocus misalignment to be removed interferometrically.

4.6.3 Rotation of rod about the optical axis (tilt)

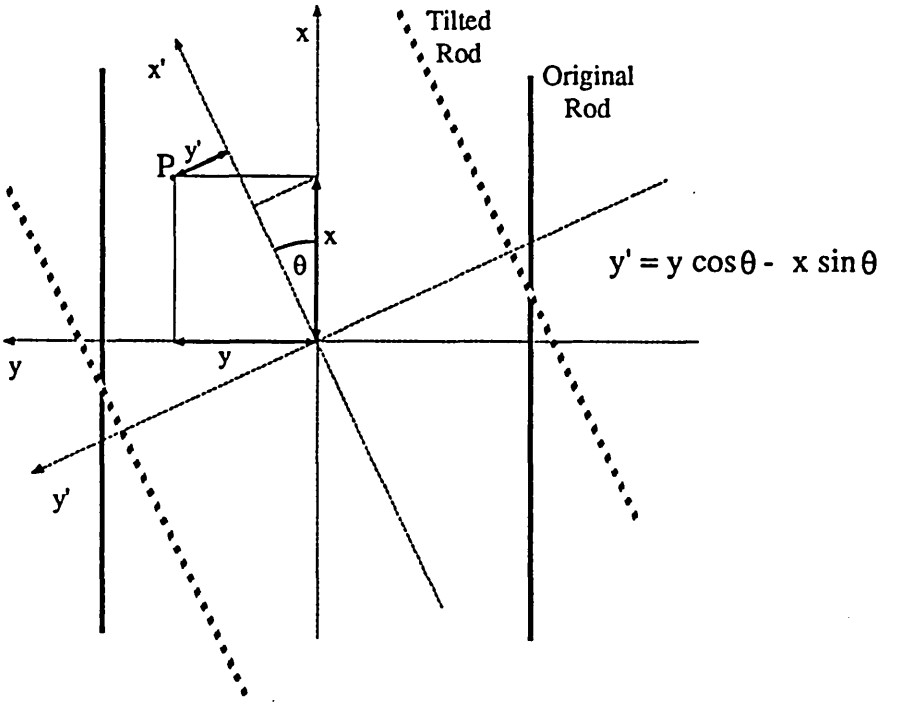
As well as the translational misalignment of the test rod position there is the possibility of the rod being tilted with respect to the standard rod. To quantify the effect of this, we take the case of a test rod having an identical profile to the standard rod but upon insertion into the optical cell it is rotated about the optical axis by an amount $\theta$ (it remains in the x-y plane). The rotation (tilt) misalignment is illustrated in figure 4.14 below.

At the point P in figure 4.14, the rotational shearing interferogram, will have fringe contours given by

$$4.27 \quad S(y) = W(y) - W(y') = W(y) - W(y\cos\theta - x\sin\theta)$$

where we assume the index distribution does not vary with the length (x direction) of the rod. The interferogram for a rod rotated by 1 degree about the optical axis is shown in figure (4.15). The pattern is asymmetric and so the effect of a tilt can be removed by rotating the rod until the pattern has symmetry about the vertical x- axis.

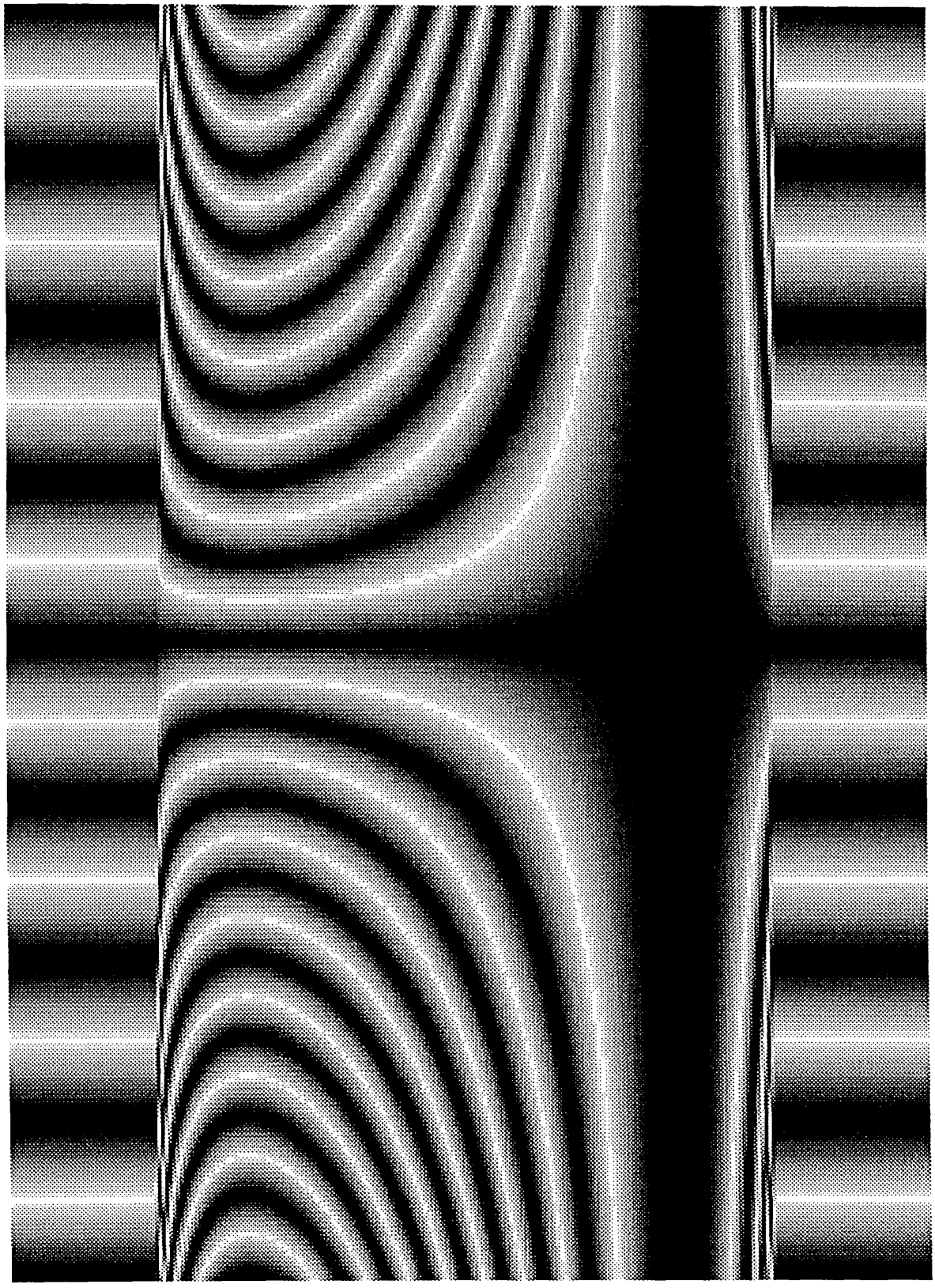
Figure 4.14: Rotation of Rod about the Optical Axis




4.6.4 Conclusion

In this section on effects due to a misalignment of the test rod position with respect to the standard rod, it is quite clear that there must be some mechanism for accurately translating and tilting the test rod in the optical cell. The shearing and tilt misalignments produce an assymmetrical fringe pattern and we can assume that they can be removed by adjusting the rod orientation until the pattern has symmetry, in a manner similar to that in a conventional interferferometer. However, the defocus effect produces a symmetrical fringe shift and so defocus cannot be simply removed in the above manner. In chapter 6, we shall discuss the practical procedure for realigning the test rod with the standard rod and we shall plot the experimental counterparts of figures 4.11, 4.13 and 4.15.

Figure 4.15: Theoretical interferogram :
Rotation of rod about optical axis



Rod 1 : $\sqrt{A}$ = 0.2500
Dn = 0.0000
Rod 2 : $\sqrt{A}$ = 0.2500
Dn = 0.0000

Matching oil index = 1.516
Reference rod diameter = 2.0 mm
Angle of rotation = 1°

## 4.7 Refractive index matching oil

The GRIN rod is immersed in index matching oil in the optical cell to remove the otherwise strong refraction that would take place at the air-rod boundary. Ideally, the refractive index of the matching oil should be identical to the glass index at the edge of the rod. In practice this may not be the case and we must consider the effect of this upon the comparison method, and also account for a possible fluctuation in the refractive index of the oil during the course of the experiment.

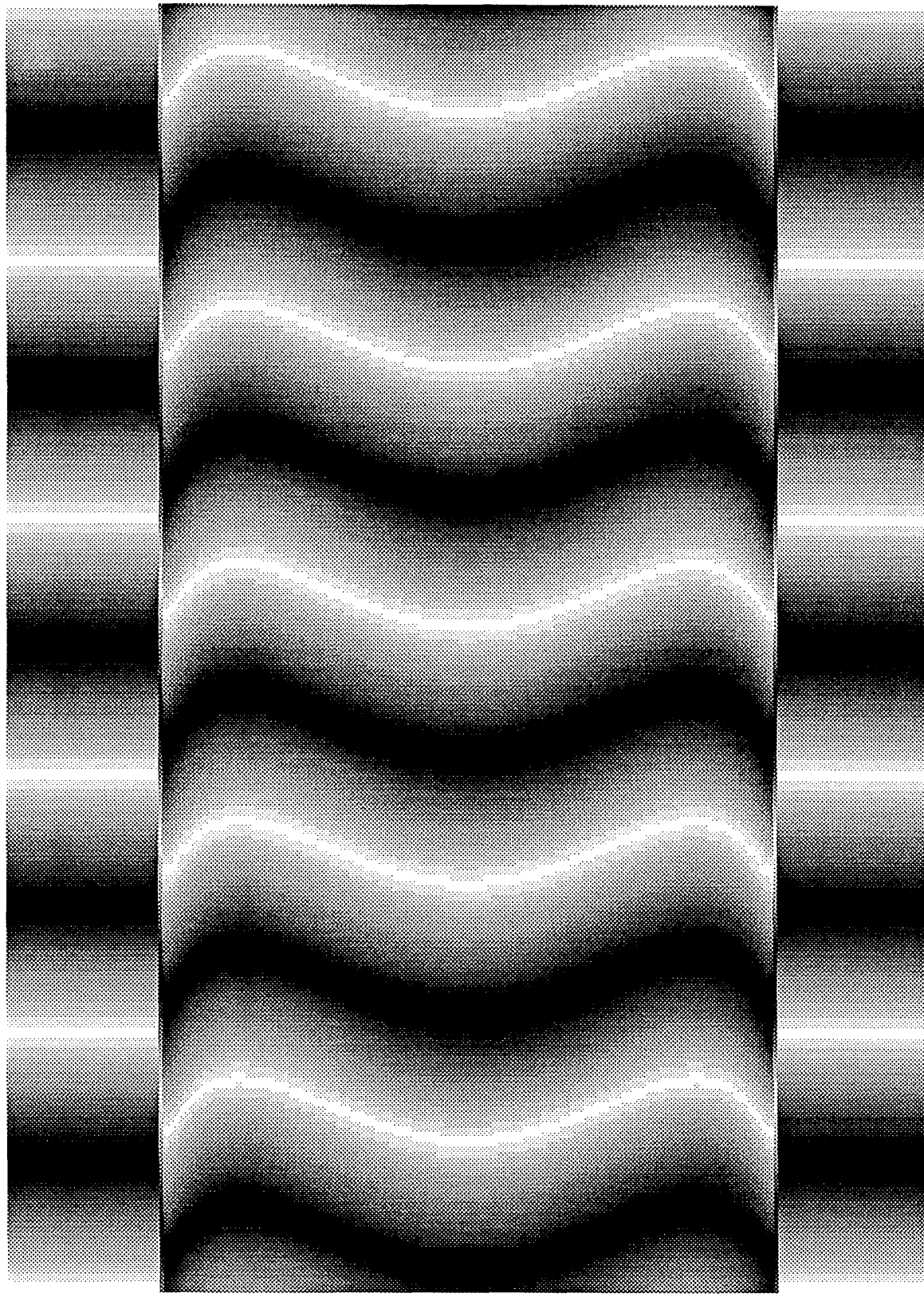
### 4.7.1 Effect of an index mismatch

The effect of an index mismatch between the index of the matching oil and the edge of the glass rod, can be calculated by considering the index difference to be in the form of an offset in the profile Dn as discussed in section 4.5.2. Thus when calculating the interferograms as in the preceding sections, the effect of the index mismatch can be determined by redefining the profiles of both the rods using equation 4.15 where the value of Dn will include the difference between the oil refractive index and the glass edge refractive index. The resulting wavefront transmitted through the rod will be a simple addition of equations 4.10 and 4.17.

The resulting interferograms are similar to those produced when the oil index is matched to the rod, with exception of the shearing and diameter variation shearing interferograms. These new patterns are plotted in figures 4.16 and 4.17 for an index mismatch of Dn= 0.004 and they should be compared with figures 4.8 and 4.11 respectively. The major observable difference is at the edge of the rod where there is a marked discontinuity in the fringe shape. In the previous interferograms, the fringes in the rod ran continuously into the horizontal tilt fringe. Such a discontinuity in a fringe pattern is representative of a large discontinuous change in the optical pathlength across the wavefront. In both interferograms, this change is due to a combination of the index mismatch and the rod edges not being aligned together.

Figure 4.17 thus indicates that an oil-glass index mismatch can be revealed by

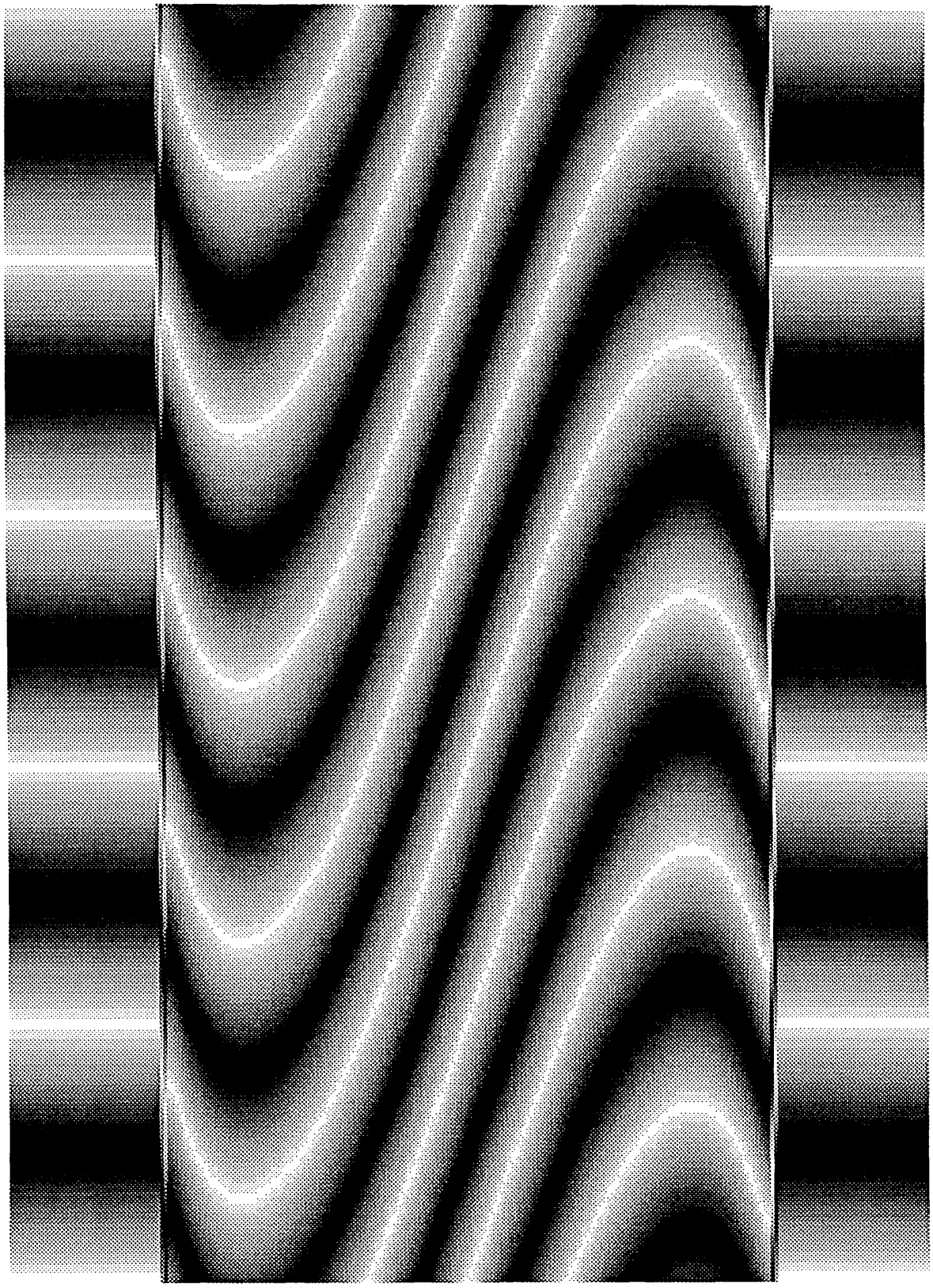
Figure 4.16: Theoretical interferogram :
Index mismatch at the rod boundary and a diameter variation



Rod 1 : √A = 0.2500
Dn = 0.0040
Rod 2 : √A = 0.2500
Dn = 0.0040

Matching oil index = 1.516
Reference rod diameter = .0 mm
Diameter variation = 10 microns

Figure 4.17: Theoretical interferogram :
Index mismatch at the rod boundary and a shearing misalignment



Rod 1 : $\sqrt{A}$ = 0.2500
Dn = 0.0040
Rod 2 : $\sqrt{A}$ = 0.2500
Dn = 0.0040

Matching oil index = 1.516
Reference rod diameter = 2.0 mm
Diameter variation = 0
Shear displacement = 10 microns

shearing the rod position and observing whether the shifted fringe rejoins the tilt fringe running horizontally through the index matching oil. In fact this method is a useful way of assessing the quality of the index matching at the rod boundary in a refractive index profiling measurement technique. (see figure 6.4 in chapter six).

4.7.2 Temperature stability of the index Matching Oil

The refractive index of the matching oil is very dependent upon it s temperature, the temperature coeficient being (approximately)

$$\frac{dn}{dT} = -0.0004 \tag{4.28}$$

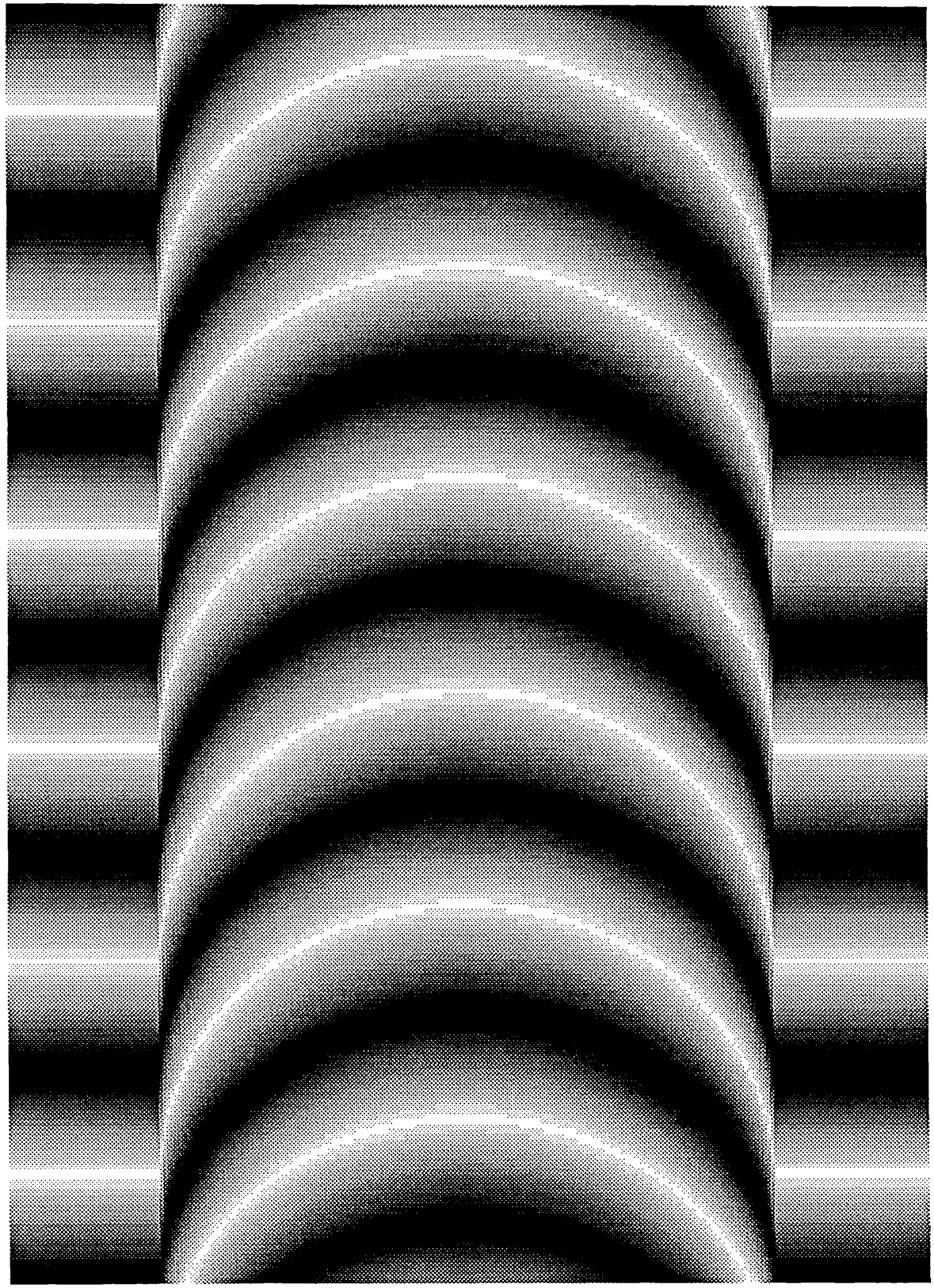
This is a few orders of magnitude higher than that for air or glass. Hence in interferometry and refractometry experiments involving liquids, great care must be taken to ensure that fluctuations of the liquid temperature and hence refractive index, do not affect the results. If the refractive index of the matching oil changes after the hologram has been recorded, then this will alter the optical pathlength across the wavefront passing transversely through the GRIN sample in 'real time'; producing an (undesirable) fringe shift on the interferogram and this will have an effect upon the desired measurement.

The effect is analysed by assuming that the index change is uniform throughout the volume of the oil and insignificant within the the glass rod. Without a glass rod in the cell, the principal effect (neglecting refraction) of an index change in the oil is to introduce a constant optical pathlength change across the whole wavefront. This would have no observable effect upon an interferogram. The presence of the glass rod in the cell then, is to effectively remove a cylindrical volume of oil from the cell and thus the change in optical pathlength is not uniform across the portion of the wavefront that passes through the rod.

The magnitude of the effect can be calculated by comparing the optical pathlength of the ray travelling through the (unaffected) glass rod and the ray passing through the matching oil which has suffered a constant change in index dn since the recording of the hologram. The calculation is essentially identical to that in §4.4.2, where a constant change in the values of the index profile was considered. The change in optical pathlength

Figure 4.18: Theoretical interferogram :

Change in the index matching oil temperature of 1°C



Rod 1 : √A = 0.2500 Matching oil index = 1.516 (at recording)

Dn = 0.0000 Reference rod diameter = .0 mm

Rod 2 : √A = 0.2500 Oil temperature change = 1°C

Dn = 0.0000 dn = - 0.0004

can be expressed as

$$(4.29) \qquad S_6(y) = 2\,dn\ (a^2 - y^2)^{1/2}$$

For a 2mm diameter rod lens, a change in the oil temperature of 1°C will produce a fringe shift at the centre of the rod of aprroximately 1 fringe (see figure 4.18 ). This pattern is obviously similar to that in figure 4.6. To reduce the fringe shift to a negligible amount, this implies stability of the matching oil temperature to less than a tenth of a degree. For a preform rod of 10mm diameter, the corresponding change is around 6 fringes and in this case the oil temperature must be maintained to less than a hundredth of a degree.

### 4.7.3 Conclusion

In this section, we have seen that the index of the matching oil must be as close as possible to the edge index of the rod, and it must be maintained precisely at this value during the course of the experiment. Accurate control of the oil temperature was a major design consideration in the construction of the interferometer and the method used is described in chapter 6.

## 4.8 The Comparison Method Applied to Preform Rods

So far in this chapter, we have described the implications of a comparison test between two similar rod micro-lenses, however, we must also consider how this test might be applied to preform rods.

Preform rods have diameters of between 5-50mm compared to 1-2mm diameter rod lenses and the sensitivity of a comparison test will be scaled up accordingly. The reason for this is that any changes in the profile parameters will be integrated through a larger amount of glass. For example consider a preform rod with core size of 10 mm and $\sqrt{A} \approx 0.2$, we calculate the forms of the interferograms using program HOLOCOMP, and we find that :

1) A 3% change in the quadratic gradient constant will produce a fringe shift similar to fig. 4.3, however the maximum shift of the pattern is around 20 fringes.

2) A change of the absolute index values of the index profile of Dn = 0.001 will produce a fringe shift similar to fig. 4.5 with a maximum fringe shift of around 15 fringes.

3) The tolerance on the diameter of an optical fibre preform is quite relaxed as a tight control can be kept upon the diameter of the target fibre when the rod is pulled. The preform diameter variation can easily be as high as ± 200 microns for a 10 - 20 mm diameter preform. A 200 μm diameter variation on 10 mm core diameter preform would contribute around 10 fringes to the interferogram.

4) Preforms made by the ion deposition technique (§1.4.2) have a profile that consists of small but discrete layers of constant index glass. This may imply that the transverse wavefront does not have the smooth form given by eq. 4.10 but instead consists of small discontinous changes in optical pathlength across the wavefront. Consequently, the experimental interferograms may not have the smooth form of the patterns plotted in this chapter.

The comparison technique is thus likely to be very sensitive to any changes in the index distribution in a large diameter preform rod, and indeed we must consider whether the technique is in fact too sensitive to profile changes, and in particular changes in the rod parameters that are not particulary important to the ultimate transmission properties of the fibre (the rod diameter for example).

## REFERENCES

1) D. Marcuse, "Principles of Optical Fibre Measurements," Academic Press, 1979.

2) I.S. Gradshteyn and I.M. Ryzhik, "Tables of Integrals, Series and Products," 4th Edition, Academic Press 1980.

3) K. Koizuma, K. Nishizawa and K. Sono, "Selfoc Lens Handbook," Nippon Sheet Glass Company Limited, Japan, 1981.

4) Selfoc Lens Catalogue , Nippon Sheet Glass Company Limited, Japan, 1986.

# CHAPTER FIVE

## DESIGN AND CONSTRUCTION OF A LIVE FRINGE HOLOGRAPHIC INTERFEROMETER

This chapter describes the design considerations for a live fringe holographic phase interferometer. A holographic system is very flexible, and a variety of arrangements were tested before the final working set-up was achieved. Many of the developments described here were established by trial and error.

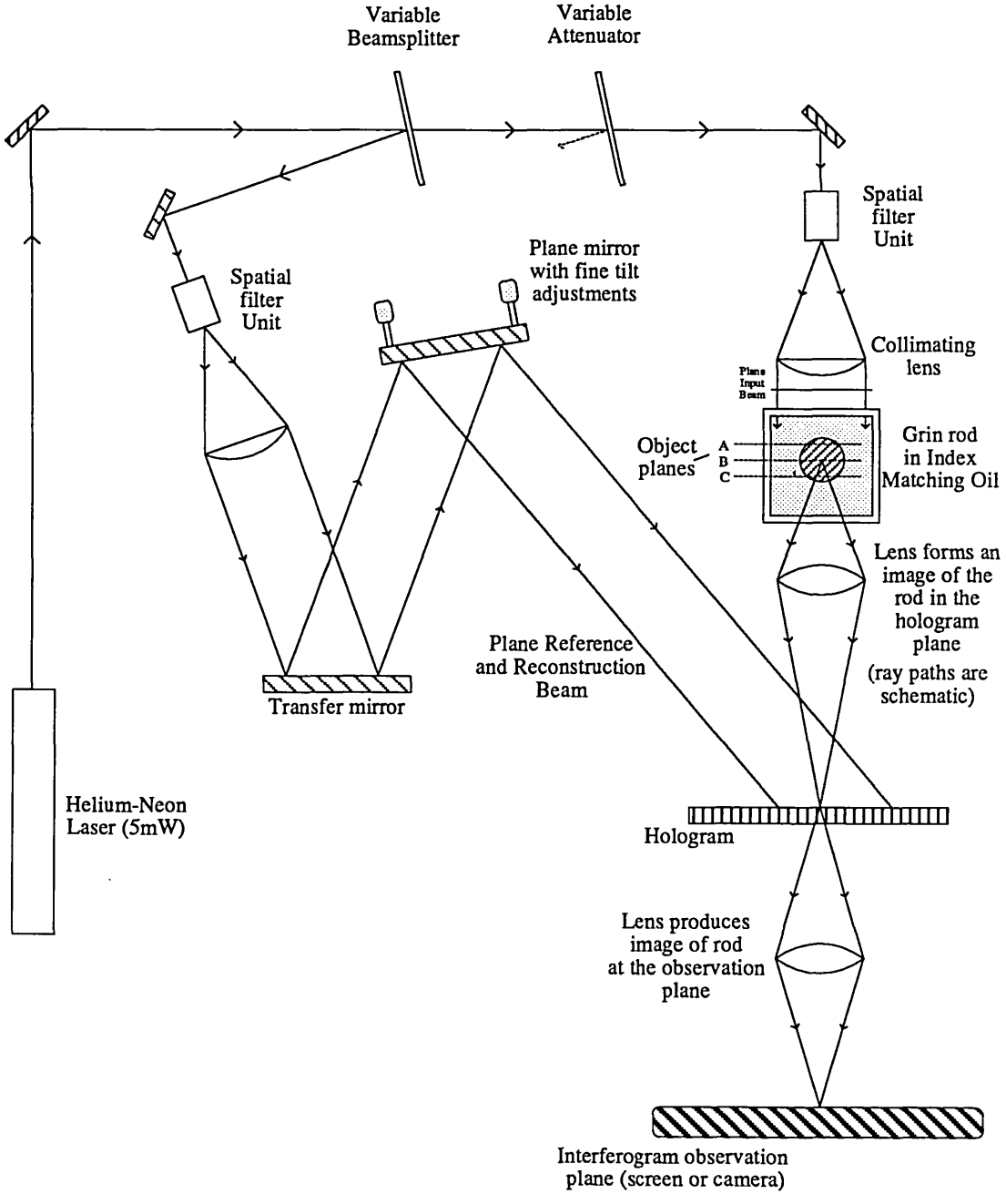
At this point, we shall not discuss in any great detail the use of the working interferometer in analysing graded index samples. Thus the system described here could be applied to almost any phase object. The more essential design considerations required for refractive index profiling via a comparison technique shall be described in the following chapter.

### 5.1 The Basic Layout and Components

The layout of a typical holographic (phase) interferometer was schematically illustrated in Figure 3.2 (page 51). The practical system used in this work is shown in Fig 5.1, note that this arrangement includes the use of a mirror for tilting the reference beam and lenses for imaging the phase object onto a suitable viewing plane.

The apparatus was constructed in the workshop rather than from a conventional optical bench kit as it was considered that this would provide a more accurate and flexible system that could be modified as the project progressed. With the need for great stability of holographic apparatus, emphasis was made upon the rigidity of the components; in particular the beam height above the table was kept as low as possible for this purpose. The components of the interferometer were attached to the optical table either magnetically or by using foot clamps. The table itself was supported on partially inflated inner tubes to

Figure 5.1: The Holographic Interferometer



prevent vibrations being transmitted to the apparatus.

Finally, a hardboard housing was built over the table. Such a housing prevents draughts from disturbing the beams of the interferometer, provides an effective barrier to dust and allows the interference fringes to be observed with the room lights on.

### 5.1.1 The laser

A 5mW linearly polarised Helium-Neon laser ( $\lambda = 632.8$nm) was used as the light source. This satisfies the coherence requirements of holography and is sufficiently powerful to reduce exposure times to under a second and produce fringes easily and safely viewable with a naked eye. The plane of polarisation of the light should be arranged to be orthogonal to the plane of the table, and this ensures maximum interference between the object and reference beams.

### 5.1.2 Beamsplitter and beam ratios

In practical holography, it is often necessary to vary the relative intensities of the object and reference beams (to ensure a linear holographic recording for example[1]). A variable reflectivity beamsplitter is extremely useful for this purpose as it can be easily used to provide a range of reference to object beam ratios. They are also very useful as they can be further used as variable beam attenuators. The simplest arrangement for a variable beamsplitter is to coat a circular glass substrate with a varying thickness of a reflecting material (ie. inconel )[2], the relative intensities of the reflected and transmitted beams can be then be altered by rotating the beamsplitter. Several such beamsplitters were utilised in the holographic interferometer.

To maximise the contrast of the live fringes on the final interferogram, it is usually necessary to adjust the beam ratio after the recording of the hologram. Typically, the diffraction efficiency of the hologram may not be high enough to provide high contrast fringes and one needs to increase the relative intensity in the reference beam. It is not advisable to change the beam ratio upon reconstruction by further rotating the variable

beamsplitter as in practice, the reflected beam 'walks-off' as the beamsplitter is rotated. Thus a variable attenuator should be placed in either of the beams for use upon reconstruction of the hologram. The recording arrangement varied for the various experiments that were tried but typically, an approximate 1:1 reference-to-object beam ratio was used in the recording of the hologram with a variable attenuator in the reference beam so that upon reconstruction, the intensity of the diffracted image could be increased if necessary to maximise the contrast of the live interference fringes.

### 5.1.3 Beam expansion

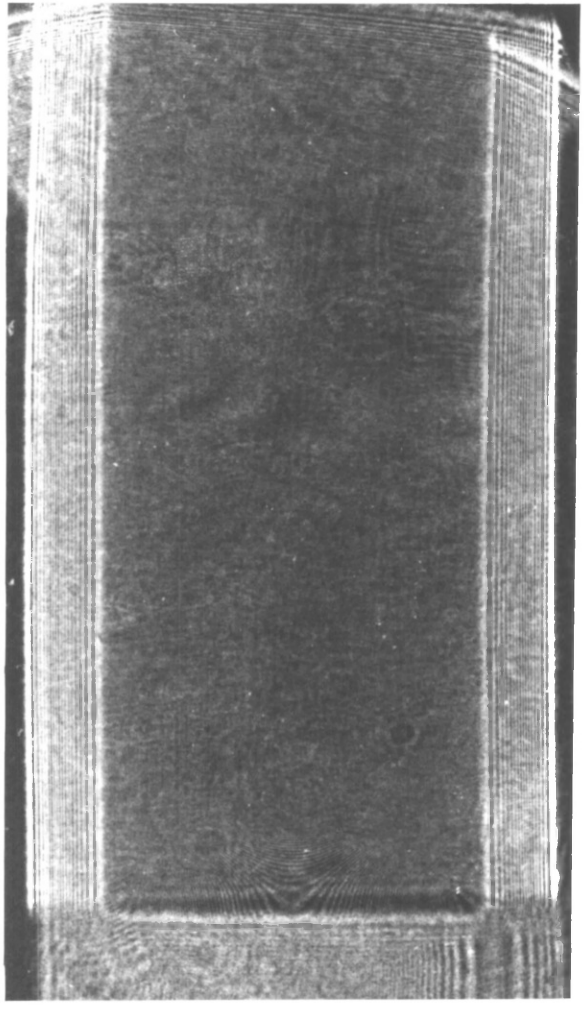
It is advantageous to expand the beam at the latest possible stage, after the initial optical components (transfer mirrors and beamsplitters). This reduces the tolerance on the optical quality (and also the cost) of these elements.

The laser beam must be expanded from it s initial 2mm diameter to the final working diameter of about 40mm. This is best achieved by using a microscope objective and pinhole assembly, referred to as a spatial filter unit. The objective focusses the beam to a tiny spot and the beam then diverges away from this point. The pinhole is used to filter or 'clean-up' the beam, and it must be accurately positioned at the focus of the objective using micrometer-like adjustment screws. Without the pinhole assembly, the expanded beam will contain noise in the form of diffraction rings, which arise from dust and dirt on any of the intitial optical elements. The microscope objective and the precision pinhole must be carefully matched to each other, a 20x objective and 10 micron pinhole were used in this case.

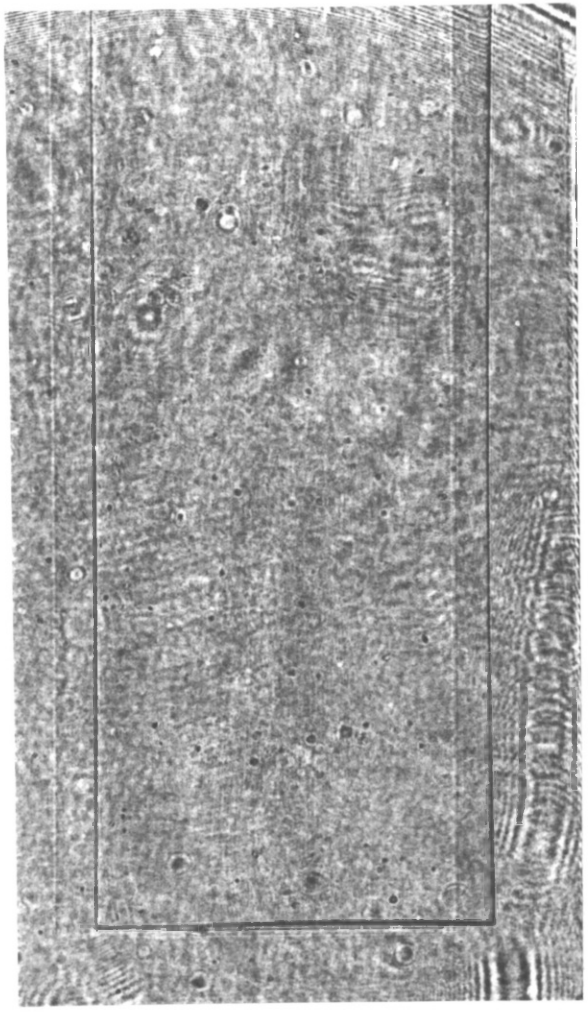
### 5.1.4 Beam Collimation

A working aperture of about 40mm was chosen to accommodate preform rods of 10-20mm diameter into the object beam. The beams were collimated by placing the spatial filter assemblies at the focus of two 152mm focal length, 40mm diameter collimating doublets.

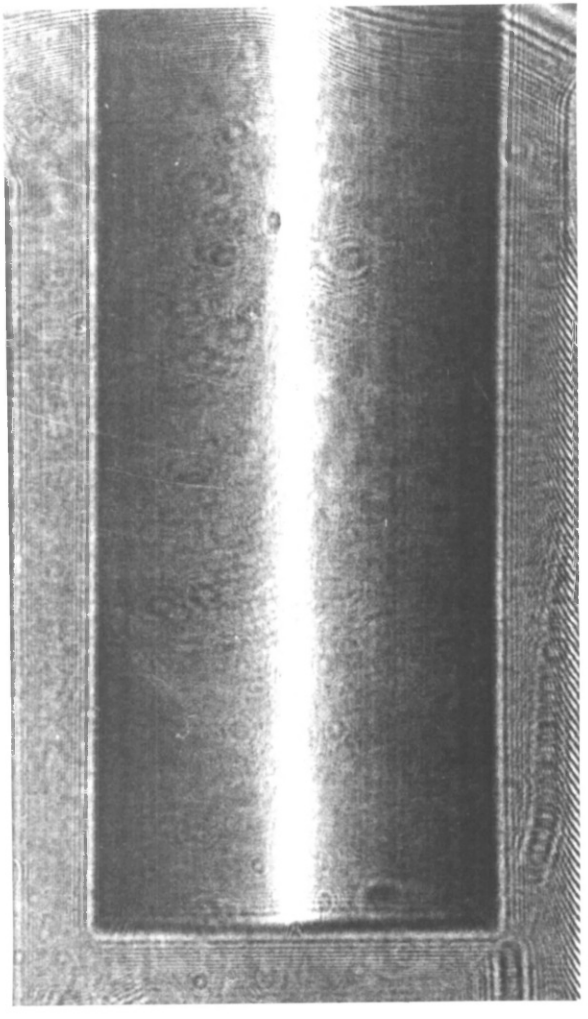
Figure 5.2: Through focus images for a transversely illuminated graded index rod



a) Object plane A



b) Object plane B



c) Object plane C

5.2 Practical recording of the object wave

The GRIN element is immersed in refractive index matching oil to reduce refraction in the object wave. Nevertheless, the index gradient in the core is sufficiently strong enough to refract and focus the incident plane wave and when illuminated in this manner, a rod lens has a (transverse) focal length of about 7mm in oil. The light diverges away from this focus and the angle of divergence is also further increased when the light is further refracted as it passes from the optical cell into air. To usefully record the object wave information then, a (field) lens must be used to collect all of the divergent light. A field lens must have a numerical aperture greater than that of the emergent light, and in this case an f=50mm focal length camera lens was used with the aperture stop set between F/1 and F/2.

A further consideration in the recording of the object wave was in establishing the best position for the hologram plane. This was found by trial and error to be at the plane where the image of the rod (produced by the field lens) was in sharpest focus. At positions away from this plane, the image of the rod contains caustics and so ultimately, the developed hologram was not of uniform density. Figure 5.2 shows typical 'through focus' images of a GRIN rod (misfocus of object plane $\approx \pm$ 7mm). Figure 5.2a corresponds to a negative misfocus ie. a plane that is displaced from the central plane towards the collimating lens (plane A in figure 5.1). Figure 5.2b is the plane of best focus that corresponds to the object plane passing (very near) through the centre of the index distribution (plane B in figure 5.1). Figure 5.2c corresponds to a positive misfocus with the object plane displaced from the central position towards the hologram (plane C in figure 5.1). At the plane of best focus (fig. 5.2b), the caustics disappear and with close index matching, the edges of the rod can hardly be seen at all. The intensity across the object wave in this plane is essentially uniform and ideal for the holographic recording and reconstruction process.

In chapter 7, the reason why the various images have the forms illustrated in figure 5.2 is clarified (§7.4.4)

## 5.3 Hologram processing technique

### 5.3.1 Silver halide chemistry

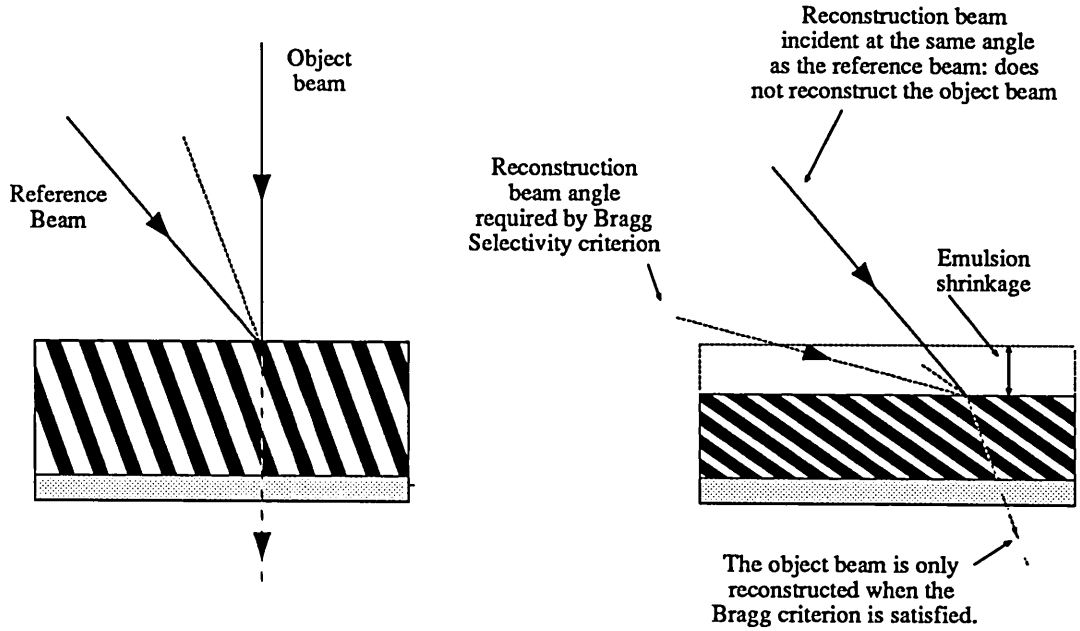
This work has only considered holograms recorded using conventional silver halide chemistry as the technology is fairly well established and convenient to use. The holograms were recorded on AGFA 8E75 Holotest holographic plate which is a high resolution silver-halide emulsion coated onto plate glass. These plates are supplied in a batch of 25 4 x 5 inch plates and they can be quartered to produce an economical 2 x $2^1/2$ inch plate that could be easily mounted on a kinematic plateholder. The plates are sensitive to the Helium-Neon laser wavelength, and after exposure to the interfering reference and object beams, a latent image of the fringe pattern is established in the emulsion. When the plate is developed, the latent image is converted to a silver image, and ideally there is linear relationship between the amount of developed silver and the exposure at any position on the plate. The developed image is then made permanent by 'fixing' the emulsion. In the fixing step, any undeveloped silver halide is removed from the emulsion.

The processed hologram has the form of an extremely complex diffraction grating, and the thickness of the emulsion and the nature of the recording set-up will determine whether the hologram behaves as either a volume or a plane diffracting element[3]. In the arrangement of figure 5.1, the hologram can be considered to act as a volume transmission grating[3] and this has an important effect in determining the diffraction efficiency of the hologram. A volume hologram contains fringe planes that are arranged throughout the depth of the emulsion (figure 5.3a) and the diffraction efficiency of the hologram is dependent upon the angle of incidence of the reconstruction beam and the orientation and spacing of the fringe planes.

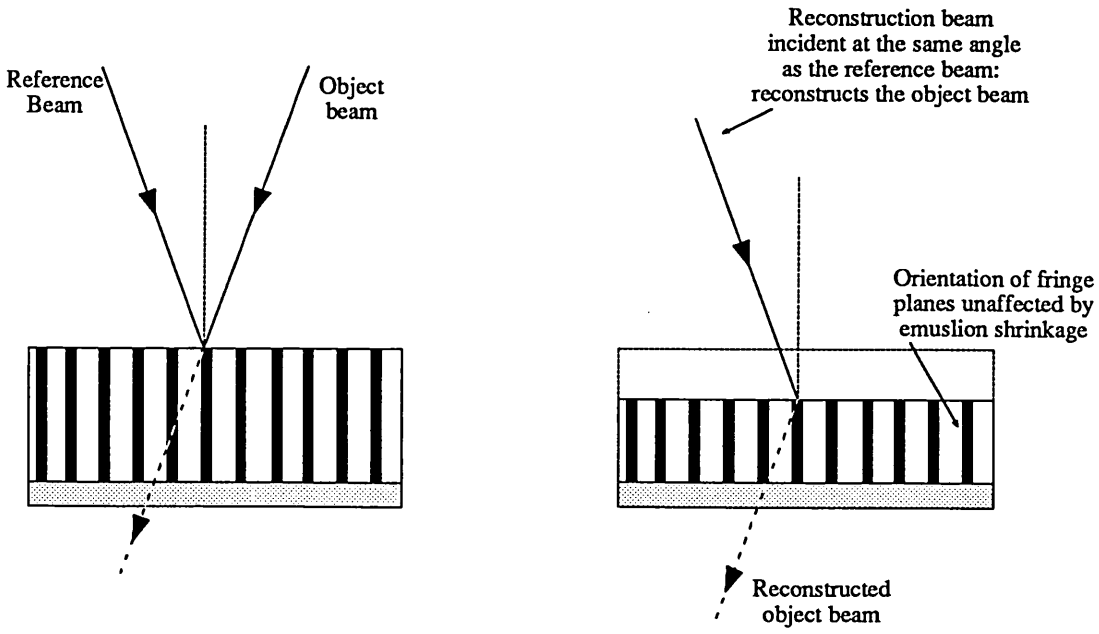
A hologram can be further classified as either an 'amplitude' or a 'phase' hologram depending upon whether the hologram modulates the amplitude or phase of the incident reconstruction beam. In general, phase holograms characteristically have higher diffraction efficiencies than amplitude holograms as physically, amplitude holograms must attenuate a portion of the reconstruction beam.

## Figure 5.3: Effect of Emulsion Shrinkage upon a Volume Hologram

a) Hologram Plane Normal to Object Beam




b) Normal to the hologram plane bisecting reference and object beams



5.3.2 The holographic plateholder

In live fringe holography, the processed hologram must be replaced identically into the apparatus to accurately reconstruct the object beam. A simple procedure for achieving this is to construct a kinematic plateholder, and holograms can be processed and replaced into the reconstruction beam with surprising accuracy . Fine re-alignment of the plate can be further achieved by attaching micrometer heads to the plateholder.

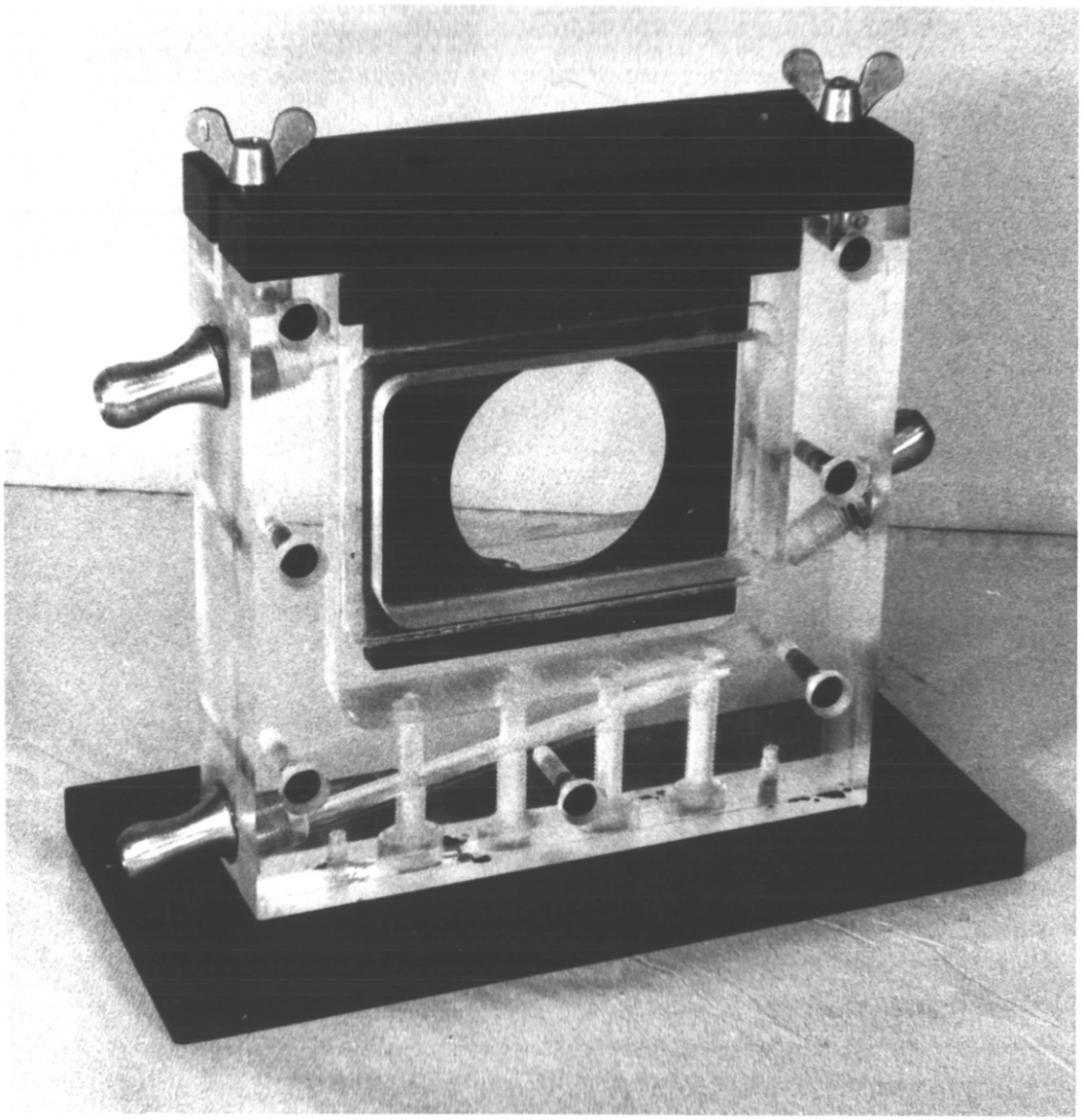
Although suitable results were obtained with such a kinematic mount, it was decided to design a system for processing the plate *in situ* as this provides some important advantages to the processing of the hologram.

A liquid gate plateholder was constructed using a simple design proposed by Hariharan in 1971[4]. The body of the gate was constructed out of two pieces of perspex, and the windows consisted of ordinary plate glass (figure 5.4). The holographic plate was mounted upon a dural support plate that could could be fixed rigidly in position in the gate. The exposed plate was processed in situ by passing the various chemicals sequentially through the cell.

An *in situ* processing system totally removes any plate re-alignment problems and it also significantly simplifies and improves the hologram processing procedure. This is because the 'wet' chemical processing of a hologram can prove troublesome particularly the emulsion does not dry evenly as this can distort the fringes on the interferogram. Usually, the hologram must be carefully rinsed in various concentrations of an alcohol and left to dry for several minutes. This problem can be neatly avoided if the hologram is exposed and re-illuminated whilst immersed in distilled water as obviously, the plate does not need to be dried out. It should be pointed out that the quality of the hologram tends to deteriorate if it is left for too long (ie. a week) in the water. Ideally the hologram should be carefully dried out when not in use.

The liquid gate enabled holograms to be exposed and reconstructed in about 10 minutes.

Figure 5.4 : The liquid gate holographic plateholder



5.3.3 Processing procedure

In this work, the holograms were processed using P.A.A.P. developer, Agfa G334 fixer and a Ferric Nitrate bleach (GP-431). (See appendix C for formulae.) It is worth pointing out that there are a vast range of chemicals and procedures that can be adopted (for example see Holography handbook[5]) and each worker develops his own preferred method.

In this work, the precise procedure varied between different experimental layouts, but was typically:

1) PRE-SOAKING (unexposed plate immersed in distilled water in the liquid gate and left for 2 minutes)
2) EXPOSURE ($\approx$ 15μJ per $cm^2$, plate in distilled water)
3) DEVELOP (2 minutes in PAAP, hologram density between D $\approx$ 1.0 - 2.0)
4) STOP BATH (30 seconds)
5) FIX (G334, 4 minutes)
6) BLEACH (until the plate just clears)
6) RECONSTRUCT (hologram in distilled water)

The liquid gate should be thoroughly rinsed with distilled water between each processing step, to prevent contamination of the processing chemicals. The bleaching step is not usually desirable in holographic interferometry as it can introduce an excessive amount of scattered light into the interferogram, reducing the contrast of the live interference fringes. However, in this work, the bleaching stage was almost essential, and to see why, we must consider further the silver-halide chemical processing of the hologram.

In the chemical processing of a hologram, most problems arise at the fixing stage, where undeveloped silver-halide is removed from the emulsion. A consequence of this is that the emulsion shrinks and this changes the orientation of the fringe planes in the

emulsion (figure 5.3a). This change in the orientation of the fringe planes alters the Bragg reconstruction angle of the hologram and with the reconstruction beam necessarily incident upon the hologram at a fixed angle, this can result in a dramatic loss in the diffraction efficiency of the hologram[6]. Ultimately, the hologram must be rotated to restore the diffracted image. With the recording arrangement of figure 5.1, it was found that a fixed and unbleached hologram had a negligible diffraction efficiency due to emulsion shrinkage.

Several workers have considered solutions to the problem of emulsion shrinkage: Duffy[7] suggests recording a low density hologram and removing the fixing stage altogether. However, this method produces a relatively unstable hologram, liable to fade when left in water. A reversal bleach[5] may be used to convert the developed amplitude hologram to a phase hologram with no need for a fixing step. This also increases the diffraction efficiency of the hologram. However, the common reversal bleaches (examples PBQ and Mercuric Chloride[5]) are potentially toxic and very awkward to use in practice. Their continual use in a working environment is not recommended.

A simple, practical solution to the problem of emulsion shrinkage is to record the hologram with the normal to the hologram plane bisecting the reference : object beam angle. The recorded fringe planes in the emulsion are then orientated normally to the plane of the hologram (fig. 5.3c). The fringe orientation and spacing will not change upon shrinkage of the emulsion and so the Bragg selectivity conditions are preserved. Unfortunately, this method could not be employed in this interferometer. The reason for this was due to the hologram (and liquid gate windows) reflecting a portion of the reference beam directly onto the front surface of the field lens and this light is in turn was reflected back along the direction of the object beam. This unwanted light appeared in the observation plane and degraded the observed interferogram.

The only remaining solution to the problem of emulsion shrinkage was to consider ways of re-swelling the emulsion back to its original thickness. Hariharan[4] has suggested that the emulsion thickness of a hologram in a liquid gate can be altered by varying the ph of the final viewing solution (towards acidity). It was found by trial and error, that the

ferric nitrate bleach caused considerable re-swelling of the emulsion of the hologram so that the Bragg reconstruction condition was recovered. The hologram could subsequently be viewed in distilled water with the Bragg reconstruction condition maintained. The bleaching step is normally included in the chemical processing of a hologram to increase the diffraction efficiency (by converting the amplitude hologram to a phase hologram). However this is achieved at the expense of an increase in the amount of scattered light which can in turn degrade the contrast of the live interference fringes. GP-431 ferric nitrate bleach is considered to be a low noise bleach (Phillips[8]) and this helps to keep the amount of scattered light to a minimum. It was found experimentally that low density holograms ($D \approx 1.0$) produced the least amount of noise in the final interferogram.

5.4 Choice of observation plane

In holographic interferometry involving weakly refracting phase objects, the interferogram may be observed at any suitable plane beyond the hologram. However with strongly refracting phase objects, the position of the observation plane depends upon the nature of the phase object and the imaging lenses.

For the case of a cylindrically symmetric refractive index distribution, the observation plane should be the plane passing through the centre of symmetry of the object (see chapter 7). Practically, this corresponds to sharpest image of the rod which is the plane where the edges of the rod can hardly be observed (see figure 5.2b). Figures 5.2a and 5.2c illustrate unacceptable rod images. The focussing range over which the image of a 2mm GRIN rod was acceptably sharp, was found practically to be about 100 microns.

The theoretical motivation behind the choice of observation plane and the error introduced by a misfocus are discussed in detail in chapter Seven.

## 5.5 Fringe Analysis

### 5.5.1 The digitiser

In fringe analysis, we need to obtain useful information from an interferogram. The earliest techniques involved taking a photographic record of the fringe pattern and fringe shifts were measured either by hand or by a microdensitometer. Modern methods now involve the use of a camera, video digitiser and a computer to get the maximum information from the interferogram. The cost and size of the system will determine the maximum obtainable resolution. A high resolution system would employ a digitiser that can convert a screen of information into an array of 1024 x 1024 pixels, with perhaps 512 grey levels. But this would be extremely expensive.

Because of the limitations of time and cost in this work, a digitiser that was relatively cheap and compatible with a BBC micro-computer was chosen (supplied by Gladstone Electronics Ltd, Cambridge). This digitiser conveniently allowed the fringe information to be analysed on the BBC micro-computer in the laboratory. The resolution of the digitiser was, 160 x 256 pixels, with 8 grey levels. This is probably the minimum allowable resolution for useful interferometric work.

### 5.5.2 Following a Fringe Shift

Having digitised a fringe pattern, the problem remained to measure the shift of a chosen fringe. The digitised fringe pattern, could be stored in RAM in the computer and displayed on the monitor. A computer program was written to allow a cursor to be manually moved around the screen and in this way any fringe of interest could be investigated. The technique used to select a chosen fringe was to use the cursor to define the upper and lower edges of the fringe. The intensity levels across the fringe between the upper and lower datum points were then stored in an array and a parabola could be fitted (by the least squares method) across the fringe. The centre of the fringe produced by the least squares fit routine could in turn be displayed on top of the chosen fringe. This process was continued for the entire fringe and the resulting line of information could be

Figure 5.5.: Digitized Interferogram and Fitted Fringe Centre



stored in an array and fed directly into the program that analysed the fringe information (see chapter 7).

Figure 5.5 shows a typical digitised fringe pattern and the fitted centre of a chosen fringe.

5.6 Choice of index matching oil

The index matching oil must have a refractive index close to the refractive index at the edge of the GRIN rod. In the case of optical fibre preforms, the cladding index is normally fabricated from fused silica glass having the (constant) refractive index of 1.457. A silica matching oil was kindly supplied by York Technology Ltd, Hampshire.

In GRIN lens fabrication, the edge index is dependant upon the ion exchange process and it cannot be accurately determined from the given profile parameters (§2.2.2). The Nippon Sheet Glass Company handbook gives a nominal peripheral index value of $n_1 = 1.522$ ($\lambda = 632.8$nm)whereas the profile equation gives $n_1 = 1.516$.

The next problem was to find an oil with a refractive index close to this. Although it is possible to buy matching oils across a range of indices, these oils frequently consist of potentially toxic chemicals (Benzene derivatives). Therefore it was to decided to produce the correct oil by carefully mixing two available oils.

The two oils used were:

Ethyl Salicylate $n_D = 1.5219$

Bromo-Napthalene $n_D = 1.666$

Ethyl salicylate is an apparently harmless and non-viscous oil, however Bromo-Napthalene is toxic but only a very small amount (literally several drops) is required to raise the index of the Ethyl Salicylate to the correct value.

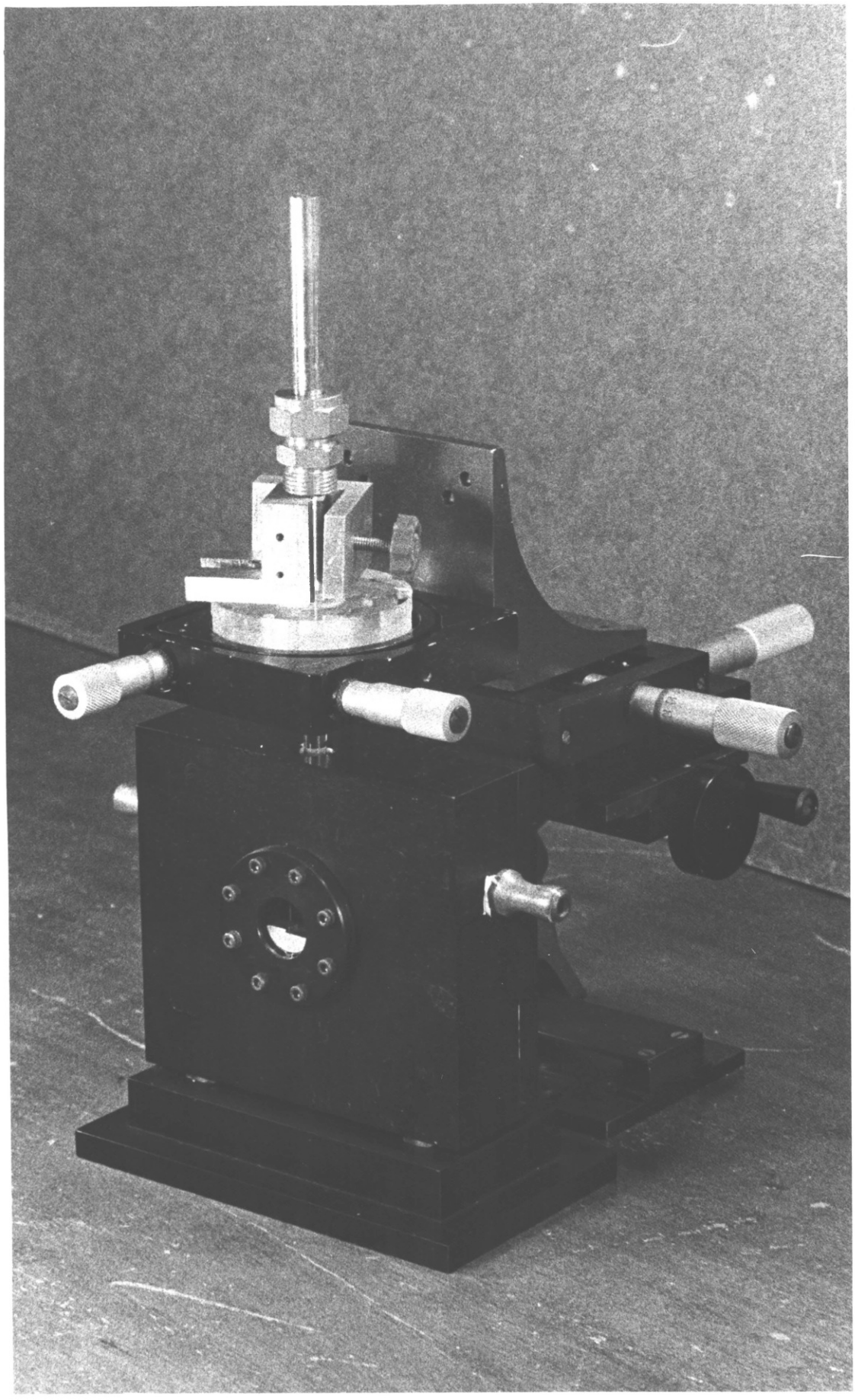
The technique for establishing close index matching and the design of the optical cell is described in detail in the following chapter.

5.7 Graded index rod mounting techniques

We have seen in chapter Four that comparison testing will require accurate positioning (and repositioning) of the rod samples under test. For precise re-alignment purposes, the rods have to be translated and tilted whilst in position in the optical cell. The technique for achieving this was to attach the rod lenses to the end of a set of 3/8" steel (or glass) rods which could be located on a kinematic mount attached to the various translation stages mounted over the optical cell. The steel rod could be lowered to insert the rod lens into the cell. The mounting apparatus is illustrated in figure 5.6 . The 6mm rod lens samples had to be glued in position at the end of the rod. Although this was technically a destructive mounting technique, it was vital in the development of the working interferometer. Longer 25mm GRIN samples were later supplied and these could be inserted and located into a bore hole drilled in the end of the rod. A small disc of rubber provided the necessary grip on the glass rod. This latter mounting technique demonstrated that longer GRIN samples could be satisfactorily mounted in a non-destructive way. .

There was no problem in mounting the preform rods as these were large enough to be attached directly to the kinematic mount supported on the translation stages.

Figure 5.6: The optical cell and rod lens mounting apparatus



## REFERENCES

5.1 R.J. Collier, C.B. Burkhardt and L. H. Lin, "Optical holography," Academic press, (1971)

5.2 Ealing Electro-optics product guide, Ealing Electro-optics plc, Greycaine Rd, Watford.

5.3 H.M. Smith, "Holographic recording materials," Springer- verlag, 1977.

5.4 P. Hariharan and B.S. Ramprasad, "Rapid in situ processing for real-time holographic interferometry," Journal of Physics E: Scientific Instruments 6, p. 699, 1973.

5.5 F. Unterseher, J. Hansen and B. Schlesinger, "Holography Handbook," Ross books, Berkeley California, 1982.

5.6 D.H.R Vilkomerson and D. Bostwick, "Some effects of emulsion shrinkage upon a holograms image space," Applied Optics 6, p. 1270, 1967.

5.7 D.E. Duffy, "Reducing photographic emulsion shrinkage for real-time holographic interferometry," Journal of Physics E: Scientific Instruments 3, p. 561, 1970.

5.8 N.J. Phillips and D. Porter, "An advance in the processing of holograms," Journal of Physics E: Scientific Instruments 9, 631, 1976.

# CHAPTER SIX

# PRACTICAL IMPLEMENTATION OF THE HOLOGRAPHIC COMPARISON METHOD

This chapter considers some of the problems posed by the practical implementation of the holographic comparison method described in chapter 4. In particular, it describes some of the necessary modifications made to the holographic interferometer in order for useful results to be produced. The basic aim of the work in this chapter was to ensure that a rod lens could be removed and then replaced in the optical cell with sufficient accuracy that an index profile assessment could be made from the interference pattern. For a GRIN rod with perfectly symmetrical index distribution, we would therefore expect to see undeviated tilt fringes running across the interferogram.

Experimental interferograms are shown for a 2mm rod lens with profile characteristics similar to those for the 'theoretical' lens described in chapter four. The experimental fringe patterns in this chapter can thus be compared to the theoretical patterns plotted previously.

## 6.1 Temperature control of the index matching oil

In section 4.7, a theoretical analysis of the comparison method revealed that the temperature of the index matching oil had to be held constant to less than a tenth of a degree. Figure 6.1 shows the fringe shift produced by a 1°C change in the oil temperature, this interferogram is similar to theoretically predicted pattern (figure 4.18).

The main cause of the temperature variation of the oil was the fluctuation in room temperature, practically, an interferogram could be used for about 25 minutes before the temperature effects had to be taken into account. Without an effective control on the temperature, holograms had to be made at least every hour.

Initial attempts to reduce the problem involved the use of blocks of polystyrene and

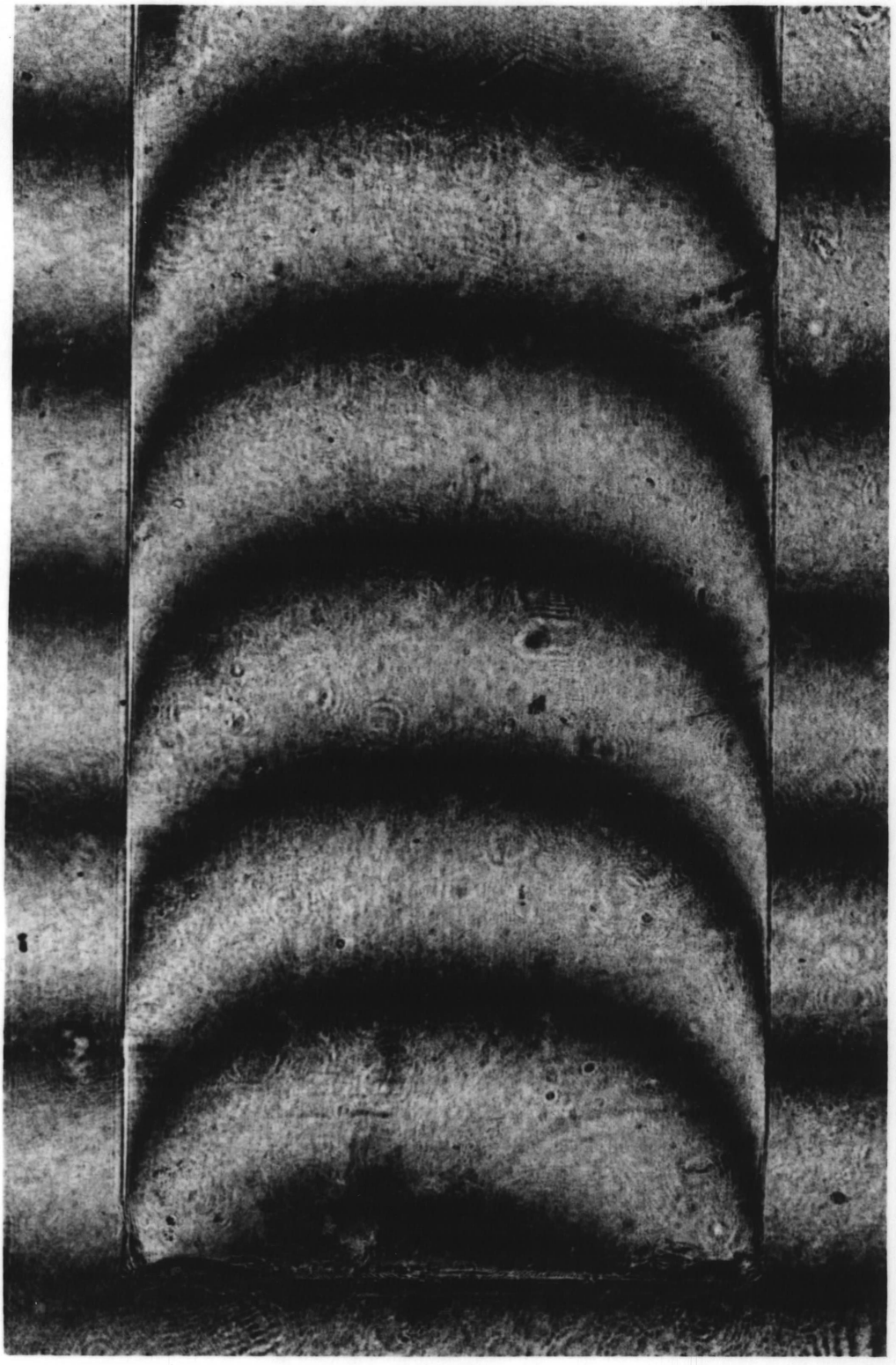


Figure 6.1: Experimental interferogram :
Change in the matching oil temperature of 1°C

foam rubber to insulate the optical cell from the environment. However this did not produce satisfactory results, firstly because complete insulation could not be achieved because of the need to provide access holes for the illumination beam and the rod lens supporting rod. Secondly, there was still no way of preventing a change in the oil temperature when test rods with different temperatures were inserted into the optical cell. For these reasons, a dynamic system of temperature control was required.

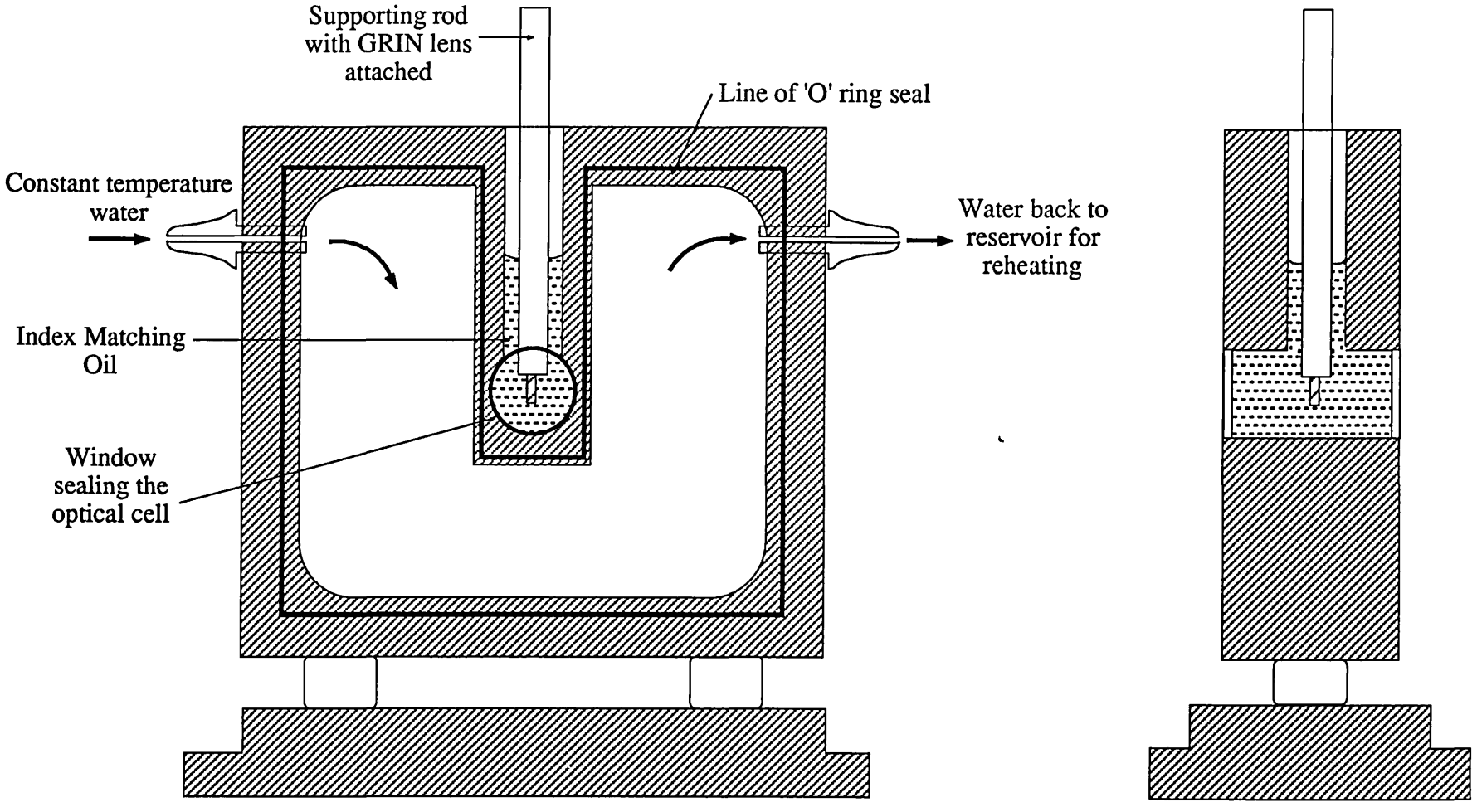
A common method for actively controling the temperature of matching oils in refractrometry experiments is to pass a temperature controlled liquid around the outside walls of the cell containing the oil. For example, this technique is required in a Hilger-Chance refractometer. It was decided to follow this approach and a suitable optical cell was designed and constructed (see figures 6.2 and 5.6).

Water is pumped into the chamber from a temperature controlled reservoir and flows around three sides of the cell before returning to the reservoir for reheating. The major design consideration was the provision of access holes for the illumination beam and the sample support rod. These holes had to be kept as small as possible to ensure that heat loss was a minimum. For ease of construction, the optical cell and water chambers were milled out of a single block of dural. The oil was sealed in the central optical cell by two windows, one of which could be removed for access. A metal face plate (not illustrated in fig 6.2) and a rubber gasket provided the necessary seal for the water chamber.

The temperature controlled water supply was derived from a thermostatically controlled 15 litre water bath supplied by Grant Instruments, Cambridge. The specification sheet for the bath claimed a temperature uniformity for the water at any point in the bath of +/- 0.015°c about the operating point..

The operating temperature of the cell was set at 30 °C, about 5 degrees above ambient. Figure 6.10 at the end of this chapter (page 12 ) shows the fringe pattern produced when a rod lens was removed from the cell and replaced after a period of 2 hours. The straightness of the fringes shows the stability of the temperature of the oil in the cell. This stability could be maintained over an almost indefinite period.

Figure 6.2: The Temperature Controlled Optical Cell



6.2 Calibration of the refractive index of the matching oil

To produce a profiling method that measures the absolute refractive index values of a GRIN sample, it is necessary to have accurate knowledge of the refractive index of the matching oil (to at least 3 decimal places).

Because the matching oil was a mixture of two liquids, there was an uncertainty in the oil refractive index value. Furthermore, the refractive index of the oil also ultimately depends upon the operating temperature of the optical cell. For these reasons, a method for measuring the refractive index of the oil at the chosen operating temperature was required.

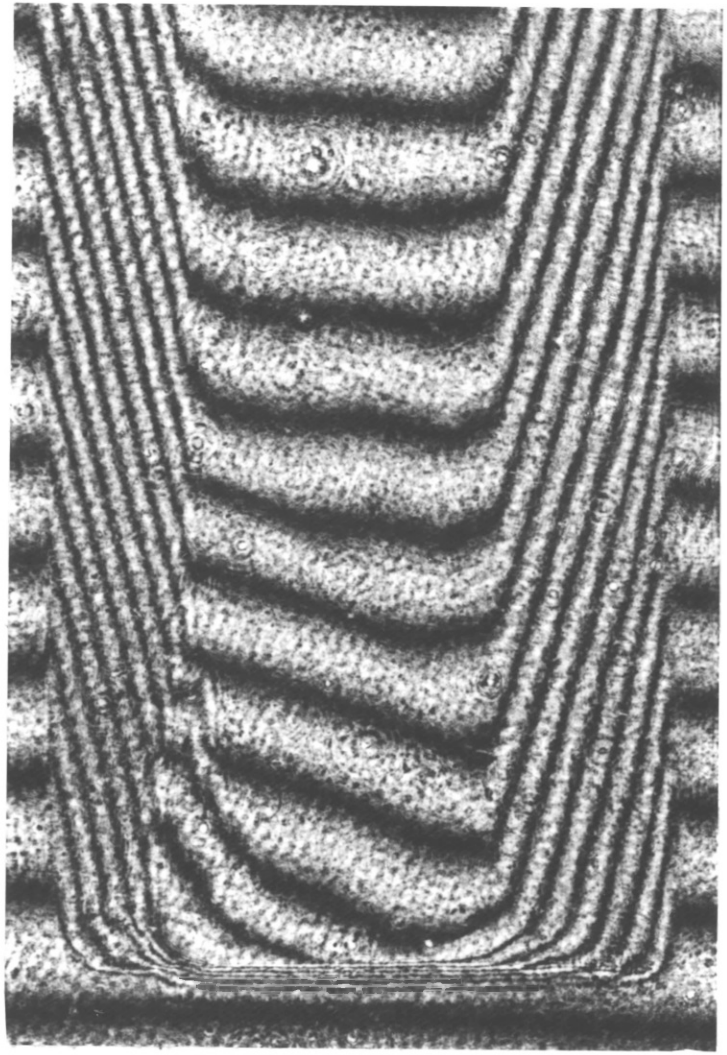
An accurate technique using the holographic interferometer was devised. This method depended upon the availability of an optical glass that had a known refractive index close to the ideal matching value ($n_{oil} = 1.522$, $\lambda = 632.8$nm). Such a glass (HC152305, $n_{glass} \approx 1.522$, $\lambda = 632.8$nm and T = 30°c) was found in the workshop. Only a small sample of the glass was required for the test. The chosen dimensions were about 4mm in diameter and 30mm long. There was no need to polish or prepare the sample and so just a chip of the chosen glass could be used.

The principle of the calibration method was to holographically record a plane wave that had passed through the (uniform index) matching oil in the optical cell. The glass sample was then inserted into the optical cell and re-illuminated with the plane wave. The wave passing through the oil and the glass was then interfered with the plane wave reconstructed from the hologram. In the initial state, with the indices of the glass and the oil unmatched, many fringes appeared in the interferogram. Figure 6.3a shows the pattern due to an index mismatch of $\Delta n \approx 0.002$. These fringes represent an increased (or decreased) optical pathlength for rays passing through the glass sample with respect to rays passing through the matching oil. From optical pathlength considerations, the shift of a fringe (F) can be written as

$$F = \Delta n \, D / \lambda \qquad (6.1)$$

Figure 6.3: Experimental interferogram: Calibration of the index matching oil

a) Index mismatch between glass chip and matching oil



b) Glass chip and matching oil are index matched

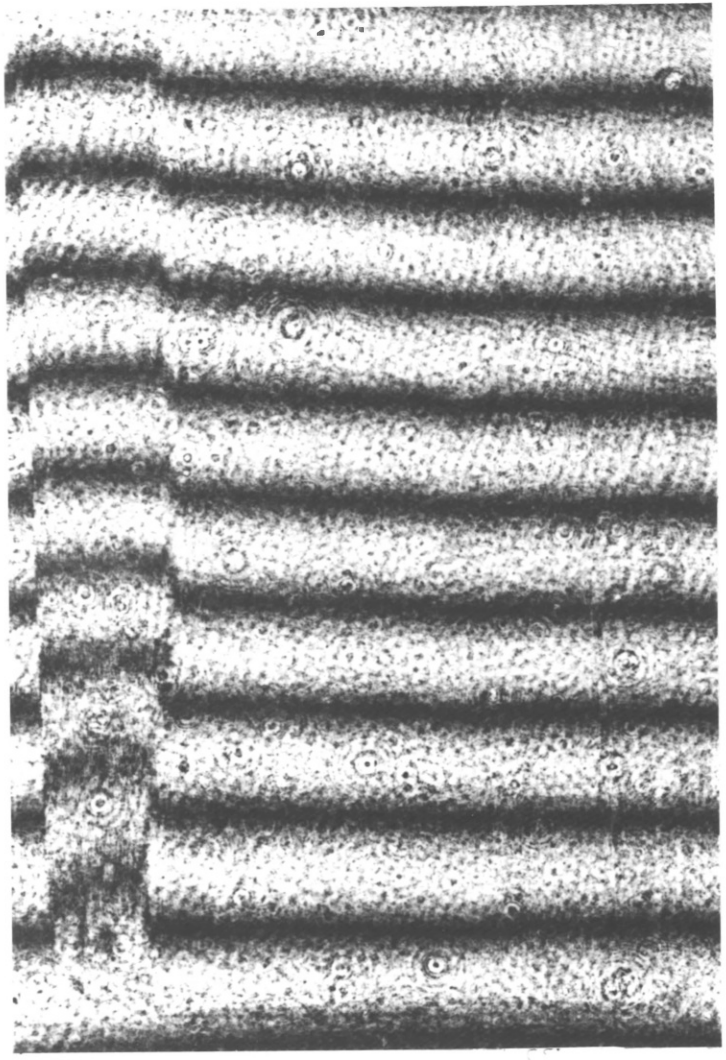
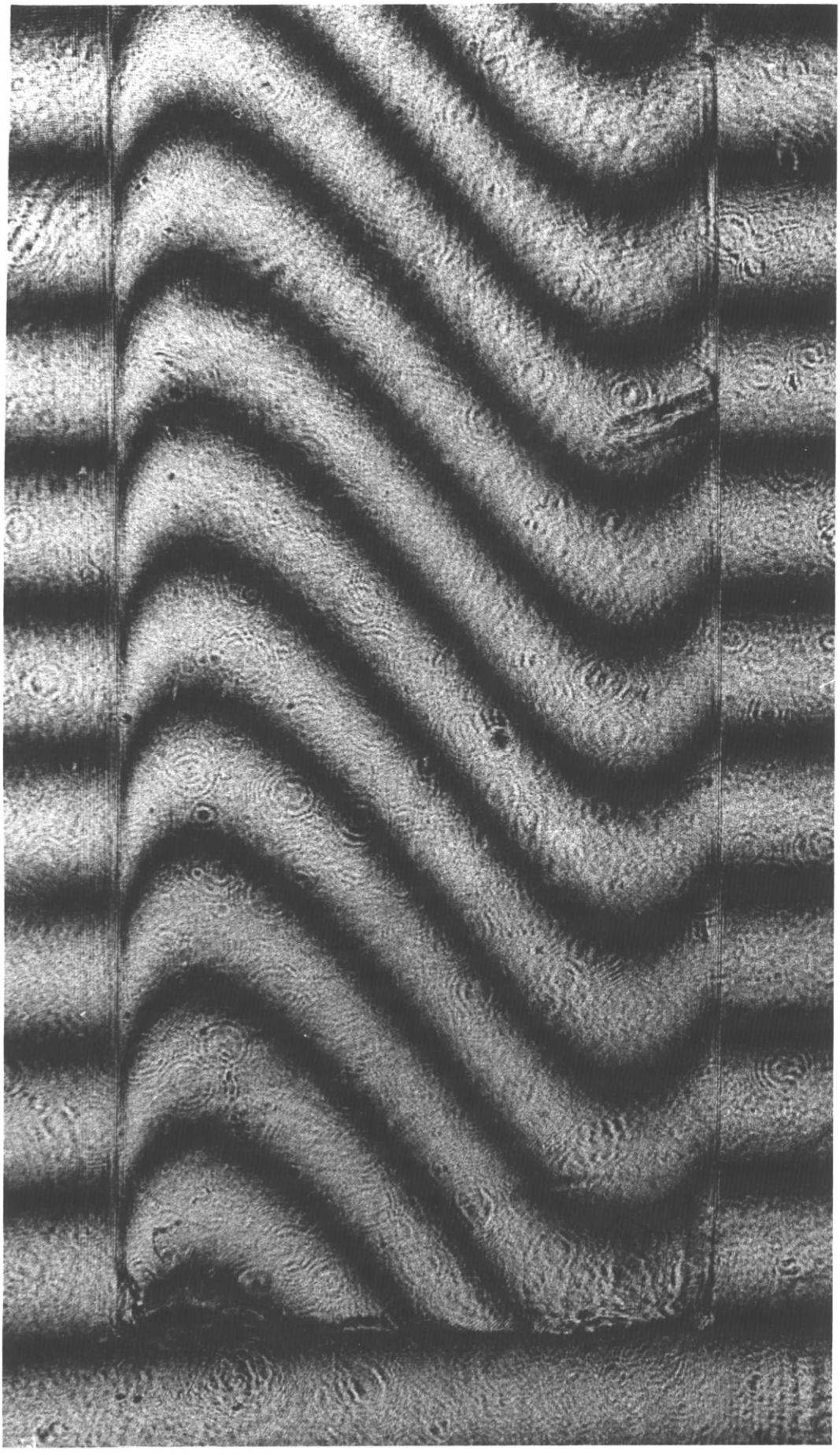


Figure 6.4: Experimental interferogram :
An imperfect index match and a shearing misalignment



where $\Delta n$ is the index difference between the glass and the oil, D is the thickness of the glass and $\lambda$ is the wavelength. For a block of glass 4mm thick, a shift on the interferogram of just one fringe corresponds to a difference in index of $\Delta n = 0.00015$. Thus extremely accurate index matching can be achieved by careful adjustment of the refractive index of the oil whilst monitoring the magnitude of the fringe shift. The refractive indices of the oil and the glass are assumed to be equal when the tilt fringes are relatively straight (say less than a fifth of a fringe by eye). The oil index could be altered by either adding drops of ethyl salicylate or bromo-napthalene, or by raising or lowering the temperature of the oil in the cell.

Figure 6.3b shows the final interferogram at very close matching ($n_{oil} \approx n_{glass}$). Note that the edges of the glass chip can hardly be observed.The slight shift of the fringe at one side of the pattern probably indicates an inhomogeneity of the glass.

A further handle on the index matching requirements can be found by observing the shearing interferogram with an index mismatch of $\Delta n = 0.004$ (noil $\approx$ 1.518). Figure 6.4 shows the corresponding fringe pattern, and note that the tilt fringe is disjointed at the edges of the rod where there is a discontinuity in the index values. This pattern can be compared with the theoretical interferogram of figure 4.17. This pattern shows that the profile equation and given optical parameters for the rod cannot be reliably used to predict the edge index values of the rod lens;where the peripheral index is given as $n \approx 1.516$.

## 6.3 Accurate repositioning of the rod samples

### 6.3.1 Initial re-alignment and elimination of shear

Before a comparison test can be made, the test rod must be re-aligned with the initial reference rod position. This can be practically achieved by altering the orientation of the rod whilst observing the fringe pattern. A misalignment of the rod across the optical axis (shear) and rotation of the rod about the optical axis (tilt) can be removed by manouvering the rod until the fringe pattern is symmetrical or at least has a simple form (§4.7.1). Figure 6.5 shows the experimental interferogram due to a tilt misalignment of the rod. The

Figure 6.5: Experimental interferogram :
Tilt misalignment of the test rod

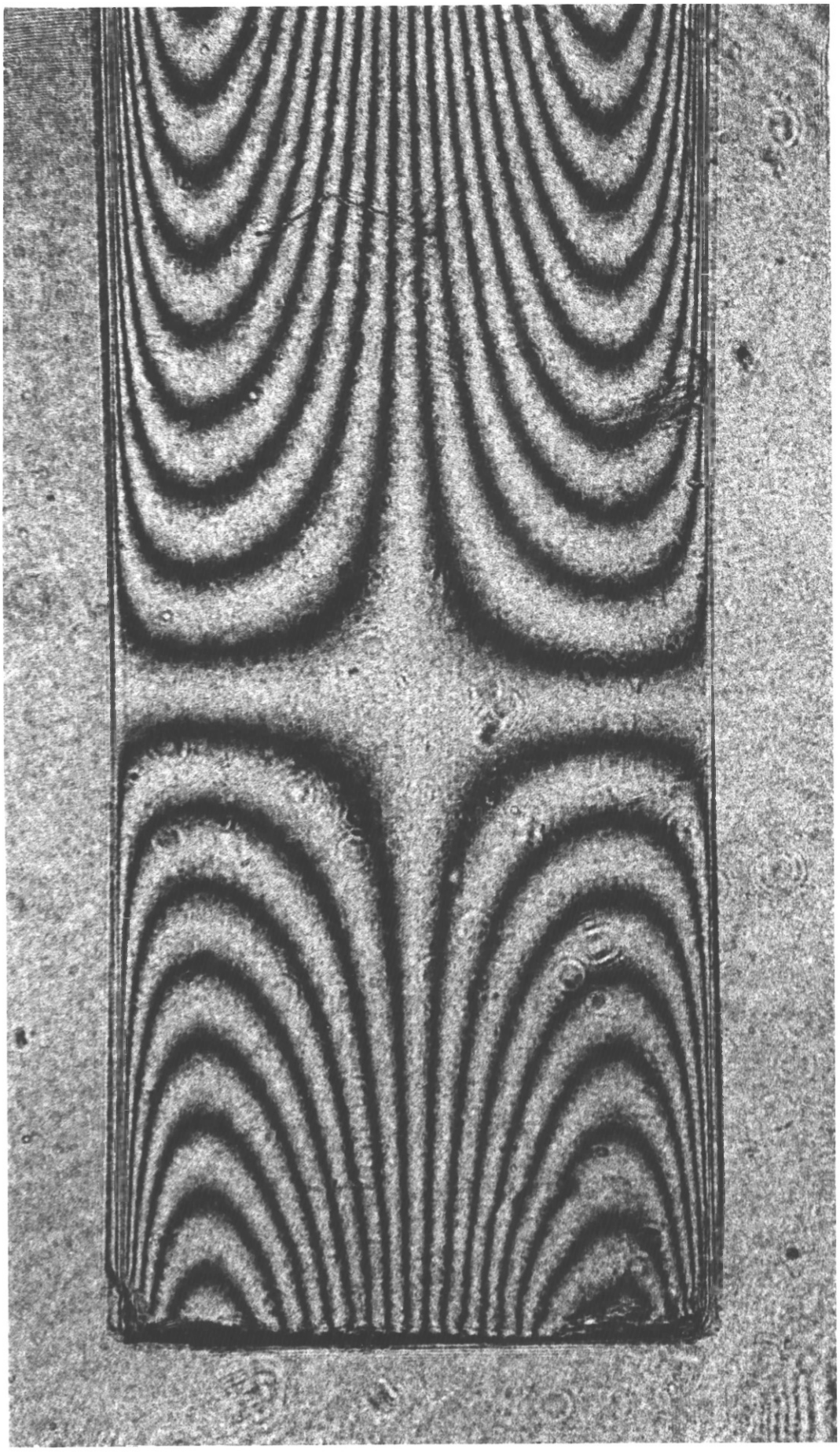
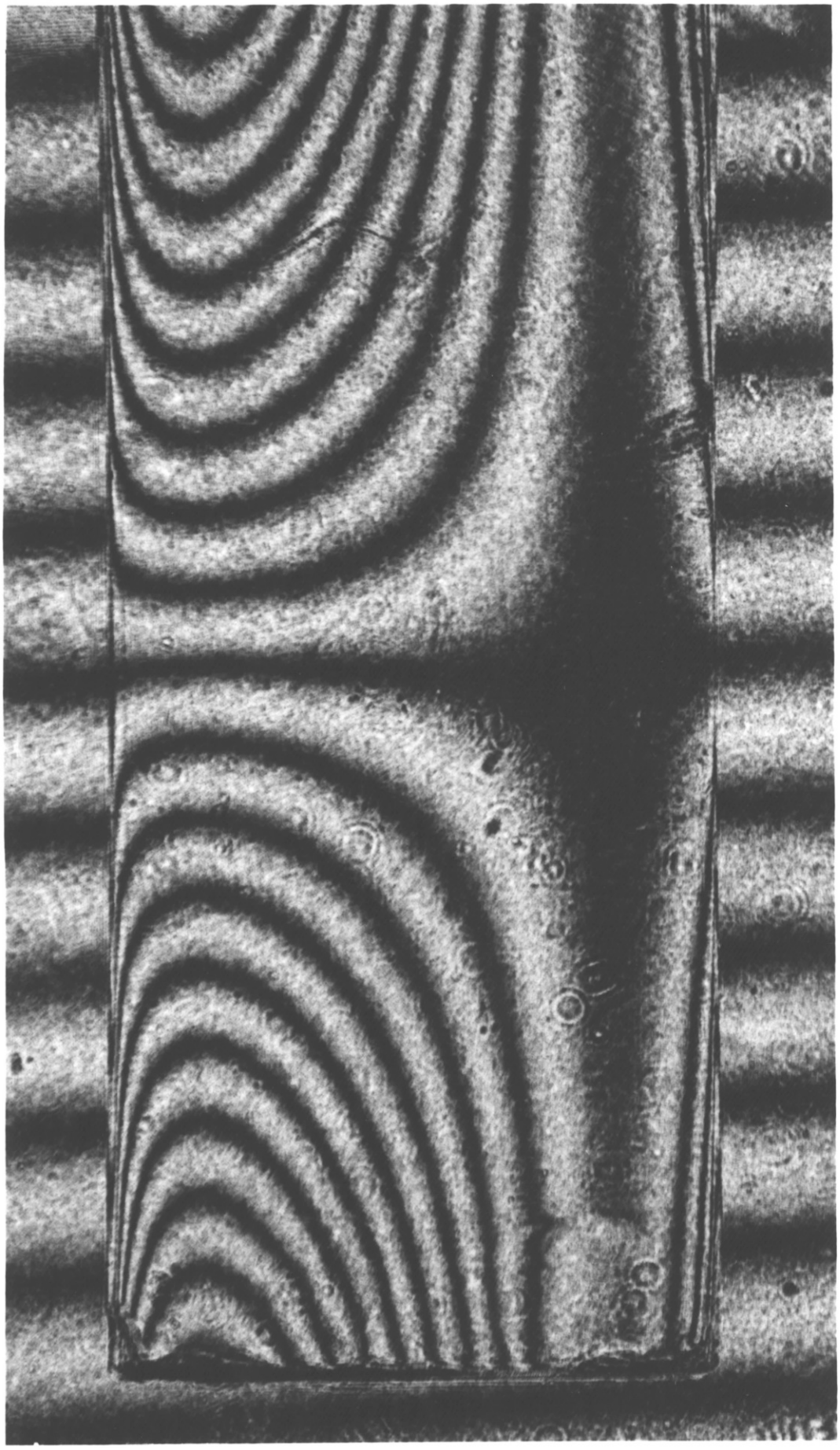


Figure 6.6: Experimental interferogram :
Towards a realignment of the test rod



pattern is otherwise 'fluffed out' (the reference or tilt fringes have been removed). This pattern looks fairly complicated however, it can easily be simplified by adjusting the appropriate tilt control so that the central zone (or turning point) of the pattern moves to one side and eventually dissappears from the image. One continuous fringe running across the interferogram will then be observed. Figure 6.6 shows a typical fringe pattern just before the turning point dissappears. The corresponding theoretical interferogram is shown in fig. 4.15, p. 83 and the two figures compare very favourably.

Further adjustment of the tilt and shear controls should produce a simplified and symmetrical pattern, as in figure 6.7 for example. If the fringe pattern cannot be made symmetrical, then this highlights a serious fabrication error in the rod sample under test.

### 6.3.2 Elimination of a Longitudinal Misalignment (defocus)

The experimental interferogram in figure 6.7 is due to the rod being displaced along the optical axis either side of the correct position (- 500 microns in this case). These fringes correspond to defocus in a conventional interferometer and note again that the figure compares favourably with the theoretically expected pattern (fig. 4.13). With near identical graded index rods, this defocus can be removed by translating the rod along the axis until the fringes have their most simple form. However for rods with slightly differing profiles there is no direct method for discriminating between the effects due to a defocus or those due to the change in the index profile. A computer simulation using the program described in chapter four indeed proved that there was no way of removing the defocus problem by merely monitoring the fringe pattern. Thus a method for removing the uncertainty in the position of the rod along the axis had to be devised.

The solution to the problem lay in the observation that a slight shear misalignment of the rod (1-2 microns) produced an observably asymmetrical fringe pattern. If the defocus misalignment could be observed via a similar shearing interferometeric technique then the rod could be accurately positioned along the optical axis. The apparatus designed for removing the defocus problem is illustrated in figure 6.8a

Figure 6.7: Experimental interferogram :
Defocus misalignment of the test rod

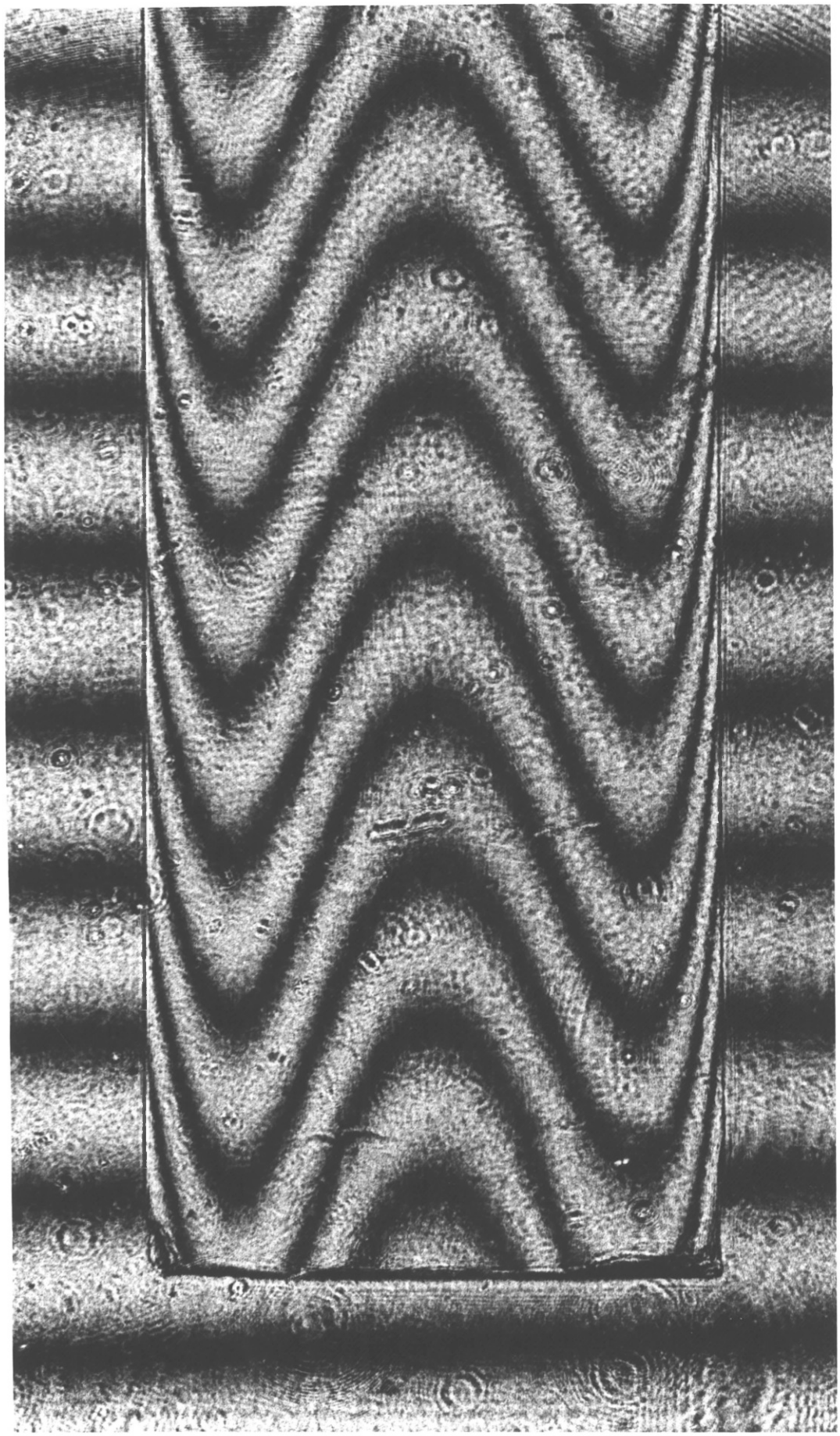
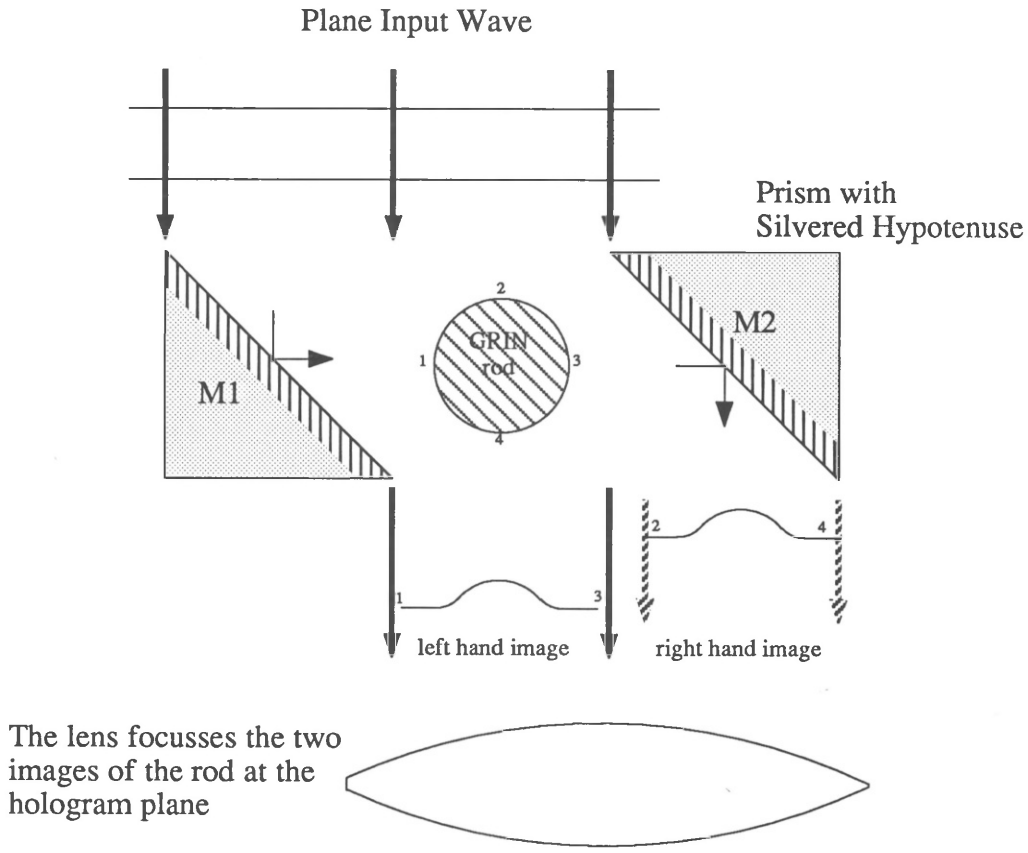
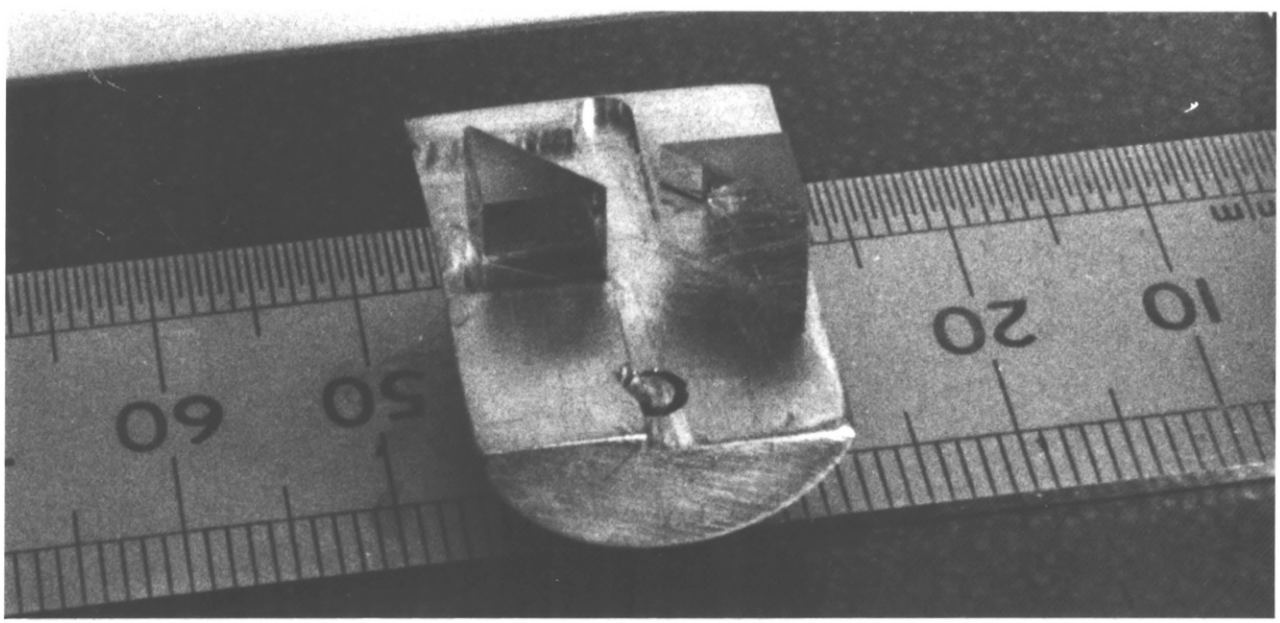


Figure 6.8: Apparatus for the elimination of the defocus problem

a) Schematic




b) Apparatus



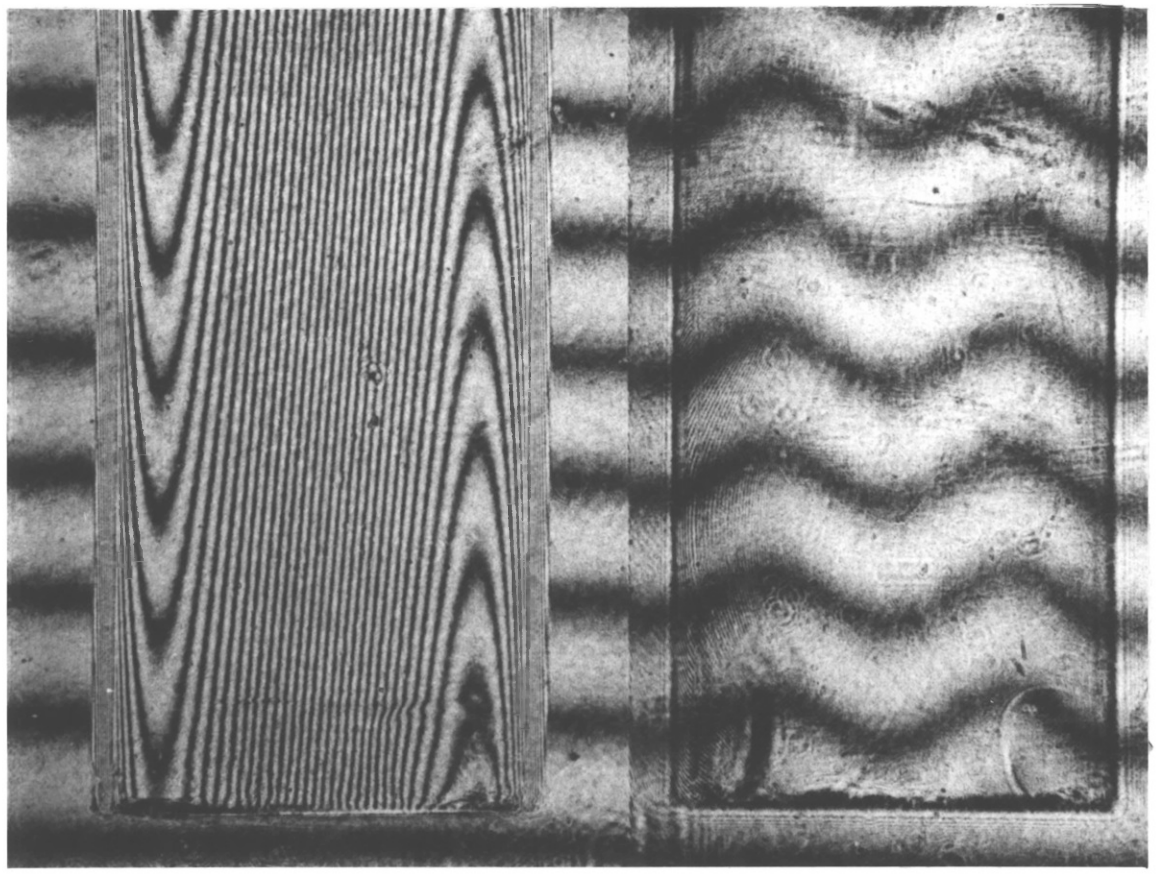
The mirror (M1) directs a portion of the plane illumination beam through the side of the rod sample, orthogonally to the optical axis. The second mirror (M2) redirects the transmitted light through the collecting optics and onto the hologram and observation planes. Thus two rod images (ie. object waves) are produced from the one input illumination beam. The mirrors were produced by silvering the hypotenuses of two 6mm right angle prisms. These prisms were then glued in position upon a small supporting platform (see figure 6.8b) and inserted into the optical cell. Careful design and alignment of this device ensured that neither of the two object beams were vignetted by the optical system. The two object waves could be recorded on the same hologram using a single reference beam and upon reconstruction, two interferograms were observed at the observation plane (fig. 6.9a).

The beauty of the method is that a shear misalignment in one interferogram appears as a defocus misalignment in the other pattern and vice versa. Re-alignment of the test rod with the original rod position can be achieved by adjusting the rod position until both fringe patterns have symmetry. Figure 6.9 illustrates this principle. In figure 6.9a, the rod under test has been sheared across the optical axis by a distance of 100μm, the left hand fringe pattern is characteristic of such a shear and the right hand pattern reveals this misalignment as a 100μm defocus. In figure 6.9b, the rod is defocussed along the optical axis by a 100μm and is thus sheared in the other direction; the left hand fringe pattern has the typical defocus form, and the right hand pattern has that of a shear. Thus, a defocus misalignment can be removed by adjusting the rod position along the axis until the corresponding shear pattern (RHS in this case) becomes symmetrical. Because of the extreme sensitivity of the fringe pattern to a shear misalignment, the rod can be re-positioned in the optical cell to within 1-2 microns of the original position.

The transmitted wave produced by the reflected illumination beam follows a slightly longer pathlength to the hologram and observation planes than the straight through beam. Thus it was impossible to produce two identically focussed images of the rod sample and so only one (focussed) image could be used in the final analysis of the fringe pattern. The other image was used purely for alignment purposes.

Figure 6.9: Elimination of the defocus problem

a) 100 microns shear misalignment (left hand image)



b) 100 microns defocus misalignment (left hand image )

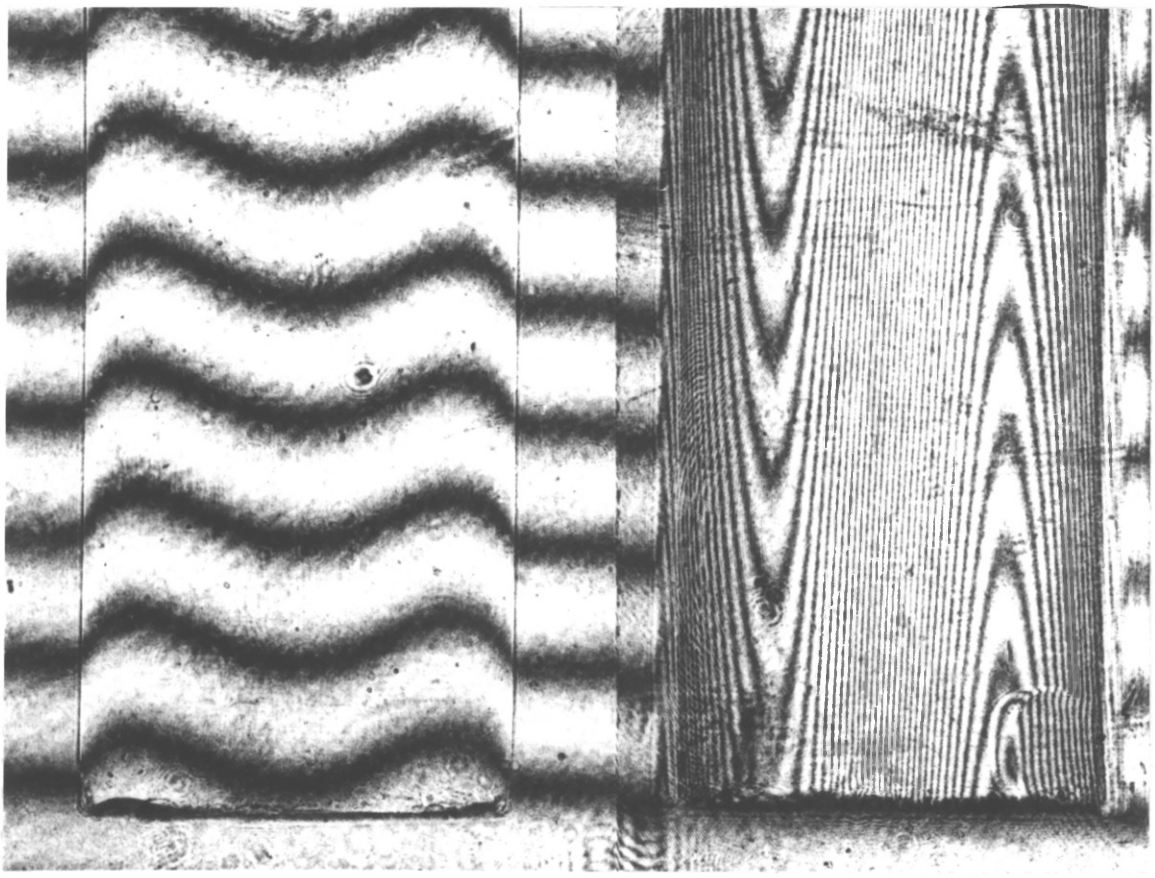
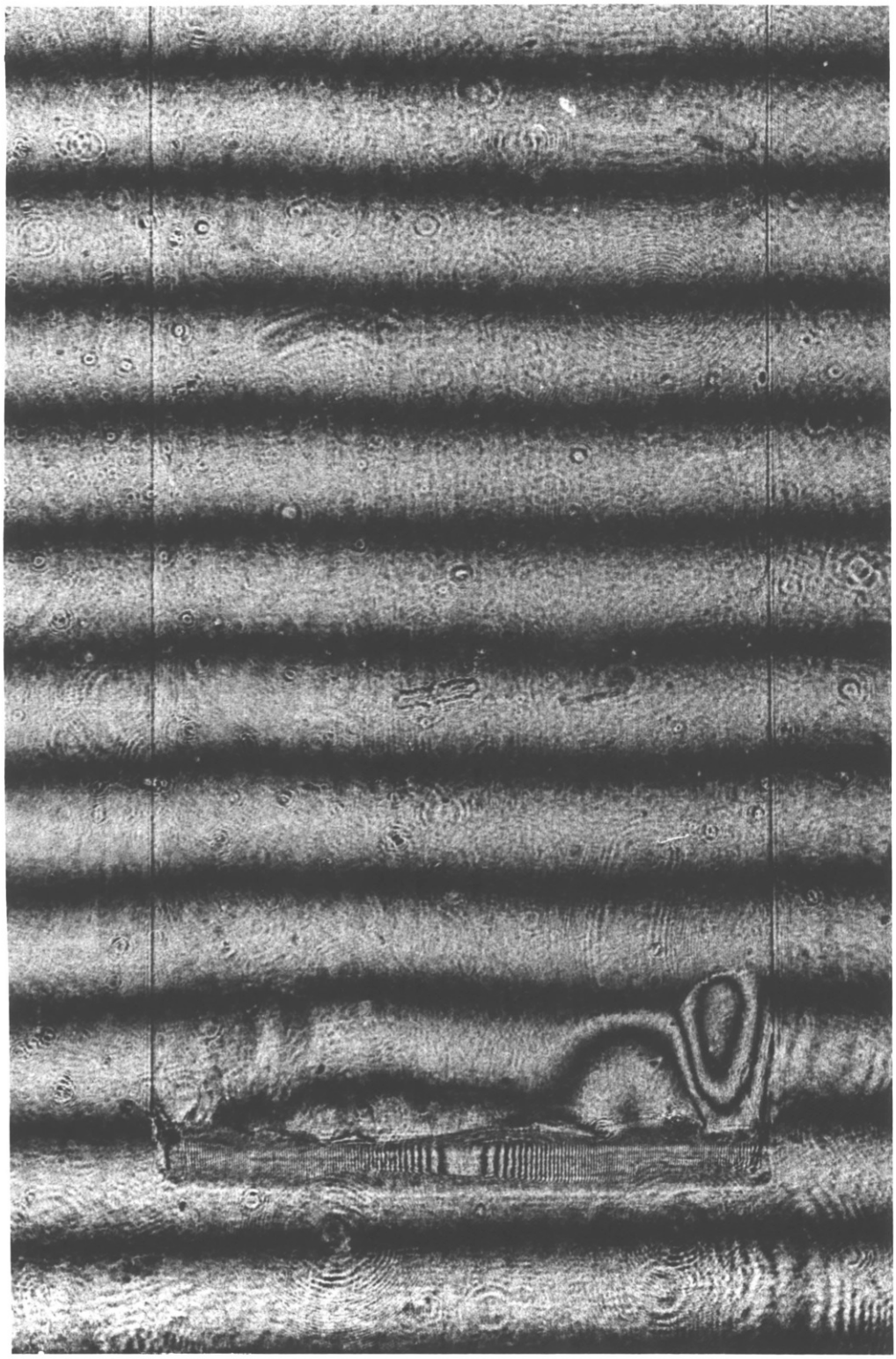


Figure 6.10: Experimental interferogram :
Test rod realigned in the optical cell



## 6.4 Conclusion

Figure 6.10 shows the fringe pattern for a rod lens that has been removed, replaced and re-aligned in the optical cell (at a random orientation) after a period of two hours. The straightness of the fringes testifies to the stability of the index matching oil temperature and to the uniformity both axially and rotationally of the index profile in the rod lens.

Because the rod lens can be removed and replaced accurately into the optical cell, we can now attempt to compare different rod lenses (chapter 9) knowing that the contributions to the fringe shift on the interferogram due to a rod misalignment and a change in the matching oil temperature can be reduced due to a negligible amount.

So far, we have avoided the problem that arises when we attempt to compare GRIN rods that have different diameters. In the following chapter, the error in the index measurement that a typical diameter variation produces is quantified. This problem could not be solved within the time limits of this research, however in the conclusion we shall consider some possible steps that may reduce the diameter variation effect as much as possible.

# CHAPTER SEVEN

## REFRACTIVE INDEX PROFILE RECONSTRUCTION IN THE HOLOGRAPHIC COMPARISON METHOD

In this chapter we describe in detail the trajectories of rays passing transversely through a radially symmetric GRIN field and discuss methods for reconstructing the index profile from the measured data. The refractionless limit (ie. neglection of ray curvature) has been adopted throughout this thesis and we must quantify the error that this approximation introduces to the holographic comparison technique.

We will consider a typical parabolic GRIN distribution and calculate the fringe patterns that we would observe in an interferometer using both the refractionless limit approximation and a more precise ray tracing technique. We show that the fringe patterns are indeed similar, and furthermore that the profile can be accurately reconstructed using algorithms that do not need to take ray curvature into account.

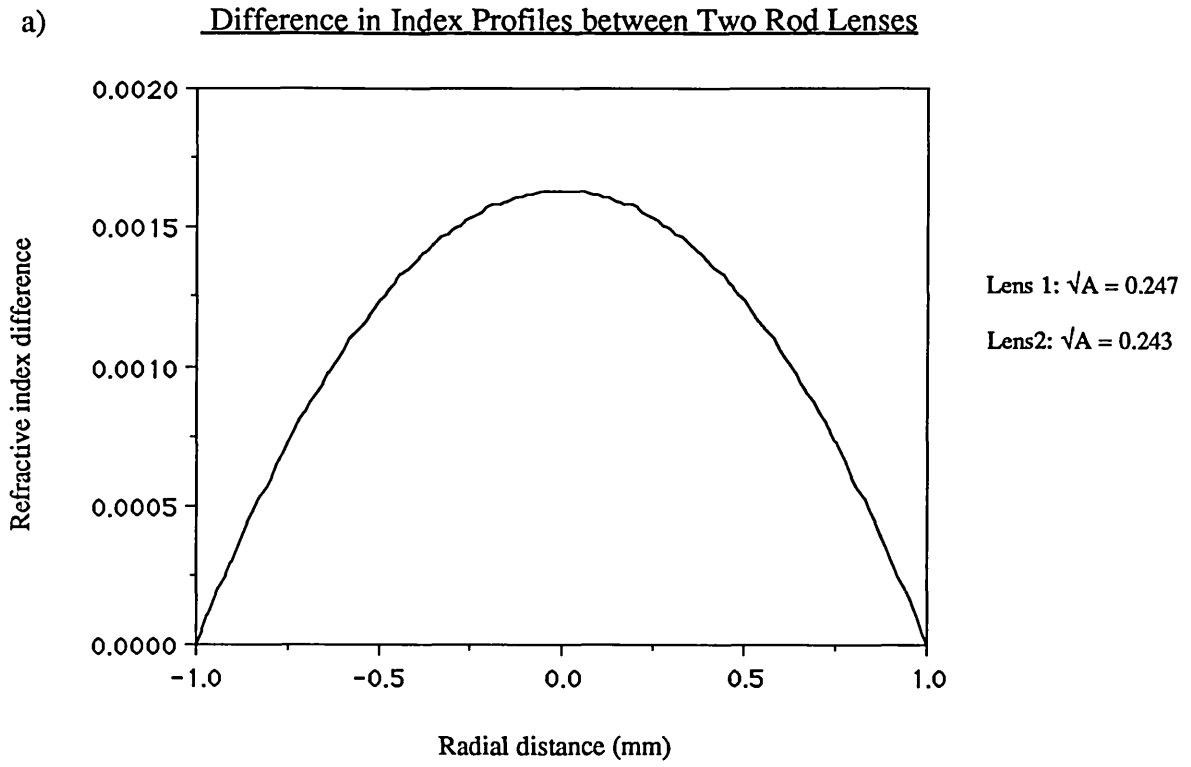
### 7.1 Profile reconstruction and the Abel transform pair

So far we have not described how the index profile may be reconstructed from the measured pathlength data. The most direct approach is to adopt the refractionless limit and in this case, the profile may be calculated using a well established transform pair. As we shall shortly see, this does not necessarily imply a great loss of accuracy for the profiling method. For the case where ray refraction cannot be ignored, some fairly complex reconstruction algorithms are required. (For example see Iga (1977) and Sochaki (1986).) Even so, ray refraction can only be sensibly incorporated in deflection function profiling methods (see §2.4) as will be shown in section 7.5.

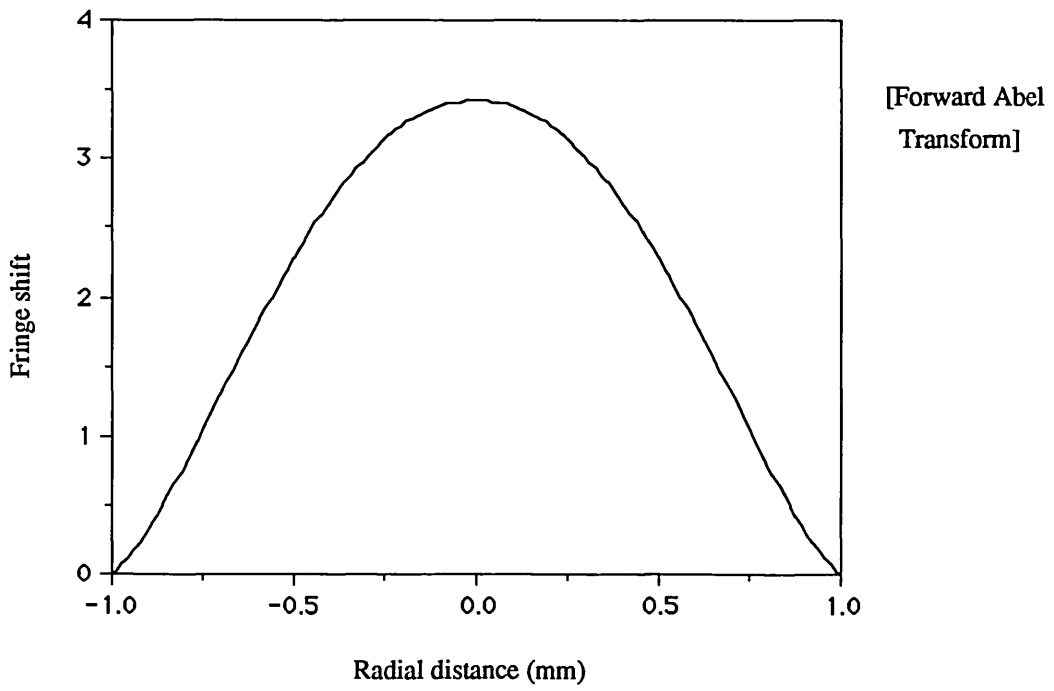
In chapter four (§4.3) we have calculated the optical pathlength for a transverse ray using the refractionless limit approximation as

Figure 7.1: The forward and inverse Abel transform as applied to refractive index profiling

a)




b)



$$(7.1) \qquad W(y) = 2\int_{y}^{a} \frac{n(r)\, r\, dr}{\sqrt{r^2 - y^2}}$$

This equation is known as the Abel Transform and it has a well known inverse transform [Marcuse[1], Bracewell[2]], which can be used to relate the refractive index distribution n(r) to the measured pathlength W(y), viz

$$(7.2) \qquad n(r) = \frac{-1}{\pi}\int_{r}^{a} \left(\frac{dW}{dy}\right) \frac{dy}{\sqrt{y^2 - r^2}}$$

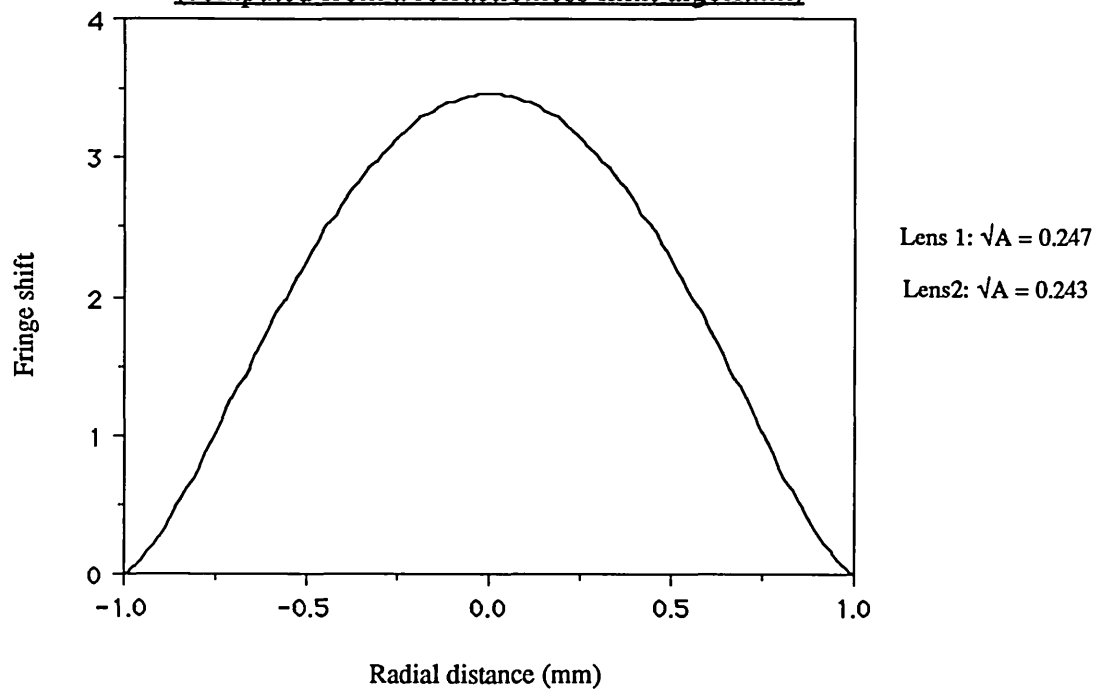
The index profile must be reconstructed by using numerical techniques of differentiation and integration and it is here (particularly the differentiation[1]) that the computation errors can easily arise.

The Abel Transform appears in a number of branches of physics[3] and many workers have considered accurate inversion schemes. An excellent review of the field is given by Hansen[3] and the author also supplies software[4] for numerically computing the forward and inverse Abel transforms. These programs were obtained and coded into the BASIC programming language to run on a BBC micro-computer and thus the comparison method could be modelled for both the computation of the fringe shifts and the reconstruction of the profile from this fringe data.

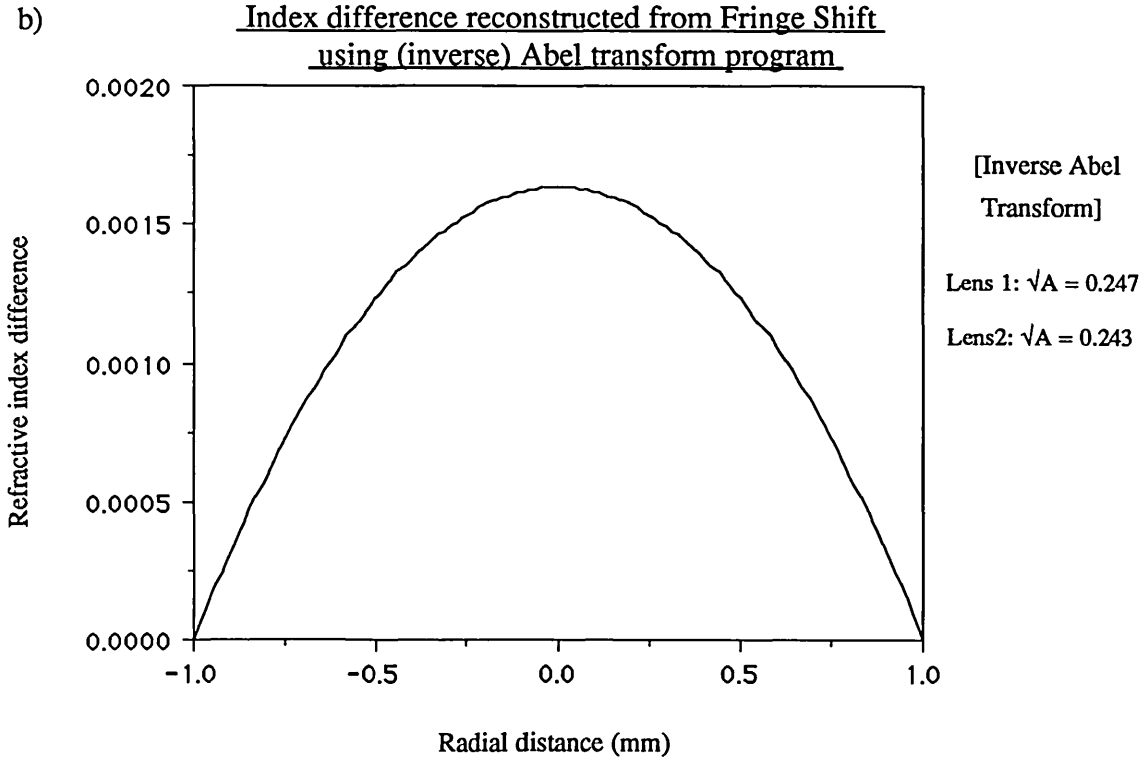
To model the comparison method, we shall consider two 2mm diameter rod lenses with a 1.5% difference in their quadratic gradient constants ie. $\sqrt{A_1} = 0.247$ and $\sqrt{A_2} = 0.243$. We expect the interferogram to have a form similar to figure 4.3, with the fringe shift reduced by about one half in magnitude. The corresponding index profile difference is plotted in figure 7.1a. Using the Abel transform program we can compute the fringe shift function (Forward Abel Transform) and this is plotted in figure 7.1b. In this figure, the plotted function can be considered to be the centre of a fringe on the interferogram and the shift is measured relative to zero, which is the tilt fringe position. The function compares favourably with that in figure 4.3 which was computed analytically.

Figure 7.2: Computation of the inverse Abel transform

a)




b)



We can also use the Abel transform to work backwards and calculate the index difference function (Inverse Abel transform) from a given fringe shift function (see figure 7.2.) and this is the conventional technique for reconstructing an index profile from transverse profiling data.

The Abel transform programs yield a great advantage to analysing refractive index profiling methods, because they work on the appropriate (fringe or index) data directly. Thus we can calculate transforms without the need to solve analytical integrals as in chapter 4. For example consider a refractive index profile that is not completely smooth, but contains a random error in the index values over a short radial range (figure 7.3a). If we compare two rods having such an error but otherwise similar parabolic profiles (fig. 7.3b), we can predict the form of the correspondingly observed comparison interferogram (Forward Abel transform). See figure 7.3c. We can thus model all kinds of profile errors directly.

## 7.2 Optical pathlength computation in the refractionless limit

We now calculate the optical pathlength of a ray passing through a GRIN field in the refractionless limit using the the forward Abel transform equation (7.1). We have already performed a similar calculation in chapter 4 but in this case we use the index profile given by eq.(1.1)

$$n^2(r) = n_0^2 (1 - A (r / a)^2) \tag{7.3}$$

We thus have the following integral to solve

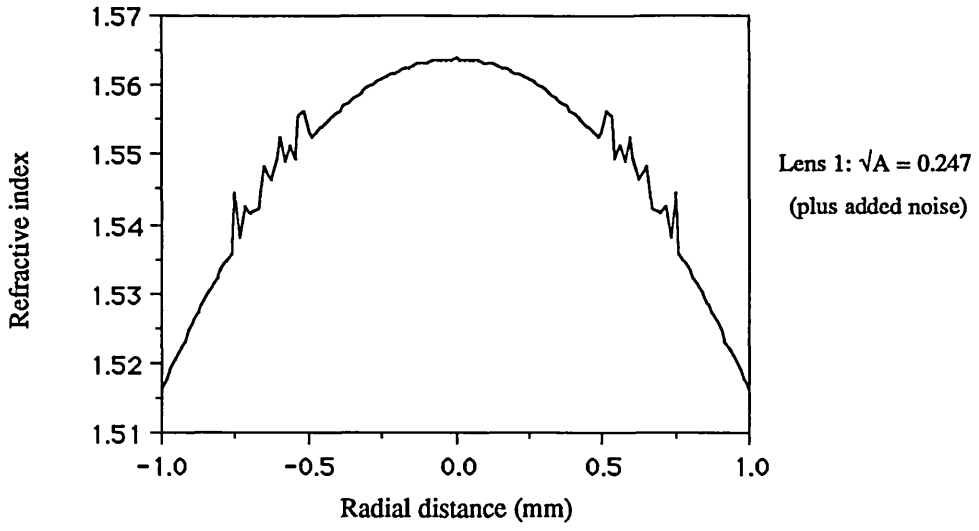
$$W_a(y) = \left(\frac{2 n_0}{a}\right) \int_y^a \left(\frac{a^2 - A r^2}{r^2 - y^2}\right)^{1/2} r \, dr \tag{7.4}$$

Making the change of variable $x=r^2$ and $2 r \, dr = dx$, this can be written in the form

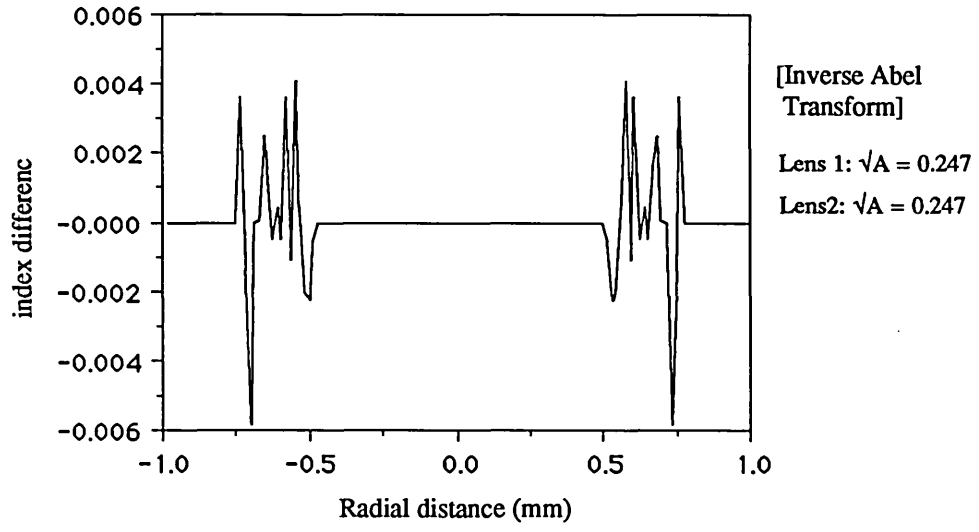
$$I = \left(\frac{n_0}{a}\right) \int \left(\frac{c + d x}{a + b x}\right)^{1/2} dx \tag{7.5}$$

Figure 7.3: Computing a fringe shift for profiles having a random fabrication error

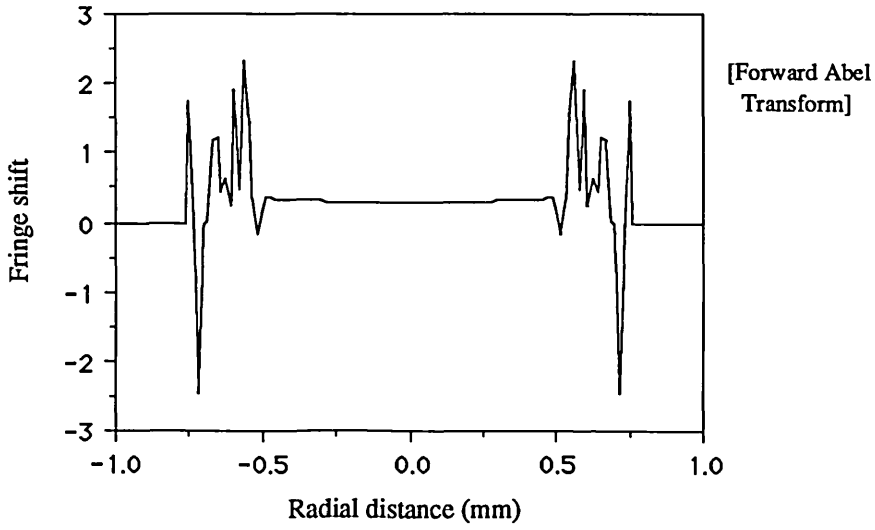
a) Refractive Index Profile with Noise




b) Difference in Refractive Index due to Noise




c) Forward Abel Transform (Fringe shift) of Index Difference



From Abromovitz and Stegun[5](pages 12-13), this equation has the solution

$$(7.6) \qquad I = \left(\frac{1}{b}\right)\left[(a+bx)(c+dx)\right]^{1/2} - \left(\frac{ad-bc}{2b}\right)\left(\frac{2}{\sqrt{-bd}}\right)\operatorname{Arctan}\left(-\frac{d(a+bx)}{b(c+dx)}\right)^{1/2}$$

Thus we must solve,

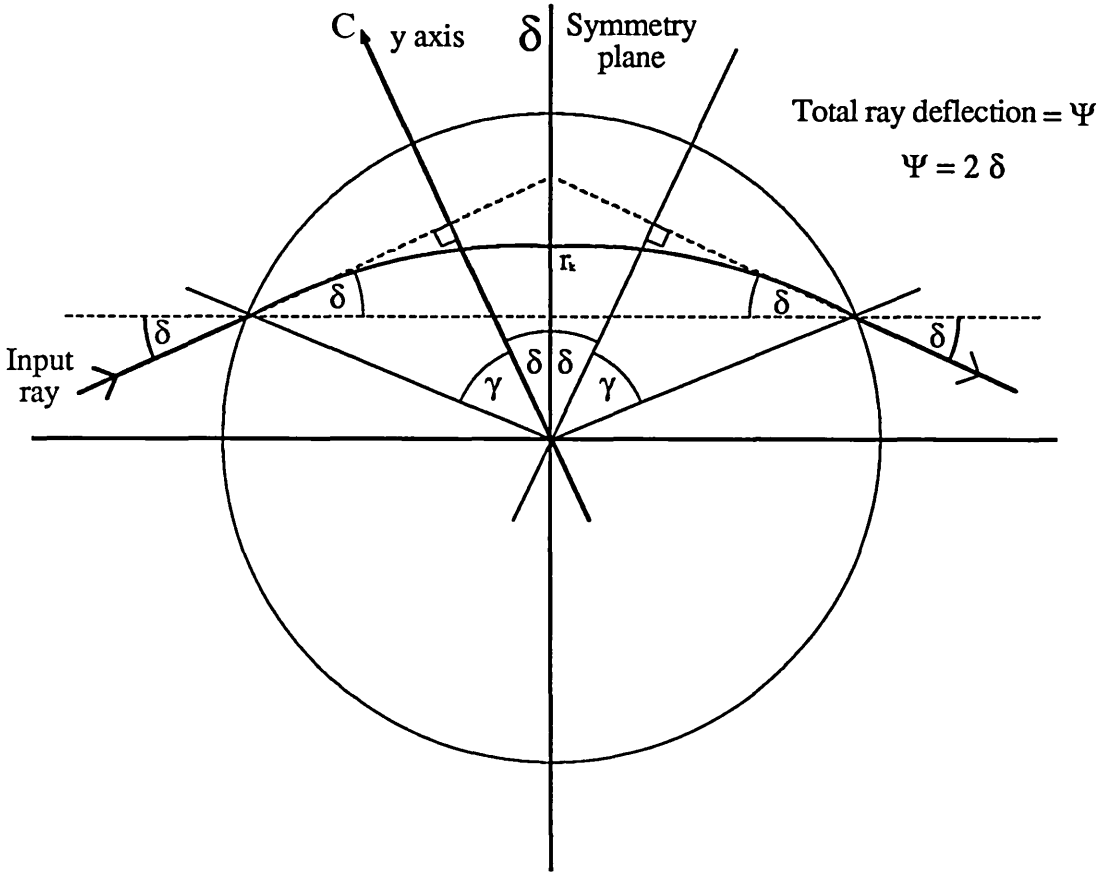
$$(7.7) \qquad W_a(y) = \left| \int_{r=y}^{r=a} \left[(r^2-y^2)(a^2-Ar^2)\right]^{1/2} + \left(\frac{a^2-Ay^2}{\sqrt{A}}\right)\operatorname{Arctan}\left(\frac{A(r^2-y^2)}{(a^2-Ar^2)}\right)^{1/2} \right|$$

Inserting the limits, the term for r=y drops out leaving

$$(7.8) \qquad W_a(y) = n_0(a^2-y^2)^{1/2}(1-A)^{1/2} + \left(\frac{n_0}{a}\right)\left(\frac{a^2-Ay^2}{\sqrt{A}}\right)\operatorname{Arctan}\left(\frac{A(a^2-y^2)}{a^2(1-A)}\right)^{1/2}$$

This final equation gives similar values to equation 4.8 where the simplified parabolic profile form (eq 1.2) was used. The comparison method can be simulated as in chapter 4 by computing and subtracting $W_a(y)$ for the two differing GRIN rods. The theoretical fringe shift for a 1.5% difference in $\sqrt{A}$ is plotted in figure 7.2a. (Note, this function was used for reconstruction of the index difference by the inverse Abel transform routine described in that section.) The complex nature of eq. (7.8) highlights why equation 4.10 was so useful in the calculations of chapter 4.

Figure 7.4: Ray path through a graded index field



## 7.3 Ray curvature and optical pathlength

### 7.3.1 Preliminaries

The effect of ray curvature in refractive index measurements has been investigated by many workers, notably, Kahl and Mylin[6] (1964), Vest[7] (1974), Kokubun and Iga[8] (1977), Chu[9](1979) and Sochacki[10] (1986). We shall follow their approach with the exception that the usual geometrical optics sign convention is maintained and the deflection of the ray (towards the axis) by the GRIN field is considered negative.

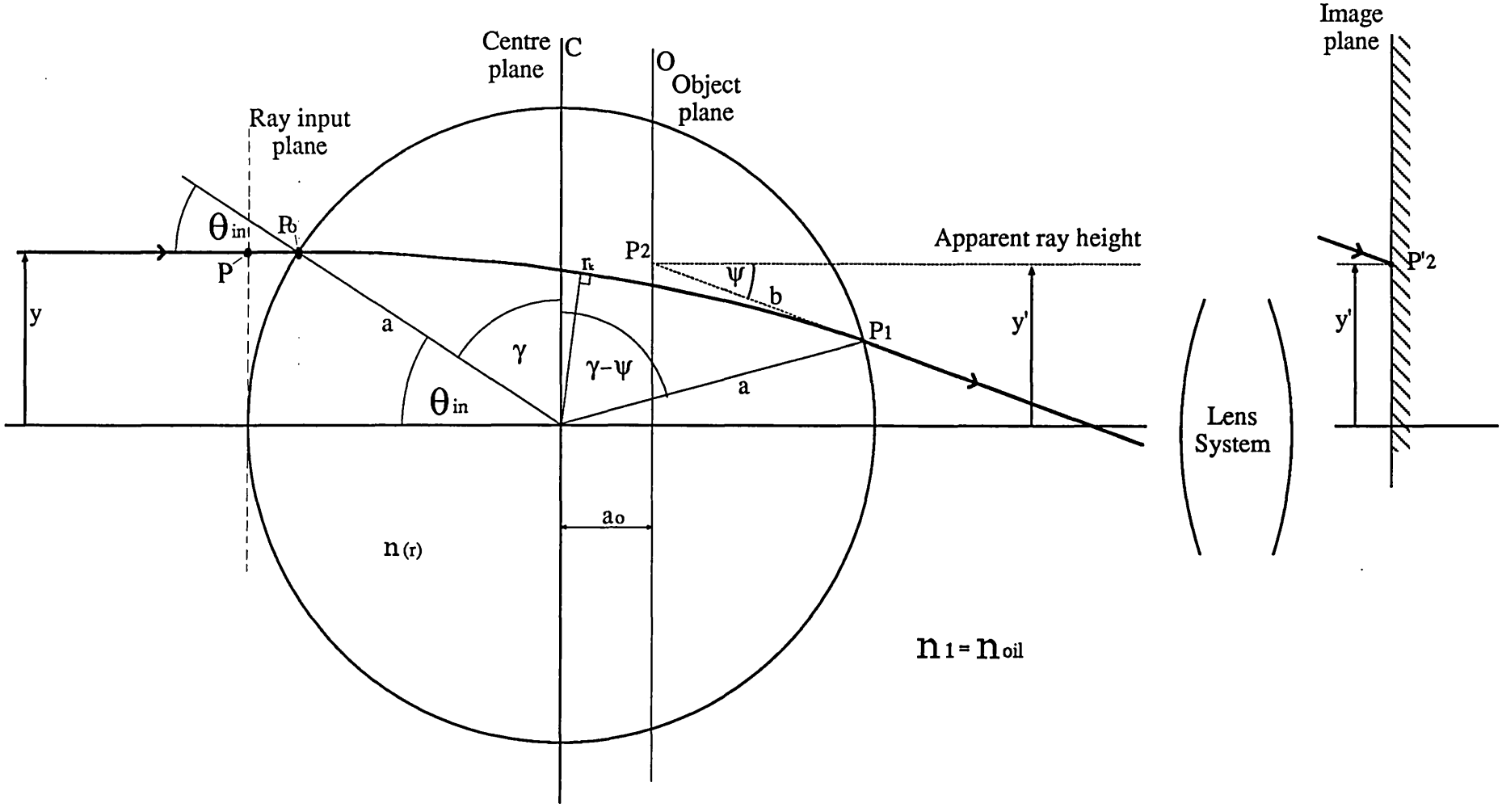
Figure 7.4 schematically illustrates the path of a typical ray through a symmetrical graded index field. The ray path is symmetric about the $\delta$ plane which also contains the point of nearest approach ($r=r_k$) for the ray. From the figure we must note that the deflection angle $\Psi \equiv 2\delta$. The centre plane C is also shown as the plane normal to the initial ray direction.

The situation for a refractive index profiling arrangement is illustrated in figure 7.5 where plane C is now orientated vertically as is typical for ray analysis in index profiling. Because of the ray curvature, lenses are required to produce an image of the GRIN rod at a suitable observation plane. We follow Kahl and Mylin and consider the case where the lens images a vertical plane (O) in the phase object and for the sake of generality, this plane is a distance $a_0$ from the plane passing through the centre of symmetry of the index distribution.

The probing ray incident upon the rod at height y from the optical axis follows a curved path through the core from $P_0$ to $P_1$, and it exits with refraction angle $\Psi$ (negative in this case). The ray is brought to a focus at the point $P_2'$ (height y') in the image plane conjugate to the plane O. At the point of emergence $P_1$, the ray can be traced back to the apparent point $P_2$ on the object plane and the refracted ray appears to have come from this point.

If we assume that the imaging lens is ideal, then the phase distribution in the object plane is precisely mapped into the image plane.We investigate the accuracy of the profiling method by calculating the optical pathlength of the input ray from input point P to object point $P_2$. The action of the lens is to faithfully preserve this pathlength information at the

Figure 7.5: Refractive Index Profiling and Ray Curvature



measurement (image) plane.

This pathlength information can only be practically determined by interference of the object wave with a suitable reference wave and so ultimately we must also calculate the optical pathlength of a reference ray from the input plane to object point P2 and subtract this from the object ray pathlength data. (The reference ray and the object ray are assumed to have equal optical pathlengths either side of the input and object planes.) The nature of the reference wave will of course depend upon the form of the interferometric test, for example in the TI method the reference rays are unrefracted and follow straight lines to the object plane.)

We wish to calculate the optical pathlength $W_r(y')$ of the ray from point P to P2. From figure 7.5,

$$(7.9)\quad W_r(y') = n_{oil}\,(a - (a^2 - y^2)^{1/2}) + \int_{P_0}^{P_1} n(s)\,ds - n_{oil}\,b$$

Where b can be found by noting that

$$(7.10)\quad a_o + b\cos\Psi = a\sin(\gamma - \Psi)$$

$$(7.11)\quad a\cos\gamma = y \qquad : \qquad a\sin\gamma = (a^2 - y^2)^{1/2}.$$

Therefore

$$(7.12)\quad b = (a^2 - y^2)^{1/2} - y\tan\Psi - a_o\sec\Psi$$

So that we have finally

$$(7.13)\quad W_r(y') = \int n(s)\,ds - n_{oil}(a^2 - y^2)^{1/2} + n_{oil}\,y\tan\Psi + n_{oil}\,a_o\sec\Psi + n_{oil}(a - (a^2 - y^2)^{1/2})$$

A similar equation is used in the literature, with the exception of the difference in sign.

Equation 7.13 reveals that there are several parameters that need to be determined before the path of the ray can be fully expressed. These are: the pathlength integral $F(y) = \int n(s)\, ds$, the refraction angle $\Psi$ and the apparent ray height y'. Before we derive these expressions, we must establish some essential basics.

For each ray incident upon the rod we can assign an impact parameter K that is given by Bouger's formula (Born and Wolf[13] (page 122))

(7.14) $K = r\, n(r) \sin i$

This relationship is a form of Snell's law and it can be derived from the Ray equation introduced in the appendix. The angle i at any point along the ray is measured between the ray direction vector and the vector r from the origin to that point on the ray. For example, at the input point Po, $r = a$, $i = \theta_{in}$ and $n(a) = n_{oil} = n_1 = n_0 (1 - A)^{1/2}$.

Now as $\sin \theta_{in} = y / a$ we therefore have for each ray

(7.15) $K = n_0 (1-A)^{1/2} y$

At the point of closest approach to the rod axis, $r = r_k$ and $i = \pi / 2$. Thus we also have

(7.16) $K = n(r_k)\, r_k = n_0 (1 - A)^{1/2} y.$

Using the profile expression, we must remember that

(7.17) $n(r_k) = n_0 (1 - A(r_k/a)^2)^{1/2}.$

7.3.2 The ray optical pathlength through the Field

We need to solve the integral

$$(7.18)\quad F(y) = \int_{P_0}^{P_1} n(s)\, ds$$

By expressing the differential arc length (ds) in cylindrical polar coordinates[7] we have

$$(7.19)\qquad ds = \frac{dr}{\sqrt{n^2_{(r)} r^2 - k^2}}$$

and thus the pathlength integral has the general form[7]

$$(7.20)\qquad F(y) = 2\int_{r_k}^{a} \frac{n^2_{(r)}\, r}{\sqrt{n^2_{(r)} r^2 - k^2}}\, dr$$

Inserting the profile expression yields an integral of the following form

$$(7.21)\qquad F(y) = 2\int_{r_k}^{a} \frac{\left(n_0^2 - \left(\frac{n_0\sqrt{A}}{a}\right)^2 r^2\right)}{\left(n_0^2 r^2 - \left(\frac{n_0\sqrt{A}}{a}\right)^2 r^4 - k^2\right)^{1/2}}\, r\, dr$$

which can be rewritten as

$$(7.22)\qquad I = \int \frac{(b + c\,x)}{(a + b\,x + c\,x^2)^{1/2}}\, dx$$

where $x=r^2$, $b=n_o^2$, $a=-k^2$, $c = -\,(n_0^2 A\ /\ a^2)$.

This has the solution ( Gradshteyn and Ryzhik[12] (§2.264, p. 83), ),

$$(7.23) \qquad I = \sqrt{R} + \left(\frac{b}{2}\right)\left(\frac{1}{\sqrt{-c}}\right) \text{Arcsin}\left(\frac{2cx+b}{\sqrt{-D}}\right)$$

where $R = a + bx + cx^2$ , $D = 4ac - b^2$. Thus

$$(7.24) \qquad F(y) = \left| \int_{r=r_k}^{r=a} n_0^2 (1 - A (r/a)^2) r^2 ) - k^2)^{1/2} \right.$$
$$\left. - \left(\frac{n_0 a}{2\sqrt{A}}\right) \text{Arcsin} \left( \frac{1 - 2A (r/a)^2}{\left(1 - \left(\frac{2k\sqrt{A}}{n_0 a}\right)^2\right)^{1/2}} \right) \right|$$

This expression can (eventually) be solved by inserting in the upper and lower limits and making use of the following trigonometric relationship (Abromovitz[5], §4.4.32 p.80)

$$(7.25) \quad \text{SIN}^{-1}(A) - \text{SIN}^{-1}(B) = \text{SIN}^{-1}\{A (1 - B^2) - B (1 - A^2)\}.$$

After a lengthy solution, the final result is

$$(7.26) \quad F(y) = n_0(1 - A)^{1/2}(a^2 - y^2)^{1/2} + \left(\frac{n_0 a}{2\sqrt{A}}\right) \text{Arcsin} \left( \frac{(2\sqrt{A}) (a^2 - y^2)^{1/2}(1 - A)^{1/2}}{(a^2 - 4A(1 - A) y^2)^{1/2}} \right)$$

This result is verified by Chu[9] (1979).

### 7.2.3 The Refraction Angle

With reference to figure 7.5, the refraction angle $\Psi(y)$ can be found from

$$(7.27) \quad \Psi(y) = \pi - \Theta(y) - 2\theta_{in}$$

where $\Theta(y) = (2\gamma - \Psi(y))$ . $\Theta(y)$ can be determined from the following integral Tallents[11], Born and Wolf[13]

$$(7.28) \qquad \Theta(y) = 2\int_{r_k}^{a} \frac{k}{r} \frac{dr}{\sqrt{n^2_{(r)} r^2 - k^2}}$$

Which upon insertion of the profile expression becomes

$$(7.29) \qquad \Theta(y) = 2\int_{r_k}^{a} \frac{k}{r} \frac{dr}{\left(n_0^2 r^2 - \left(\frac{n_0\sqrt{A}}{a}\right)^2 r^4 - k^2\right)^{1/2}}$$

Making the substitution $x = r^2$ and writing $R = a + bx + cx^2$, $a = -k^2$, $b = n_0^2$ and $c = -(n_0^2 A / a^2)$, this integral may be written in the form

$$(7.30) \qquad I = \int \frac{k\,dx}{x(a + b\,x + c\,x^2)^{1/2}}$$

From Gradshteyn and Ryzhik[12] (§2.266, p. 84), this has the solution

$$(7.31) \qquad I = \left(\frac{1}{\sqrt{-a}}\right) \text{Arctan}\left(\frac{2a + bx}{\sqrt{a}\ \sqrt{R}}\right)$$

Thus we have

$$(7.32) \qquad \Theta(y) = \left| \text{Arctan}\left(\frac{n_0^2 r^2 - 2k^2}{2k\,(n_0^2 (1 - A\,(r/a)^2)\, r^2 - k^2)^{1/2}}\right) \right|_{r = r_k}^{r = a}$$

Which we solve by inserting the limits, taking particular note that the $r = r_k$ term yields $\text{Tan}^{-1}(-\infty) = -\pi / 2$.

$$(7.33) \qquad \Theta(y) = \text{Arctan}\left(\frac{a^2 - 2(1 - A)\,y^2}{2(1 - A)(a^2 - y^2)^{1/2} y}\right) + \left(\frac{\pi}{2}\right)$$

The refraction angle may finally be written as

$$(7.34) \qquad \Psi(y) = \left(\frac{\pi}{2}\right) - \text{Arctan}\left(\frac{a^2 - 2(1-A)y^2}{2(1-A)(a^2-y^2)^{1/2}y}\right) - 2\,\text{Arcsin}\left(\frac{y}{a}\right)$$

The deflection function $\Psi(y)$ for $\sqrt{A} = 0.25$ is plotted in figure 7.6a.

7.3.4 The Apparent Ray Height y'

$P_2$ and $P'_2$ are conjugate object and image points respectively. If we assume unit magnification, then the profiling method associates the optical pathlength information with the axial height y' rather than the input height y. (In the refractionless limit, heights y' and y are assumed to be the same.) The apparent ray height y' can be found from the relationship (see figure 7.5)

$$(7.37) \quad y' = a\cos(\gamma - \Psi) - b\sin\Psi.$$

Therefore

$$(7.38) \quad y' = y\sec\Psi + a_0\tan\Psi$$

The difference in the ray heights (y'-y) is plotted in figure 7.6b for a typical GRIN lens ($\sqrt{A} = 0.247$) for the case $a_0 = 0$. Note that the difference is positive and is at most only a few microns in magnitude. This difference will certainly be below the resolution of the video digitiser. If we calculate the difference in ray heights as a function of the misfocus $a_0$ we find: a negative misfocus tends to increase the discrepancy and a positive defocus reduces the apparent ray height until it is below the input value For example, $a_0 = -50$ microns gives a maximum difference of y'-y of $\approx 5$ microns. Whereas $a_0 = +50$ microns gives a value of $\approx 2$ microns. At the plane around $a_0 = +15$ microns the difference between the ray heights is everywhere less than 0.5 microns.

We may conclude from this section then, that the disrepancy between the apparent

Figure 7.6: The deflection function for a graded index rod lens

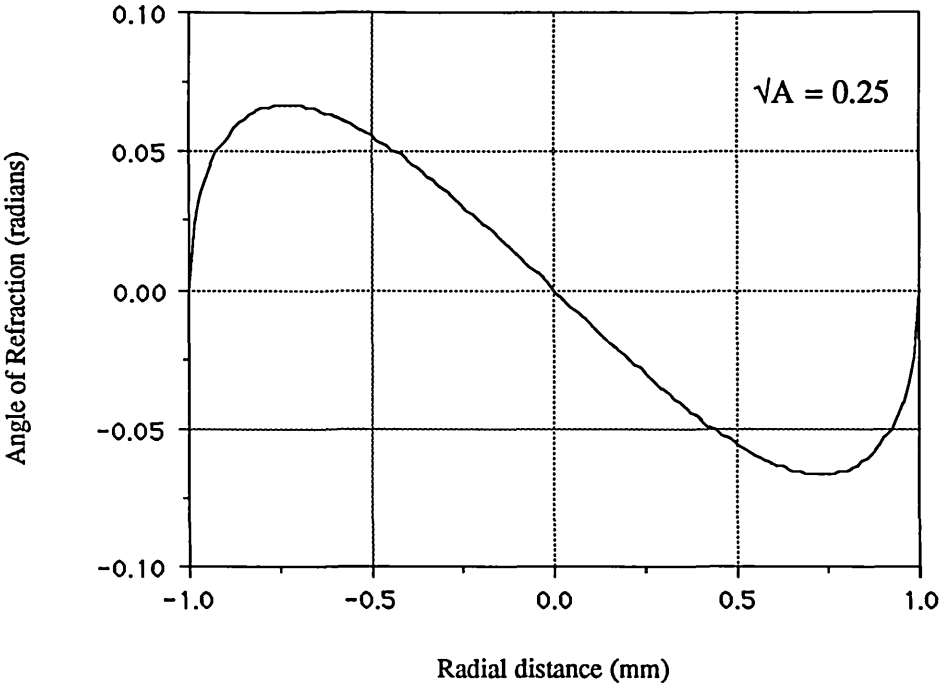
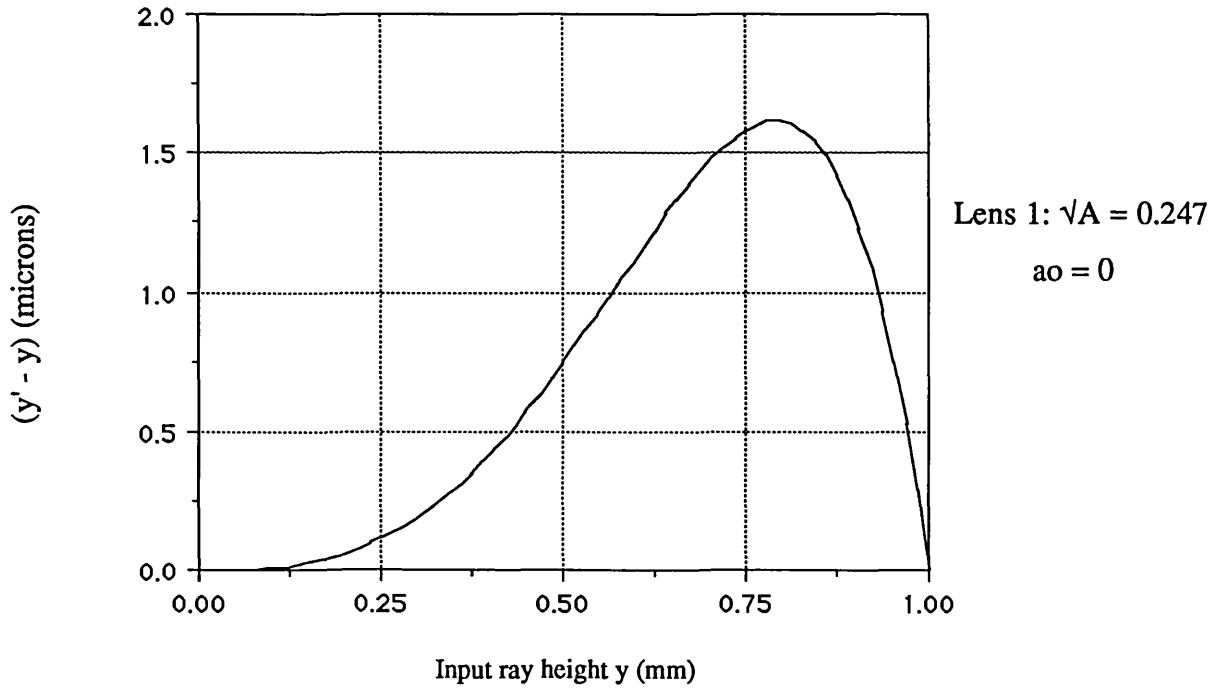



Figure 7.7: Difference between Apparent ray height and Input ray height



and input ray heights is at a negligible value if the observation plane is focused on the central plane of the index distribution. Furthermore, this error can be kept to a mimum by maintaining a slightly positive ( $0 \leq a_0 \leq 50$ μm) misfocus of the observation plane. This can be arranged in practice, by monitoring the image of GRIN rod the as the observation plane is moved. For a negative defocus, caustics are observed at the rod (image) edges. These arise because of a relative increase in the amount of light in this region as the effect of the lens is to effectively 'bunch ' the refracted light rays together. Conversely, for a positive misfocus, there is an observed absence of light at the rod edges where the light is refracted out of the image. The extent of this 'shadow' region increases with the misfocus distance. The photographs in chapter 5 (figure 5.3) , show extreme ($a_0 \approx \pm$ 7mm) examples of the effect of a misfocus.

7.3.5 Optical pathlength from input to object plane

We have derived all the necessary formulae to describe the refracted path of a ray passing through a parabolic GRIN field. Combining these terms and inserting into equation 7.13, we thus have

$$(7.37) \quad W(y') = n_0(1 - A)^{1/2} \left(y \tan\Psi(y) + a_0 \sec\Psi(y) + (a - (a^2 - y^2)^{1/2})\right) + \left(\frac{n_0 a}{2\sqrt{A}}\right) \text{Arcsin} \left(\frac{(2\sqrt{A})\,(a^2 - y^2)^{1/2}(1 - A)^{1/2}}{(a^2 - 4A(1 - A)\,y^2)^{1/2}}\right)$$

7.4 Ray curvature error analysis for the comparison method

We have calculated the various expressions required for following ray paths through a graded index field. We can now quantify the error of using the refractionless limit in analysing the comparison method and we shall consider the interferometric comparison of two GRIN rods with a 1.5% difference in their quadratic gradient constants.

7.4.1 The fringe shift function

We compute the theoretically observed fringe shift function using both the refractionless limit approximation (Wa(y') and the ray tracing formulae (Wr(y') derived above.

For the case where ray refraction cannot be neglected, the two interfering waves have passed through similar graded index fields and so we must take ray curvature into account in both of these waves. Thus at the point y' in the image plane, the optical pathlength difference is given by

(7.38) $S_r(y') = W_{r1}(y') - W_{r2}(y')$.

The subscripts denote the two different index fields. We must note that equation (7.38) is in terms of the final (apparent) ray height y' and we need to find the associated input ray height y for insertion into equation 7.37. Note also that in general, the ray input height y is not the same for both of the index distributions and we thus have a problem of finding an indentical set of y' values for use in $W_{r1}(y')$ and $W_{r2}(y')$. (To achieve this, an iteration routine had to be used to produce an evenly spaced set of (nearly) identical y' values for the two terms in the RHS of eq. 7.38. However, the iteration routine could not find exact matching values of y' and this accounts for the 'bumpiness' of the following theoretical fringe shift functions.)

In the refractionless limit we apply equation 7.8 such that.

(7.39) $S_a(y') = W_{a1}(y') - W_{a2}(y')$.

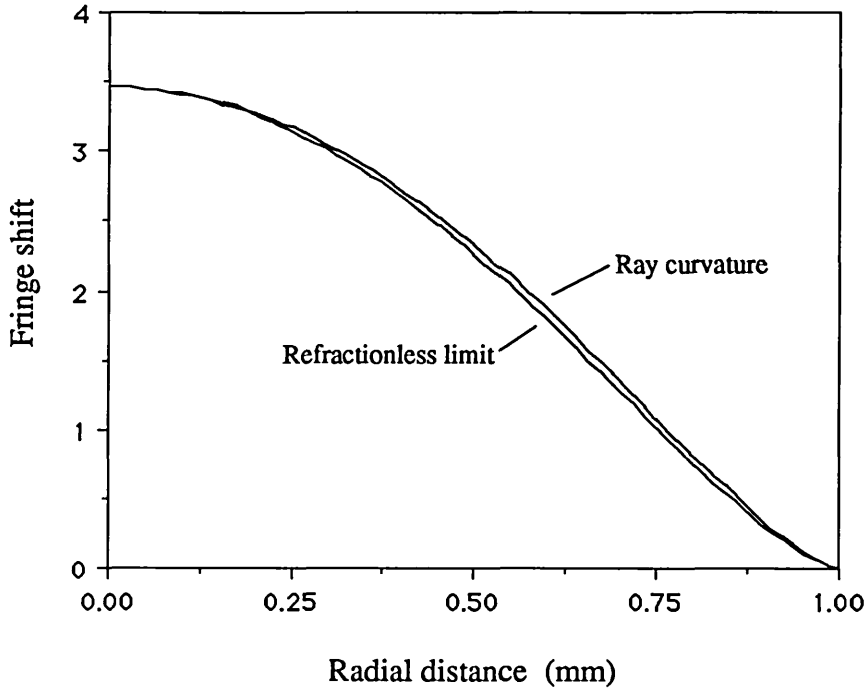
The ray height is assumed to be unchanged for every ray and so y' = y.

Figure 7.8a is a plot of the theoretical fringe shift calculated using both the exact and the approximate expressions. To quantify the difference between the two functions, we compute the (normalised) percentage fringe shift difference, defined as

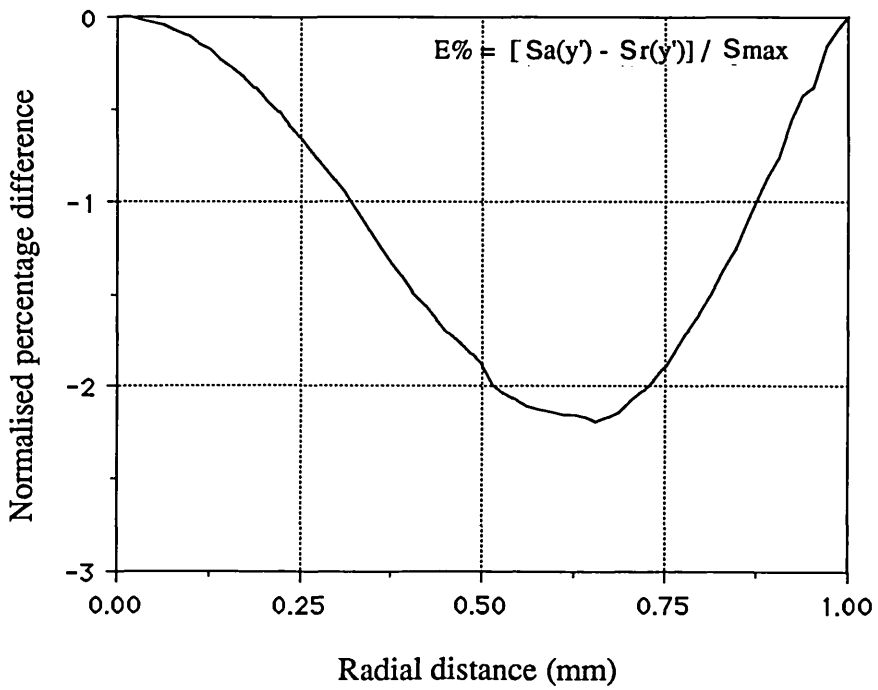
(7.42) $E_f(y') = (S_a(y') - S_r(y')) / S_{max}$

Figure 7.8: Fringe shift computation error of the refractionless limit applied to the holographic comparison method

a) Fringe shift due to difference in index




b) Normalised percentage difference between fringe shifts computed from the Refractionless limit and the ray tracing methods



where the denominator is the maximum of the fringe shift function (W(o)). This function is plotted in figure 7.8b where we see that the error is at most around -2% of the maximum fringe shift. In particular we note that the error has its maximum value around the radial positions where the rays are refracted the most (figure 7.6a); this is to be expected.

The nature of the comparison method is such that this percentage fringe shift difference will increase for index distributions having a greater index difference and be exactly zero for two identical GRIN rods. We can conclude then that the refractionless limit approximation is sufficiently accurate enough for calculating the expected fringe patterns observed in the holographic method.

### 7.4.2 Reconstructing the Index Difference and the GRIN Rod Profile

We have stated that the index profile can be reconstructed from the fringe shift function by using the refractionless limit approximation (inverse Abel transform). To quantify the error that this produces, we apply the inverse Abel transform to the theoretical fringe shift data ($S_r(y')$) and thus reconstruct the difference in refractive index between the two GRIN distributions. (Which we know is given by $\sqrt{A_1} = 0.243$, $\sqrt{A_2} = 0.247$ in this case.) Because the fringe shift function includes the effect of ray refraction, we can consider it to be almost identical to the fringe shift we would expect to measure using the holographic interferometer.

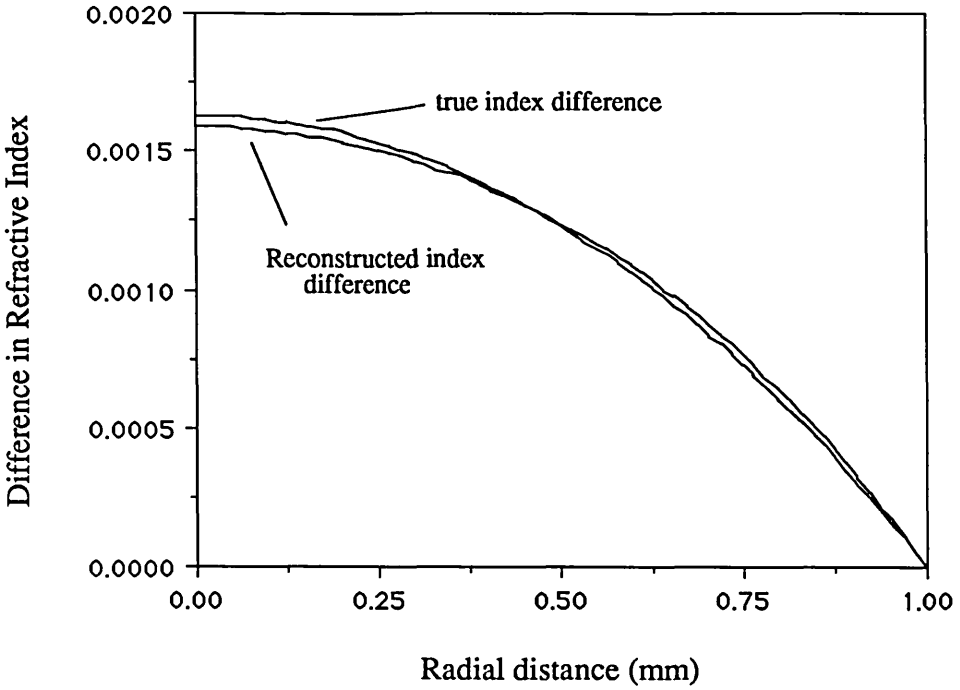
The reconstructed index difference and the true index difference are plotted together in figure 7.9a; the functions are closely similar.To quantify the difference between the two functions, we compute the percentage error in a similar fashion to that above (plotted in figure 7.9b). The maximum error is around ±3% of the maximum index difference, this includes an approximate 1% error introduced by the computer program algorithm.

Finally, we use the (measured) index difference to find the the precision $\varepsilon n(r)$ with which the refractive index values of an unknown rod lens can be determined by the comparison method. $\varepsilon n(r)$ is given by

$$(7.43)\quad \varepsilon n(r) = n_{calc}(r) - n_{true}(r)$$

Figure 7.9: Error of reconstructing the refractive index difference using the refractionless limit approximation

a) Refractive index difference reconstructed using the refractionless limit approximation




b) Percentage error of index difference reconstruction using the refractionless limit approximation

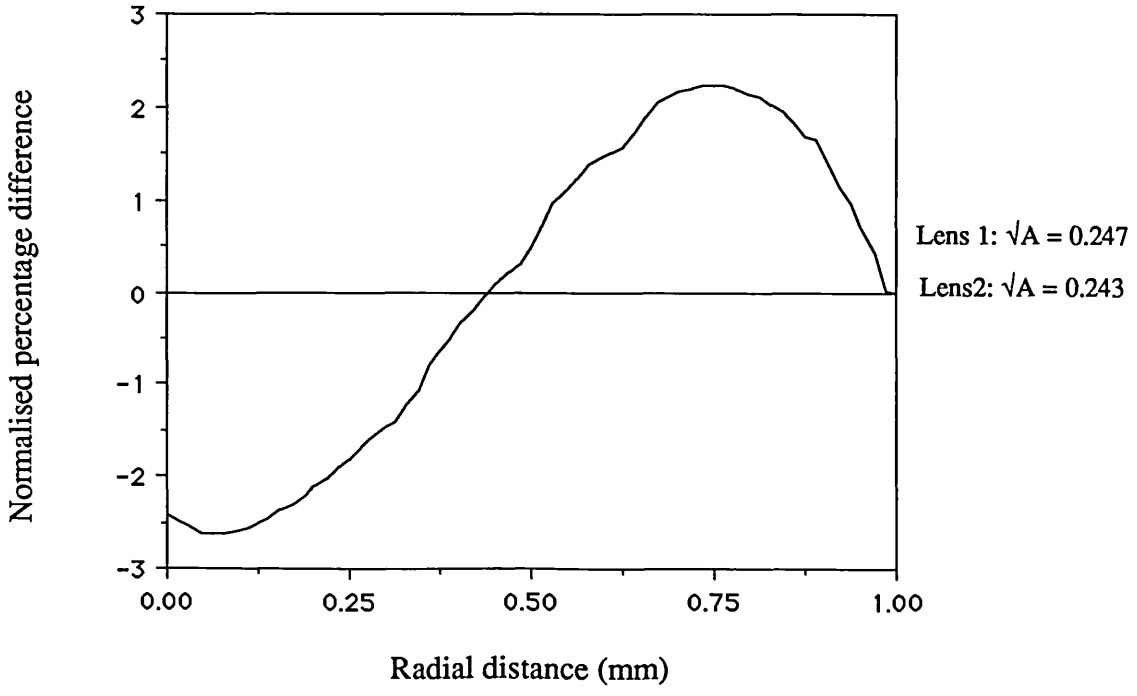


Figure 7.10: Error in the refractive index values of the profile reconstructed using the refractionless limit

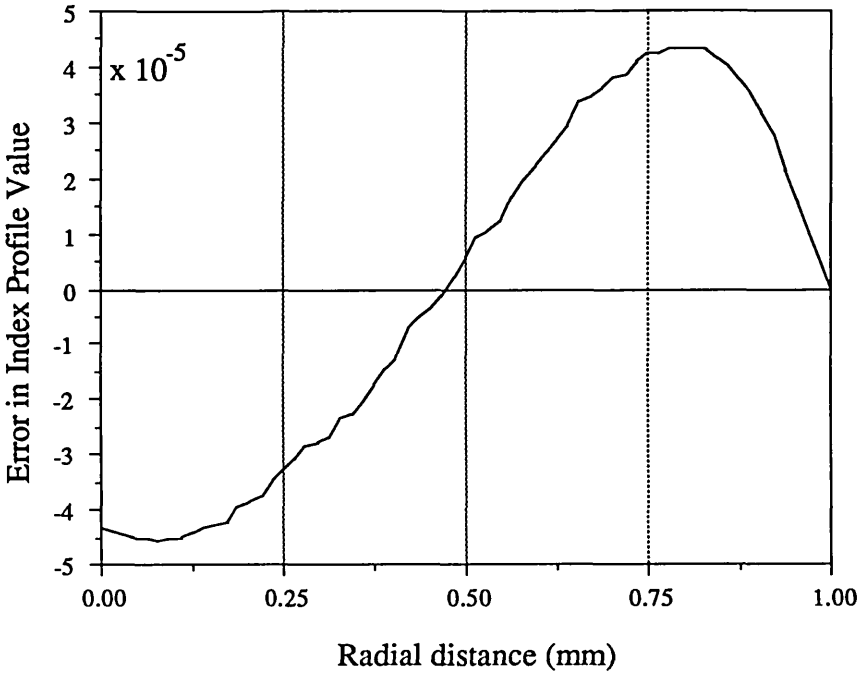
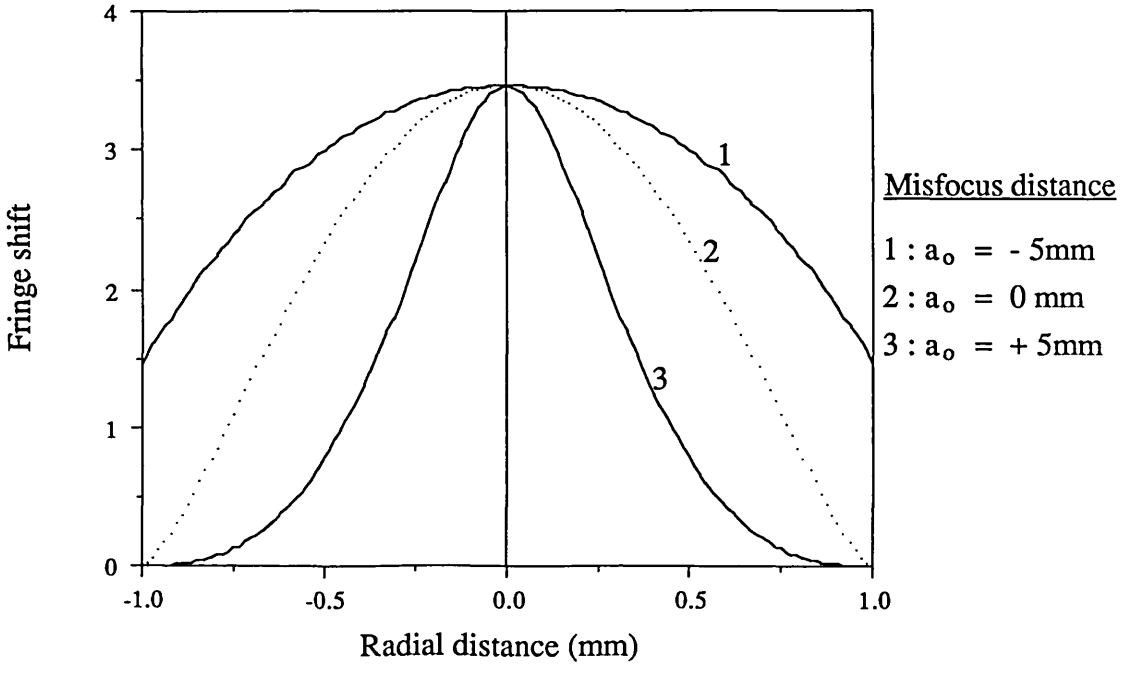



Figure 7.11: Fringe shift as a function of the misfocus of the observation plane



To find $\varepsilon n(r)$, we add the measured difference in index between the two rods to the index profiles values of the known rod, and this yields the index profile values of the unknown rod. For example, let the the rod with the known index distribution have the quadratic gradient constant $\sqrt{A_2} = 0.243$. To the index profiles of this rod, we add the reconstructed index difference values (from above), the resulting index values should correspond to the profile of the rod with quadratic gradient $\sqrt{A_1} = 0.247$. We then find $\varepsilon n(r)$ using equation 7.41.

This function is plotted in figure 7.10, where we see that the theoretical precision of the index measurement is thus $\varepsilon n \approx \pm 5 \times 10^{-5}$. (This is approximately 0.08% of the difference in refractive index between the axial and peripheral index values.)

We may conclude therefore that the refractionless limit is sufficiently accurate enough to reconstruct an index profile from a fringe shift measured using holographic comparison interferometry. As we shall shortly see in the following sections, this theoretical precision can be dramatically limited by the practical reconstruction of the profile from real (noisy) data.

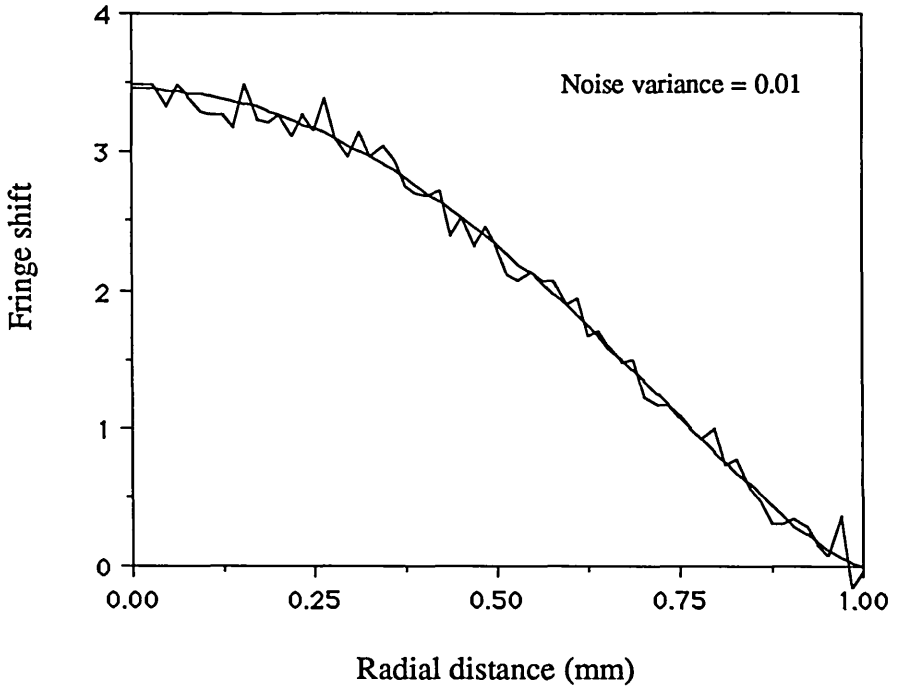
### 7.4.3 Misfocussing Error

The preceding calculations have assumed that the lens is focussed on the central plane of symmetry of the index distribution (ie. $a_0 = 0$). We have seen the effect of a misfocus on the apparent ray height position, and found that there is a region of best focus for a GRIN rod of up to + 50 microns from the central plane. But what effect will such a misfocus have on the observed fringe pattern and ultimately the reconstructed refractive index profile?

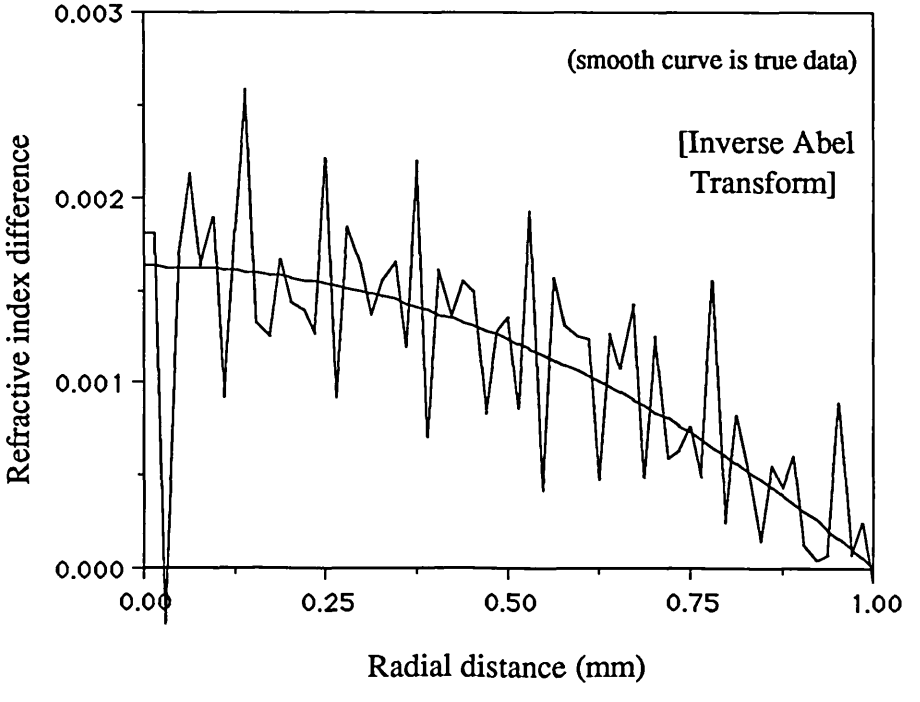
To take into account the effects of a mis-focus, we repeat the above calculations for varying values of $a_0$ and plot the form of the observed fringe shift (figure 7.11). From the figure, we see that misfocusing the observation plane distorts the fringe shape quite noticeably from the $a_0 = 0$ position. If we measure the fringe shift with a misfocus of $a_0 = 1\text{mm}$ and reconstruct the index profile of the unknown rod, we find that the precision in the determination in the refractive index is then at best $\varepsilon n \approx 2 \times 10^{-4}$.

Figure 7.12: Computation of the inverse Abel transform in the prescence of noise

a) Fringe shift with added noise




b) Index difference reconstructed directly from inverse Abel transform



Thus for maximum accuracy, we must ensure that the observation plane is focussed as closely as possible on the central plane of symmetry of the refractive index distribution.

## 7.5 Practical reconstruction of the index profile

### 7.5.1 The inverse Abel transform in the presence of signal noise

We now consider techniques for practically reconstructing the index profile from the measured (noisy) pathlength data.The major problem in solving eq. (7.2) lies in the need to find the dW/dy term. This term amplifies any noise contained in the experimental data and this can ultimately produce almost meaningless results. For example, consider figure 7.12a, which shows a the fringe shift function with noise superimposed upon the signal. The noise (≈ 1/10th of a fringe deviation) could be introduced when the image is digitised perhaps. If we attempt to reconstruct the profile from the noisy signal, we get the function shown in figure 12b. From the figure it can be seen that no sensible assessment of the reconstructed index function can be made. This error is attributable almost entirely to the dW/dy term in the inverse transform.

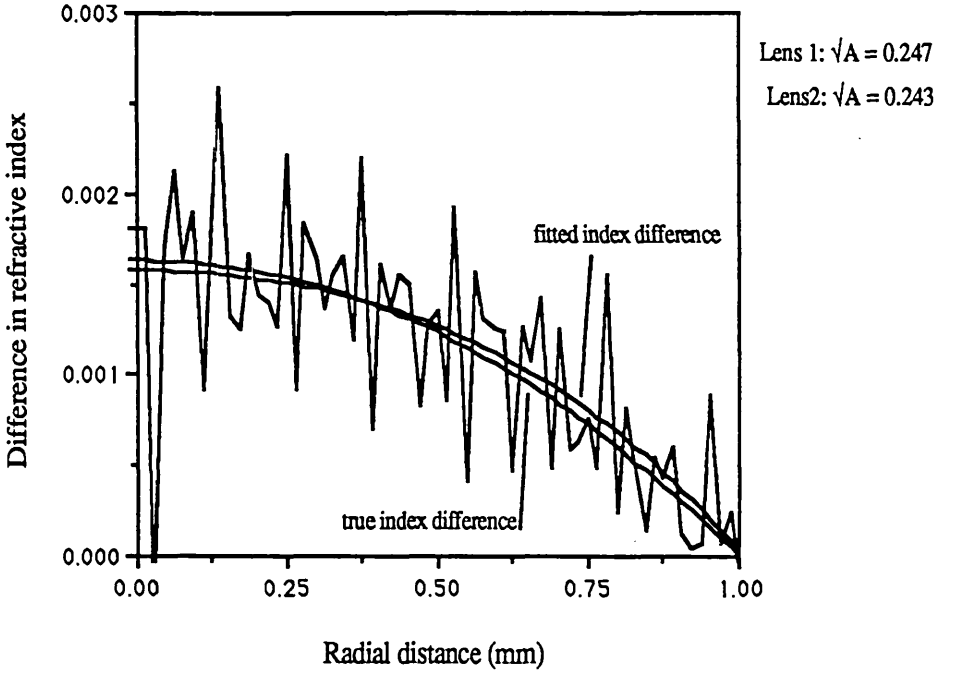
In an attempt to extract some useful information from the reconstructed signal, an even order power series can be fitted to the noisy index values and this is shown in figure 13 above. This process at least yields the index difference in a more presentable form. However, we could probably fit any function to the noisy index data and get an improvement on figure 7.12b!

If we wish to differentiate the measured data prior to insertion into equation 7.2, we should measure the fringe shift as accurate as possible (perhaps with a resolution of a 1000th of a fringe!) and this will cut down the error in dW/dy. Note that this problem does not arise in the index profiling techniques that measure the deflection function directly, as this function contains dW/dy implicitly.

In this work, the experimental data is derived from laser fringe patterns and these inherently contain an excessive amount of noise. The noise value is also increased by the use of a relatively low resolution digitiser. Because of the high amount of noise and the

great sensitivity to noise of the inverse transfrom we must consider some signal smoothing processes for the practical computation of eq 7.2.

Figure 13: Fitting an even order power series to the reconstructed index difference




7.5.2 Least squares smoothing

A popular technique for Abel inversion[1] is to fit the measured data with a smoothing function that has a known inverse Abel transform. Thus we may consider the measured fringe shift to be composed of an even power series of the form

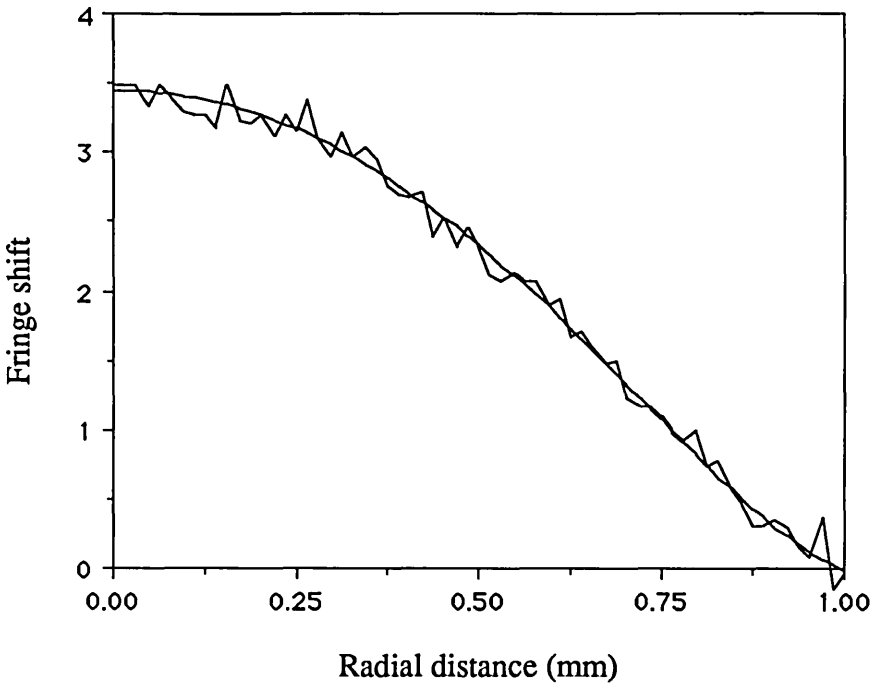
(7.42) $W(y) = a_0 + a_2 y^2 + a_4 y^4 + a_6 y^6 + .... a_i y^i$

Even terms are only considered as the function is assumed to be symmetrical. Having determined the coefficients $a_i$ using a least squares fit routine, equation 7.9 can be differentiated thus

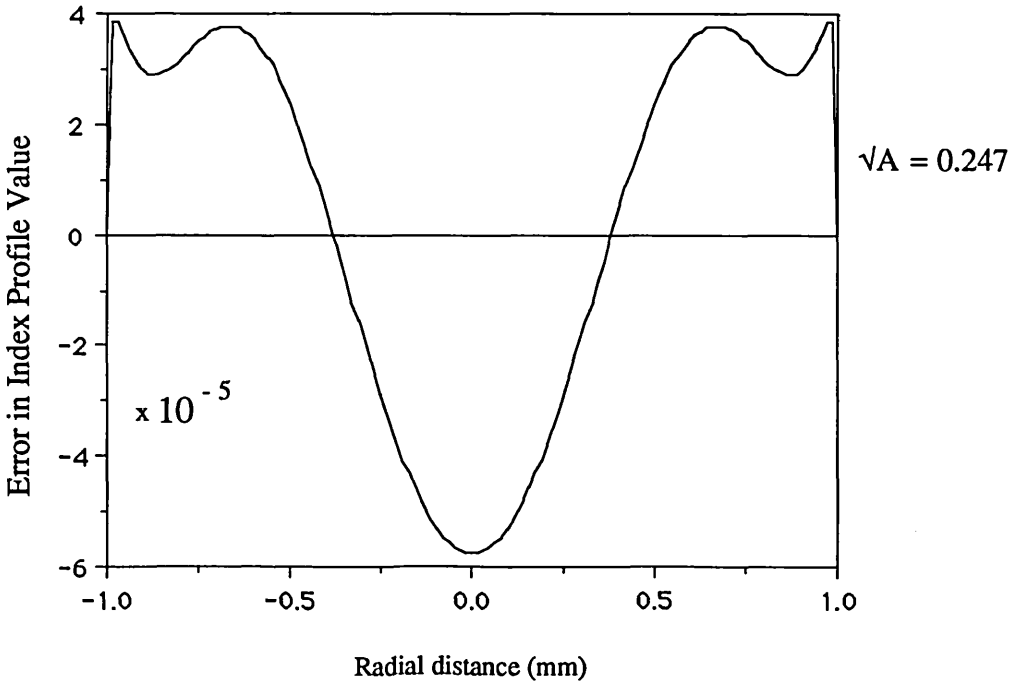
(7.43) $dW(y)/dy = 2 a_2 y + 4 a_4 y^3 + 6a_6 y^5 + .... i a_i y^{i-1}$

Figure 7.14: Fitting a Power Series to the Noisy Fringe Data

a) Sixth order power series fitted to Noisy Fringe data




b) Error in the Refractive Index Values of the Reconstructed Profile



The inverse Abel transform then consists of a set of known analytic integrals of the form

$$(7.44) \qquad I_i = \int_r^a \frac{y^{i-1}dy}{\sqrt{y^2 - r^2}}$$

The solution to this form of integral can be found in Gradhstein and Ryzhik[12] (§2.27, page 86 ) and the index profile can be reconstructed directly from

$$(7.45) \qquad n(r) = (-1/\pi) \; [\; 2\,a_2 I_2(r) + 4\,a_4 I_4(r) + \ldots\ i\,a_i I_i(r) \;]$$

For example, figure 7.14a the noisy fringe function fitted with an even power series up to 6th order. Figure 7.14b shows the theoretical precision of the resulting index profile measurement. The result is far more useful than that of fig. 7.12b and it can be calculated very quickly on the computer. This power series fitting method is applied to experimental fringe data in chapter nine.

The problem with this technique lies in the choice of functions used to fit the signal. There are many sets of functions that can be tried and it is up to the operator to decide the most useful. For example with extremely noisy data, only a 4th expansion should be used as the power series can begin to 'follow' the data and produce meaningless results. However such a low expansion may overlook some important trends in the signal and so great care must be taken when using this approach.

### 7.5.3 Fringe Fitting Procedure

The least squares fit procedure of the previous section provides insight into a useful way in which the profile can be reconstructed from the measured fringe shift. In chapter 4, the expected fringe patterns were calculated and found in terms of relatively simple functions. The most important of which were those produced by a change in the value of the gradient constant or a change in the offset of the profile. Which are respectively,

$$(7.46) \qquad S_1(y) = \left(\frac{2n_1}{3a^2}\right)\left(\frac{dA}{1-A}\right)(a^2 - y^2)^{3/2}$$

$$(7.47) \qquad S_2(y) = -2\,Dn\,(a^2 - y^2)^{1/2}.$$

We may consider fitting these functions to the measured fringe shift, and thus directly predict the values of A and dn. This a priori fitting technique may seem somewhat artificial and biased towards the results desired by the experiment. However we can attempt to justify it with the following argument:

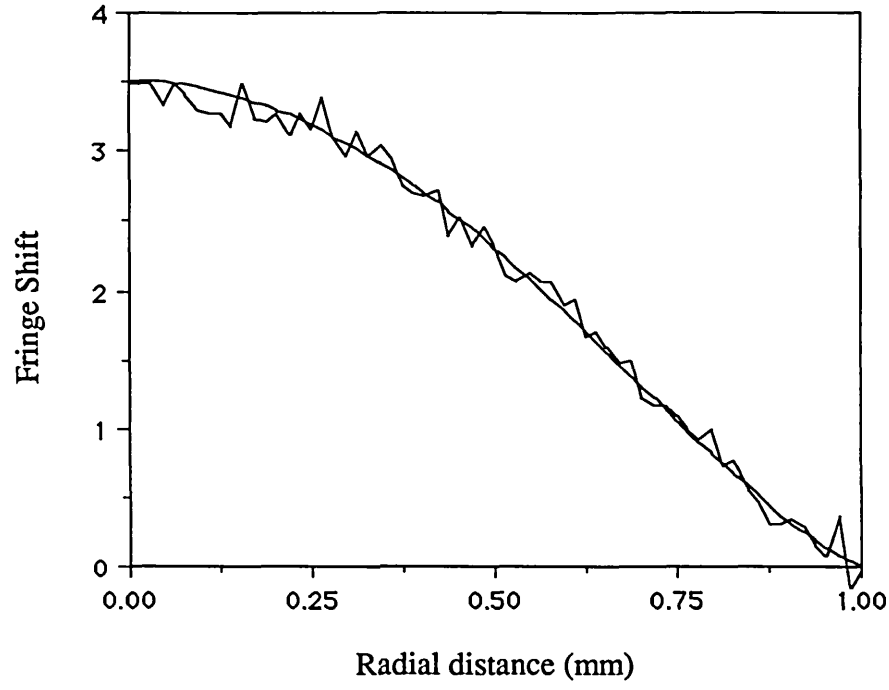
Firstly, we have already seen that unless we have a very accurate fringe fitting procedure, accurate inversion of the Abel transform requires some smoothing procedure. The results of which will be biased towards the chosen functions. Fitting the measured signal towards expected functions is perhaps more accurate than the use of other arbitrary functions. Furthermore, as the index profile information is usually desired in the form of knowing the parabolic strength of the index gradient and the absolute refractive index values, it is sensible to fit the Abel transforms of these functions to the observed fringe shift, rather than fit the functions directly to the (noisy) reconstructed index difference data.

Secondly, we must remember that the aim of the comparison method is to produce a fast and direct index profile assessment. The sensitivity of the comparison method is such that only closely matched profiles can produce a detectable fringe pattern. A profile that differs substantially from the expected form can be detected by observation of the fringe pattern alone (for example see the results of chapter 9). Thus it must be emphasised that this fringe fitting procedure can only be accurately used in tandem with the comparison method where we are certain of the parabolic form of the index profile in the standard rod.

To show the theoretical accuracy of the fitting technique, figure 7.15a. shows the equations 7.46 and 7.47 fitted to the noisy fringe data. From this fitted curve, $\sqrt{A} = ($ 0.2470) is estimated to be $\sqrt{A} \approx 0.2471$, which is obviously very close enough to the true value but perhaps not unexpected since we have assumed that both profiles are parabolic.

Figure 7.15: Profile reconstruction by fringe fitting with expected functions

a) Noisy fringe data fitted with expected functions




b) Error in the Refractive Index Values of the Reconstructed Profile

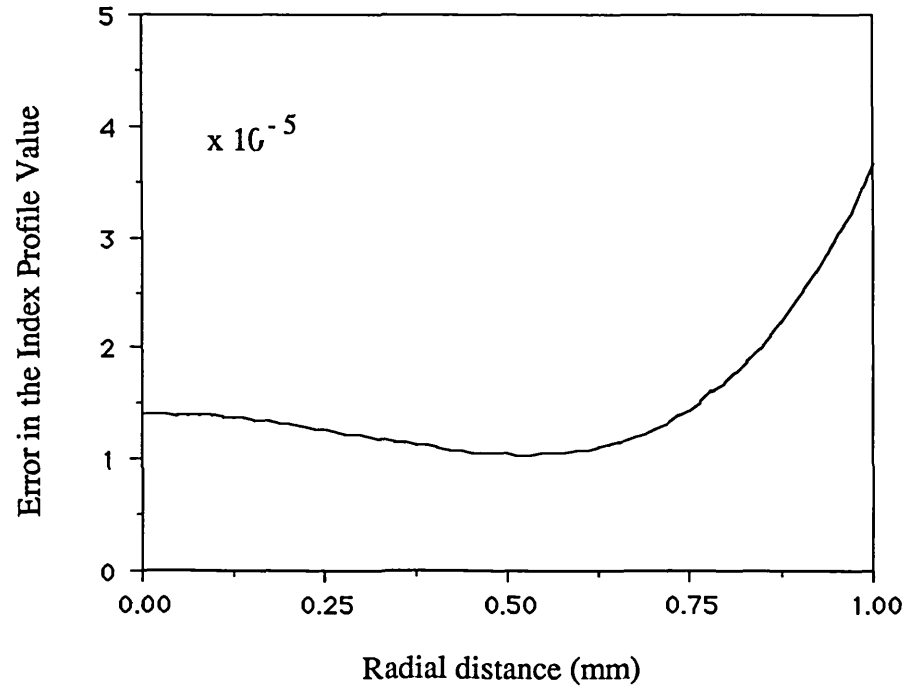


Figure 7.15b shows the theoretical difference between the calculated and measured values, from the figure, the precision of the index measurement is $\varepsilon n \approx 4 \times 10^{-5}$. Which is similar to the value calculated for profile reconstruction of the ideal fringe data. Note that the technique has also calculated a difference in the absolute index values between the profiles (which is zero in theory) of Dn = 0.00004.

At this stage, it is hard to calculate how well this method will hold up in a practical situation and we should be wary of relying on the computer simulation. Nevertheless, in chapter nine this method is used for assessing the profiles of several GRIN micro-lenses where it is particularly useful in that the differences in $\sqrt{A}$ and dn between the rod lenses can be estimated very quickly from the interferogram.

## 7.6 The Effect of Rod Diameter Variations upon Index Profile Reconstruction

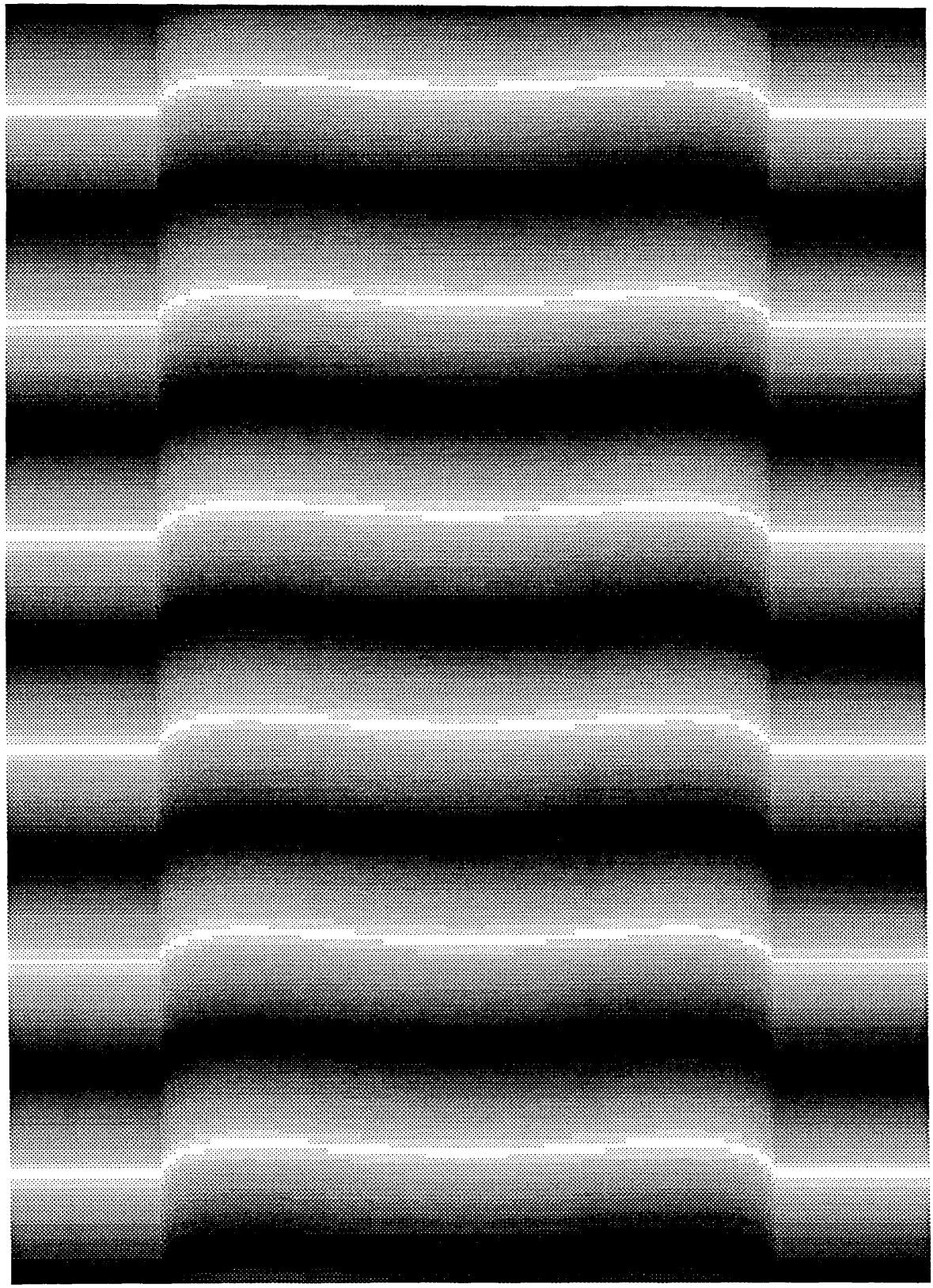
In this chapter, we have assumed that the rods undergoing the comparison test have had identical diameters. However as we have seen in chapter 4, a slight discrepancy between the rod diameters contributes fringes to the interferogram that can confuse the fringe analysis procedure.

Figure 4.8 (page 72), revealed the form of the interferogram produced by the comparison of two 2mm GRIN rods having identical profiles but with a diameter variation of 10 microns. If we overlooked the diameter change, and treated the fringe shift as corresponding to change in the index distribution, then we can calculate the apparent difference in the index values (using the inverse Abel transform or fringe fitting procedure). The reconstructed index difference (figure 7.16) is at most around $\varepsilon n = 5 \times 10^{-4}$ and the quadratic gradient constant of the unknown lens ($\sqrt{A} = 0.2500$) is estimated a: $\sqrt{A} = 0.2488$.

Figure 7.17 shows the theoretical interferogram produced by the comparison of two GRIN rods that have a 2 micron diameter difference. The reconstructed 'apparent' index difference is also plotted in figure 7.16, where $\varepsilon n = 1 \times 10^{-4}$ with $\sqrt{A} = 0.2498$ and Dn = 0.0001.

This last calculation is very important as it defines the practical accuracy of the

Figure 7.17: Theoretical interferogram :
A 2 micron change in the diameter of a 2mm rod lens

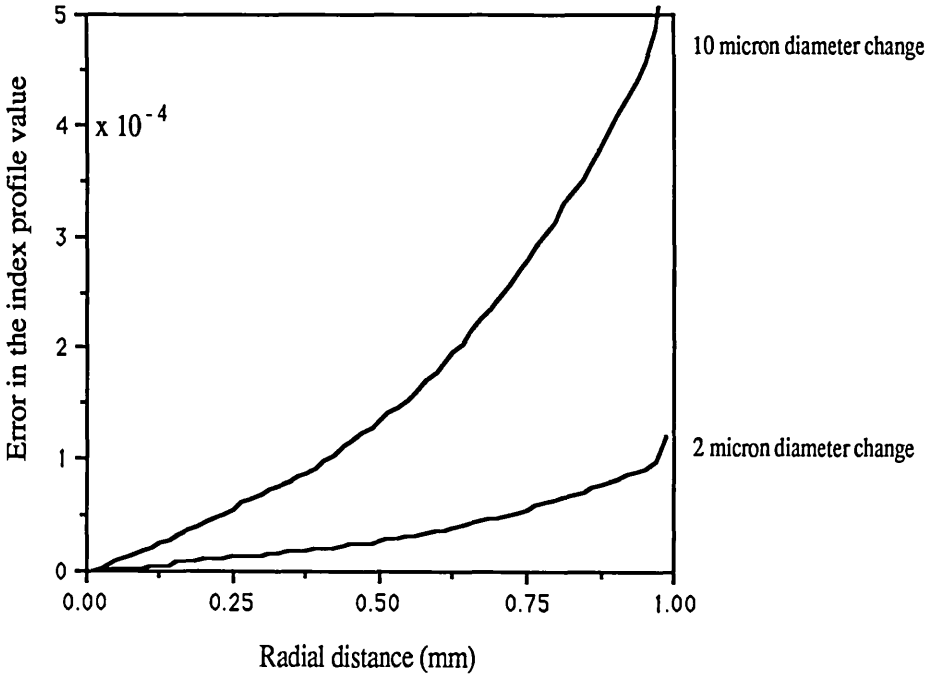


Rod 1 : $\sqrt{A}$ = 0.2500
Dn = 0.0000
Rod 2 : $\sqrt{A}$ = 0.2500
Dn = 0.0010

Matching oil index = 1.516
Diameter variation = 2 microns

comparison method when the rods under test have diameters all within 2 microns of each other. When we measure the profiles of rod lenses in chapter nine we assume a diameter variation of around 2 microns, and the precison of the index measurement is thus limited to $\varepsilon n \approx 0.0001$, correspondingly we quote $\sqrt{A}$ to four figures.

Figure 7.16: Profile Reconstruction Error for a GRIN Rod with a slight Diameter Variation



## 7.7 Summary

The refractionless limit is a valid and accurate approximation method that can be used both for calculating the theoretically expected fringe shift functions and also for reconstructing an unknown index profile. With ideal (noise free) data, the precison with which the index profile values of a GRIN rod can be measured using the comparison method is shown to be $\varepsilon n = 5 \times 10^{-5}$.

Although this figure could be improved upon with an algorithm that incorporates ray refraction, there is little point in attempting this in practice unless the dW/dy term in the Abel transform can be found with great accuracy. If the measured transverse wavefront W(y) contains noise, smoothing procedures are required to extract useful profile information from the interferogram.

Finally, the comparison of GRIN rods with slightly differing diameters gives rise to a fringe shift on the interferogram that is not necessarily related to a change in the index profile values. For 2mm GRIN rods with diameters within 2 microns, the precision of the index measurement is $\varepsilon n = 1 \times 10^{-4}$.

## REFERENCES

1) D. Marcuse, "Principles of Optical Fibre Measurements," Academic Press, 1979.

2) R.N. Bracewell, "The Fourier Transform and its Applications," McGraw-Hill, 1978.

3) E.W. Hansen and P. Law, "Recursive Methods for Computing the Abel Transform and its Inverse," J.O.S.A, 501, 1985.

4) E.W. Hansen, "Recursive Methods for Computing the Abel Transform and its Inverse", Software Distribution, Thayer School of Engineering, Dartmouth College, New Hampshire, USA.

5) M. Abromovitz and I.A. Stegun, "Handbook of Mathematical Functions," Dover Publications, New York, 9th edition 1972.

6) G.D.Kahl and D.C.Mylin, "Refractive deviation errors of interferograms", J.O.S.A 55, 364, 1964.

8) C.M.Vest, "Interferometry of strongly refracting axisymmetric phase objects", Appl. Opt. 14, 1601, 1974.

9) Y.Kokubun and K.Iga, "Precise measurement of the refractive index profile of optical fibres by a nondestructive method", Transactions of the IECE of Japan 60, 702, 1977.

10) J.Sochacki, "Accurate reconstruction of the refractive index profile of fibres and preform rods from transverse interferometric data", Appl. Opt. 25, 3473, 1986.

11) C.J. Tallents, M.D.J. Burgess and B. Luther-Davies, "The Determination of Electron Density Profiles from Refraction Measurements obtained using Holographic Interferometry," Optics Communications 44, 384, 1983.

12) I.S. Gradshteyn and I.M. Ryzhik, "Tables of Integrals, Series and Products," 4th Edition, Academic Press 1980.

13) M.Born and E. Wolf, "Principles of Optics," Pergamon Press, Sixth edition, 1980.

# CHAPTER EIGHT

## RESULTS:
## HOLOGRAPHIC SHEARING INTERFEROMETRY

Refractive index profiling via the technique of shearing interferometry was described towards the end of chapter two. A holographic interferometer can be used to measure the profiles of GRIN rods using a shearing technique, and indeed Chu[1] describes a double exposure ('frozen' fringe) method. The holographic system used in this work can also be applied to shearing interferometry using a relatively simple 'live'fringe technique. We must note then that the holographic interferometer can thus be used to establish the profile of the 'standard' rod required for the comparison method.

### 8.1 Experimental procedure for the shearing method

In the shearing method, the rod under test is placed in the optical cell of the interferometer, illuminated with a plane wave and the transmitted wavefront is stored in the hologram as usual. Upon reconstruction of the wavefront, the rod is re-illuminated and displaced by a known distance (S) across the optical axis so that a live fringe shearing interferogram is observed at the observation plane (§4.6.1). The form of the fringe is (from eq. 4.18)

$$(8.1) \qquad S_3(y) = S \frac{dW(y)}{dy}$$

and for a parabolic profile this has the form (from eq. 4.19)

$$(8.2) \qquad S_3(y) = \left( \frac{2n_1 A}{a^2(1 - \frac{1}{2}A)} \right) (y\ S)\ (a^2 - y^2)^{1/2}$$

In the shearing methods, the index profile can be reconstructed from (eq. 7.2)

$$(8.3) \qquad n(r) - n_{oil} = \left(\frac{-1}{\pi S}\right) \int_{r}^{a} \frac{S_3(y)\, dy}{\sqrt{y^2 - r^2}}$$

This expression is extremely useful because it implies that the profile can be reconstructed from the fringe pattern without the troublesome need to differentiate the data. For this reason, there is no need to use fringe smoothing techniques described in the previous chapter and the profile can be calculated directly using the chosen Abel inversion alogorithm. Apart from this computation, the accuracy of the shearing method is limited by the fringe measurement system and the precision of the shearing displacement. This latter point is particularly interesting, because it implies that the translation of the rod must be reliably known to less than 1 micron.

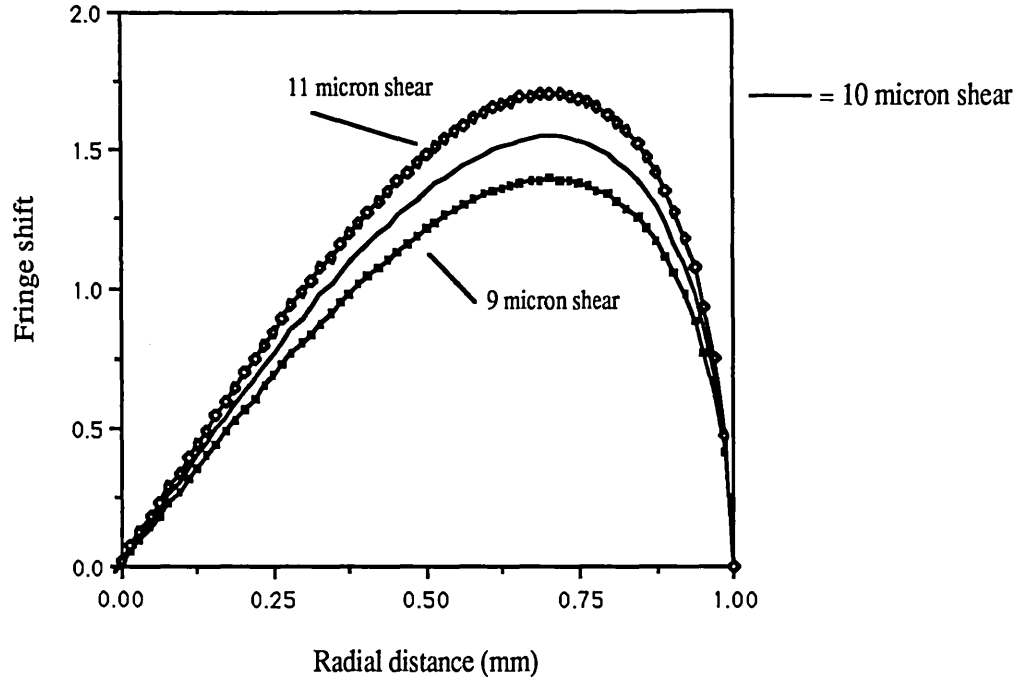
For example, figure 8.1 shows the expected fringe shifts for 2mm GRIN rod ($\sqrt{A}$ = 0.2500) with shearing displacements of 9,10 and 11 microns (calculated from equation 4.19). An error in the reconstructed profile can easily arise if we associate an observed fringe shift with an incorrect shearing distance $S_{error}$. From equation 8.3 we can show that the 'incorrect' reconstructed index profile is related to the 'true' profile by

$$(8.4) \qquad n_{(r)error} = \left(\frac{S_{true}}{S_{error}}\right) n_{(r)true}$$

For example, consider an index profile $n_{true}$ (defined by a gradient constant $\sqrt{A} = 0.25$), the correspondingly measured shearing fringe shift $S_3(y)$ for a 'true' shearing distance of $S_{true}$= 10 microns. If we had mistakenly measured the shearing distance as $S_{error} = 9$ microns then the strength of the index gradient is overestimated such that $\sqrt{A} \approx 0.262$ and $\varepsilon_n \approx 5 \times 10^{-3}$. Conversely for $S_{error} = 11$ microns, $\sqrt{A} \approx 0.238$ and $\varepsilon_n \approx -5 \times 10^{-3}$.

Thus we require precise knowledge of the shearing distance and unfortunately, this high tolerance could not be adeqately met with the rather cumbersome rod lens mounting arrangement (see figure 5.6). In the following sections then, we shall be satisfied in showing that the fringe shift has the expected form of equation 8.2 and also we will show the reconstructed profile remembering that there will be a possible scaling error in the index difference values.

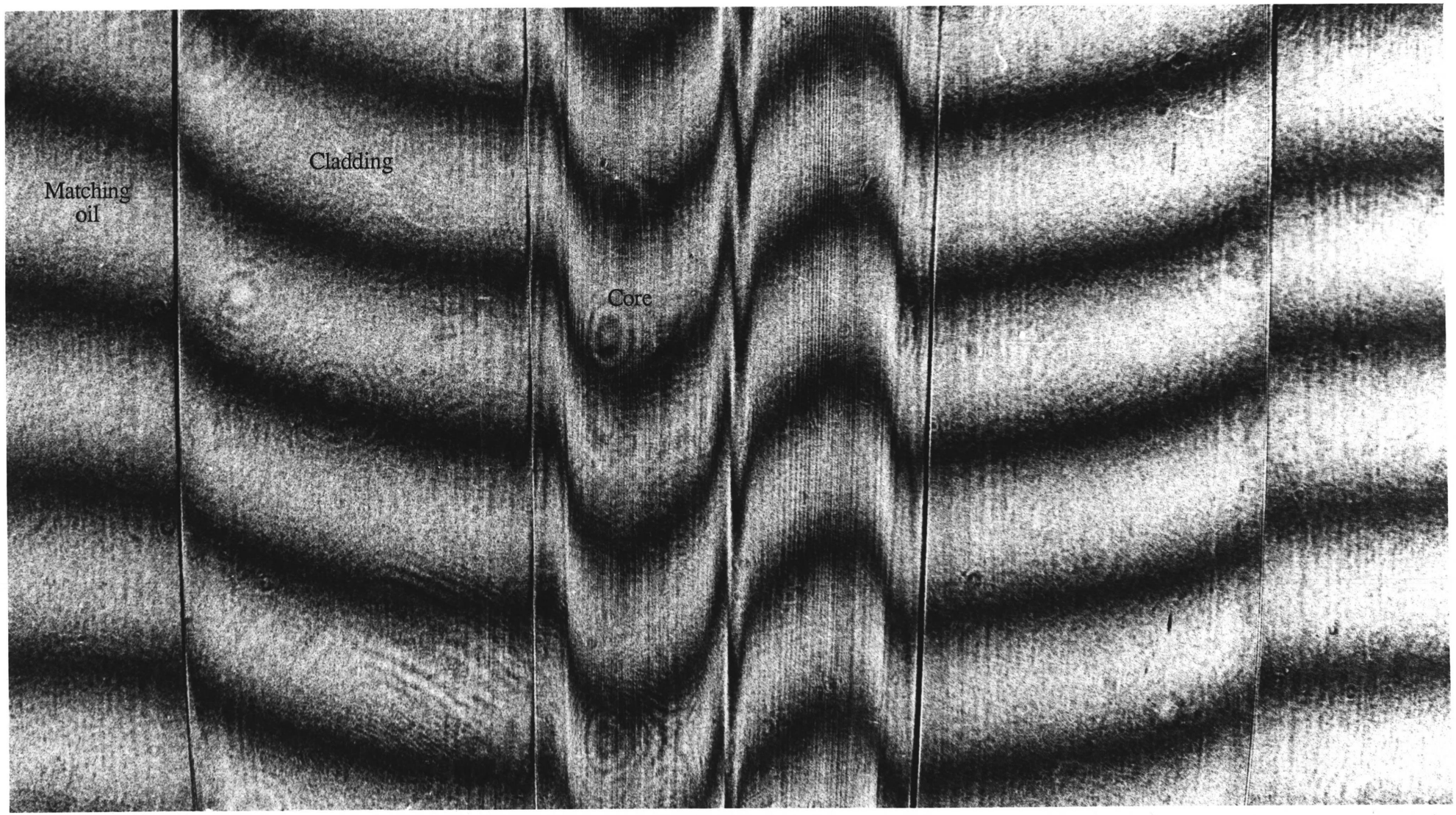
Figure 8.1: Dependence of the magnitude of the fringe shift upon the shearing distance




8.2 Results: BICC Ion Deposition Preform

Figure 8.2 is the experimental interferogram produced by the shearing method applied to a 16mm ion deposition type preform (§1.4.2) kindly supplied by BICC, Shepherds Bush, London. The pattern contains the characteristically asymmetric shape of figure 4.11. The discontinuities in the pattern also reveal the locations of fairly sharp changes in the index profile. This is to be expected in a deposition type preform where the profile consists of individual layers of glass, and there is also a cladding. The discontinuity at the centre of the rod corresponds to a sharp drop in the refractive index values at the position - this is characteristically referred to as the central index dip and it is produced when the preform is collapsed into a solid rod at the end of the deposition process. The slight curvature of the fringe at the oil - cladding region is indicative of a small change in the temperature of the index matching oil during the experiment. (There was no system of temperature control employed in the preform optical cell.)

Figure 8.2: Shearing interferogram : Ion deposition preform



8.3 Results: Pilkington ion stuffing preform

Figure 8.3 shows the shearing interferogram of a 6mm preform fabricated by a diffusion process (§1.4.1) referred to as the ion stuffing technique[2]. In this process, the homogeneous glass blank is chemically treated prior to the ion diffusion stage, so that it essentially changes state from a 'solid' glass rod into a porous glass sponge ('phase separation'). Upon immersion into the ion bath, ions can diffuse into the pores in the glass and this technique allows larger exchange ions to be used in the fabrication process than would otherwise be possible, this in turn yields a potentially higher change in the index values. After the diffusion process, the glass is returned to its normal state and a cladding is coated onto the rod.

The interferogram of figure 8.3 (shearing distance 10 microns) reveals a fairly sharp rise in the index values at the cladding-core boundary. The fringe shifts within the core of the preform are quite difficult to account for as they tend to indicate rapid index fluctuations in the core index profile and this is perhaps unusual for a diffusion type graded index rod. (More information will be revealed about the index profile of this preform by the comparison method in the next chapter). Figure 8.4a shows the fringe shift measured using the video digitiser and figure 8.4b shows the reconstructed index values (measured relative to the cladding index of 1.457). The profile is symmetrical because we have averaged the fringe shift measured for the left hand side and right hand side of the rod.

The profile of the rod was also measured using a preform profiler (P102 Preform Profiler , York Technology, Southhampton) operating upon the transverse refraction angle principle (§2.4.2). The resulting deflection function of the rod is shown in figure 8.5 and we recall that this can be directly related to the fringe shift of fig. 8.3 by equation 2.2; the patterns reveal similar discontinuities. The corresponding refractive index profile of the rod is shown in figure 8.6, and it can be compared with that in figure 8.4b.

Figure 8.3: Shearing interferogram : Ion stuffing preform

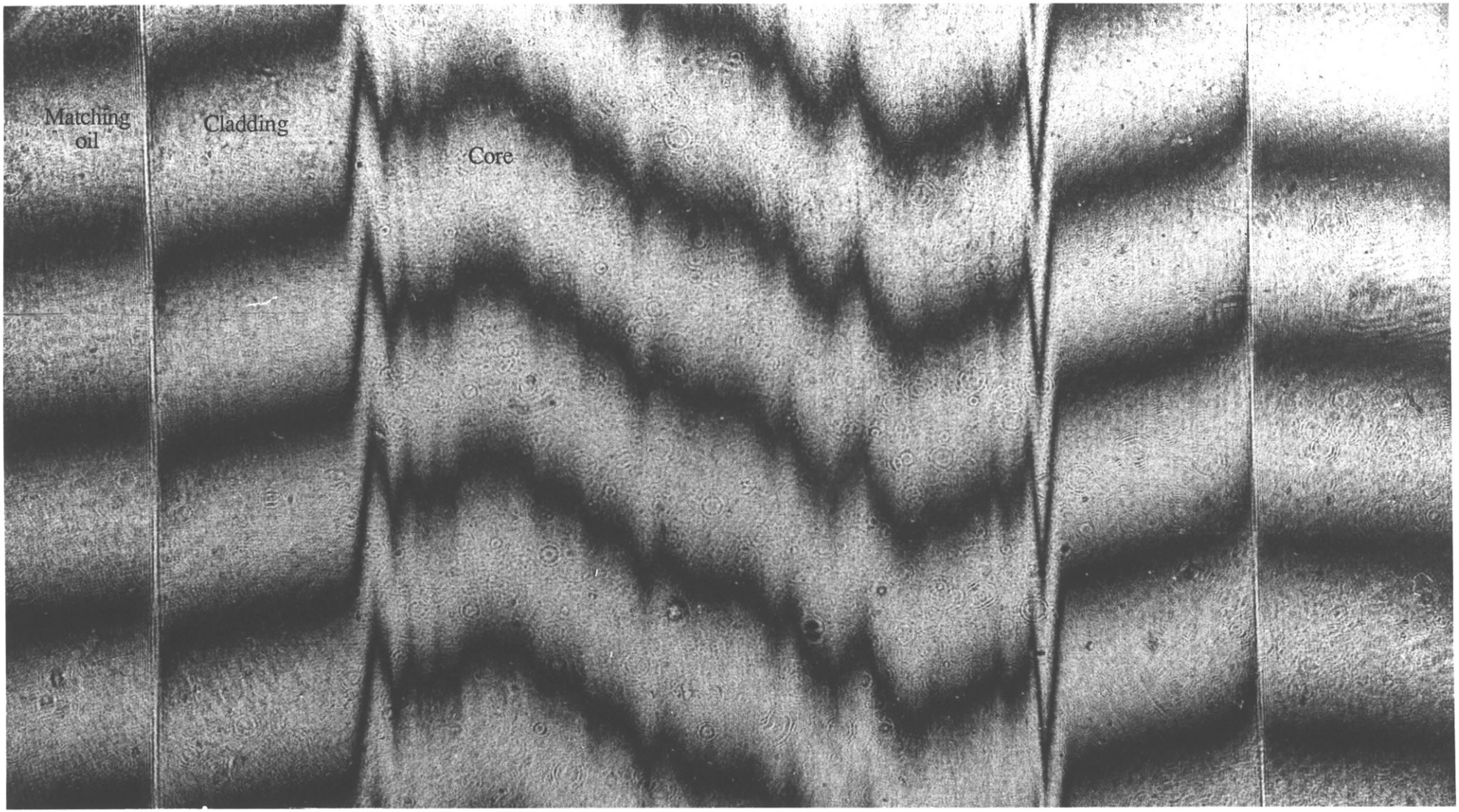
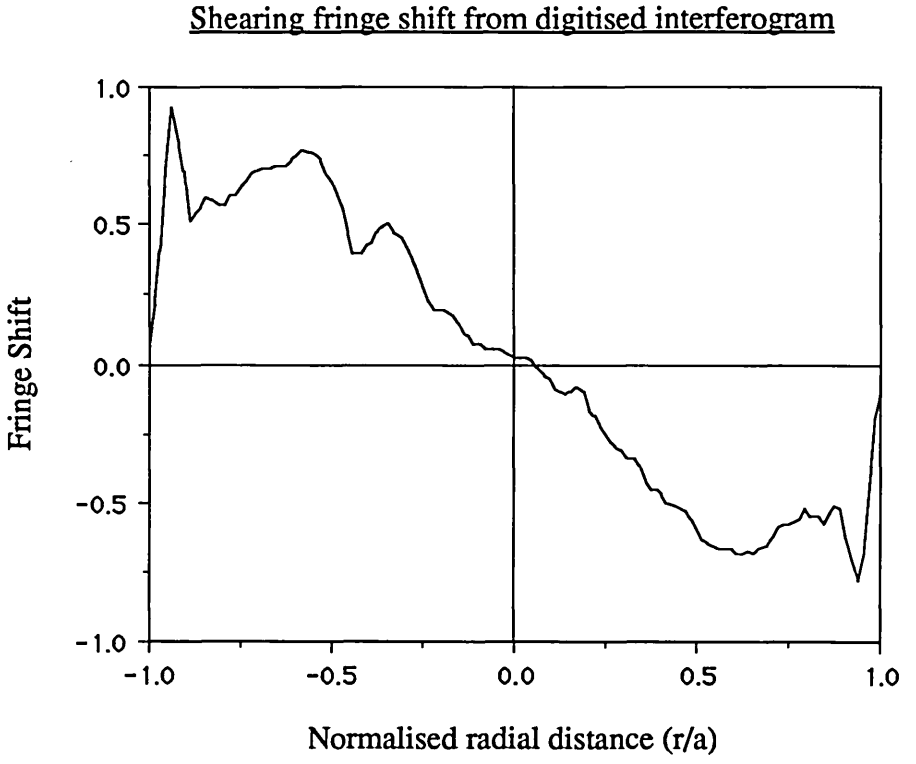


Figure 8.4: Refractive index profile of ion stuffing preform measured via holographic shearing interferometry

a)




b)

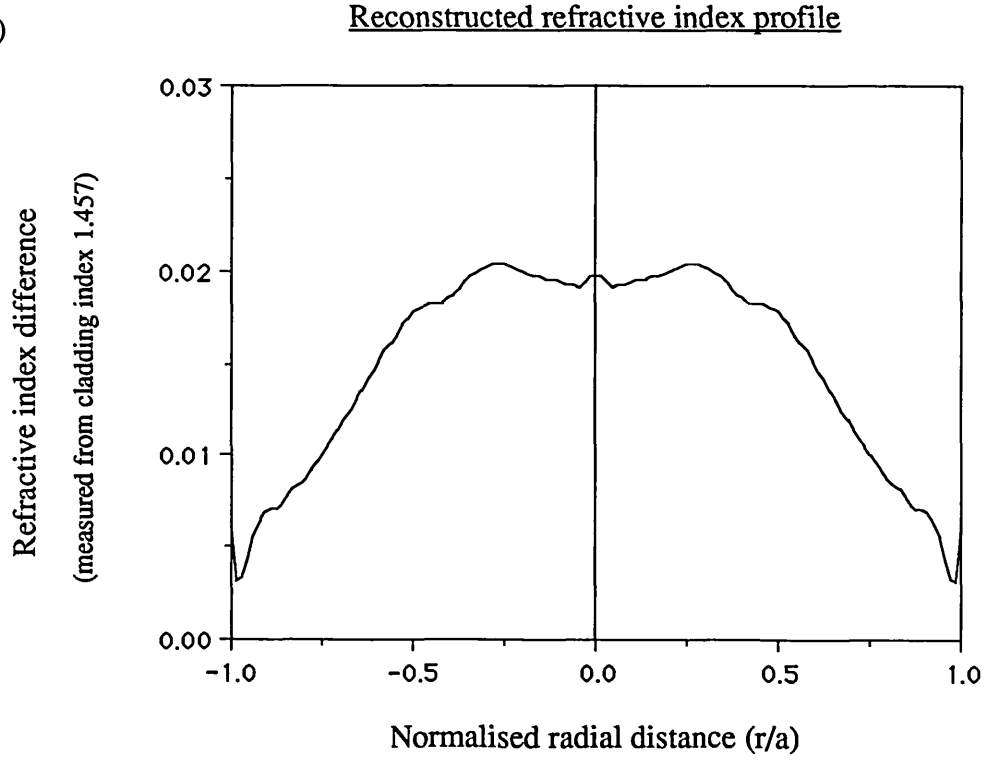


Figure 8.5;Deflection function of the ion stuffing preform measured by the transverse refraction angle method

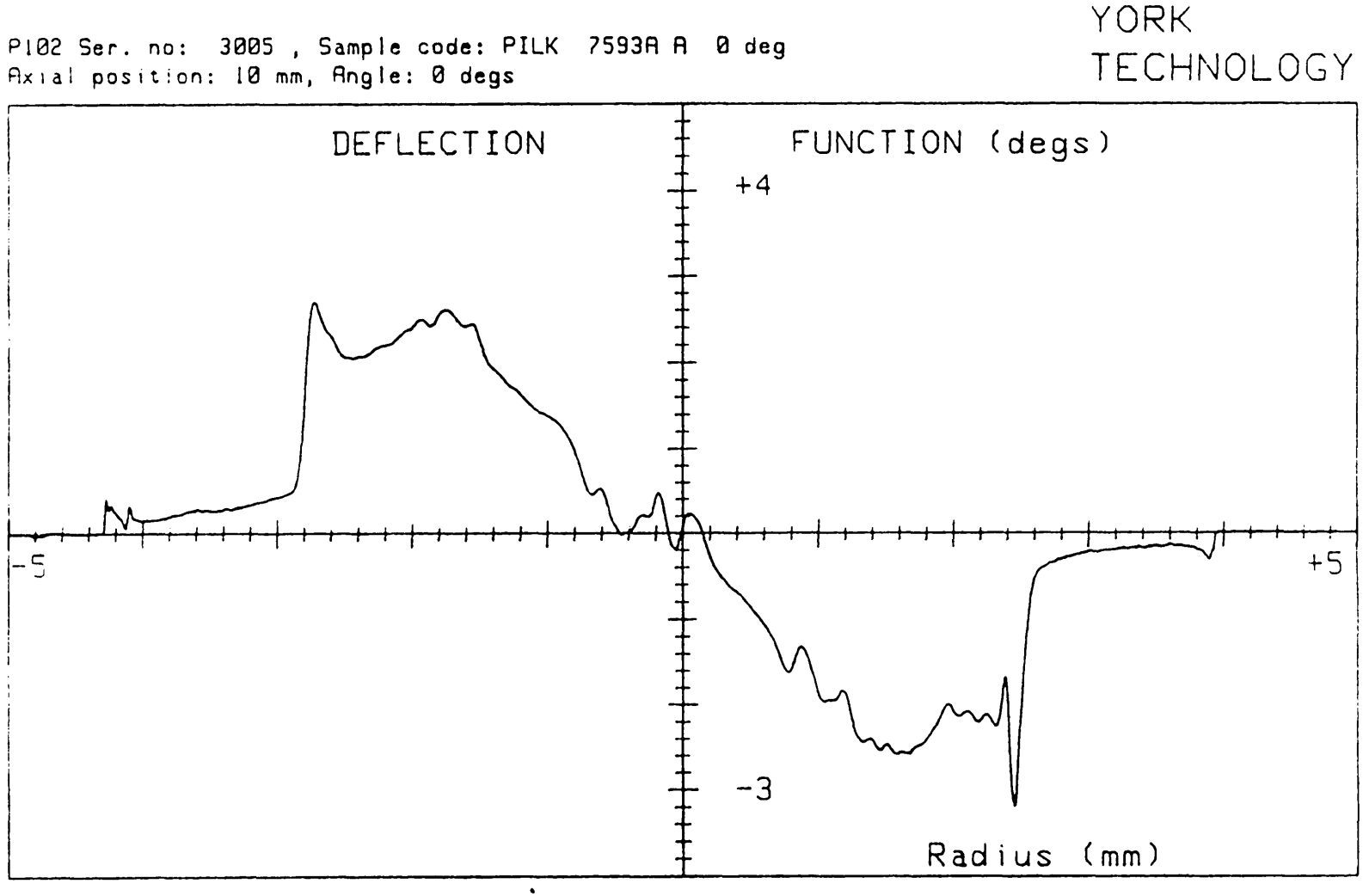
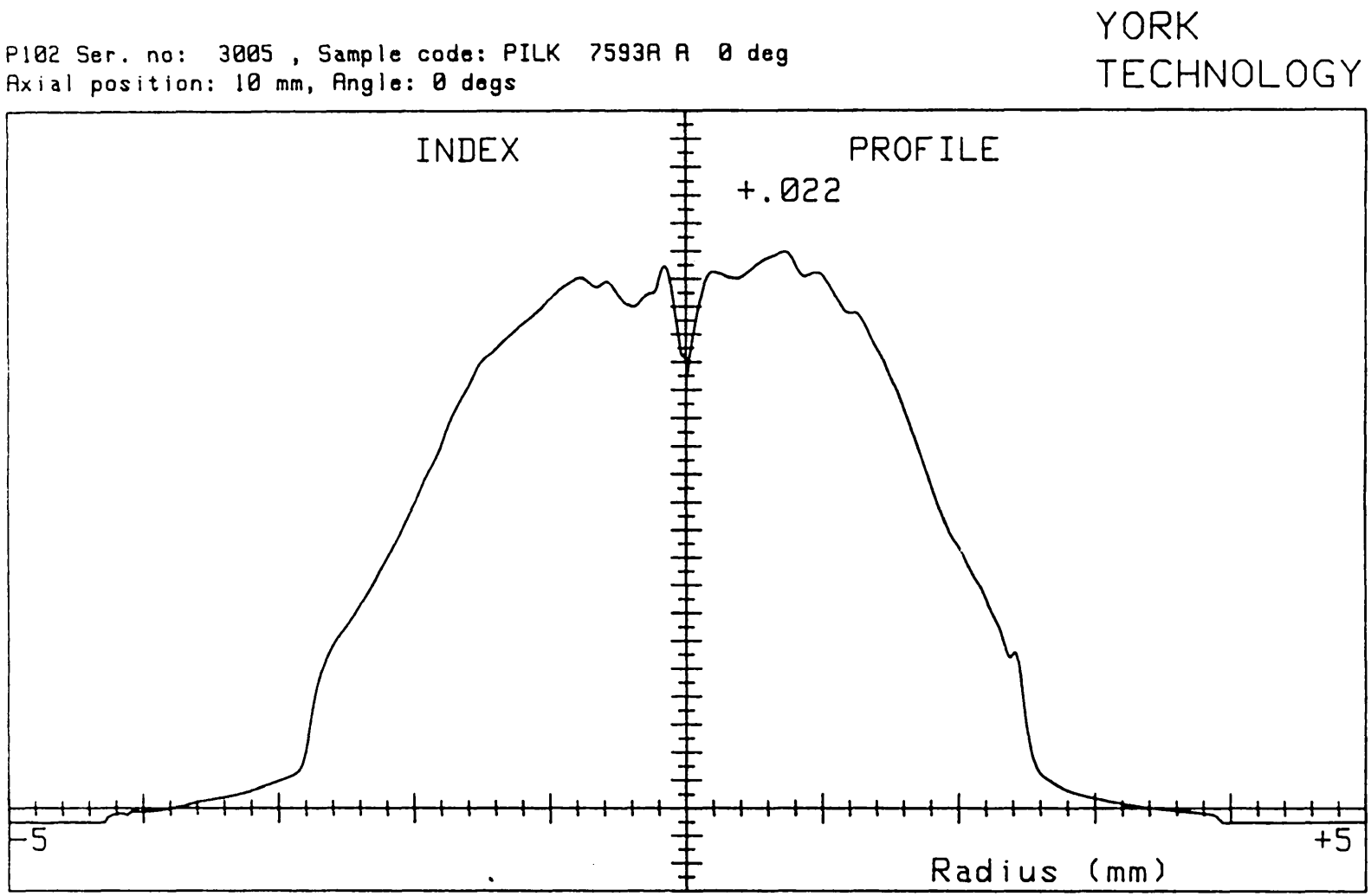


Figure 8.6:Refractive index profile of the ion stuffing preform calculated from the transverse refraction angle method



8.4 Results: Nippon Sheet Glass Company - Rod micro-lens

Figure 8.7 shows the shearing interferogram for a 2mm rod lens ($\sqrt{A} = 0.247$, $\lambda = 0.632 \times 10^{-3}$mm) supplied by the Nippon Sheet Glass Company of Japan and fabricated by the ion exchange method. The smoothness of the pattern highlights the absence of any sharp discontinuities in the index values of the profile (there is no cladding). Using a micrometer dial guage, the shearing displacement was measured to be around 10 microns (reading error estimated to be ± 2 microns at best). The digitised fringe centre is shown in figure 8.8a, and it can be compared with the corresponding theoretical interferogram of figure 4.11 on page 76. The reconstructed profile is shown in figure 8.8b. The quadratic gradient constant was calculated to be $\sqrt{A} = 0.25$ (from a least squares parabolic fit to the reconstructed profile). Because of the reading error, there is little point in quoting $\sqrt{A}$ to more than 2 decimal places. The value of $\sqrt{A}$ is close to the expected value, but more importantly, we have at least reconstructed the parabolic form of the index profile of the GRIN rod. Note that this data is quite smooth because we have avoided the differential step normally required in computing the inverse Abel transform.

Figure 8.7: Shearing interferogram : Graded index rod micro lens

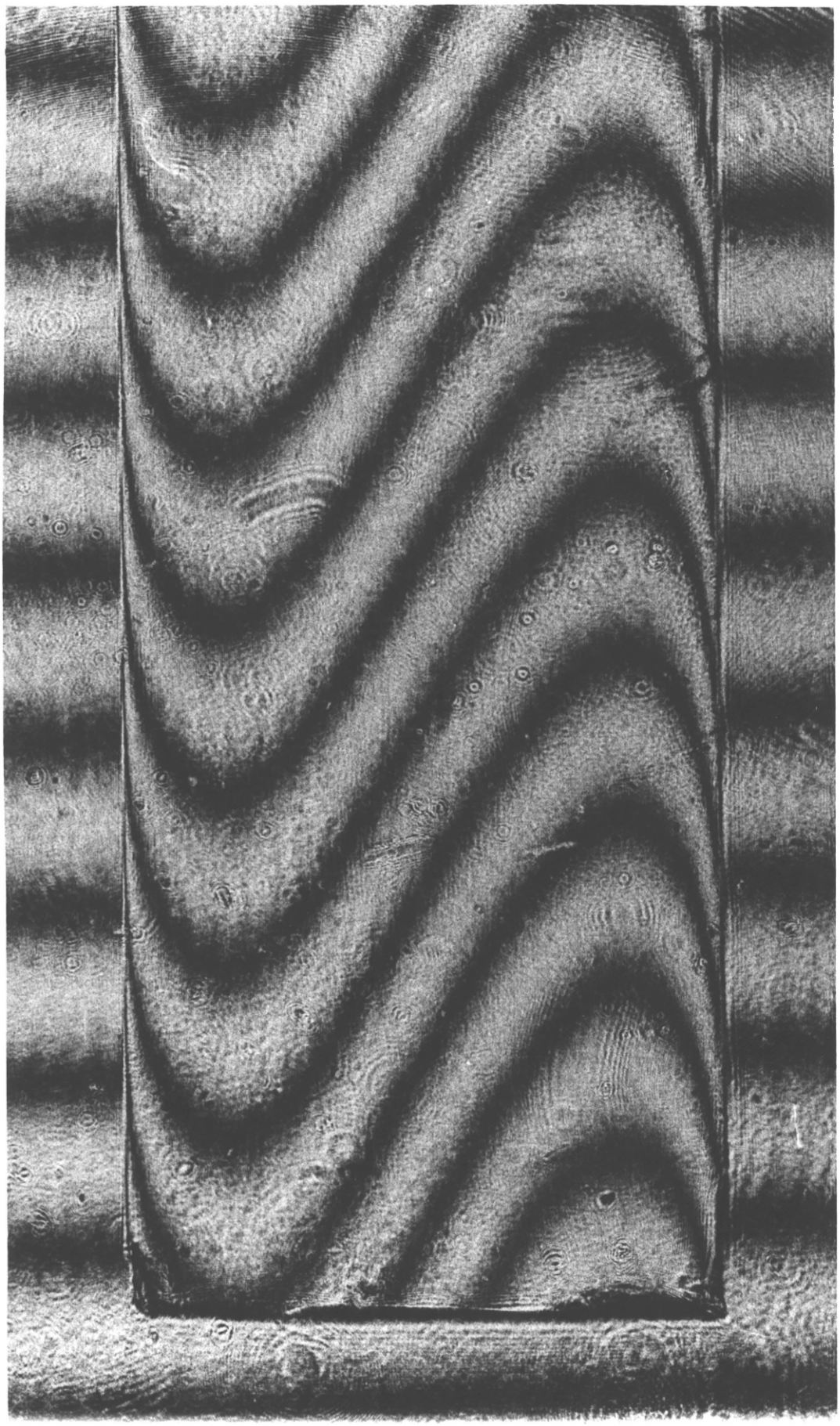
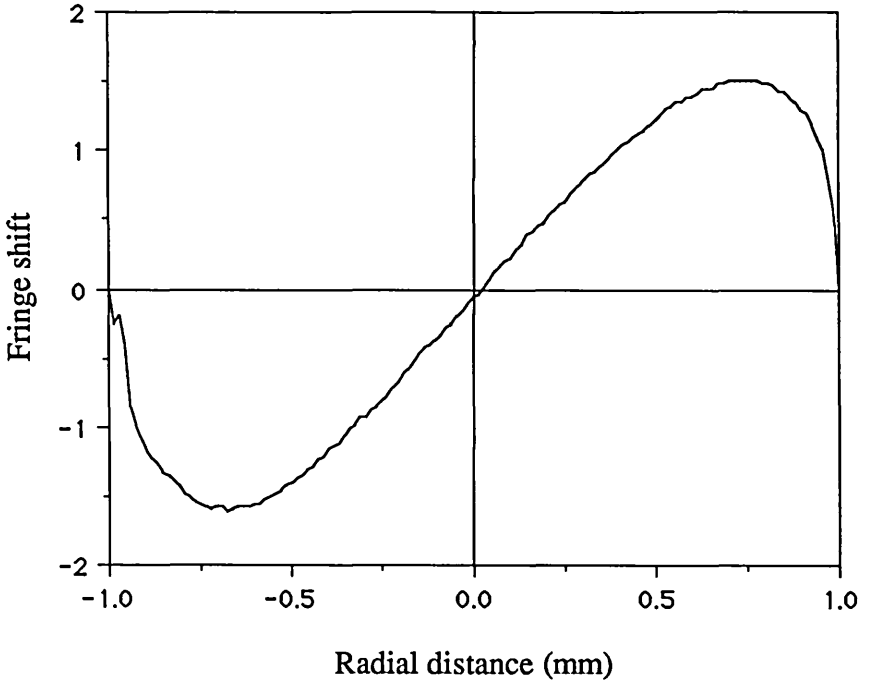
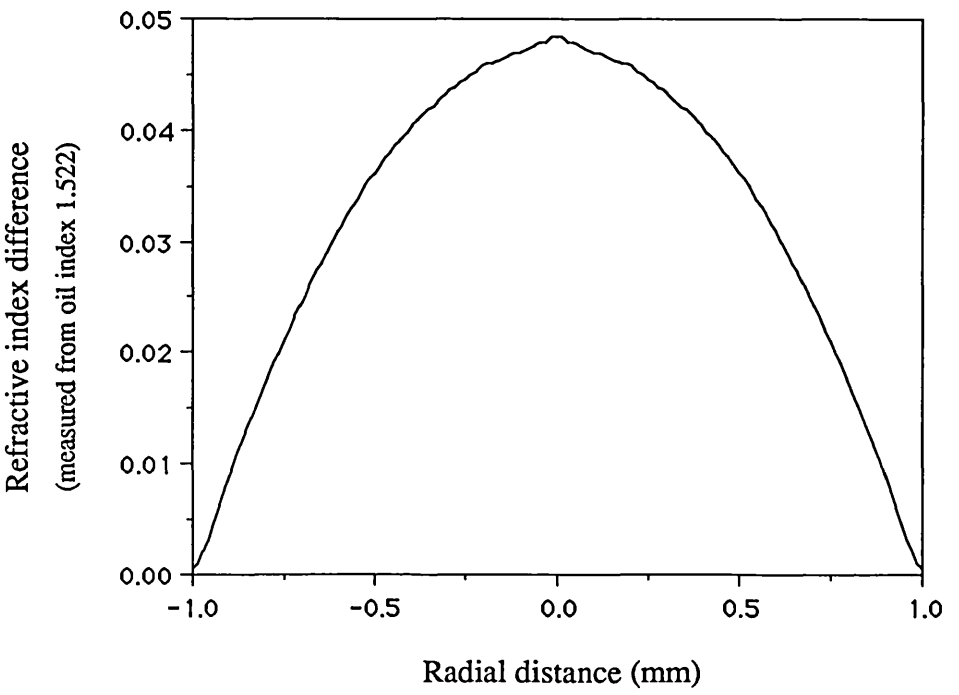


Figure 8.8 : Refractive index profile of a graded index micro-lens measured by holographic shearing interferometry

a) Fringe shift measured from shearing interferogram




b) Reconstructed index profile



## 8. 5 Summary

In this chapter we have seen how the holographic interferometer can be easily adapted to measure the index profile of an unknown GRIN rod lens via a shearing technique. The method could be used for making measurments upon large diameter GRIN rods, and is perhaps one of the only ways that the index distribution of preforms can be measured interferometrically.

In the reconstruction of the profile, there is no need to differentiate the measured data and the method would seem to be limited by the precision with which the shearing displacement can be measured. The GRIN rod mounting technique used in the apparatus was designed particularly for implementation in the comparison method and would need re-designing for a practical shearing method.

## REFERENCES

1) P.L. Chu, "Holographic measurement of the refractive index profile of an optical fibre preform," Electronics letters 16, 877, 1980.

2) D.T. Moore, "Gradient index optics: a review," Applied optics 19, 1035, 1980.

# CHAPTER NINE

# RESULTS:
# HOLOGRAPHIC COMPARISON INTERFEROMETRY

## 9.1 Introduction

In this chapter, we present the results of the comparison method applied to GRIN preforms and rod lenses. There are two types of comparative test that can be made upon a rod sample:

1) A control test, in which the wavefront emerging from the rod is compared with the wavefront emerging from the same rod at at different axial position or after a rotation about the rod axis.

2) A comparison test, in which the index distribution in the rod is compared to that in another rod having a similar index profile.

We must note that a failure of the control test for a certain class of GRIN rod will almost certainly imply that comparison testing between different rods of the same class will not provide useful results.

## 9.2 Results: BICC Ion deposition preform

Comparison testing of a 20 mm diameter, 1metre long preform was not easy using the apparatus that was principally designed for making measurements upon the very small (2mm diameter) rod-micro lenses. In particular, the sheer size of the rod made the very necessary tilt and translation adjustments awkward as the rod had to be suspended in a cantilever manner over the optical cell. Thus the following interferograms may contain fringes shifts that could perhaps be 'simplified' by further adjustments of the rod position however the general form of the fringe still indicate the types of index changes revealed when comparison testing a preform. Because of the uniformity of the index of the

Figure 9.1: Experimental interferogram - Ion deposition preform

Preform rotated about its axis by 90°

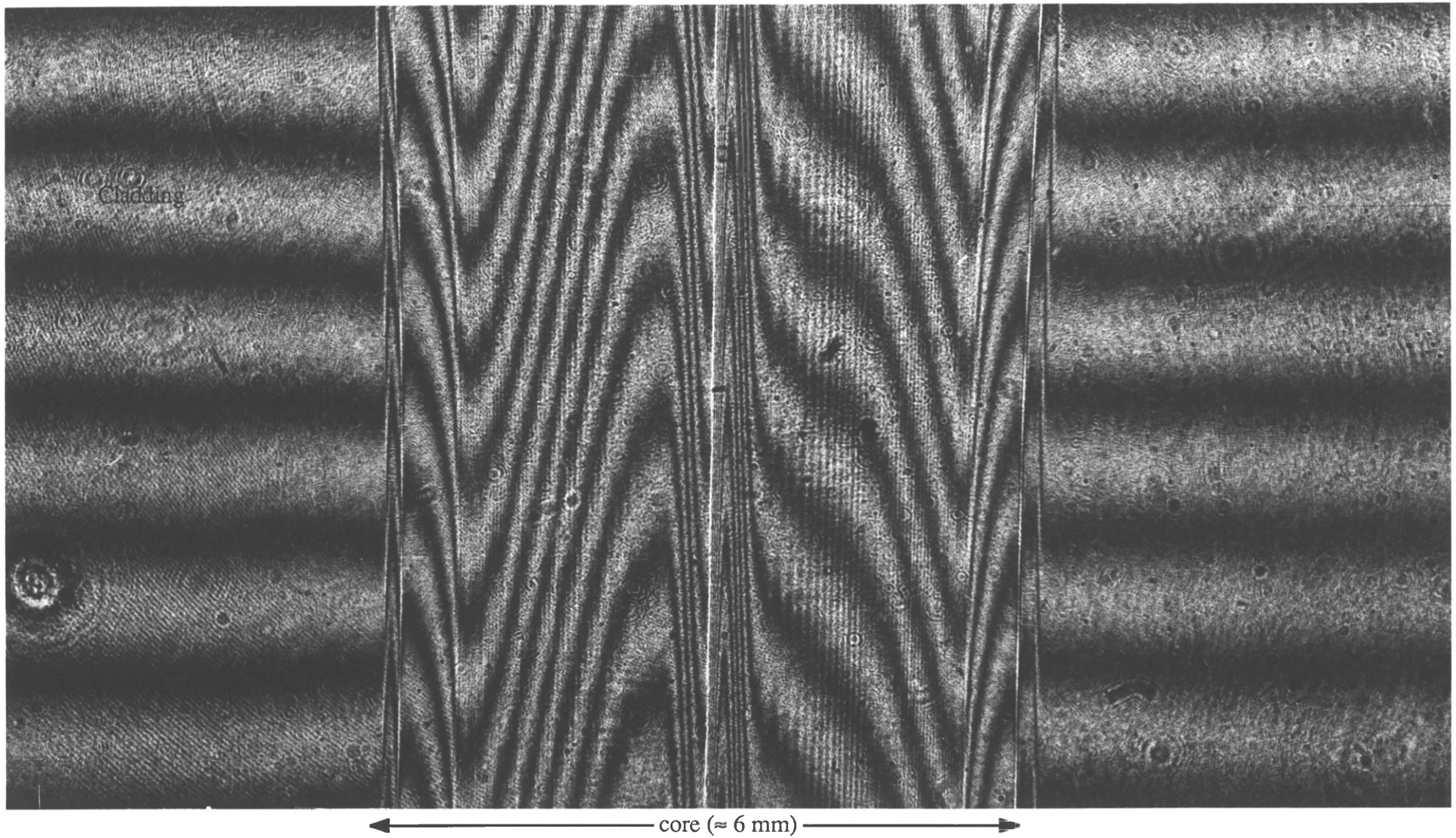
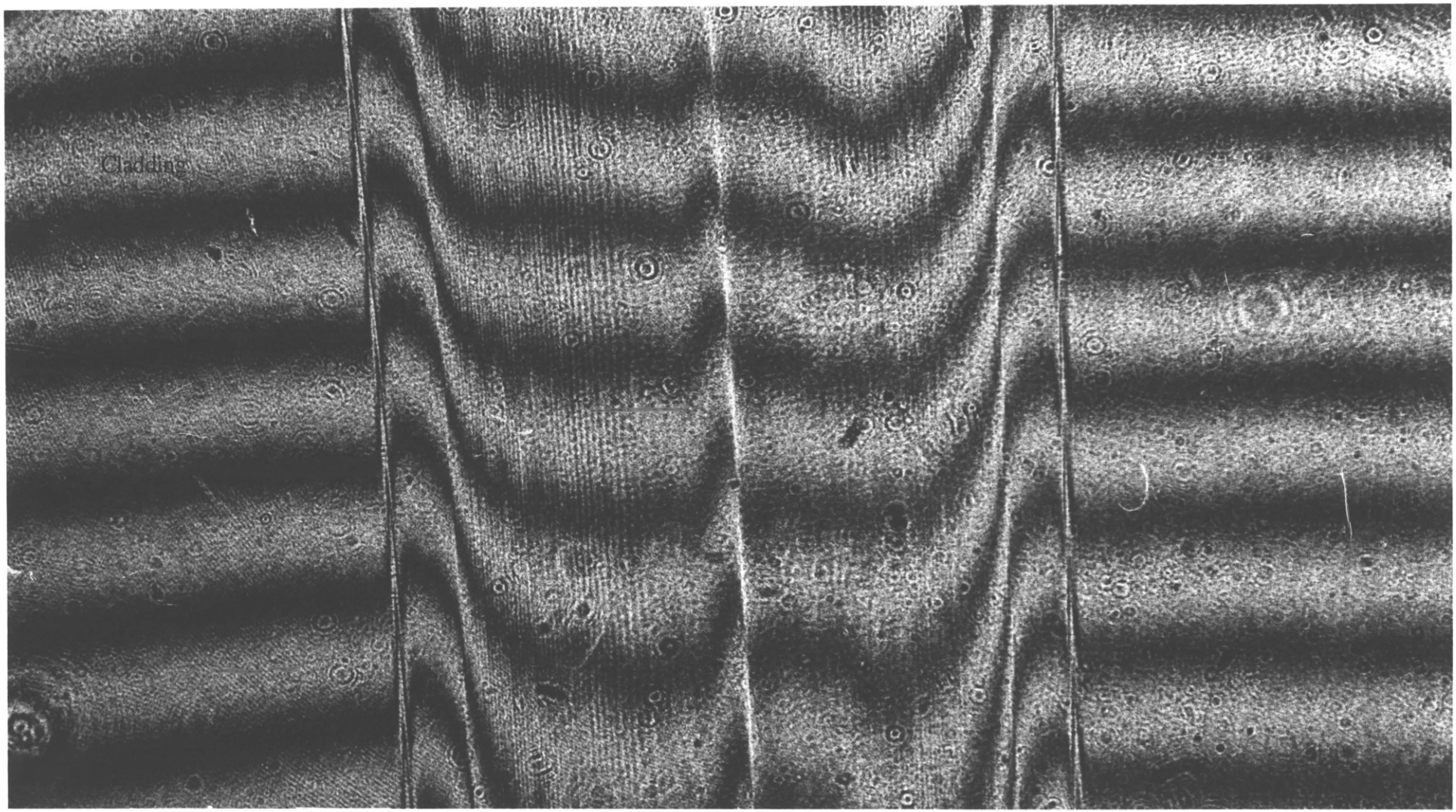


Figure 9.2: Experimental interferogram - Ion deposition preform

Preform displaced vertically by ≈ 10 mm



cladding, the interferograms presented in the following pages concentrate on the graded index core region of the preform rod which was estimated to be about 7mm in diameter. Only one preform rod was available for testing (they are quite valuable) and so testing different rods was unfortunately not possible. Thus we investigate the index distribution in the preform by using the control test to check for the circular symmetry and variation with rod length of the index profile of the rod.

Figure 9.1, is the interferogram produced after the preform had been rotated by 90° about its axis. There is quite a significant fringe shift, and it has a form similar to the theoretical pattern of figure 4.7 . The pattern reveals a lack of circular symmetry of the index distribution in the rod - this could be due to a combination of a slight ellipticity of the core region (diameter variation effect) and an asymmetry of the index profile (change of profile parameters $\sqrt{A}$ and Dn). It is hard to ascertain from the pattern which effect dominates and the assessment is further complicated by the discontinuities in the fringe at the edges and centre of the core.

The fringe shift towards the centre of the pattern is estimated to be around 5±1 fringes. From the analysis at the end of chapter 4, we have seen that only a slight variation in the index distribution is sufficient to produce quite a large fringe shift. For example, a 0.5% of the quadratic gradient constant ($\sqrt{A} = 0.2$) would produce a fringe shift of five fringes at the centre. These very slight changes in the index distribution are not particularly important when we consider that the rod is to be pulled and reduced in size by a factor of x 1000 but nevertheless, they are detected on the interferogram. The fringe pattern of figure 9.1 which reflects only minor changes in the index profile is perhaps just too complicated for the kind of simple, production line inspection desired in a comparison test.

Figure 9.2, is the interferogram produced by raising the rod 10 mm in the optical cell and this tests the axial variation of the profile. The pattern has the characteristic flattened 'M' (or 'W') form that indicates a change in the diameter of the rod (see figure 4.8, page 72). This is not surprising considering that the preform rod was analysed close to its tip where the rod is tapered in preparation for the drawing stage. Using the program in chapter

4, the change in rod diameter is estimated to be ≈ 25 microns.

9.3 Results: Pilkington Ion Stuffing Preform

In chapter 7, shearing interferometry applied to the ion stuffing type preform revealed discontinuties in the sheared fringe shift, and these were related to sharp changes in refractive index across the rod profile. We can further investigate the index distribution in these rods by using the comparison technique.

We can study the variation of the profile along the rod axis and with a rotation of the rod. Figure 9.3 shows the interferogram produced by rotating the rod by just 0.5 degrees about the axis. Several kinks can be observed across what should ideally be a straight fringe. Figure 9.4 shows the interferogram produced by a further rotation of the rod by 90 degrees. The pattern is practically indecipherable! Figure 9.5 shows the interferogram produced after the rod was raised by about 5mm - once again it is hard to come to any conclusions as to the nature of the index change represented by the fringe shifts.

In figure 7.3 in chapter 7, we showed the expected fringe patterns produced by the comparison of GRIN rods with a random error in the profile over a localised region - the pattern has the same kind of fringe fluctuations as in figures 9.3 - 9.5. Thus we can conclude that the profile of the rod is not smooth but must consist of fairly discontinuous changes in refractive index with little or no circular symmetry to the profile. Because these patterns were produced by the comparison of a test rod with itself, it is fairly obvious that the inter-comparison of several different rods is out of the question! This proved to be the case in practice where it was extremely difficult to even remove and replace a rod and re-establish a fringe pattern. Comparing different rods produced at best a pattern like figure 9.4 and at worst no resolvable fringes at all.

We may conclude from this section that the comparison technique cannot be applied to ion stuffing preform rods. However this does not necessarily negate the usefullness of such a test because the interferograms of figures 9.3 - 9.5 reveal important information about the nature of the index distribution in the rod. The index profile does not appear to

Figure 9.3: Experimental interferogram - Ion stuffing preform:
Preform rotated about its axis by 0.5°:

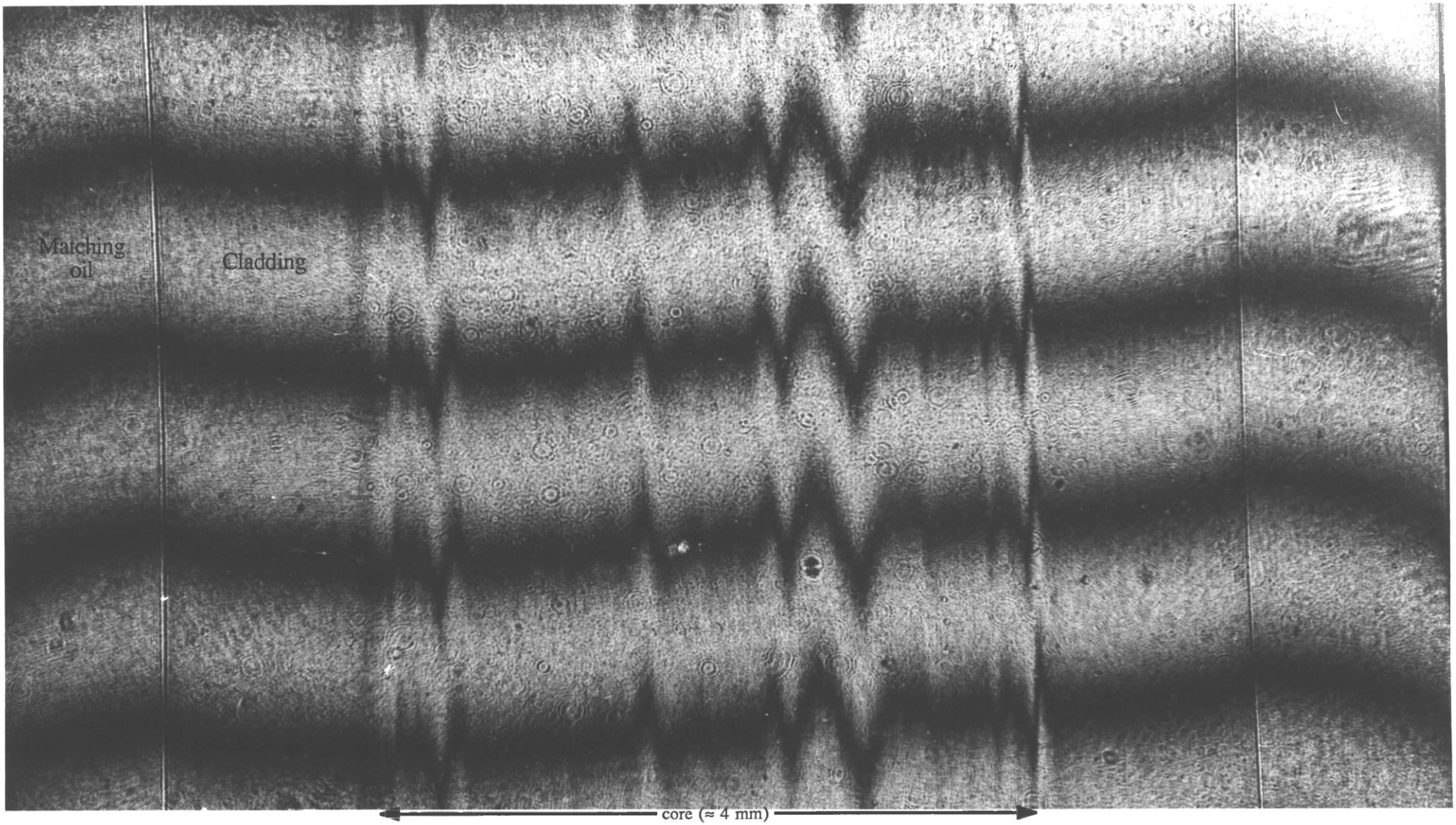


Figure 9.4: Experimental interferogram - Ion stuffing preform:
Preform rotated about its axis by 90°:

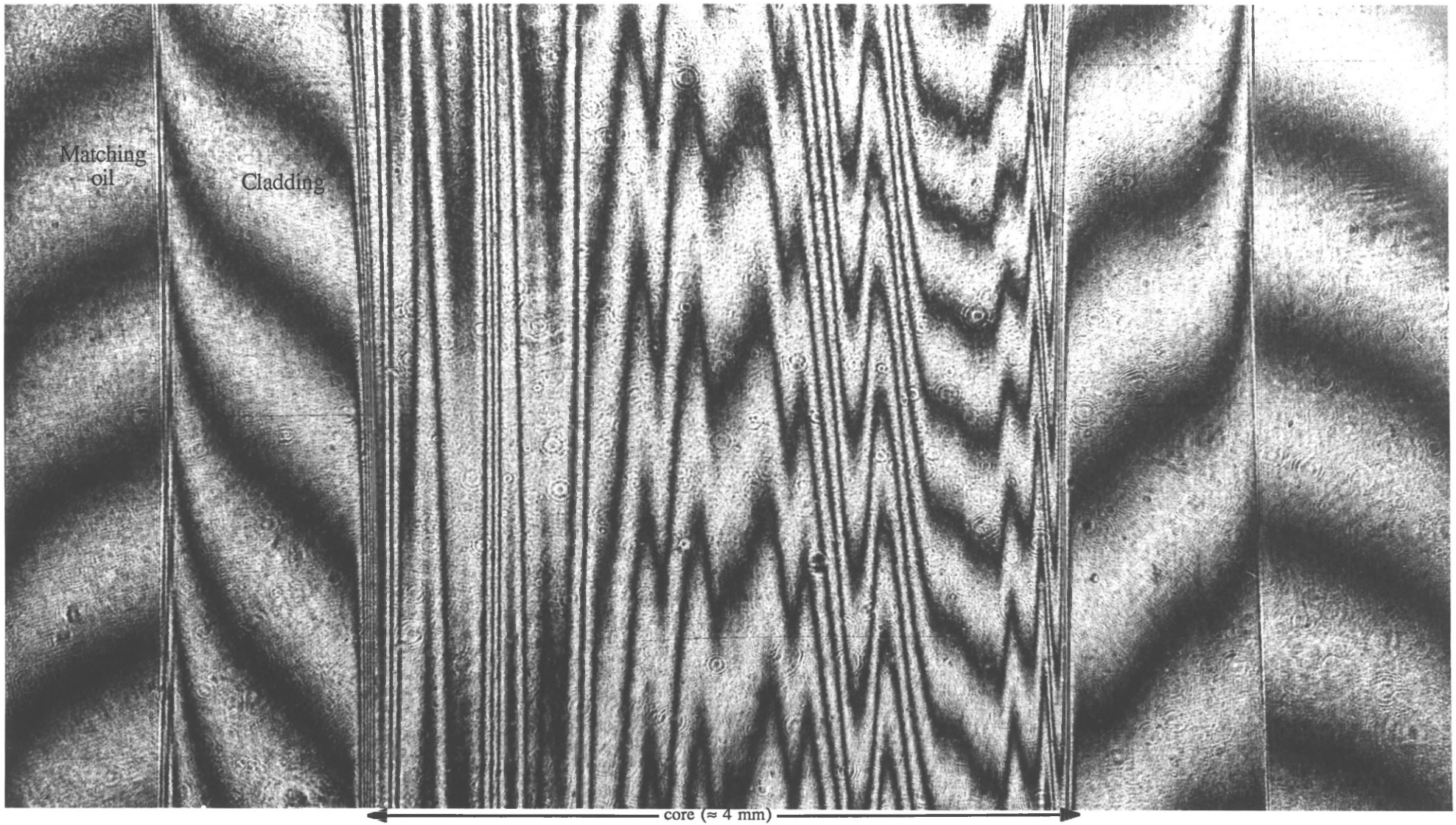
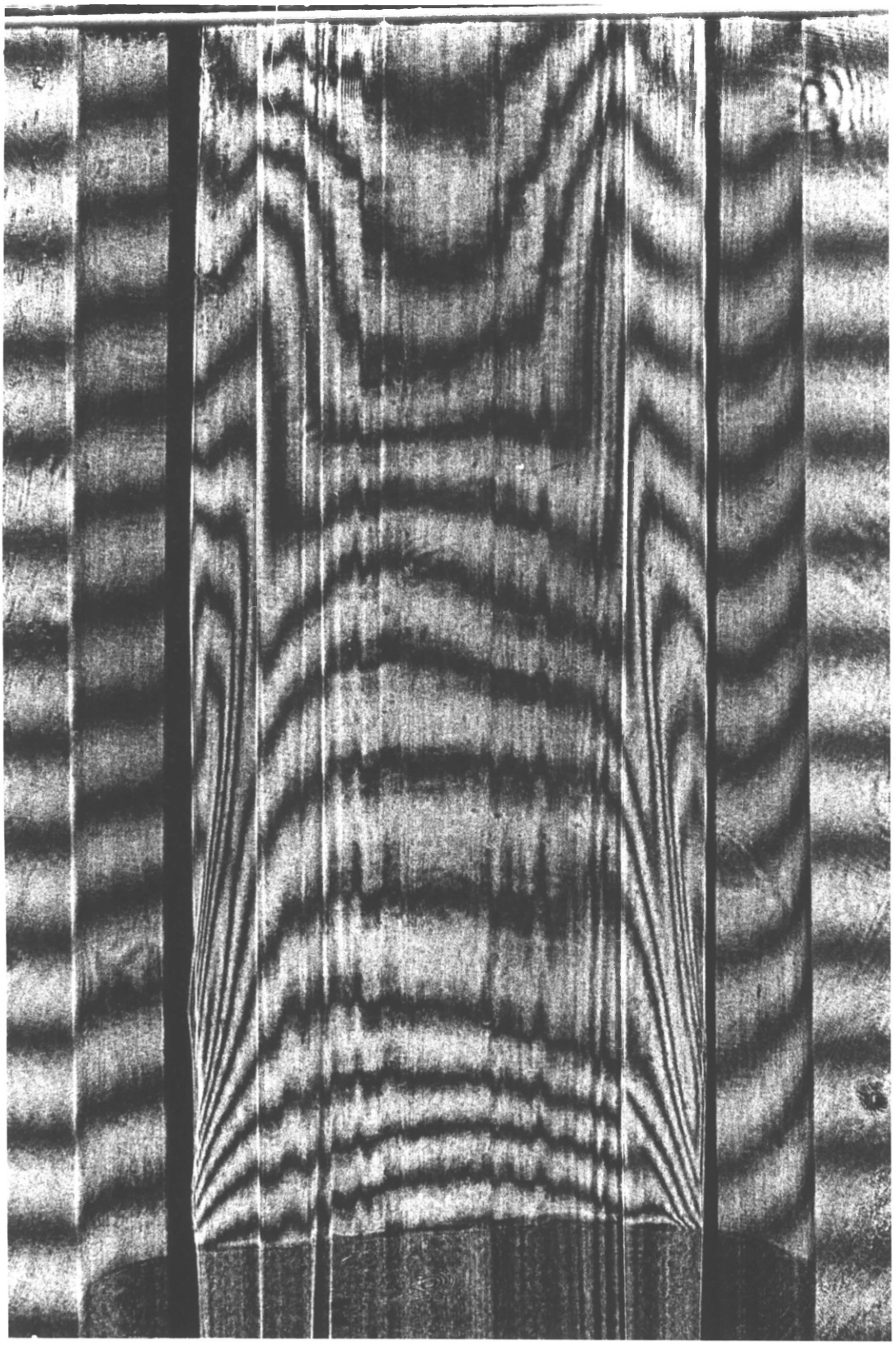


Figure 9.5: Experimental interferogram - Ion stuffing preform: Axial variation of the index distribution.



(Core ≈ 4mm)

have the smooth parabolic form required for a graded index element, and the profile varies sharply both with rotation and axial displacement. It is worthwhile considering whether such a rod can be used as a suitable GRIN transmission device, and evidently, the ion stuffing technique has fallen out of favour as a viable graded index fibre/lens material*.

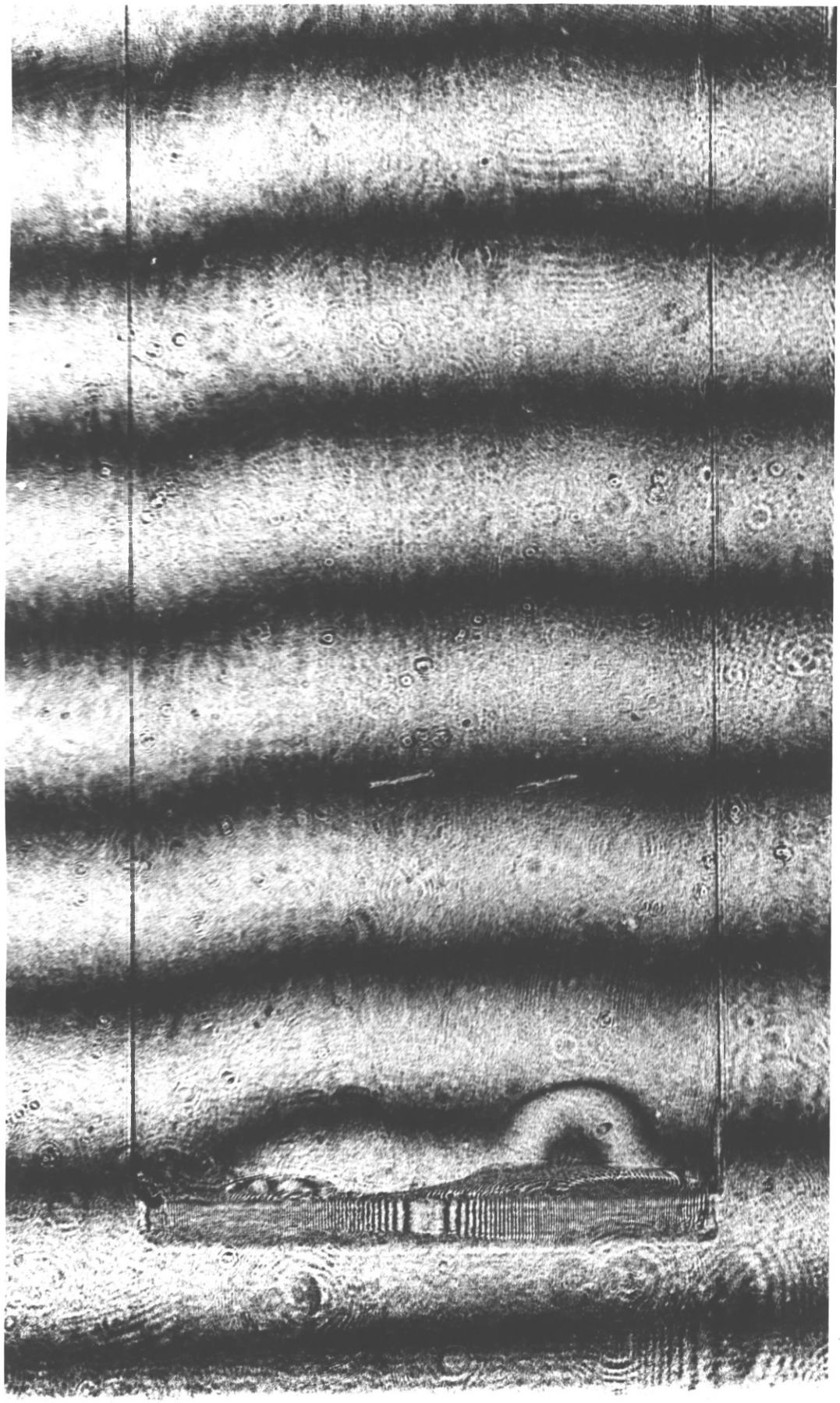
## 9.4 Nippon Sheet Glass Company - Rod Micro-Lens

We need now describe the comparison test applied to 2mm diameter GRIN rod micro lenses. In this section we must overlook the possible effects of diameter variations between different rods as no simple and satisfactory method for eliminating this problem could be established during the period of the research project. Some potential solutions to the problem are suggested in the conclusion of this thesis. Using an accurate vernier screw gauge micrometer the variation in diameter within a set of 25 rod lenses was found to be within $\pm$ 3 microns. This is a surprisingly high tolerance for a manufactured glass rod sample, and apparently, it is achieved by cutting the set of lenses from one long length of a precision drawn glass rod. We have seen in chapter 7 that the effect of a 2 micron diameter change is to introduce a fringe shift of around a tenth of a fringe (see figure 7. ) and ultimately the precison of the index measurement is limited to $\varepsilon n \approx 1 \times 10^{-4}$. In the following analysis, we shall assume a possible diameter variation of 2 microns and thus we can only quote the the refractive index values to at the most 4 decimal places.

We have already seen the control test applied to a GRIN lens in chapter 6, where we considered the problem of removing and replacing a rod into the optical cell as a basis for any modifications to the design of the holographic interferometer. The chapter showed that a rod sample could be replaced and re-aligned in the optical cell by adjusting the rod and monitoring the fringe pattern until it has a simple form. The smoothness of the fringes in the interferograms revealed the absence of any sharp discontinuities in the index profile. Figure 6.10 (page 125) was the resulting pattern after a rod had been removed and replaced

*(D.T. Moore, University of Rochester, USA - personal communication).

Figure 9.6: Experimental interferogram - Graded index rod lens: Comparison of rods produced within the same production lot.



at a random orientation and the straightness of the fringes along the length of the pattern shows the remarkable circular symmetry of the profile and it s uniformity along the length of the rod.

Satisfied with such a control test, comparison measurements could be made between different rod lenses. Over the period of the research project, three different sets of GRIN lenses were obtained from the Nippon Sheet Glass Company at yearly intervals. We shall label these different sets A, B and C and they all have the same nominal specification data of 2mm diameter and $\sqrt{A} = 0.247$ at $\lambda = 0.632$ μm.

### 9.4.1 Comparison of rods produced within the same production lot

The first test is to compare two rod lenses from within the same production lot. Figure 9.6 is the comparison interferogram of two rod lenses from set A. The tilt fringes are relatively straight, however they appear to contain the flattened 'M' shape that we associate with a diameter variation. For example, the experimental fringe pattern compares well with figure 7.17 on page 160 which is the theoretical interferogram for a 2 micron rod lens diameter variation. Otherwise, the straightness of the fringes shows that index profiles of the rods are very similar, certainly within the tolerance of the fabrication process. This information is revealed directly from the pattern and would thus be ideal for a production line inspection of a GRIN rod.

### 9.4.2 Comparison of rods from seperate production lots

We now compare the index distributions in rod lenses produced from different production lots. We shall assume the profile constants of sample set A to be $\sqrt{A} = 0.2500$, $n_1 = 1.522$ at $\lambda = 632$ nm and we shall attempt to quantify the difference in the index distributions of the three rod lenses. We shall use the reconstruction procedures described towards the end of chapter seven (§7.5). In the following experimental interferograms, a vertical fringe shift corresponds to an increase in optical pathlength and hence the index values for the rod under test.

Figure 9.7: Experimental interferogram - Graded index rod lens: Comparison of rod samples A and B.

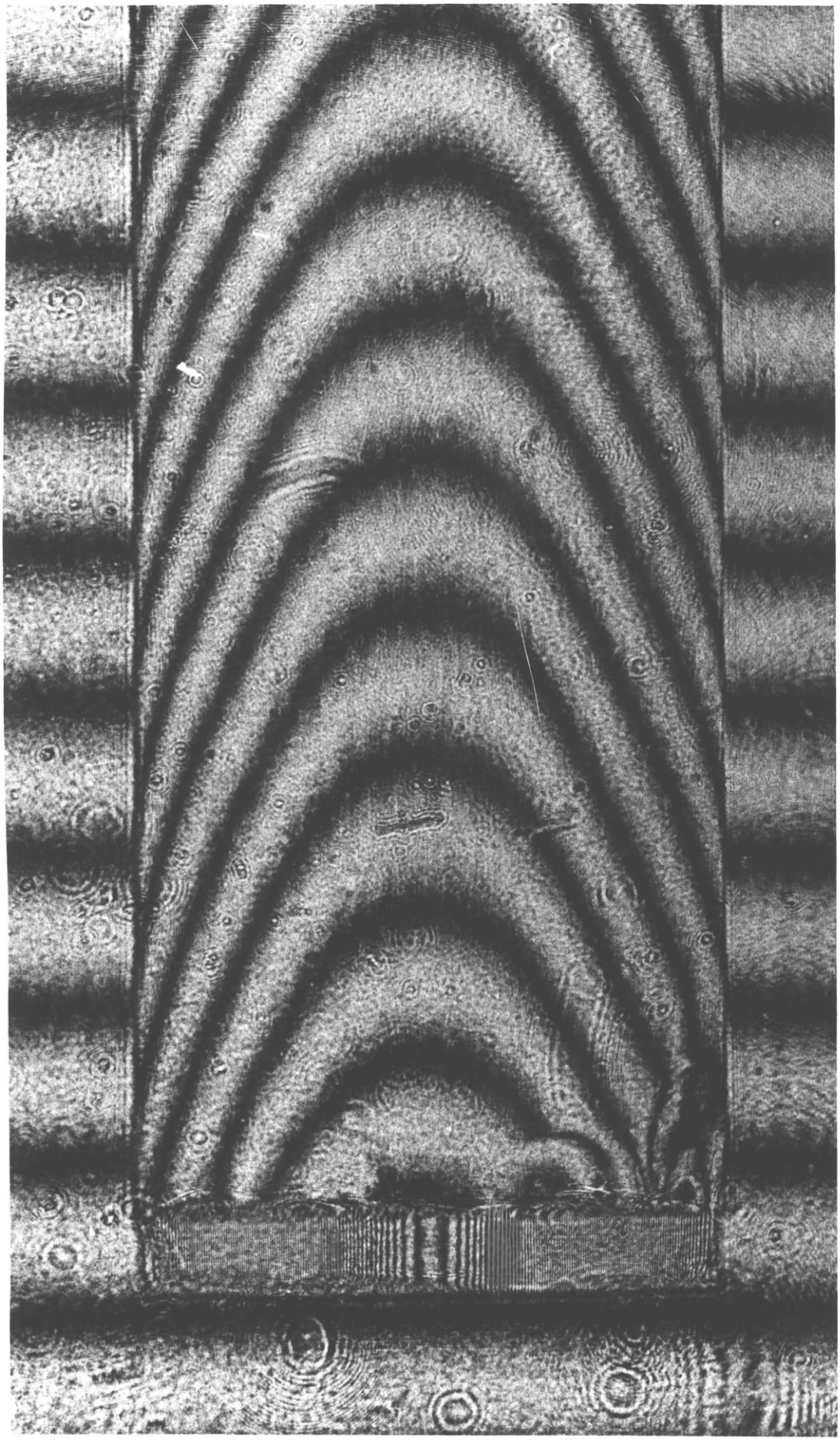
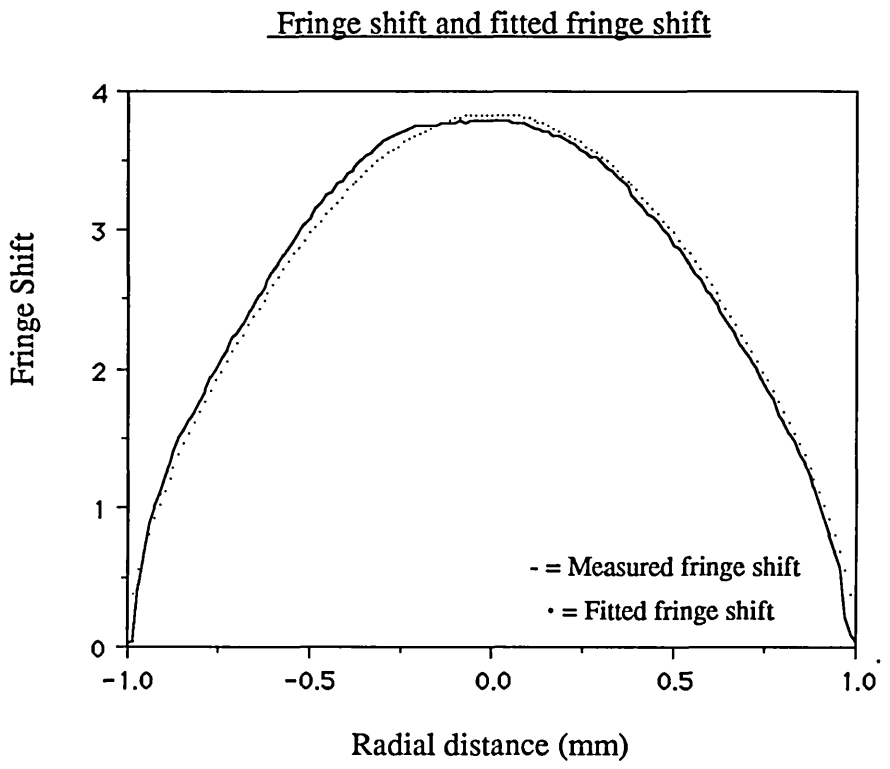
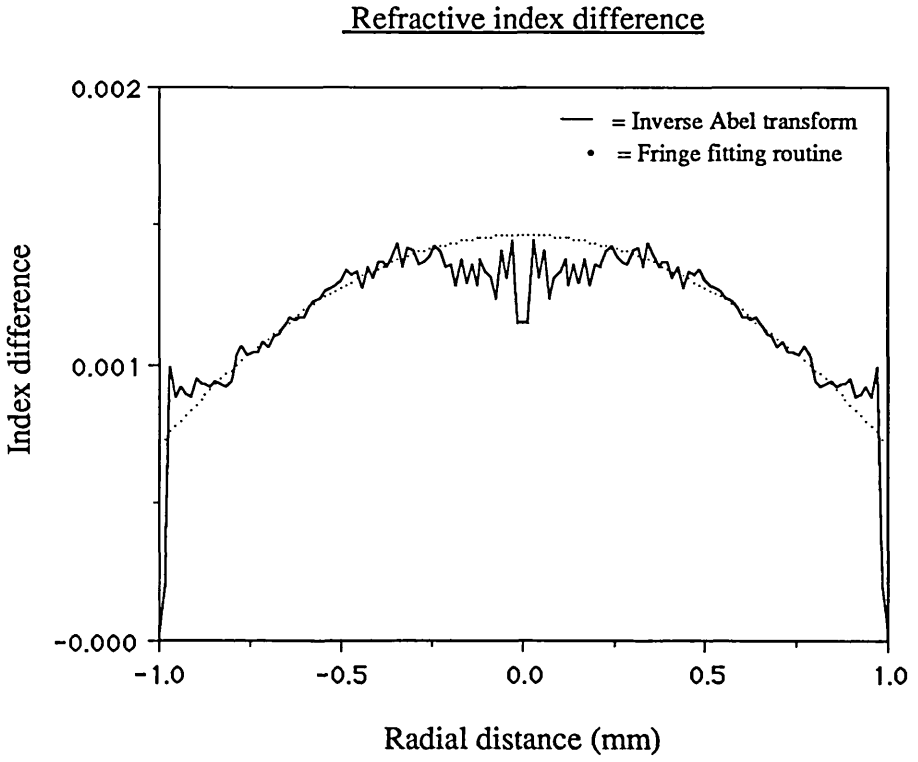


Figure 9.8: Results for comparison of GRIN rod samples A and B

a)




b)



1) Comparison of rod A with rod B

Figure 9.7 shows the interferogram produced by comparing a rod from sample A with a rod from sample B The fringe shift is of the order of 3 fringes at the centre of the rod and thus the index values of rod B are higher than those of rod A. Figure 9.8a shows the digitised fringe shift and to this is fitted the expected fringe shift functions (§7.5.3). From this fringe fit, the profile contants are calculated to be -

Rod A: $\sqrt{A} = 0.2500$ Dn = 0.0000

Rod B: $\sqrt{A} = 0.2519$ Dn = 0.0007.

The corresponding index difference is calculated and plotted in figure 9.8b. The smooth curve is from the fringe fitting procedure and the noisy function is the produced by the inverse Abel transform program. The functions are quite similar, however there is a noticeable drop in the axial index values computed by the inverse Abel transform routine (the fringe fit procedure assumes only parabolic differences and could not reflect such a feature). It is difficult to say whether this index drop is a genuine feature of the index distributions or an artifact of the numerical computation of the inverse Abel transform. In any case we can be certain that the difference in index between the two rods is less than $dn < 0.0015$.

2) Comparison of rod A with rod C

Figure 9.9 is the interferogram produced by the comparison of rod A and rod C. The resulting fringe shift is -2 fringes at the centre and the index values of rod C are on the whole less than those of rod A. Note that the fringe shift changes sign, and also the resulting fringe fit is quite poor (figure 9.10a). Nevertheless, the fringe fitting procedure yields the profile constants of the rod as

Rod A: $\sqrt{A} = 0.2500$ Dn = 0.0000

Rod C: $\sqrt{A} = 0.2474$ Dn = 0.0001.

Figure 9.9: Experimental interferogram - Graded index rod lens: Comparison of rod samples A and C.

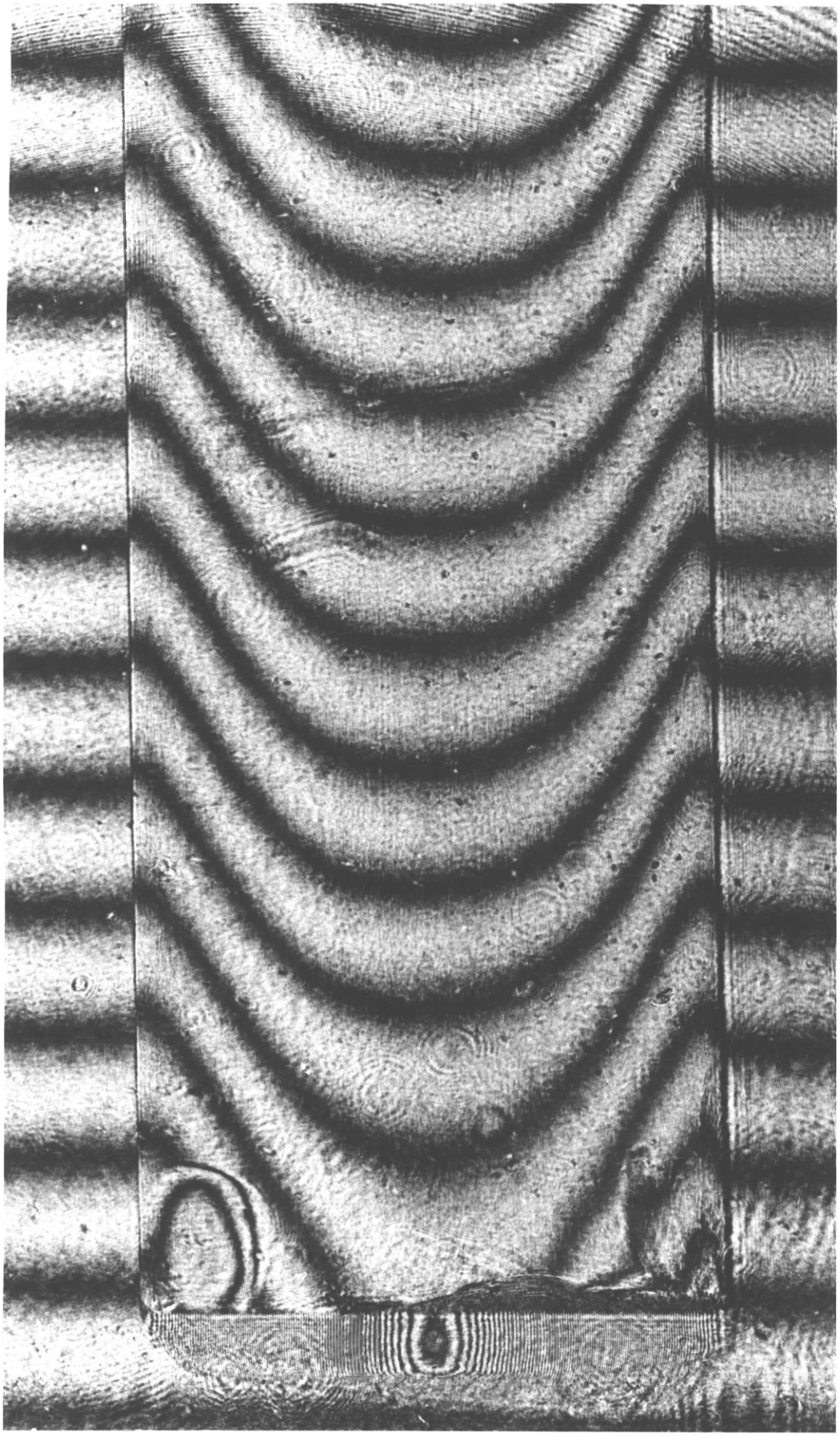
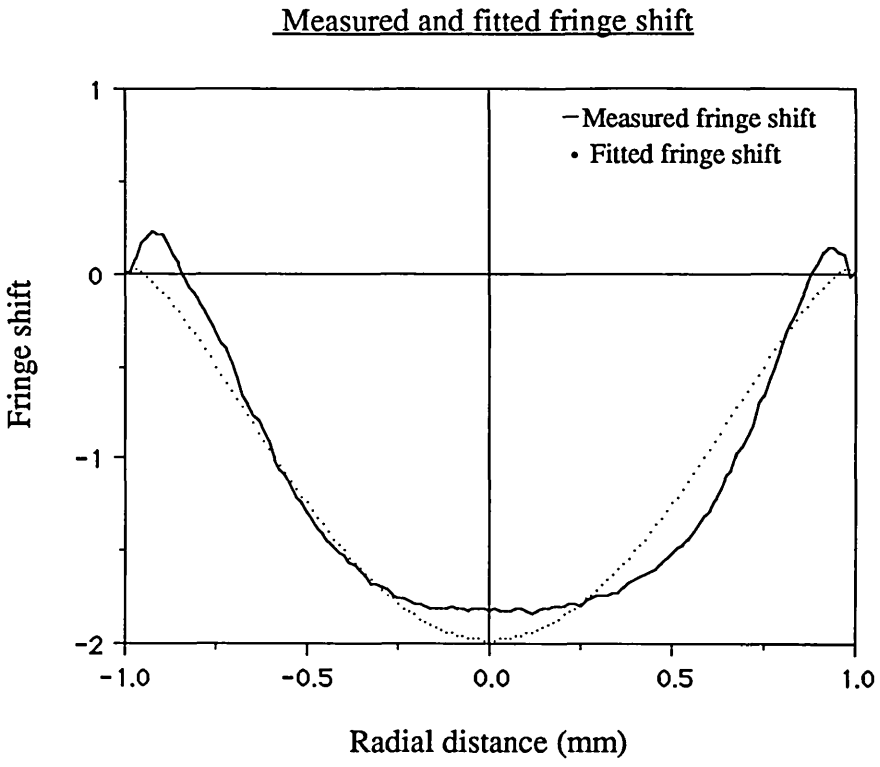


Figure 9.10: Results for comparison of GRIN rod samples A and C

a)




b)

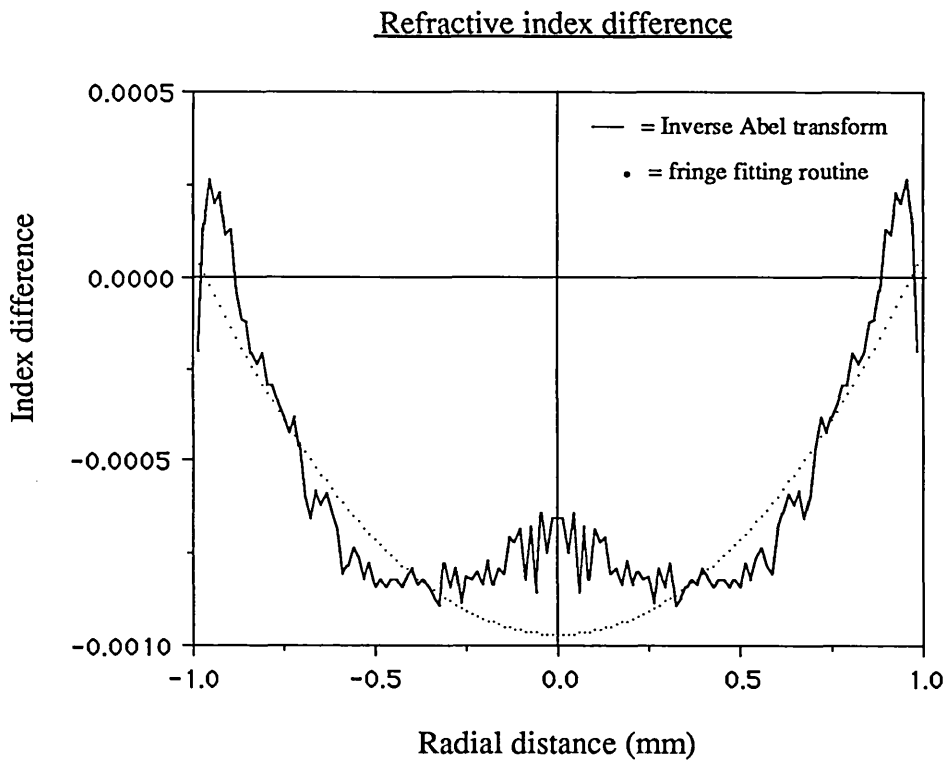
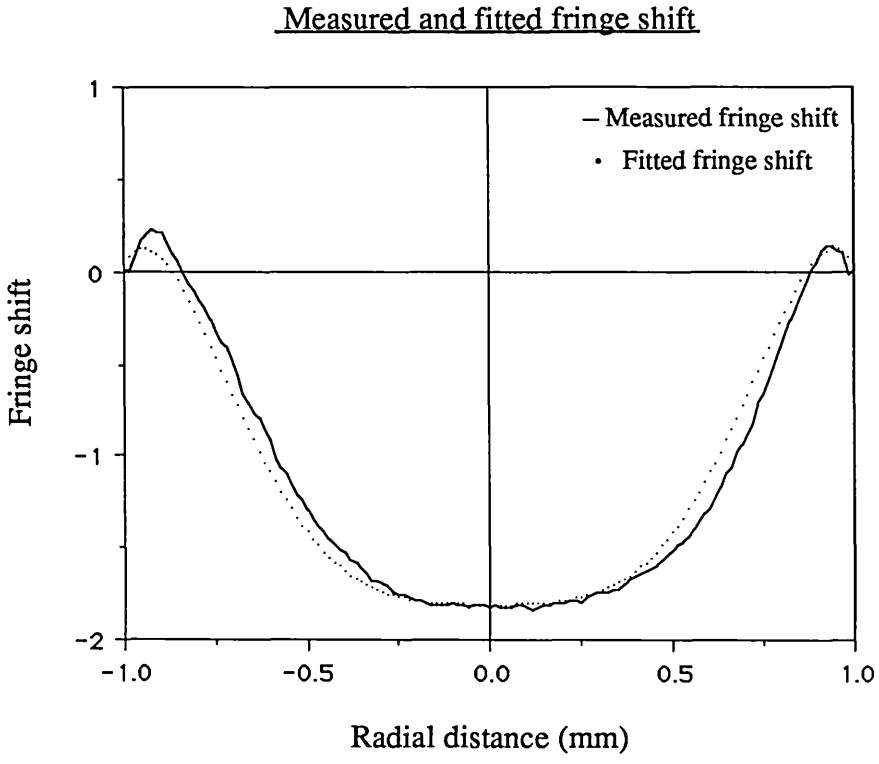
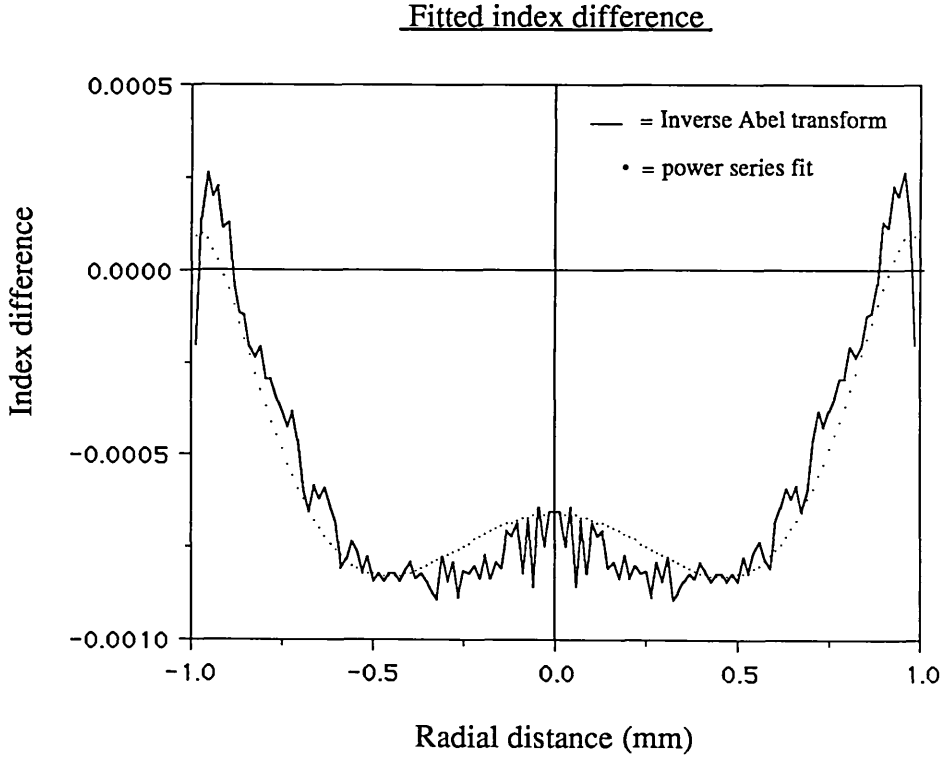


Figure 9.11: Further analysis of the results of the comparison of GRIN rod samples A and C

a)




b)



The calculated index difference is plotted in figure 9.10b along with the results of the produced by the inverse Abel transform program. Once again there is a noticeable dip in the index difference values in the central region of the figure. We can deduce from the figure that the difference in index between samples A and C is $dn \leq -0.001$.

Because of the poor fit of the fringe in figure 9.10a, we can further analyse the fringe data by using the power series fitting procedure described in chapter 7 (§7.5.2). The results for a 6th order (even powers only) fit to the digitised fringe shift are shown in figure 9.11. The fit to the fringe is far better than in figure 10, and the corresponding index difference (fig. 9.11b) follows closely the form of that computed numerically from the inverse Abel transform program. This only serves to emphasise how the results of the computation of the inverse Abel transform follow the choice of fitting functions.

3) Comparison of Rod C with Rod B

We have so far used the comparison technique to determine how the index distributions in GRIN rod samples B and C differ from the distribution in sample A. We now compare rod samples B and C directly and see if the results follow logically from the previous analysis (sections 1 and 2 above). For example, from the interferograms of figure 9.7 and 9.9, we can expect the fringe shift on the C-B interferogram to be of the order of $3 - \bar{2} \approx 5$ fringes and indeed in figure 9.12, we can see that this is the case. The digitised fringe shift and resulting index difference are shown in figure 9.13. Apart from the poor correspondence of the index difference functions in fig. 9.13b, we see that the difference in index is at most $dn \approx 0.002$. This follows on fairly well from the index difference figures 9.9b, and 9.10b, where we can estimate that the nett difference between samples B and C (calculated with respect to lens A) is $dn \approx 0.002$.

Figure 9.12 : Experimental interferogram - Graded index rod lens: Comparison of rod samples C and B.

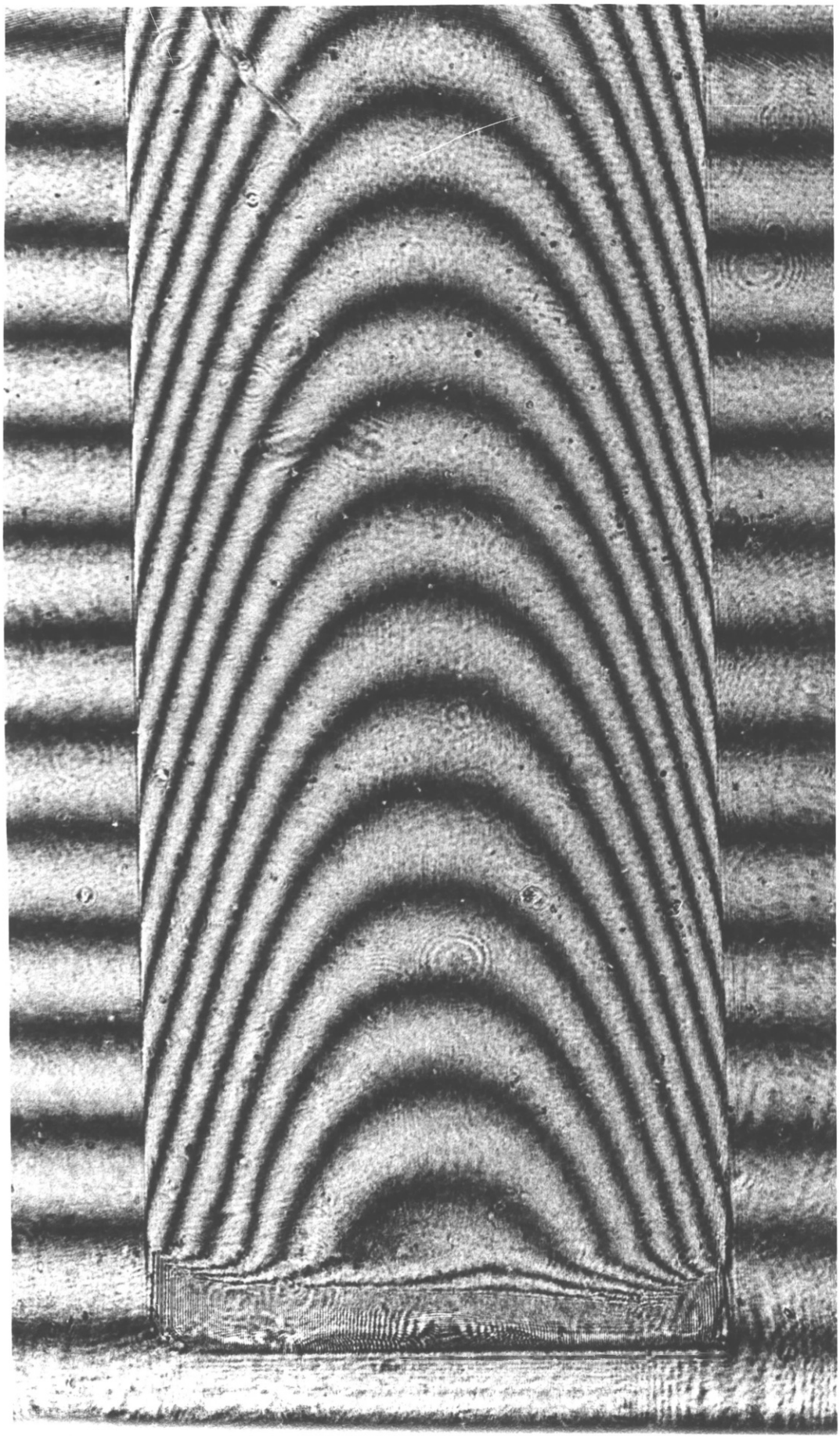
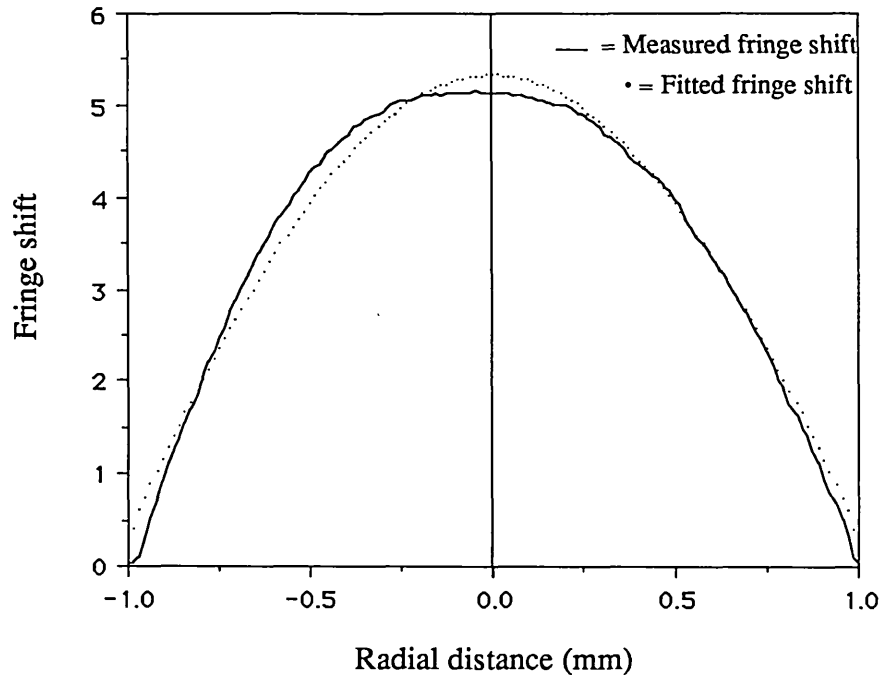
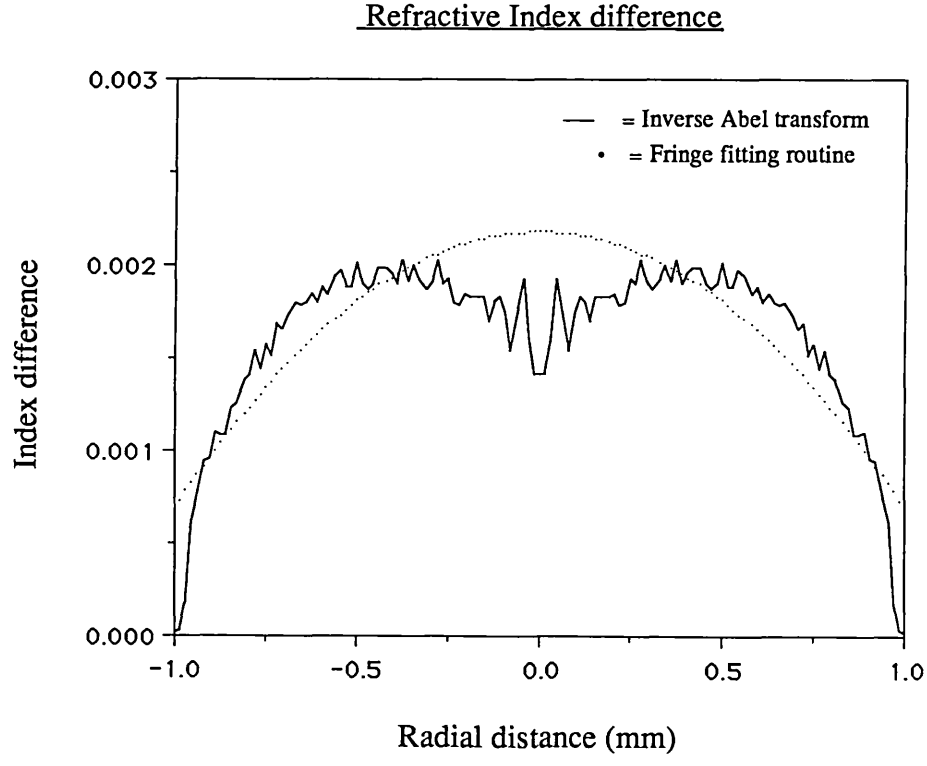


Figure 9.13: Results for comparison of GRIN rod samples B and C

a)




b)



9.5.Summary

The results of the comparison method applied to GRIN rod micro lenses are quite promising. The fringe patterns do not contain the sharp discontinuities that seem to be a characteristic of the preform rods and the shape of the fringe shift is repeated quite well along the length of the rod. Practically, there were certainly none of the problems posed by the comparison of the large preform rods and it is worthwhile noting how well the comparison method highlights the remarkable difference in the form (smoothness) of the index distributions of the ion stuffing and ion diffusion graded index rods.

A problem arises with the comparison method when we wish to quantify the difference in the refractive-index distributions of two GRIN samples from the measured fringe shift. The results of the previous section, highlights quite clearly the difficulty and indeed confusion that can arise when we compute the inverse Abel transform with noisy experimental data.

Fringe fitting with expected functions produces the results in a simple and attractive form (ie. a parabolic and/or constant change in the index profile), but the results rely upon the assumption that the differences in the index distributions can be ascribed straightforwardly to simple functions. The power series fitting technique produces results that follow quite closely to those produced by the inverse Abel transform program and there is no bias of the results. This fringe fitting procedure is probably the simplest and most reliable practical Abel inversion procedure.

On a more encouraging note, we must not overlook the possibilty of a direct analysis of the comparison interferograms without involving any index reconstruction procedure. For example, figure 9.6 shows directly that the profiles between the two rods under test are almost identical and hence in a prodction line environment we could confidently continue with the production process. Furthermore, a tolerance could be set upon the maximum permitted shift of the fringe from the tilt fringe position and thus GRIN rods could be accepted or rejected on the basis of whether the resulting comparison fringe shift

was within the accepted tolerance. We have seen in chapter 4 that the production line tolerance on the quadratic gradient constant $\sqrt{A}$ of a Nippon Sheet Glass micro-lens was $\pm$ 3% and the corresponding fringe shift was of the order of 6 fringes at the centre (see figure 4.4). Rod samples A, B and C all fall within this limit, and this is quite surprising considering that the rods were produced over a period of three years.

## CONCLUSION OF THESIS

We conclude this thesis with a summary and review of some of the important issues that have been raised by the research project.

### Holographic interferometry

We have used a holographic interferometer to perform comparative measurements upon the refractive index distributions of nominally similar graded index rods. It will be useful to discuss the relative advantages and disadvantages of using a holographic system rather than a conventional optical interferometer (a Mach-Zehnder (§2.4.1) being the most likely example).

A Mach-Zehnder interferometer could be used for a comparative test by placing the standard (or 'known') graded index sample in an optical cell in the reference arm of the interferometer, the rod sample having an unknown index distribution would be placed in an identical cell in the test arm of the apparatus. This system would avoid the need to record and process a hologram, and also it would eliminate some of the problems posed by long term (time dependent) instabilities of the apparatus ie. matching oil temperature fluctuations. However the significant disadvantage with the Mach-Zehnder lies in the cost of the components and in particular the need to construct two matched optical cells. In a research project , this latter factor could hinder the trial and error development necessary in establishing the best optical system. In a holographic interferometer, only one optical cell is required in the apparatus and any imperfections in the optical quality of this cell are cancelled out by the holographic recording and reconstruction procedure ( for a striking example of this see Vest[1] , pages 267 - 269). In this research project many different kinds of optical cell were employed with a minimal tolerance on the optical qualities. For example excellent results were obtained with optical cells machined out of perspex and polished by hand in the workshop.

A further important feature of a holographic system lies in the possibility of using a computer generated hologram from which the desired 'standard' wavefront may be

reconstructed. This would remove the need to produce a rod sample with a known index distribution, and in principle we create almost any kind of standard wavefront.

Holographic shearing interferometry

Refractive index profiling via 'live fringe' holographic shearing interferometry was investigated in chapter eight, and encouraging results were obtained for both preforms and rod lenses. The index distribution can be reconstructed from the measured fringe shift by using the inverse Abel transform and the problem posed by needing to differentiate the data is neatly avoided. The accuracy of the shearing method depends quite heavily on the precision with which the shearing displacement is known. This problem could be possibly be overcome by using a precision translation stage or by employing a shearing 'block' (§2.4.4) to introduce the necessary displacement of the transmitted wavefront.

Holographic comparison interferometry

The main thrust of this thesis has been to investigate the viability of refractive index profiling by comparing the refractive index distributions in two similar graded index rods. The theoretical basis of the method was described in chapter four and the theoretically predicted interferograms plotted in that chapter compared very favourably with the experimental fringe patterns produced further on in the thesis. This close agreement between experiment and theory also indirectly verified the use of the refractionless limit in analysing the optical pathlengths for rays passing transversly through graded index media.

The results of the comparison method applied to several classes of GRIN rod were presented in chapter nine. From this chapter we may conclude:

The comparison method is not readily applicable to refractive index profiling of preform rods. The large (10 mm plus) diameters of these rods have the effect that only slight variations in either the the dimensions of the rod or the index distribution produce correspondingly large fringe shifts on the interferogram. The method is found to be too

sensitive to these changes and in particular those changes that are not of great importance in determining the transmission properties of the resultant optical fibre (ie. preform diameter fluctuations or ellipticity).

Furthermore, the nature of the index distributions in preform rods complicates the fringe analysis procedure. Ion deposition preforms contain large index changes at the the edges and centre of the GRIN core and corespondingly they give rise to rapid fringe fluctuations that cannot be sensibly followed by the measuring system. Ion stuffing preforms have a graded index distribution that is not smooth and only a slight rotation or displacement of the rod in the optical cell is sufficient to 'lose' the fringe pattern altogether. The comparison method dramatically revealed why the ion stuffing method is no longer considered to be viable for GRIN fibre production.

The results of the comparison method applied to rod micro-lenses were very encouraging. The profiles in these rods are sufficiently smooth to enable several different rods to be interferometrically compared with each other. Also, the index distributions in the rod showed little variation with rod length or with a rotation of the rod. However, problems can arise when we attempt to accurately associate an observed comparison interferogram with the corresponding difference in the index distributions. The fringe shift must be measured with great precision if the direct numerical computation of the inverse Abel transform is to be used for this calculation, otherwise the slightest noise on the data is amplified by the reconstruction algorithm. The measured fringe shift can be fitted with certain smoothing fringe fitting procedures described in in chapter seven however this produces results that are dependent upon the choice of the fitting functions. In theory, the accuracy of the index measurement of the index values of a 2mm GRIN rod lens is of the order of $\varepsilon n \approx \pm 5 \times 10^{-5}$.

It is possible to analyse the comparison interferograms directly by setting a tolerance on the maximum allowed deviation of the fringe from the uniform tilt fringe position. For example the production line tolerance on the quadratic gradient constant ($\sqrt{A}$) for Nippon

Sheet Glass rod micro-lenses would correspond to a shift of approximately 6 fringes on a comparison interferogram (§4.4.1). Nominally identical graded index rod samples were obtained from the Nippon Sheet Glass company at yearly intervals. The interferometric comparison of these samples produced fringe shifts that were all within the above tolerance limit (chapter nine). The fact that this could be observed simply and quickly by eye, by an unskilled operator implies that the comparison method would be very useful for a production line go/no-go test in the fabrication of these rod samples.

The fluctuation of GRIN rod diameters poses a fairly significant problem to comparison testing. Firstly, there is in principle no simple way of discriminating between the pattern due to a change in the profile parameters and that due to a diameter variation (ie. it is possible to produce identical interferograms from the two different effects, cf. figures 4.7 and 4.8 ). Secondly, the shape of the index profile is of far greater importance to an index profiling method rather than the overall dimension (or scale). This is particularly the case in preform production, where a strict control of the rod diameter can be kept upon the fibre at the pulling stage. For rod lenses with diameter variations all within 10 microns the precison of the index measurement is (in theory) limited to $\varepsilon n \approx \pm 5 \times 10^{-4}$.

## FUTURE WORK

Future work on the comparison method would involve the development of a more accurate fringe interpretation procedure and an attempt to eliminate the problem posed by the comparison of rods with different diameters.

An accurate fringe interpretation procedure would require a high resolution video digitisation system and an inverse Abel transform algorithm that is not too sensitive to signal noise (for example, Hansen[2] has described how a Kalman filter can be used for practical computation of the Abel transform).

One possible approach to the diameter variation problem is to devise a method for ensuring that the reference and test rods have the same diameter before performing the comparison test. This will require an accurate technique for measuring the diameter of a rod lens and for this we could use a gauge interferometer (Ditchburn[3],page 269). In this interferometer, a cylinder (or perhaps a ball bearing) of a known diameter is used as the reference sample to which cylinder of unknown diameter can be accurately calibrated. The method can measure diameter variations to at least within $\lambda/2$ and preliminary experiments using a Fizeau interferometer indicated that the method has potential in measuring diameter variations between rod micro-lenses.

Having found the diameter of the rod under test we would need to produce a standard rod with almost an identical diameter.One method is to have a set of reference holograms and a kinematic holographic plateholder. The holograms (perhaps computer generated) would contain the profile information of the known standard rod for a range of rod diameters, 1 micron intervals for example. Prior to comparison testing, the diameter of the rod under test can be measured using the technique above , and the appropriate hologram selected and inserted into the plateholder. There would thus be little or no ambiguity in the ultimate fringe analysis.

A further extension of this idea would be to have a tapered standard rod, with the diameter along the rod varying between the maximum and minimum possible diameter variations ( ± 20 microns for example). The test rod diameter could then be measured and

the resulting fringe information derived at the diameter matching point on the interferogram.

## REFERENCES

1) C.M. Vest, "Holographic Interferometry," Wiley, (1979).

2) E.W. Hansen and P. Law, "Recursive Methods for Computing the Abel Transform and its Inverse," J.O.S.A, 501, 1985.

3) R.W. Ditchburn, "Light," Blackie & Son Ltd, 1953.

# APPENDIX A

## Ray Paths in Graded Index Media

Ray trajectories in refractive media can be described by a differential equation (M. Born and E. Wolf[1] page 121) that is often referred to as the Ray Equation

$$(a.1) \quad \frac{d}{ds}\left(n_{(r)}\frac{dr}{ds}\right) = \nabla n_{(r)}$$

r = position vector for a point on the ray

n(r) = refractive index value at position r

$\nabla$n(r) = gradient of the scalar (index) field; specifies how the index is changing in x,y,z directions.

s = distance measured along the (curved) ray path

$dr/ds$ = unit vector tangent to the ray path at r, specifying the ray trajectory at that point.

Given any index gradient ($\nabla$n) we may determine the ray trajectory at any point in the medium from this general ray equation. Thus we now show (after Ghathak and Thyagarajan[2]) that rays follow sinusoidal paths in the typical graded index media of rod lenses and optical fibres.

## A.1 Paraxial Approximation

For rod with a parabolic profile given by

$$(a.2) \quad n^2_{(r)} = n_0^2 \left(1 - A\left(x^2 + y^2\right)\right)$$

only paraxial rays (rays making small angles with the (z) axis of the rod) are focussed with an identical period.

Because there is no variation of the refractive index in the z direction, the ray

equation becomes for the z component

$$(a.3) \quad \frac{d}{ds}\left(n_{(r)}\frac{dz}{ds}\right) = 0$$

ie.

$$(a.4) \quad n_{(r)}\left(\frac{dz}{ds}\right) = C$$

where C is a constant.

If at the point $x_0, y_0$, the ray makes an angle $\gamma_0$ with the z axis, then

$$(a.5) \quad C = n(x_0, y_0)\cos\gamma_0$$

The x component of the ray equation is

$$(a.6) \quad \frac{d}{ds}\left(n_{(r)}\frac{dx}{ds}\right) = \frac{dn}{dx}$$

$$(a.7) \quad \frac{dn}{ds}\cdot\frac{dx}{ds} + n_{(r)}\frac{d^2x}{ds^2} = \frac{dn}{dx}$$

Rearranging equation (a.4) gives

$$(a.8) \quad \frac{d}{ds} = \left(\frac{C}{n_{(r)}}\right)\frac{d}{dx}$$

Thus eq. (2.7 becomes

$$(a.9) \quad \left(\frac{C}{n_{(r)}}\right)^2\left(\frac{dn}{dz}\right)\left(\frac{dx}{dz}\right) + n_{(r)}\left(\frac{C}{n_{(r)}}\right)^2\frac{d^2x}{dz^2} = \frac{dn}{dx}$$

Thus as $dn/dz = 0$

$$(a.10) \quad \frac{d^2x}{dz^2} = \left(\frac{n_{(r)}}{C^2}\right)\frac{dn}{dx}$$

or

$$(a.11) \quad \frac{d^2x}{dz^2} = \left(\frac{1}{2C^2}\right)\frac{dn^2}{dx}$$

For the parabolic profile of eq. (a.2) it can be shown that a solution of equation (a.11) is

(a.12) $$x(z) = K \sin\left(\frac{\sqrt{A}\, n_0\, z}{C}\right)$$

From this equation we see that in general the oscillation of the ray is dependent upon the input angle of the ray (C). However for the paraxial case where the rays travel at small angles close to the rod axis, we may write $\cos \gamma_0 = 1$ and thus

(a.13) $$x(z) \;\alpha\; \sin(\sqrt{A}\, z)$$

ie. ray paths are sinusoidal with a period ($p = 2\pi/\sqrt{A}$), independent of the ray input angle.

I.2 Ideal Index Profile

We have seen above that a parabolic profile will only focus paraxial rays with an identical period of oscillation. For identical focussing of all meridional rays (rays passing through the axis), the profile should be given by the expression

(a.14) $$n(x) = n_0 \operatorname{sech}(\alpha x)$$

To show that all rays propagating in such a medium, are guided with the same period of oscillation regardless of input angle, we refer back to equation (a.11) and multiply through with 2 (dx/dz) dz, which yields

(a.15) $$2\left(\frac{dx}{dz}\right)\left(\frac{d^2x}{dz^2}\right)dz = \frac{1}{C^2}\left(\frac{dn^2}{dx}\right)\left(\frac{dx}{dz}\right)dz$$

and this becomes

(a.16) $$\frac{d^2x}{dz^2} = \frac{n^2(r)}{C^2} + K$$

The constant C was defined earlier as $C = n(x_0,y_0)\cos\gamma_0$, and for a ray arbitrarily input on axis (z=0) and in the x plane (y=0) at the point $x_0$ we have $dx/dz = \tan\gamma_0$. With these input conditions, it can be shown that K = -1 and so equation (a.16) becomes

(a.17) $$\left(\frac{dx}{dz}\right)^2 = \frac{n^2}{n^2(x_o)\cos^2\gamma_o} - 1$$

Using the above expression for the refractive index profile gives

(a.18) $$\left(\frac{dx}{dz}\right)^2 = B^2\mathrm{sech}^2(\alpha x) - 1$$

where

$$B = \frac{n_o}{n(x_o)\cos\gamma_o}$$

Therefore

(a.19) $$\int \frac{1\,dx}{(B^2\mathrm{sech}^2(\alpha x) - 1)^{1/2}} = \int dz$$

Multiplying through by Cosh(αx) yields

(a.20) $$\int \frac{\cosh(\alpha x)\,dx}{(B^2 - \cosh^2(\alpha x))^{1/2}} = \int dz$$

If we make a change of variable

(a.21) $$\phi = \frac{1}{(B^2 - 1)^{1/2}}\sinh(\alpha x)$$

(a.22) $$d\phi = \frac{\alpha}{(B^2 - 1)^{1/2}}\cosh(\alpha x)\,dx$$

The integral becomes

(a.23) $$\frac{1}{\alpha}\int \frac{d\phi}{1 - \phi^2} = z + D$$

(D is a constant of integration) which is a trigonometric integral with the standard solution

(a.24) $$\frac{1}{\alpha}\,\mathrm{Arcsin}(\phi) = z + D$$

Therefore

(a.25) $\sinh(\alpha x) = (B^2 - 1)^{1/2} \sin[\alpha(z + D)]$

Thus the ray path is

(a.26) $x(z) = \frac{1}{\alpha} \text{Arcsinh}\{(B^2 - 1)^{1/2} \sin[\alpha(z + D)]\}$

Although this expression is rather complicated, the ray paths are periodic in z with a period $p = 2\pi / \alpha$ that is independant of $x_0$ and $\gamma_0$ ie. the ray input position and injection angle.

1) M. Born and E. Wolf, "Principles of Optics," 6th Edition, Pergamon Press, 1983.

2) A.K. Ghatak and K. Thyagarajan, "Contemporary Optics," Plenum Press, New York, 1978.

# APPENDIX B

```
/*
PROGRAM HOLOCOMP
Program to plot the interferogram produced by the holographic
comparison of two cylindrical graded index rods with parabolic
refractive index profiles.


Original source     N.R.Haigh, Ph.D Thesis Imperial College London Oct.1987
Rewritten in C-code          N.J.Wooder, Imperial College London

Calculates comparison fringes due to :
1)      Difference in rod radii.
2)      Difference in index profile (gradient constant + index offset)
3)      Shear misalignment of rods.
4)      Defocus misalignment of rods.
5)      Rotational misalignment of rods.

COMPILE using cc -f68881 -O fringes.c -o fringes -lm

*/
#include <errno.h>
#include <stdio.h>
#include <math.h>

#define XLEN 256            /* Size of screen array */
#define YLEN 256

/* Set up structure for lens data */

typedef struct {
                    float   radius1;        /* Radius of rod number 1 */
                    float   radius2;        /* Radius of rod number 2 */
                    float   constant1;      /* Gradient constant A of lens 1 */
                    float   constant2;      /* Gradient constant A of lens 2 */

                    float   offset1;        /* Constant offset of rod peripheral */
                    float   offset2;        /*  index from matching oil value */

                    } lens_data_type;

/* set up another structure for the system data */

typedef struct {
                    float  shear;                   /* Displacement of rod across
                                                       optical axis */

                    float   defocus;                /* Longitudinal displacement
                                                       of rod along optical axis */

                    float   number_of_tilt_fringes;/* ,in interferogram */
                    float   lens_tilt_angle;/* Angle of rotation of rod
                                                       about axis */
                    float   cos_angle;
                    float   sin_angle;
                    } system_data_type;

main()
{
        float   N_oil = 1.516;          /* Refractive index of matching oil */
        float   LAMBDA = 0.632E-3;      /* HeNe wavelength in millimeters */

        lens_data_type lens_data;
        system_data_type system_data;

        /*_____End of type declarations _____*/
```

```
        /* get relevant data from file or keyboard ,put data in structures */

        get_lens_data(&lens_data);
        get_system_data(&system_data);

        /* Print out all data to a file for checking purposes */
        print_all_data(lens_data,system_data);

        /* main section of program */
        plot_fringe(LAMBDA,N_oil,lens_data,system_data);


}

get_lens_data(lens_data)
        lens_data_type *lens_data;
{
/* Get all the data for the lens system in use */
        float       rootA1,rootA2;

        fprintf(stderr,"Radius of first rod\n");
        scanf("%f",&(lens_data -> radius1));
        fprintf(stderr,"Radius of Second rod\n");
        scanf("%f",&(lens_data -> radius2));

        /* Read in the square root of the constant A , then square it
         lens one first */
        fprintf(stderr,"Quadratic Gradient Constant of lens #1 \n");
        scanf("%f",&rootA1);
        fprintf(stderr,"What is the offset in lens #1 profile values \n");
        scanf("%f",&(lens_data -> offset1));

        /* Now lens two */
        fprintf(stderr,"Quadratic Gradient Constant of lens #2 \n");
        scanf("%f",&rootA2);
        fprintf(stderr,"What is the offset in lens #2 profile values \n");
        scanf("%f",&(lens_data -> offset2));

        (*lens_data).constant1 =rootA1 *rootA1;
        (*lens_data).constant2 =rootA2 *rootA2;
}

get_system_data(system_data)
        system_data_type *system_data;
{
 /* Get data relevant to positioning of rod 2 in the system */

        float temp;

        fprintf(stderr," Shearing Distance (microns) = \n");
        scanf("%f",&temp);
        /* Read in Shear in microns, convert to millimeters */
        (*system_data).shear = temp *1E-3;

        fprintf(stderr,"Defocus Distance (microns) = \n");
        scanf("%f",&temp);
        /* Read in Defocus in microns, convert to millimeters */
        (*system_data).defocus = temp *1E-3;

        fprintf(stderr,"What is the Rod Tilt Angle (degrees) = \n");
        scanf("%f",&temp);

        /* Theta converted from degrees to radians*/
        (*system_data).lens_tilt_angle= M_PI/180.0 * temp;

        /* Calculate cos and sin of angle now to improve speed of run */
```

```
        (*system_data).cos_angle= cos((*system_data).lens_tilt_angle);
        (*system_data).sin_angle= sin((*system_data).lens_tilt_angle);

        fprintf(stderr,"Number of TILT fringes \n");
        scanf("%f",&(system_data -> number_of_tilt_fringes));
}
print_all_data(lens_data,system_data)
        system_data_type system_data;
        lens_data_type lens_data;
{
/* Print out all the data, lens and system to a file called info */
        FILE *out_file;
        float    temp;

        out_file=fopen("info","w");

        fprintf(out_file,"Radius of first rod %f \n",lens_data.radius1);
        fprintf(out_file,"Radius of second rod %f \n",lens_data.radius2);
        temp= sqrt((double)lens_data.constant1);
        fprintf(out_file,"Quadratic Gradient Constant of lens #1 %f \n",temp);
        fprintf(out_file,"Offset first rod profile values %f \n",lens_data.offset1);
        temp= sqrt((double)lens_data.constant2);
        fprintf(out_file,"Quadratic Gradient Constant of lens #2 %f \n",temp);
        fprintf(out_file,"Offset second rod profile values %f \n",lens_data.offset2);
        fprintf(out_file,"Shearing Distance (microns) %f \n",system_data.shear*1000.0);
        fprintf(out_file,"Defocus Distance (microns) %f \n",system_data.defocus*1000.0);
        temp =system_data.lens_tilt_angle * 180.0/M_PI;
        fprintf(out_file,"Rod Tilt Angle (degrees)  %f \n",temp);
        fprintf(out_file,"%f tilt fringes \n",system_data.number_of_tilt_fringes);
        fclose(out_file);

}

/*_____________________________________________________________*/


plot_fringe(LAMBDA,N_oil,lens_data,system_data)
        float    LAMBDA,N_oil;
        system_data_type system_data;
        lens_data_type lens_data;

/* Main procedure for ploting interferogram */

{
        int      ytop,xtop;              /* Top of screen */
        int      xoffset,yoffset;        /* Centre of screen */
        int      ypix,xpix;              /* Pixel coordinates */
        float    xdist,ydist;            /* Physical dimensions of interferogram (mm) */
        float    xscale,yscale;          /* Scaling  factors for pixel to real coords */
        float    yvalue,xvalue;          /* Scaled pixel coords */
        float    tilt;                   /* Scale tilt fringes to interferogram */
        float    opt_path_length;                /* Optical path length */
        float    Intensity;              /* Intensity of a pixel */
        float    phase;                  /* Phase of ray */

        float    calculate_opt_path_length();            /* Declare procedure */

        FILE   *out_file;            /* File for the calculated output data */

        /* Main routine */

        /* SET_SCALE */

        ytop=YLEN;
```

```
        xtop=XLEN;
        xoffset=xtop/2;
        yoffset=ytop/2;
        xdist=3.0; /* set physical dimension to 3mm */
        ydist=3.0;
        xscale=xdist/(float)xtop;
        yscale=ydist/(float)ytop;

        tilt=LAMBDA* system_data.number_of_tilt_fringes /ydist;

        out_file =fopen("data_f_256_256.d","w");
        fprintf(stderr,"\nFile opened\n");

        /* Now go through whole 256 by 256 array and calculate optical path
                length for each ray and hence phase */

        /* Go through virtual pixel cords from -offset to offset */
        for(ypix= -yoffset; ypix<yoffset ;++ypix)
        {
                yvalue = ypix*yscale;
                for(xpix= -xoffset; xpix<xoffset ;++xpix)
                {
                        xvalue = xpix*xscale;

                        /* Find the optical path length at each pixel coord */
                        opt_path_length =yvalue*tilt+
                         calculate_opt_path_length(xvalue,yvalue,N_oil,lens_data,system_data);

                        phase=2*M_PI*opt_path_length/LAMBDA;
                        Intensity=(1+cos(phase));

                        /* Write out intensity at the point xpix,ypix
                        to the output file. Intensity is a float so write out
                                the four bytes needed */
                        fwrite(&Intensity,4,1,out_file);
                }
        }
        fclose(out_file);
        fprintf(stderr,"\nProgram finished, File closed\n");

}

/*_____________________________________________________________________*/

float calculate_opt_path_length(x,y,N_oil,lens_data,system_data)
        float   x,y;    /*      Scaled values of coords */
        float  N_oil;
        system_data_type system_data;
        lens_data_type lens_data;
        /* Procedure to calculate the optical pathlength at a
                point x,y on the interferogram */
{
        float   shft(),offset();                /* declare procedures */

        float   R;      /* Readjusted radial coord of second rod relative to rod 1 */
        float   shift1=0,shift2=0;              /* Transverse wavefront retardation through rod */
        float   defocus_value;                  /* Opt.Path.Increment due to defocus */
        double  phi;                            /* Ray refraction angle in second wavefront */

        /* end of declarations */

        R=x* system_data.cos_angle - y* system_data.sin_angle + system_data.shear;

        /* Subroutine to calculate the change in the readjusted radial coord due to a defocus */

        find_defocus(&defocus_value,&phi,lens_data.radius1,x,lens_data.constant1,system_data.defocus,N_oil);
```

```
        R -= system_data.defocus * tan(phi);

        shift1= shft(lens_data.radius1,lens_data.constant1,x,N_oil) +
                offset(lens_data.radius1,lens_data.offset1,x);

        shift2= shft(lens_data.radius2,lens_data.constant2,R,N_oil) +
                offset(lens_data.radius2,lens_data.offset2,R);

        return((shift1-shift2)-defocus_value);

}

/*_____________________________________________________________________*/

float offset(radius;offset_value,x)

        float radius,offset_value,x;
        /* Procedure to calculate wavefront retardation for wave passing
          transversly through a circularly symmetrical field of
          constant index */
{
        x= fabs((double)x);
        if (x > radius) return(0.0);
        else    return(2*offset_value*sqrt(radius*radius-x*x));
}

/*_____________________________________________________________________*/


find_defocus(defocus_value,phi,radius,x,constant,defocus,N_oil)
        float   *defocus_value;
        double  *phi;
        float  radius,defocus,x;
        float  N_oil;
        float  constant;
        /* Procedure to calculate shape of defocus wavefront */
{
        double rhs,secphi;

        if(((fabs((double)x)) > radius ) || (defocus == 0.0))
        {
                *defocus_value =0.0;
                *phi=0.0;
        }
        else
        {

                rhs= ((double)(2.0*x/(radius*radius))) *sqrt((double)(radius*radius-x*x));

                *phi = atan((double)( -1.0 * (constant/(1.0-0.5*constant))) * rhs);

                secphi= 1.0/cos(*phi);

                *defocus_value = (double)(N_oil * defocus) * (secphi-1.0);

        }

        /* Return defocus_value  and phi */

}

/*_____________________________________________________________________*/
```

```
/*_____________________________________________________________*/

float shft(radius,constant,x,N_oil)
        float   radius,constant,x,N_oil;

        /* Procedure to calculate wavefront retardation for wave passing
          transversly through a circularly symmetrical parabolic index field */
{
        float   beta;
        x= fabs((double)x);
        if(x > radius) return(0.0);
        else

        {
                beta=(2*N_oil*constant/(3*radius*radius*(1-0.5*constant)));
                return(beta * (float)pow((double)(radius*radius-x*x),1.5));
        }
}
```

# APPENDIX C

## Chemicals for processing silver halide holograms

Developer: P.A.A.P

| | |
|---|---|
| Sodium hydroxide | 12 g |
| Ascorbic acid | 18 g |
| Sodium phosphate dibasic | 28.4 g |
| Phenidone | 0.5g |

Comments: Dissolve in distilled water in the order above and make up to 1 litre.

Fixer: Agfa G334 or Hypam

Bleach: GP - 431

| | |
|---|---|
| Ferric-nitrate - 9 hydrate | 150g |
| Potassium bromide | 30g |

Comments: Make up to 1 litre of distilled water. Use 1 part of the bleach to 4 parts of water, and bleach plate until 60 seconds after it becomes transparent.

PHYSICS LIBRARY
BLACKETT LABORATORY
IMPERIAL COLLEGE
PRINCE CONSORT ROAD
LONDON SW7 2BZ